Inkjet Printing of Two Dimensional Materials

A thesis Submitted to the University of Manchester for the Degree of Doctor of Philosophy in the Faculty of Science and Engineering

2016

Pei He

School of Materials

Contents

Inkjet Printing of Two Dimensional Materials
The University of Manchester
Doctor of Philosophy
Pei He 2016

Abstract

Over the last decade, two dimensional (2D) materials have attracted considerable attention from both the scientific and engineering community due to their unique properties. One important advance of 2D materials is that they can be exfoliated into nanosheets suspended in a liquid phase and that this allows the formulation of 2D nanomaterials inks. Such inks can be deposited as functional components through low-cost inkjet printing techniques. Many 2D materials based inks have been produced over the years. This thesis investigates the use of inkjet printing to deposit 2D materials such as graphene oxide (GO) and black phosphorus (BP).

GO, a derivative of graphene, has been widely used to produce graphene-based conductors via inkjet printing owing to its good stability in readily available solvents such as water. In this work, highly conductive reduced graphene oxide (rGO) films with bulk conductivity in excess of 2×10^4 Sm^{-1} have been prepared by inkjet printing a GO aqueous ink, with mean flake size 35.9 μm, through a 60 μm inkjet printing nozzle followed by a reduction step. Experimental results showed that individual GO flakes up to 200 μm diameter can be successfully printed with no instances of nozzle blocking or poor printing performance. The mechanism by which this occurs is believed to be GO sheet folding during drop formation followed by elastic unfolding during drop impact and spreading. In addition, the influence of GO flake size on rGO film conductivity has been investigated. It was found that the rGO film conductivity increased about 60% when the mean flake size of the GO flakes in the ink increases from 0.68 μm to 35.9 μm.

The drying behaviour of printed GO droplets has been studied on eight GO aqueous inks in which the mean flake size of GO was varied over a range from 0.68 to 35.9 μm. It was found that the coffee ring effect (inhomogeneous drying of a droplet to leave a ring like deposit) of dried droplets of the GO ink weakened and disappeared when the flake size increasing. It was found that, with a printed deposit around 340 μm in diameter, the coffee ring effect (CRE) was suppressed with the mean flake size > 10.3 μm. The critical flake size for CRE suppression reduced to 5.97 and 3.68 μm when the substrate temperature was 40 and 50 °C, respectively. It was further found that the CRE weakened with decreasing printed drop size, with the critical flake size reducing to 1.58 μm with a printed drop diameter of 30 μm.

The interaction between BP nanometre thickness flakes and humid atmospheres was investigated using an inkjet printed BP sensor. The BP sensor showed was very sensitive to changes in humidity with a response time of a few seconds and the effect is reproducible in minutes. However, long term exposure to humid air with a relative humidity (RH) > 11% leads to a significant chemical change in the BP films, with Fourier transform infra-red spectroscopy (FTIR) indicating partial hydrolysis of the BP to form phosphate and phosphonate ions. Low temperature heat treatment of BP films under dry conditions after exposure to elevated RH leads to a partial recovery of the impedance response and reversion to a chemical state similar to that before exposure to a humid environment. The recovery of BP properties is most complete after exposure to lower humidity environments (RH < 11%), although exact replication of the original impedance response and FTIR spectrum was not possible.

Declaration

No portion of the work referred to in the thesis has been submitted in support of an application for another degree or qualification of this or any other university or other institute of learning.

Copyright Statement

i. The author of this thesis (including any appendices and/or schedules to this thesis) owns certain copyright or related rights in it (the "Copyright") and he has given The University of Manchester certain rights to use such Copyright, including for administrative purposes.

ii. Copies of this thesis, either in full or in extracts and whether in hard or electronic copy, may be made only in accordance with the Copyright, Designs and Patents Act 1988 (as amended) and regulations issued under it or, where appropriate, in accordance with licensing agreements which the University has from time to time. This page must form part of any such copies made.

iii. The ownership of certain Copyright, patents, designs, trademarks and other intellectual property (the "Intellectual Property") and any reproductions of copyright works in the thesis, for example graphs and tables ("Reproductions"), which may be described in this thesis, may not be owned by the author and may be owned by third parties. Such Intellectual Property and Reproductions cannot and must not be made available for use without the prior written permission of the owner(s) of the relevant Intellectual Property and/or Reproductions.

iv. Further information on the conditions under which disclosure, publication and commercialisation of this thesis, the Copyright and any Intellectual Property and/or Reproductions described in it may take place is available in the University IP Policy (see http://www.campus.manchester.ac.uk/medialibrary/policies/intellectual-property.pdf), in any relevant Thesis restriction declarations deposited in the University Library, The University Library's regulations (see http://www.manchester.ac.uk/library/aboutus/regulations) and in The University's policy on presentation of Theses.

Acknowledgements

During the period of my PhD study, there are too many people to acknowledge for their advice, support, encouragement and caring. First I would like to thanks my supervisor Professor Brian Derby for leading me to the wonderful research area. I also express my sincerely gratitude to him for his patient guidance, visionary advices and unconditional support in my studies. In addition, I would also like to thank you for the countless time and comments provided during the final thesis writing, without which my thesis would not have been accomplished to this part.

I would like to thank all the colleagues in the Derby group, particularly Mr Andy Wallwork, Dr Tianming Wang, Dr Rachel Saunders, Dr Xuegen Zhao, Mrs Yuanyuan Liu, Dr Will Williams, Mr Andy Forrest, Mr Keshav Sharma and Dr John Robert Brent for their help and support in last four years. They are not only just colleagues but also good friends.

I also need to give my thanks to Dr. Cristina Vallés and Professor Ian A. Kinloch for advice and supporting in this project. I would like to thank Professor Robert J. Young for his advice in annual viva. I would also like to thank Prof Paul O'brien, Dr David Lewis, Dr Andrew G. Thomas, Mr. Andrij Zadoroshnyj, Mrs Polly Greensmith and otherl staff in school of materials for their help.

In addition, I would like to thank my friends and colleagues in school of materials, including Dr Zheling Li, Dr Daishu Qian, Dr Bin Liu, Dr Gaoxiang Cao, Mr Xin Zhao, Dr Ruizhi Pei, Dr Jiantao Qi, Dr Yue Lin, and Dr Jianyun Cao. I also would like to thank the special couple, Dr Linrun Feng and Mrs Alice Yang. The full list of people is endless. Thanks to all of you guys, which made my life in UK interesting and colourful. I also appreciate the funding support from China Scholarship Council (CSC) and EPSRC.

Finally, I would like to give special thanks to my family. To my parents, grandparents and brother for their consistent supporting and caring of my studying and life over the years. Last, but not means least, to my dear wife, Siying (Clare) Li. Thanks for your supporting. The beginning of our marriage life makes my PhD life has a wonderful ending.

My most brilliant achievement was my ability to be able to persuade my wife to marry me.

Winston S. Churchill

List of Tables

List of Figures

Chapter 1 Introduction

1.1 Background

Over the last two decades, inkjet printing as a low cost manufacture technique has been investigated widely in flexible and large area electronics.[1] Due to its unique advantages, a number of application areas have been explored, including transistors, displays, organic light-emitting diodes (OLEDs), enzyme-based sensors, solar cells, radio-frequency identification (RFIDs) devices, and touch screens.[2] However, the commercialization journey of inkjet-printed devices is still challenging due to the required performance expectations compared to current technologies. Generally speaking, for electronic applications, the performance of inkjet-printed electronical components, such as semiconductor devices and conductors, should be competitive to incumbent materials and the cost of the functional materials should be as low as possible.

Ideal inkjet-printed device components should have a smooth, uniform morphology, which requires the functional inks to be suitable not only for the generation of droplets, but to also have a good substrate interaction, solidification and sintering stability. Generally, for a printable ink, it is believed that the size of suspended particles should be smaller than 1/20 of the nozzle diameter to prevent clogging,[2] and that the viscosity and the surface tension of inks should within the range of 1-25 mPa·s and 25-50 mNm^{-1} respectively to enable stable drop formation.[3] In addition, it is known that the evaporation behaviour of the spreading droplet during drying can influence the morphology of inkjet-printed films. The "coffee staining" effect, derived from the ring morphology of the solute or particles accompanying the evaporation of solvent from an isolated drop,[4] results in an undesirable non-uniform morphology of inkjet-printed components, which can be disadvantageous to device performance.

Thus, an ideal material for printed electronics applications should meet the following requirements: (a) good electronics properties in either mobility or conductivity; (b) high physical or mechanical stability under device operating conditions; (c) low cost of source materials and ink preparation process; (d) homogeneous distribution in the ink state, (e) good drop ejection stability, and (f) uniform deposit morphology after solvent evaporation.

Graphene oxide (GO), a derivative of graphene, is normally produced through exfoliation of graphite oxide to monolayer configuration by sonicating or dispersing graphite oxide in appropriate solvents. The graphite oxide itself is synthesized by reacting graphite with a strong oxidizing agent, such as $KMnO_4$ and concentrated H_2SO_4 mixture.[5] GO can be converted to reduced graphene oxide (rGO) by a chemical reduction process, which is a material similar to pristine graphene although still containing a level of structural defects. Unlike GO, which can be readily dispersed in either water or organic solvents to form a stable homogeneous ink,[6] rGO can only achieve a stable suspension in particular organic solvents,[7] which are often harmful to the environment and the human body. This limits the use of rGO use in printing electronics. An alternative method to obtain graphene-based electronic components is to inkjet print GO in an aqueous ink following by the reduction process. Such printed rGO components show good electronic conductivity and mechanical flexibility, similar to printed graphene conductor from solvent exfoliated pristine graphene inks. Although the intrinsic carrier mobility of rGO-based transistor can reach up to 5000 $cm^2 V^{-1} s^{-1}$, which is close to that of pristine graphene (~ 10^4 $cm^2 V^{-1} s^{-1}$), the on/off ratios are in the range of 1 - 10,[8] which makes the use of rGO in the role of a semiconductor in transistors unrealistic.

Recently, black phosphorus (BP), a member of two dimensional crystalline family, has attracted great attention due to its properties for electronic applications. Unlike graphene, which has no or only a very narrow band gap, BP has a direct band gap of 0.3 - 2.0 eV depending on the number of atomic layers in the 2D crystal. The carrier mobility of few layered BP based transistors can reach up to ~ 200 - 1000 $cm^2V^{-1}s^{-1}$ with on/off ratios in the range of 10^4 - 10^5.[9] Moreover, BP can be exfoliated to few-layer or even mono-layer by liquid phase exfoliation (LPE) process,[10, 11] which indicates that BP has great potential for printed transistors. However, it has been reported that few-layered BP is unstable under ambient conditions and exfoliated BP degrades when exposure to ambient O_2 and H_2O. This phenomenon has been observed in both mechanically exfoliated and LPE few layered BP.[12, 13] Although many strategies have developed to prevent contact between BP materials and ambient air in both the material exfoliation and device characterization process, the mechanism of BP degradation in ambient air is still unclear.

1.2 **Motivation and Outline of the Thesis**

Inkjet printing is a promising technique for manufacturing low cost and large area electronic devices, since it can deposit functional materials directly on demand, hence reducing the amount of material needed and reducing wastage inherent in many rival technologies. 2-dimensional (2D) materials are potential materials for future printed electronic applications due to their competitive intrinsic electronic properties compared with other materials, and, moreover, availability by scalable solution processing. Based on functionality, 2D materials can be used in electronic devices, for example as: conductors (graphene and rGO), semiconductors (MoS_2, BP, and other suitable band gap materials), or as a dielectric (*h*-BN) layer. However, there are few examples 2D materials-based electric components produced by inkjet printing. This thesis reports on the of use inkjet printing technique to deposit 2D materials, in particular GO and BP. The morphology of printed patterns will be studied by optimizing the material synthesis method and printing conditions. Moreover, the stability of printed BP devices will be investigated. It is hoped that the using of printing technology to deposit 2D materials will bring a new route for producing functional electrical components based on 2D materials.

A summary of each chapter is as follows.

Chapter 1 provides the background to and motivation for this research. The outline of the thesis is also summarized.

Chapter 2 gives a brief overview of the inkjet printing technique, as well as the 2D materials graphene oxide and black phosphorus. Firstly, the development of inkjet printing, the formulation of printable inks for stable inkjet drop ejection, the interaction between the droplets and substrates, and the solidification of printed patterns are discussed. Secondly, the synthesis methods used to create GO and the main models for its structure are summarized. The reduction methods used to convert GO to rGO are discussed, the techniques used for the characterization of GO and graphene, and the applications of GO and rGO deposited by inkjet printing process are summarized as well. Thirdly, the fabrication and applications of BP are summarized as well as the future challenges for its practical application.

Chapter 3 describes the inkjet printing and subsequent reduction of GO films with conductivity up to 2.51×10^4 Sm^{-1}. GO sheets with mean size of 35.9 μm were synthesized through a modified Hummers' method and the consequent GO aqueous ink was deposited on the substrate by inkjet printing. The mechanism that allows the printing of such large size GO flakes is investigated. After deposition, the GO films were reduced with HI acid vapour to form rGO films. The relationship between conductivity and film thickness was studied. Moreover, GO inks with different flake size were prepared by treating the original GO ink with tip sonication for different times. The various sizes of GO inks were printed and the influence of GO size on the conductivity of rGO films was discussed.

Chapter 4 describes mechanisms for controlling the coffee ring effect observed with the drying of GO aqueous droplets. The shape of GO droplets deposited on substrates with different surface energy was discussed. A mechanism is proposed that compares the evaporation dynamics and flake transport mechanism in drying GO droplets to explain the onset of coffee ring formation. Additionally, the influence of GO flake size, substrate temperature, and drop size to the final shape of drying droplets was investigated.

Chapter 5 describes the response, degradation and recovery of inkjet-printed few layer BP devices in humid atmospheres. The preparation of BP ink using the LPE process and printing BP devices is described. The response of BP device under different humidity level conditions is characterised and the degradation and recovery mechanisms of BP devices in humidity conditions are studied and discussed in detail.

Chapter 6 presents the conclusions of this thesis and gives an outline for possible future work.

References

1. Kamyshny, A. and Magdassi, S., Conductive nanomaterials for printed electronics. *Small*, 2014. **10**(17): p. 3515-35.

2. Derby, B., Inkjet Printing of Functional and Structural Materials: Fluid Property Requirements, Feature Stability, and Resolution. *Annual Review of Materials Research, Vol 40*, 2010. **40**: p. 395-414.

3. Cummins, G. and Desmulliez, M.P.Y., Inkjet printing of conductive materials: a review. *Circuit World*, 2012. **38**(4): p. 193-213.

4. Deegan, R.D., Bakajin, O., Dupont, T.F., Huber, G., Nagel, S.R., and Witten, T.A., Capillary flow as the cause of ring stains from dried liquid drops. *Nature*, 1997. **389**(6653): p. 827-829.

5. Hummers, W.S. and Offeman, R.E., Preparation of Graphitic Oxide. *Journal of the American Chemical Society*, 1958. **80**(6): p. 1339-1339.

6. Paredes, J.I., Villar-Rodil, S., Martinez-Alonso, A., and Tascon, J.M.D., Graphene oxide dispersions in organic solvents. *Langmuir*, 2008. **24**(19): p. 10560-10564.

7. Park, S., An, J.H., Jung, I.W., Piner, R.D., An, S.J., Li, X.S., Velamakanni, A., and Ruoff, R.S., Colloidal Suspensions of Highly Reduced Graphene Oxide in a Wide Variety of Organic Solvents. *Nano Letters*, 2009. **9**(4): p. 1593-1597.

8. Wang, S., Ang, P.K., Wang, Z.Q., Tang, A.L.L., Thong, J.T.L., and Loh, K.P., High Mobility, Printable, and Solution-Processed Graphene Electronics. *Nano Letters*, 2010. **10**(1): p. 92-98.

9. Liu, H., Du, Y., Deng, Y., and Ye, P.D., Semiconducting black phosphorus: synthesis, transport properties and electronic applications. *Chemical Society Reviews*, 2015. **44**(9): p. 2732-2743.

10. Brent, J.R., Savjani, N., Lewis, E.A., Haigh, S.J., Lewis, D.J., and O'Brien, P., Production of few-layer phosphorene by liquid exfoliation of black phosphorus. *Chemical communications*, 2014. **50**(87): p. 13338-13341.

11. Yasaei, P., Kumar, B., Foroozan, T., Wang, C., Asadi, M., Tuschel, D., Indacochea, J.E., Klie, R.F., and Salehi-Khojin, A., High-quality black phosphorus atomic layers by liquid-phase exfoliation. *Advanced Materials*, 2015. **27**(11): p. 1887-1892.

12. Castellanos-Gomez, A., Vicarelli, L., Prada, E., Island, J.O., Narasimha-Acharya, K.L., Blanter, S.I., Groenendijk, D.J., Buscema, M., Steele, G.A., Alvarez, J.V., Zandbergen, H.W., Palacios, J.J., and van der Zant, H.S.J., Isolation and characterization of few-layer black phosphorus. *2D Materials*, 2014. **1**(2): p. 025001.

13. Hanlon, D., Backes, C., Doherty, E., Cucinotta, C.S., Berner, N.C., Boland, C., Lee, K., Harvey, A., Lynch, P., Gholamvand, Z., Zhang, S., Wang, K., Moynihan, G., Pokle, A., Ramasse, Q.M., McEvoy, N., Blau, W.J., Wang, J., Abellan, G., Hauke, F., Hirsch, A., Sanvito, S., O'Regan, D.D., Duesberg, G.S., Nicolosi, V., and Coleman, J.N., Liquid exfoliation of solvent-stabilized few-layer black phosphorus for applications beyond electronics. *Nature Communications*, 2015. **6**: p. 8563.

Chapter 2 Literature Review

2.1 Inkjet Printing

2.1.1 Introduction

Inkjet printing is one of the most widely used printing techniques in the publishing and graphics industries, which has origins that can be traced back to the nineteenth century.[1] In the last two decades, this technology has found applications away from its traditional area of use to become a versatile fabrication tool for the deposition of functional materials. These materials, or inks, can be printed to form a range of components for various areas of optoelectronic applications, including displays, plastic electronics, OLED, photovoltaics, sensors, solder dispensing for flip-chip manufacturing, and lighting.[1, 2] In the electronics industry, techniques to deposit electronic components typically use photolithographic etching or controlled vapour deposition processes, which are normally both time and material intensive, and have a high energy cost. The development of electronics-use functional inks and the use of inkjet printing to additively pattern is one of the most promising solutions to reduce costs.[3] However, the application of inkjet printing for electronic component deposition results in a range of new challenges, including ink formulation, print head and print system design, positioning of and interaction of droplets on a substrate, and control of solvent evaporation or solidification mechanisms.[1]

2.1.2 The Road Map of Inkjet Printing Technique

The original concept of inkjet printing can be traced back to the eighteenth century when Abbé Nollet described the certain phenomenon of a stream of droplets generated by static electricity.[4] This phenomenon was further investigated by Felix Savart who, in 1833, described that mechanism of the breakup of liquid flow into a series of separated droplets is due to the law of fluid dynamics.[5] Later, in 1856, Plateau demonstrated the generation of jets from circular nozzles and further indicated the influence of jet dimeter to the drop size.[6] In 1858, the first practical inkjet printer, which was called the Siphon recorder, was proposed by Lord William Kelvin,[7, 8] although it is unclear if an example was ever made. This machine was proposed as a method to automatically record data for the electric telegraph from submarine cables. In this case, the ink was drawn from

the capillary tube by means of electric force and the paper receives the ink by a succession of fine contacts. In 1878, a series of publications considered mecahnisms for the formation of trains of individual droplets from liquid streams. Rayleigh [9] later produced a model that explained Plateau's observation of the instability of a free flowing liquid stream in terms of surface energy minimization.

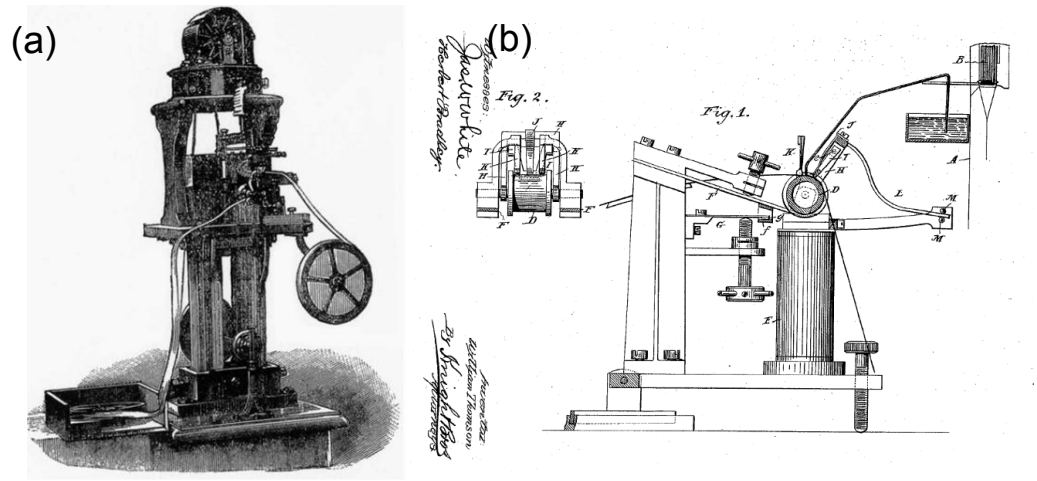

Figure 2.1. (a) The first practical inkjet device: Siphon recorder and (b) a side elevation of the paper-feed and recording mechanism for the Siphon recorder. Reprinted from ref. 8.

More than half a century later, in 1948, based on Rayleigh's outcomes, the first commercial inkjet printer was invented by Rune Elmqvist,[10] an engineer from Elema-Schönander, a Swedish company which later became Siemens-Elema. This machine, which was called as *Mingograph*, was used to transcribe analogue physiological signals. Later, in 1965, the first continuous inkjet (CIJ) printer system was invented by Richard Sweet from Stanford University.[11] In this printer, ordinary stream of ink was divided into a uniform series of individual drops formed at a rate of 100 000 s^{-1} by an electrical signal. The trajectory of individual drops was controlled by charged deflectors onto the desired substrate and undeflected drops gathered by a collector. Depending on the deflection mechanism, the CIJ printing system can be divided into binary-deflection mode and multiple-deflection mode. A schematic diagram of both CIJ printing modes is shown in Figure 2.2. The first commercial CIJ printer used for character printing was introduced by the A. B. Dick Company in 1968, which was named as Videojet 9600. Based on Sweet's invention, in 1976, IBM also introduced a CIJ printer system and named it the IBM 4640 printer.[12] Subsequently, commercial CIJ printers have been widely used in the industrial coding, marking and labeling markets, as well as in the graphic arts, and high-speed on-demand printing market.[13]

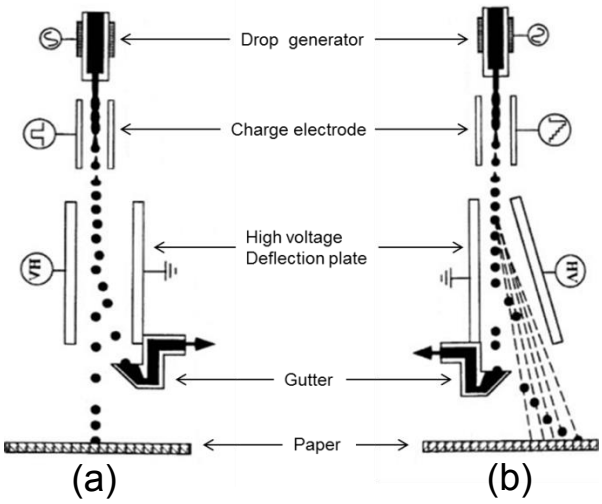

Figure 2.2. Schematic diagram showing the principles of a CIJ printer system working at (a) binary-deflection mode and (b) multiple-deflection mode. Reprinted from ref. 13.

During the same period, another inkjet printing technology, which is known as drop-on-demand (DOD) inkjet printing, was invented. Compared to CIJ, DOD inkjet printers produce individual droplets when required, which is more efficient with ink delivery and thus more economical.[1] Depending on the generation principle of the pressure pulse that ejects a droplet, DOD inkjet printers can be divided into thermal inkjet, piezoelectric inkjet, and electrostatic inkjet printing.

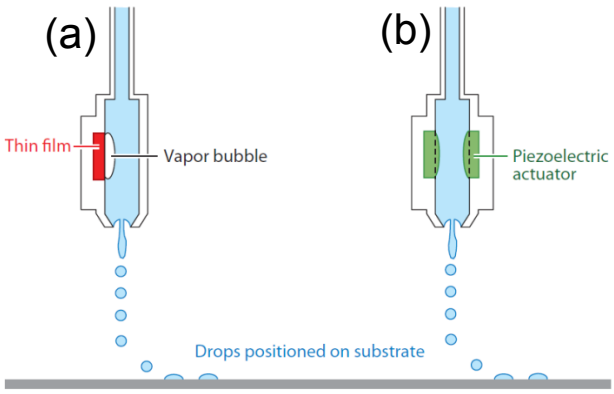

Figure 2.3. (a) Schematic diagram of the thermal (a), and piezoelectric (b) DOD inkjet printing system. Reprinted from ref. 1.

The basic idea of the thermal DOD inkjet printer was developed in 1965 by Mark Naiman from the Sperry Rand Corporation.[14] In this printer, the individual dot was generated by a matrix composed of individual print heads, which means it can be used for printing a particular form of character or symbol. Base on Mark's design, in 1979, the Canon company developed the first commercial thermal inkjet print head.[15] Almost at the same time, Hewlett-Packard developed its first thermal inkjet printer in 1981.[16]

During the last decades, Canon and Hewlett-Packard have produced large numbers of desktop or domestic thermal printers under the brand of Bubblejet and Thinkjet. Generally, in a thermal DOD printing system, the drops are ejected by a pressure pulse generated by a vapour pocket or a bubble formed using a small thin-film heater that vaporizes the liquid in immediate contact with it, as shown in Figure 2.3a. Although the thermal DOD printer is easily miniaturized, the need to generate a bubble during printing limits its usage to liquids with a low boiling temperature and high vapour pressure. Moreover, the thermal cycling in the print head makes it unsuitable for printing functional materials, which can be heat sensitive.[12]

With piezoelectric DOD printing (Figure 2.3b), the drop generation pressure pulse is produced by direct mechanical actuation with a piezoelectric transducer. The first idea of using the piezoelectric effect in a DOD printer was produced by the Radio Corporation of America in the late 1940s.[17] The patent document mentioned that the printer can be applicable to either facsimile recording or various painting and spraying operation. However, it was never developed into a commercial product. After little activity for about three decades, in the 1970s, four types of piezoelectric DOD print head were developed, which were distinguished by their different piezoelectric actuation modes, as shown in Figure 2.4.

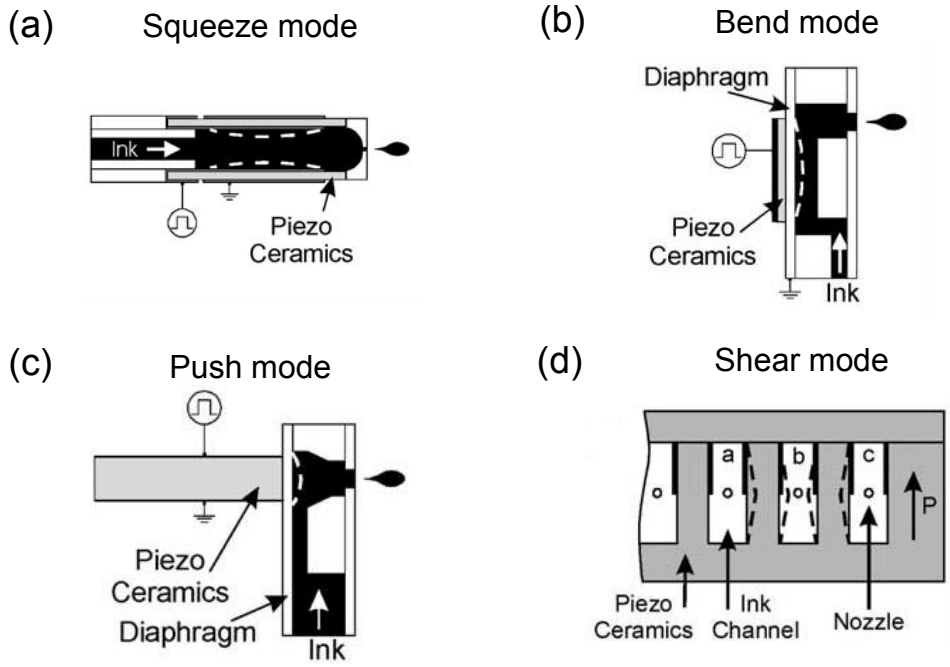

Figure 2.4. Different types of piezoelectric DOD print head classification by the deformation modes for drop generation. Reprinted from ref. 18.

The first type (Figure 2.4a) is the squeeze mode print head, which was invented by Zoltan form the Clevite company in 1972.[19] Here, a voltage pulse with short rise time caused contraction of the piezo-ceramic transducer, which squeezing a small amount of ink out of the orifice. This design was used to both print paper work (e.g. Siemens PT-80 printer) or functional devices.[20] A second type, named as bend mode, was first mentioned in the patent by Stemme from the Chalmers University in Sweden.[21] The bend mode print head, as shown in Figure 2.4b, consists of a small pressure chamber with an inlet ink supply tube and outlet passage for ink ejection. When the piezoelectric plate was actuated by applying a voltage, the resulting flexural deformation of the diaphragm displaced the ink fluid and expelled it from the nozzle.[18] This technique has been used widely in commercial printers sold by Xerox, Tektronix, Epson, and Kyocera.[12] The third type is the push mode print head (Figure 2.4c), which was invented by Howkins of the Exxon Company.[22] In this design, the ink was expelled from the orifice by the expansion of piezoelectric rods. This kind of print head has been used for the printers produced by Hitachi, Brother, Trident, and Epson.[12] The last type is the shear mode print head (Figure 2.4d), which was invented by Fischbeck and Wright from the Xerox Corporation in 1986.[23] In the shear mode print head, the droplet is ejected by flexing of the upper and lower half of the channel into a chevron shape, which was shear-deformed by the piezoelectric elements. The shear mode print head is found in commercial products sold by Fujifilm Dimatix and Xaar.[12]

Unlike the thermal and piezoelectric DOD printing system, the ejection of ink droplets in the electrostatic inkjet printing system is generated by an electrostatic field which normally acts between the nozzle and a conductive platen. This technique was first patented in 1958 by Winston.[24] In this patent, an electrostatic force attracts free charges within the ink and generates a force that exceeds the surface tension of the ink to deposit the ink on controlled areas. As the drop size is dependent on the electrical potential difference between the nozzle and the electrode plate, very small drops or fine lines can be formed with the electrostatic printing system. However, due to the requirement of a conductive ink, this system is not a practical technique for printing multifunctional materials and is used for graphics applications by Tonejet.

A summary of the different inkjet printing techniques and their relationships is shown schematically in Figure 2.5. Although CIJ printing has many advantages, such as high drop ejection frequency (20-60 kHz), long working distance between the substrate and

print head due to the high drop velocity (> 10 m/s), and freedom from nozzle clogging, it is not suitable for printing functional materials due to the many unwanted drops in the CIJ printing system that are recycled. These can be affected by environmental exposure that occurs during ink recycling from the gutter.[1] Nowadays, the CIJ technique is normally used in high speed but low quality graphical applications (e.g. labelling and marking).[25] Thermal DOD inkjet printing can generate very small drop sizes and high nozzle density, which allows manufacture of print heads at low cost.[26] Thus, this technique has been used widely in the desk top colour printing market. However, the narrow window of suitable inks, which must be able to resist ultra-high local temperatures, makes the thermal inkjet unsuitable for depositing fluids with functionality, e.g. polymers.[26] Thus piezoelectric DOD inkjet printing is currently used most widely for emerging industrial applications. Piezoelectric print heads have a long service life time and can be used for printing various types of fluids without the risk of ink damage, which makes this technique promising for printing functional materials.[12]

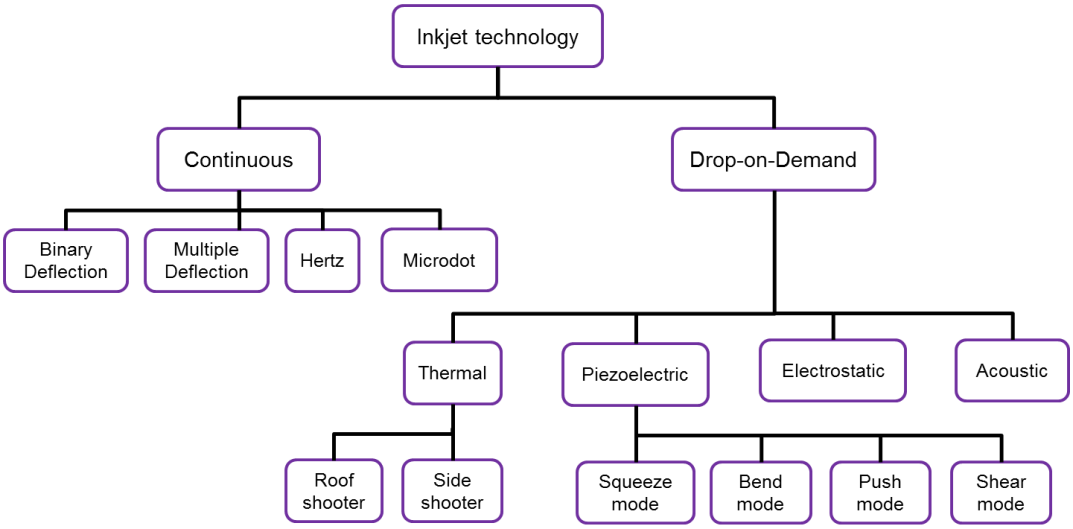

Figure 2.5. The technology map of inkjet printing. Reprinted from ref. 13.

After decades of development, the commercial thermal DOD inkjet printer is now widely used for transferring electronic data to paper in most office and household applications. The main concern for using inkjet technology in text output and graphic arts printing is reducing cost and improving efficiency.[27] However, in recent years, there has been increasing interest in developing inkjet printing as a versatile tool for manufacturing functional components, such as plastic electronics, displays, rapid prototyping (3D printing), ceramic component manufacture, and tissue engineering.[28] Although other solution processes such as screen-printing and spin-coating have been

used to deposit functional materials, these techniques typically need a die or photomask, which can be material and time consuming.[12] Thus, the use of inkjet printing, which offers advantages in deposit-on-demand combined with digital deposition, is one of the most promising solutions for low cost manufacturing.[27]

Piezoelectric DOD inkjet printing is the main method chosen for the deposition of functional materials using inkjet technology.[28] However, the application of inkjet printing to the deposition of functional materials results in a range of new challenges, including ink formulation, print head and print system design, positioning of and interaction of droplets on a substrate, and control of solvent evaporation or solidification mechanisms.[1]

2.1.3 **Printable ink Formulation**

Preparation of an ink suitable for inkjet printing can be complex due to the intricate property and challenging fluid and materials requirements of printable inks. In addition, unlike the requirement for the conventional inks, which normally need long shelf life and appropriate colour properties, inks containing functional materials should have specific physicochemical properties for various applications.[29] Normally, printing a functional ink is more complex than printing a solvent graphics ink as the functional ink is either a particulate suspension or a relatively concentrated polymer solution and always needs special treatment to make the functional material stable in the ink. For example, when preparing an ink composed of silver nanoparticles, a charged polymeric stabilizer is normally used to stabilize the silver nanoparticles. Thus, when formulating functional inkjet inks, the influence of each component on the total performance of the ink should be considered.[29] Generally, the major factors that are considered for a printable ink are its stability (against sedimentation as well as chemical stability) and fluid rheological properties such as viscosity, surface tension and density.[12] However, for various dispersions of functional materials, the conditions for making stable inks are different. Thus, this section will mainly consider rheological properties.

The viscosity of the ink is very important not only for its jettability but also for the spreading behaviour of ejected drops on the substrate after deposition. The viscosity of the ink can be influenced by the concentration of dispersed solids or solutes, solvent composition, surfactants, and flocculation.[29] Normally, for Newtonian inks, which have a constant viscosity over a range of shear rates, the recommended viscosity values for

printable inks should be below 20 mPa·s and 3 mPa·s for piezoelectric print heads and thermal print heads, respectively.[29] For non-Newtonian inks, these values represent the viscosity of inks at high shear rate (> 1000 s^{-1}) as the work frequency of print heads is typically higher than 1 kHz.[1] Similar to viscosity, the surface tension of the ink can also effect the drop formation and printed drop spreading on the substrate after contact. In order to prevent unwanted dripping and break away of the ejected droplets from the nozzle, the surface tension is recommended to be between 25 and 50 mNm^{-1}.[12]

2.1.4 **Drop Ejection**

In order to characterize and quantify the influence of viscosity, surface tension and other factors such as density and the nozzle dimeter to the eject behaviour of inkjet fluids, a number of dimensionless physical constants are used. These are the Reynolds (*Re*), Weber (*We*) and Ohnesorge (*Oh*) numbers.[1] The Reynolds number is defined as the ratio of the inertial forces to the viscous force or friction force, which can be expressed as

$$R_e = \frac{v\rho a}{\eta} \tag{2.1}$$

where v, ρ, a, and η are the droplet velocity, fluid density, nozzle diameter, and the dynamic shear viscosity of the fluid, respectively. The Weber number is the ratio between the inertial force and the surface tension force, and can be expressed as

$$W_e = \frac{v^2\rho a}{\gamma} \tag{2.2}$$

where γ is the surface tension of the fluid. The Ohnesorge number represents the drop information that related to the ratio of internal viscosity dissipation to the surface tension force, which was defined by Wolfgang von Ohnesorge in 1936 as [30]

$$Oh = \frac{\eta}{\sqrt{\rho a \gamma}} = \frac{\sqrt{W_e}}{R_e} \tag{2.3}$$

Generally, the lower values of the *Oh* number the weaker are the friction losses caused by viscous forces, which means that most of the inserted energy coverts into surface tension energy (e.g. a droplet can be formed). On the other hand, at higher values of the *Oh* number internal viscous dissipation is more dominant, which means that droplet ejection in the print heads is critical or even impossible.[31] To investigate the relationship between the *Oh* number value and printable inks, Fromm defined a dimensionless number, *Z*, which is the reciprocal of the *Oh* number, to investigate the mechanisms of

drop generation.[32] He proposed that stable droplets can be ejected when the value of *Z* is larger than 2. This prediction was further refined by Reis and Derby,[33] who used numerical simulations to propose that the value of Z number for stable drop formation is in the range of 1 to 10. This printable range of Z number for mixture solvents has been further refined by experiments, which showed that the fluids can be printed within the limits of $4 \leq Z \leq 14$.[34]

Besides the *Z* number, two further limiting conditions have been used to define the performance of the drop generation process. The first limit factor is the minimum energy required for drop ejection to overcome the fluid/air surface tension barrier at the print head. Duineveld proposed that there is a minimum velocity for drop ejection [35]

$$v_{min} = \sqrt{\frac{4\gamma}{\rho a}} \tag{2.4}$$

By using Weber number with a minimum value for drop ejecting, Equation 2.4 can be reformulated as

$$We = v_{min}^2 \frac{\rho a}{\gamma} > 4 \tag{2.5}$$

The second limitation is the maximum drop velocity to prevent the onset of splashing when the drop impacts the substrate. This splashing limitation was first defined by Stow and Hadfield as [36]

$$We^{1/2} Re^{1/4} = f(R) \tag{2.6}$$

where f(R) is a function of surface roughness. It has been found that, for flat, smooth surfaces, $f(R) \approx 50$.[37] Based on Equation 2.4-2.6 and the range of Z number, a map of the Weber and Reynolds number parameter space can be used to define the fluid properties that are suitable for drop generation in the DOD printing system,[1] as shown in Figure 2.6. This predicted regime of printability can be used as useful guide for fluid properties selection in Newtonian ink systems.[38] However, for non-Newtonian fluids such as polymer solutions or concentrated dispersions of particles, which show a non-linear dynamic viscosity that changes with shear rate, the printability properties of a fluid as shown in Figure 2.6 may need to be modified or else fluid properties at an appropriate shear rate considered.[1] Generally, in Newtonian fluid systems, when the Z number is much larger than 10, the printed drops are more likely to show elongated tails,

which can destabilize into a series of satellite drops following the main drop. However for non-Newtonian fluids, these tails are longer and more stable against satellite formation and may merge into the main drop during flight.[39] Moreover, it has been reported that the long filament does not break away to become an individual drop when the fluid molecular weight is larger than 300 kDa.[40]

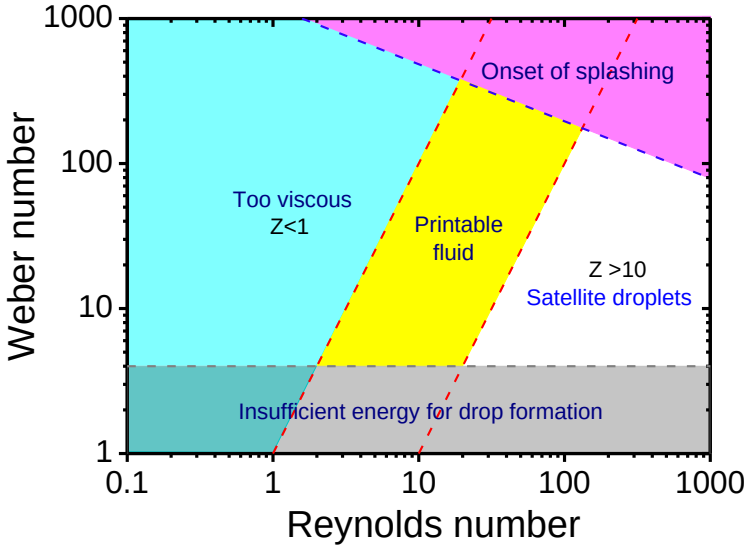

Figure 2.6. The Reynolds and Weber numbers to illustrate the possible regime for Newtonian fluids where inkjet drop formation. Redrawn and corrected from ref. 1.

2.1.5 **Drop Impact and Spreading on Substrate**

The next step after drop generation in DOD printing system is drop deposition, which is the behaviour of a liquid drop on a solid surface. This process can be divided into two stages: drop impact and spreading. The impacting stage of a drop on a solid surface is less than 1 μs duration, where the kinetic energy of the impact is dominated by inertial forces. In the spreading stage, the spreading behaviour is initially controlled by the dynamic forces and viscous dissipation, but is then dominated by the capillary forces until it approaches true equilibrium.[1]

The important dimensionless parameters such as the Reynolds, Weber and Ohnesorge numbers have been also used to determine the dominate stage to the overall behaviour of a liquid drop on a solid surface.[12] Generally, at a high Weber number the impact force driven the droplet outwards, whereas, at low Weber number the droplets are pulled by the capillarity force.[41] During the spreading stage, the Ohnesorge number can be used to determine the ink's resistance behaviour. High Ohnesorge number means that

the resistive force is dominated by viscosity, whereas low Ohnesorge number indicates it is decided by inertial forces.[12] In addition, during the drop impact and spreading, the effect of gravitational forces on the drop must also be considered. This can be considered using the dimensionless Bond number, $B_0 = \rho g a^2 / \gamma$, where g is the acceleration of gravity. However, in DOD printing, the gravitational forces can be neglected because the Bond number is usually 10^{-2} to 10^{-3}.[42] Figure 2.7 shows a graphical means of identifying the driving forces for droplet spreading by axes for the Ohnesorge and Weber numbers.[1]

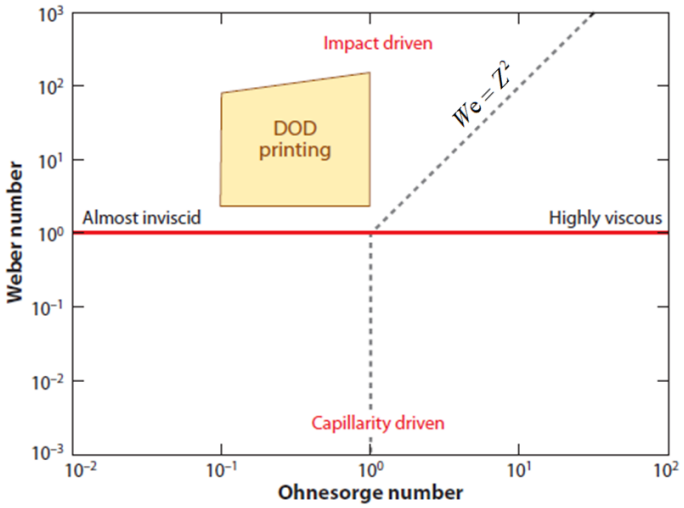

Figure 2.7. Parameter space defined by axes of Ohnesorge and Weber numbers showing the driving force for initial drop spreading after impact. Reprinted from ref. 1.

Assuming that the volume of the ejected drop is unchanged during flight, the final equilibrium spread drop will form a contact diameter or footprint, which is determined by its initial volume and the equilibrium contact angle, θ_{eqm}. The degree of drop spreading can be defined as: [43]

$$\beta_{eqm} = \frac{d_{eqm}}{d_0} = \sqrt[3]{\frac{8}{\tan\frac{\theta_{eqm}}{2}\left(3+\tan^2\frac{\theta_{eqm}}{2}\right)}} \qquad (2.7)$$

where β_{eqm} is the ratio of the diameter of the equilibrium spherical cap on the substrate, d_{eqm}, to the initial droplet diameter, d_0. Thus, for a fixed print-head, the minimum size of an inkjet-printed drop, is controlled by the diameter of its footprint, which is related the equilibrium contact angle of the drop on the surface.

Unlike conventional graphics printing, which are images made up of isolated drops, functional materials printing require the drops to overlap to form lines or continuous areas from the overlap of lines. Thus, to form stable liquid beads or lines, it is importance to understand the spreading behaviour of adjacent drops. Figure 2.8 a-e shows typical behaviours of inkjet-printed lines, which was found relative to drop spacing and delay time of adjacent drops at an intermediate temperature.[44] When the drop spacing decreases, the isolated drops (Figure 2.8a) begin to overlap and coalesce forming a scalloped line (Figure 2.8b). Further reduction of the drop spacing results in a stable line with smooth edges (Figure 2.8c), and finally a bulging instability forms (Figure 2.8d) when the drop spacing is too small. A stacked coins like line morphology occurred (Figure 2.8e) when the evaporation time of a single drop is less than the jetting period for adjacent drop deposition.

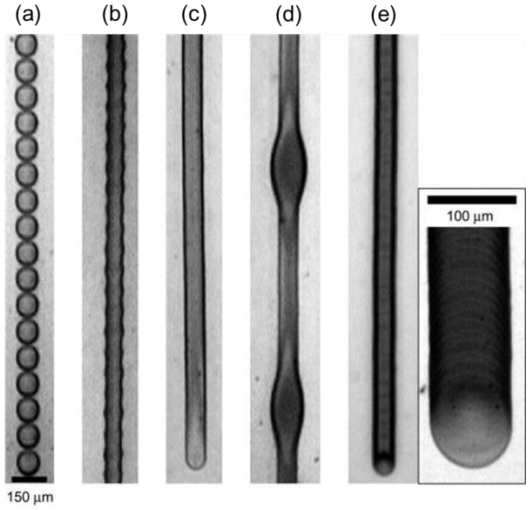

Figure 2.8. Examples of principal printed line behaviours: (a) individual drops, (b) scalloped, (c) uniform, (d) bulging, and (e) stacked coins. Drop spacing decreases from left to right. Reprinted from ref. 44.

For most applications, a stable and uniform fluid bead is required. Smith et al.[20] proposed a model based on volume conservation for the width of a stable liquid bead formed through droplet overlap. This was defined as:

$$w = \sqrt{\frac{2\pi d_0^3}{3p\left(\frac{\theta^*}{sin^2\theta^*} - \frac{cos\theta^*}{sin\theta^*}\right)}} \tag{2.8}$$

where w is the width of the bead, d is the drop diameter, θ^* is the static advancing contact angle, and p is the spacing of adjacent droplets. However, in a printing procedure with slow drop spreading and small drop size, the newly deposited drop will

have greater curvature at the liquid/air interface than the printed liquid bead. This creates a Laplace pressure and prevents the depleting bead from spreading, where it would form an equilibrium contact angle lower than the advancing contact angle.[45] Soltman and Subramanian [44] identified the dynamic nature of this limit by investigating the effect of drop spacing and time delay between adjacent drops on the final morphology of liquid bead. Stringer and Derby [43] also demonstrated a volume conservation model for a stable liquid bead width to define in the lower bound. These two models can be used in combination to predict the limiting conditions for producing stable liquid beads on a given surface.[1]

2.1.6 **Solidification of Printed Patterns**

The final step in the printing process is solidification, which is the transition from a deposited liquid phase to the final desired solid material. The evaporation behaviour during this procedure plays an important role in controlling the final morphology and distribution of solute in inkjet-printed patterns. The solute behaviour during drying can be divided into three steps (Figure 2.9): recirculation by Marangoni flow, nucleation of the solid phase at the contact edge, and self-assembly of solute by interparticle forces. When the contact line is pinned, solute segregates on the initial contact line and forms a ring like profile at the perimeter of the droplet. This phenomenon is commonly observed in the drying of inkjet-printed patterns from colloidal suspensions such as nanoparticle inks, and is commonly well-known as “coffee staining” or the “coffee ring” effect.[46]

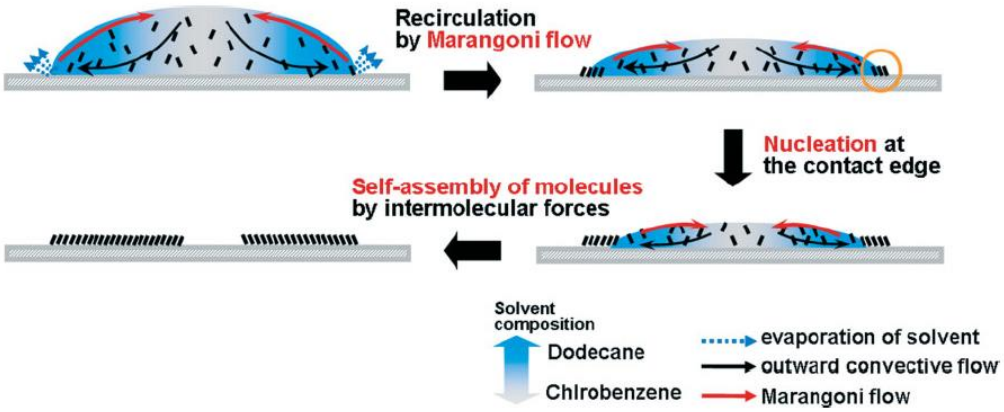

Figure 2.9. The process of printed drop drying after deposition. Reprinted from ref. 47.

Coffee ring effects (CRE) occurs due to the pinning of the contact line, which forces a radial flow to maintain liquid at the contact line and results in an undesirably uneven

distribution of material across the deposit, which can be disadvantageous to electronic device performance.[47] Most approaches to reduce coffee staining are based on modifying the driving forces for liquid flow during the evaporation process. Basically, the CRE is mainly determined by the evaporation time scale and particle movement. Negligible CRE has been observed with non-volatile solvent drying because of the long evaporation time and low outward flow resulting from solvent evaporation.[48] Based on this concept, Fukuda et al.[49] varied the ambient humidity conditions to prolong the time of the drying process. A flat pattern printed from a water-based ink was achieved at 85% RH. Moreover, Soltman and Subramanian [44] demonstrated a method to reduce the coffee staining by printing PEDOT solution onto a low temperature substrate. In this case, the evaporation ratio at the drop centre is enhanced by the faster heat transfer through the drop than toward the edge of the drop due to the low height of drop. A more efficient and practical method to reduce coffee staining is to use a multi-solvent system that contain individual solvents of different vapour pressure and surface tension. This method makes use of the evaporation-induced flow and in particular the convective and Marangoni flows that occur during droplet drying.[50] The convective flow that transports the solute to the contact line can be opposed by the Marangoni flow that is induced by the surface tension gradient between the periphery and the interior of the droplet when a solvent with either higher boiling point and a lower surface tension or low boiling point and high surface tension is used.[47]

2.2 From Graphene Oxide to Graphene

2.2.1 Introduction

Graphene is the name given to an isolated flat monolayer plane of carbon atoms with a two-dimensional honeycomb lattice with sp2 bond hybridisation.[51] Although graphene has been theoretically investigated for over 40 years, the first isolation of free standing graphene was reported in 2004.[52] A pure single-layer graphene flake isolated from bulk graphite is a semiconductor with 0 eV bandgap and has a thickness of 0.34 nm.[53, 54] Over the last decade, the study of graphene has become one of the most exciting topics in materials science and nanotechnology due to its exceptional physical properties with high intrinsic mobility (200 000 cm^2 v^{-1} s^{-1}), high Young's modulus (~1.0 TPa), high thermal conductivity (~5000 Wm^{-1} K^{-1}), good optical transmittance (~97.7%), and high electrical conductivity (~ 10^6 S/cm).[55] These particular properties make it attractive for applications in electronics and optoelectronic devices such as for conducting electrodes.

Developing methods of creating high-quality graphene in large quantities using an economical process is the first step for both research purposes and towards possible applications.[56] In the past decade, various methods have been employed to prepare graphene sheets. In general, these strategies can be considered as two approaches: bottom-up and top-down. The bottom-up approach is to manufacture graphene sheets by deposition from the gas phase using simple carbon-based molecules such as methane or ethanol. Conversely, the top-down approach is achieved by exfoliating individual complete graphene sheets from graphite.[57] After development and refinement for several years, both approaches can now produce contrasting quality and yield of graphene. However, for large scale manufacturing with high yield and low cost, the top-down method through chemical oxidation, exfoliation and reduction is the most promising route. In this method, the graphite is first converted to graphite oxide by chemical oxidizing agents. Then, the as-synthesized graphite oxide is further exfoliated to graphene oxide (GO). At last, the GO can be converted to a graphene-like material termed reduced graphene oxide, using different reduction methods and/or reducing agents. Moreover, the production and application of graphene that is produced by this wet top-down synthetic method has become one of the most popular research topics in the graphene area.

2.2.2 **Synthesis of GO**

The history of synthesizing GO can be traced back to the nineteenth century when the British chemist B. C. Brodie tried to identify the structure and molecular weight of graphite in 1859.[58] In this pioneering experiment, Brodie mixed graphite with potassium chlorate and let the mixture react in fuming nitric acid. After washing the reacted materials to remove the salt products, the material was re-oxidized using the same condition for another three repetitions to finally result in a crystal with a light yellow colour. By using elemental analysis, he found the composition ratio of C: H: O in the resulting material was 61.04: 1.85: 37.11, which indicates a molecular formula of $C_{11}H_4O_5$. In addition, he mentioned that this material can be dispersed in pure or base water, but not in acidic media, thus Brodie termed this material as "graphic acid".[58]

In 1898, L.Staudenmaier improved Brodie's method by adding concentrated sulfuric acid and multiple aliquots of potassium chlorate solution into the mixture.[59] These changes in the processing route resulted in materials with a similar C/O ratio to Brodie's method but in a one step oxidation process, which is time saving and more convenient. However, the Staudenmaier's method is still not practical as the potassium chlorate was added over a period of 7 days.

In 1958, Hummers and Offeman [60] demonstrated a rapid and relatively safe oxidation strategy by reacting graphite with a mixture of potassium permanganate ($KMnO_4$), concentrated sulphuric acid, and sodium nitrate. Although the whole oxidation process in Hummers' method lasted about 2 hours, the resulting product shows a higher degree of oxidation than that produced by Staudenmaier's method. As a shorter time was needed and the method avoided use of highly corrosive fuming nitric acid, Hummers' method has been well accepted and adopted by subsequent researchers for the oxidation of graphite. However, the product from Hummers' method contains a large quantity of incompletely oxidized graphite, some modifications has always been used during the preparation of graphite oxide by this route. Kovtyukhova et al.[61] demonstrated a modified Hummers' method to prepare graphite oxide monolayers by pretreating the graphite with a mixture of concentrated H_2SO_4, $K_2S_2O_4$, and P_2O_5. Other modification strategies include increasing the amount of the $KMnO_4$ [62] and prolonging the oxidation process time,[63] and using exfoliated graphite nanoplatelets.[64]

However, both Hummers' method and the modified Hummers' method result in the production of toxic gases, such as NO_2 and N_2O_4, due to the usage of sodium nitrate. To make the method more environmentally friendly, researchers from Tour's group [65] reported a new recipe, which uses less corrosive phosphoric acid replacing the sodium nitrate and increasing the amount of $KMnO_4$. They mentioned that this method can produce higher yield of oxidized graphene materials than Hummers' method or the modified Hummers' method, as shown schematically in Figure 2.10.

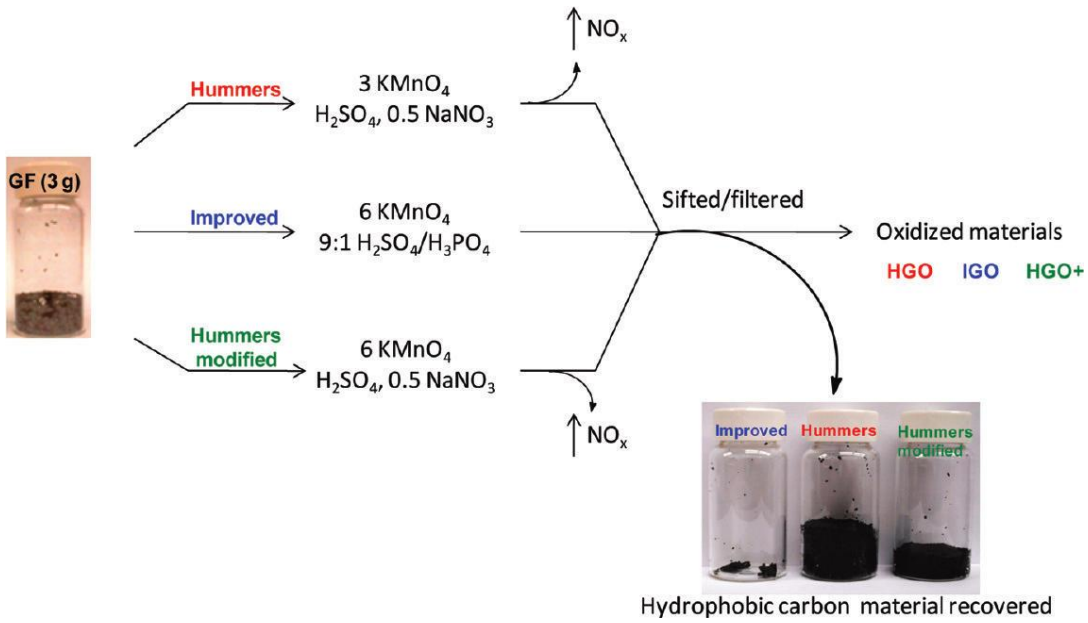

Figure 2.10. A comparison of procedures and final yields among Hummers' method, modified Hummers' method and Tour's method. Reprinted from ref. 65.

Although Tour's method avoided the generation of toxic gases during the process, the existence of polluting heavy metal ions (Mn^{2+}) is also harmful to the environment.[66] Moreover, the potential explosion risk from the presence of unstable Mn_2O_7 intermediates requires good control with the use of $KMnO_4$ in large scale production of GO. To solve this problem, Peng et al. developed a new method that uses a strong yet green oxidant, K_2FeO_4, instead of $KMnO_4$.[67] In this approach, large GO sheets with nearly 100% mono-layers can be obtained by adding graphite into the mixture of H_2SO_4 and K_2FeO_4 at room temperature for 1 hour. As K_2FeO_4 is an environmental friendly yet high efficiency oxidant with non-toxic by-products, this method is amenable to the mass production of GO.[67]

Over a period of more than 150 years, the purpose of improving the synthesis method of graphene oxide is to find more safe and efficiency alternatives suitable for scalable

production of graphene-based materials.[57] As shown in Table 2.1, the reaction time can now be finished in 1 hour and the product has similar C/O ratio to the products by the earlier several days reaction, which demonstrates that the high yield manufacturing of GO is close.

Table 2.1. A comparison of GO synthesis methods.

Method	Year	Chemical used	Reaction time	Reaction temperature (°C)	C/O	Toxic gas
Brodie [58]	1859	$KClO_3$, HNO_3	3-4 days	60	2.16	ClO_2
Staudenmaier [59]	1898	$KClO_3$, HNO_3, H_2SO_4	1-10 days	RT	-	ClO_2, NO_x
Hummers [60]	1958	H_2SO_4, $KMnO_4$, $NaNO_3$	~2 h	35	2.25	NO_x
Modified Hummers [61]	1999	H_2SO_4, $K_2S_2O_4$, P_2O_5, $KMnO_4$, $NaNO_3$	6 h 2 h	80 35	2.3	NO_x
Tour [65]	2010	H_2SO_4, $KMnO_4$, H_3PO_4	12 h	50	-	-
Peng [67]	2015	H_2SO_4, K_2FeO_4	1 h	RT	2.2	No

2.2.3 **Mechanism of the Oxidation Process**

The mechanism of graphite oxidation has been described as: the acid ions and oxidant intercalate into the interlayer spaces of graphite and react with the carbon atoms to form functional groups, then the van der Waals force between the graphene layers is largely weakened, which allows the graphite oxide to be exfoliated to mono-layer GO by dispersion in water or mild sonication.[68] However, this description is so general that it cannot be used as a practical guide for GO preparation. To understand how the oxidising agent intercalates into graphite, Pan et.al [69] investigated the oxidation process by exposing a highly ordered pyrolytic graphite (HOPG) surface to a sessile drop of

oxidizing solution based on Hummers' method. They found that the cross-planar oxidation of HOPG surface was cracked in periodic cells, in which the size remains the same for different oxidation times. By observing the oxidation of graphite particles in the oxidizing solution, it was shown that the crack propagation behaviour occurred simultaneously with the edge-to-centre interaction of the oxidizing solution.[69]

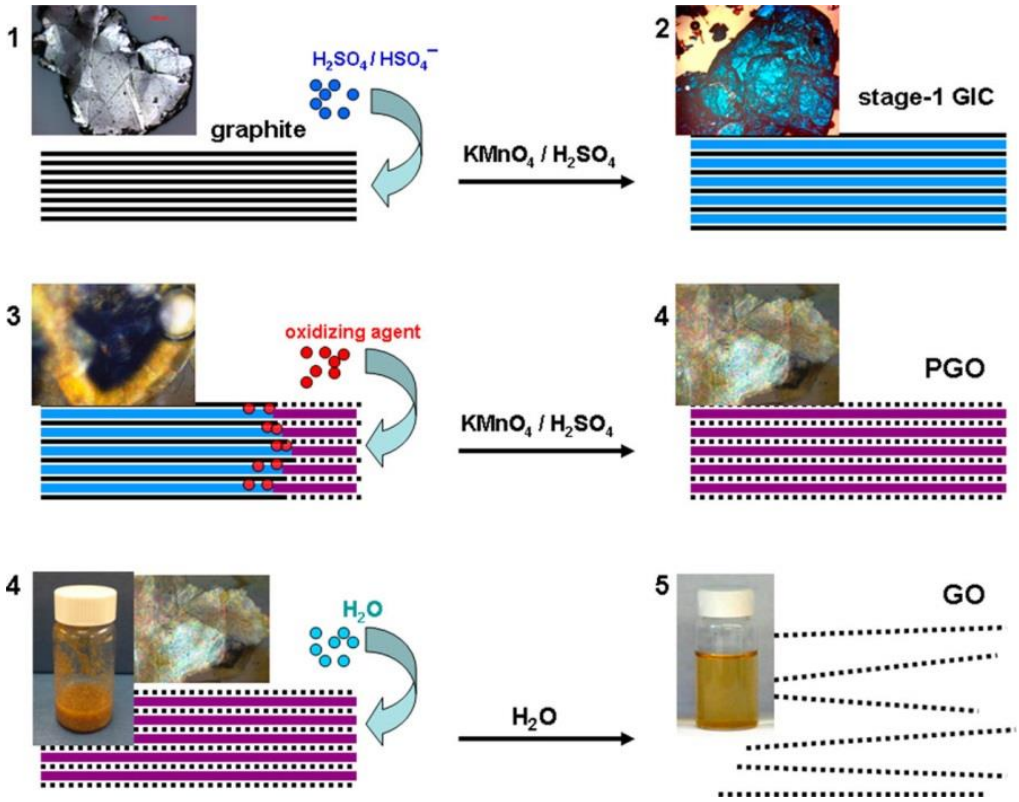

Figure 2.11. Schematics of conversion of bulk graphite into GO in modified Hummers' method. Reprinted from ref. 70.

Recently, Dimiev and Tour [70] proposed a mechanism for graphene oxide formation based on the modified Hummers' method. In this work, the whole procedure of conversion of bulk graphite into GO by oxidation can be divided into three steps, as shown in Figure 2.11. The first step begins immediately upon mixing the graphite and acid oxidizing medium, which results in the formation of a sulfuric acid-graphite intercalation compound (H_2SO_4-GIC). The acid molecules are more likely to intercalate into the graphene layer form the edge to the centre. The second step is converting the GIC to graphite oxide. In this step, the oxidizing agent diffuses into the graphite interlayer galleries and replaces the existing intercalant molecules, accompanied by the reaction with the nearby carbon atoms. The third step is conversion of graphite oxide to GO. When the graphite flake is completely oxidized, the bulk graphite oxide will

spontaneously exfoliate to mono layer GO upon exposure to water. This is due to the enthalpy of hydration of the charged GO layers by water overcoming the electrostatic attraction within the graphite oxide.[70]

The reaction mechanism for the oxidation of graphite explained by Dimiev and Tour gave a comprehensive understanding of GO formation. Although the identity of the definitive oxidizing agent species reacting with graphite interlayers is still unclear, knowing the diffusion mechanism of the oxidizing agent lets the reaction procedure to be more controllable. Based on this mechanism, the reaction time for full oxidation of graphite can be decreased by using high mesh graphite powder or disordered graphite (thermal expanded graphite or prior oxidized graphite). In addition, the high spontaneous exfoliation ability of fully oxidized graphite oxide in water makes the use of extra energy (sonication or stirring) for dispersing graphite oxide unnecessary. Thus, it is possible to produce GO with lateral sizes near to that of the initial graphite flake.

2.2.4 **Structure Models of GO**

Although the process of GO synthesis has been developed over a century, the precise chemical structure of GO is still under debate, this is due to the complex composition of the GO and the lack of accurate analytical techniques for characterizing such materials.[71] It has been found that the structure of GO is related to both the oxidation conditions and the initial graphite material used.[72] Thus, identifying and describing the precise structure of GO is challenging. Nevertheless, over the years, several structural models of GO have been proposed, including Hofmann, Ruess, Scholz-Boehm, Nakajima-Matsuo, Lerf-Klinowski, and Dékány models, as shown in Figure 2.12.

The first structural model of GO was proposed by Hofmann and Holst in 1939,[73] which contained repeating units of epoxy groups (1,2-ether) on the basal plane of graphene with a molecular formula of C_2O. This model was further modified in 1946 by Ruess, who incorporated hydroxyl groups into the carbon basal plane based on the discovery of hydrogen atoms present in GO.[74] This model is made up of sp^3 hybridised basal planes, whereas the Hofmann's model consists of sp^2 hybridised bonds. Over two decades later, Scholz and Boehm [75] proposed a model that only contains hydroxyl and ketone groups with a corrugated backbone of carbon layers. Meanwhile, Nakajima and Matsuo [76] proposed a new structure of GO, which consisted of two carbon layers linked by sp^3 carbon-carbon bonds, carbonyl and hydroxyl groups. Later, by analysing the GO

material using magic-angle spinning nuclear magnetic resonance (MAS NMR) technique, Lerf and Klinowski [77] proposed a model in which the structure of GO consists of random distributed unoxidized aromatic regions with benzene rings (graphene-like) and oxidized regions with sp^3-hybridized carbon rings. In this model, the functional groups, such as hydroxyl and epoxide, are proposed to decorate the oxidized regions in the basal plane, whereas the carboxylic acids or carboxylates groups are distributed around the edge of the sheet structure.[72] This is now the most widely adopted structure model of GO and has been supported by experimental observations using high resolution transmission electron microscopy.[78] Recently, Dékány et al.[79] proposed another model based on comprehensive characterization and analysis of GO. In this model, they described the GO as consisting of two regions: corrugated hexagonal ribbons and trans-linked cyclohexane chairs.

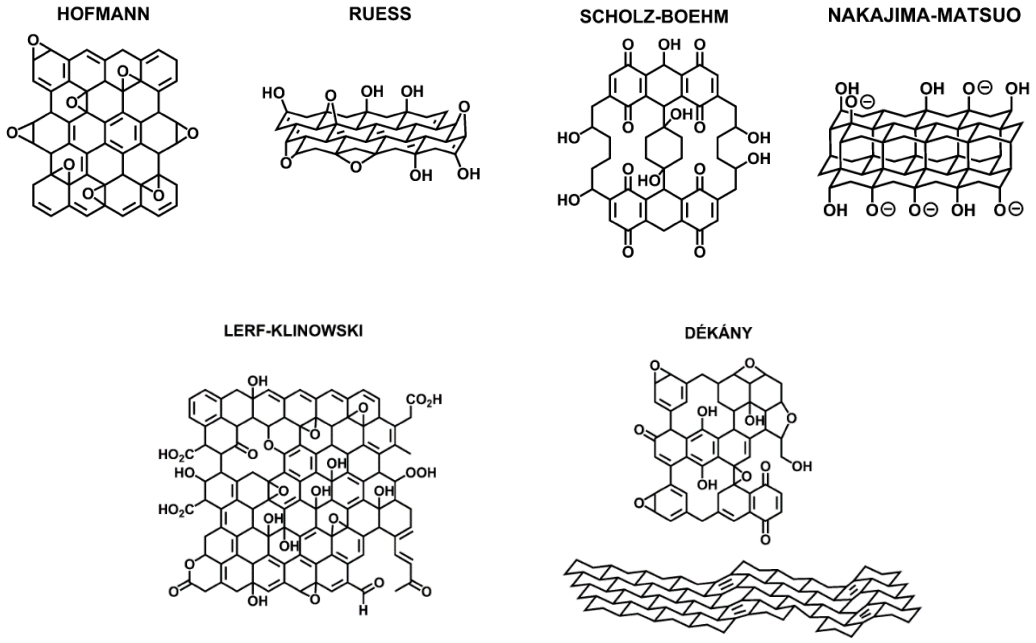

Figure 2.12. Summary of several proposed structural models of GO. Reprinted from ref. 72.

Recently, Wilson's group [63] reported a new structural model of GO, as shown in Figure 2.13. Their experiment results showed that GO prepared by the modified Hummers' method is composed of functionalized graphene-like sheets with strongly adhered oxidative debris, which acts as a surfactant to stabilize GO in water. This oxide debris-like material has been found in acid treated multi-walled CNTs aqueous suspensions.[80] Moreover, the oxidative debris can be removed from the as-prepared GO material by base-washing with aqueous sodium hydroxide (NaOH) or aqueous ammonia to obtain a

black aggregate (base washed GO), which is much more conductive than GO and cannot be resuspended in water.[81]

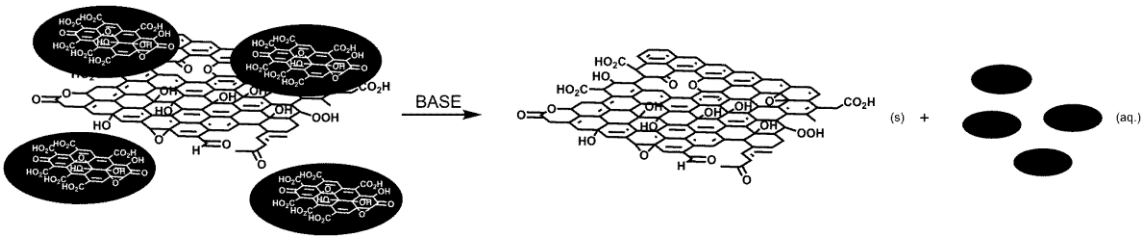

Figure 2.13. The structure model of GO with oxidative debris adhered on the surface. The as-prepared GO and oxidative debris can be separated by base washing. Reprinted from ref. 72.

2.2.5 **Reduction of GO**

Unlike graphene, GO is an electrically insulating material due to the extensive presence of oxygen functional groups on the basal plane. As the oxidation process disrupts the ordered sp^2 carbons of graphite and converts them to disordered sp^3 carbons, the π-π electronic conjugation in GO is destroyed, thus significantly decreasing the electrical conductivity.[82] To remove these functional groups from GO, a reduction process has always been used. Over the years, many reduction strategies have been achieved to transform GO to graphene-like materials. In this section, we will focus on thermal, chemical, microwave and photonic reduction pathways.

2.2.5.1 Thermal Reduction

Thermal reduction of GO is a very efficient method to produce quantities of high yield graphene-like materials in a short time. It has been stated that graphite oxide powder can be exfoliated and converted to graphene by using rapid heating (> 2000 °C/min), which results in the functional groups combining on the basal plane carbon, decomposing into CO or CO_2 gases and expanding to a graphene-like structure.[83] The high temperatures can create a huge pressure between the GO layers. Based on state equations, the pressure needed to separate two stacked GO sheets is 2.5 MPa, while the pressure generated by 200 °C is 40 MPa, this value increases to 130 MPa at a temperature of 1000 °C.[84] However, it is found that the graphene produced by a thermal exfoliation procedure always has a small individual flake size and displays a wrinkled morphology.[84] This is because not only are the functional groups decomposed into gas but also carbon atoms from within the basal plane are removed, which results in topological defects throughout the carbon plane and a breakdown of sheet size.[85, 86] The

electrical conductivity of graphene made from this procedure is in the range of 1000-2300 Sm^{-1}.[71] Although this is several orders of magnitude higher than the conductivity of GO,[87] it still much lower than that of pristine graphene,[88] indicating the weak effect of overall reduction and the restoration of the π-π electronic structure in the plane.

To obtain graphene with higher conductivity and lower defect densities, an alternative method is to first disperse the GO sheets in solvents, then depositing the GO dispersion as thin films on a substrate [89] or as a free-standing paper,[90] followed by thermal annealing. In this procedure, the conductivity of the reduced GO is significantly influenced by the annealing temperature. Wang et al.[89] reported on thermally reduced GO films with different annealing temperatures, their results showed that the conductivity of reduced GO films annealed at 550 °C was about 5000 Sm^{-1}, while for those annealed at 1100 °C the conductivity value increased more than10 times higher to 5.5×10^4 Sm^{-1} (Figure 2.14), which is near to that of polycrystalline graphite (1.25×10^5 Sm^{-1}). With further increasing the annealing temperature up to 2000 °C, the functional groups on the GO can be completely decomposed and the defects in reduced GO will be repaired due to the reorganization of carbon frameworks.[91] Graphene films with maximum conductivity of 5.77×10^5 Sm^{-1} were obtained when the annealing temperature increased to 2,700 °C.[92]

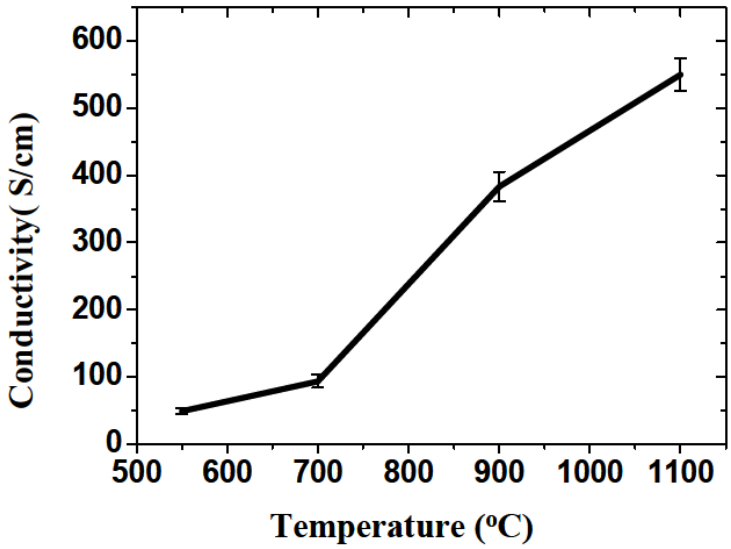

Figure 2.14. The conductivity of reduced GO films as a function of different annealing temperature. Reprinted from ref. 89.

2.2.5.2 Chemical Reduction

Although high quality graphene can be obtained by high temperature thermal annealing of GO, this procedure is not practicable due its high energy cost and incompatibility with common substrates, such as glass or plastic.[93] Alternatively, it is possibility to remove oxygen containing functional groups by chemical reductants, which can be carried out at room temperature or under moderate heating. Moreover, the required conditions for chemical reduction are not as critical as with the thermal annealing process, which makes reduction a promising process for low cost and large scale production of graphene.[83] Most reducing agents do not only react and remove the oxygen functional groups but also can introduce new groups in their place, which may in turn functionalise the graphene. Thus, graphene prepared using the chemical reduction method is normally described as chemically converted graphene (CCG).[94]

The most popular and common reducing agent for preparing CCG is hydrazine, N_2H_4. The use of hydrazine for reducing GO was first demonstrated by Ruoff and co-workers.[95] In this work, they added hydrazine hydrate into a GO aqueous colloidal suspension and the conductivity of the resulting reduced GO was about 2400 Sm^{-1}, which was 5 orders of magnitude higher than that of the as-prepared GO. Due to the absence of oxygen functional groups, which are removed by hydrazine, the reduced GO become highly hydrophobic, this can result in aggregation and sedimentation in aqueous suspension.[95] Dan et al.[96] found that the conductivity of CCG reduced by hydrazine is related to the weight ratio between hydrazine and GO. By optimizing this ratio, a conductivity of ~ 7200 Sm^{-1} was obtained at room temperature. Moreover, by adjusting the pH of the GO dispersion to about 10 by adding ammonia solution, the resulting CCG sheets can be stabilized as a dispersion in solution for several weeks. This procedure has now been widely used in solution-phase production of CCG sheets.[97-99] However, due its highly toxic and potentially explosive properties, hydrazine is not suitable for large scale commercial applications.

Ascorbic acid, also known as Vitamin C, is considered to be an environmentally-friendly substitute for hydrazine. Zhang et al.[100] reported that ascorbic acid can efficiently remove oxygen functionalities from GO at room temperature after 48 hours exposure, which resulted in a conductivity of 800 Sm^{-1} for reduced GO. Further optimizing the amount of ascorbic acid and increasing the reaction temperature to 95

°C, the reduction completion time can be decreased to 15 min, while the conductivity of reduced GO can reach 7700 Sm^{-1}, which is comparable to that of hydrazine reduction (9960 Sm^{-1}) under the same reaction conditions.[101] Other environmental friendly reducing agents such as alcohols [87] and sugars [102] have been also used for reducing GO. However, the conductivity of CCG reduced by these reductants is lower than that with ascorbic acid.

Another excellent reductant for preparing high conducive CCG is hydroiodic acid (HI). Pei et al.[103] reported a CCG with conductivity of 2.98×10^4 Sm^{-1} and a C/O ratio of 12 by immersing GO paper in hydroiodic acid at 100 °C. Similarly, Lee et al.[104] employed a mixture of HI and acetic acid as reducing agents at a temperature of 40 °C. The resulting CCG showed a conductivity of 3.04×10^4 $Sm^{-1}$and a C/O ratio of 11.5. Moreover, due to the low vapour pressure of the HI solution, rGO powder or films can also be efficiently reduced in a gaseous environment.[104]

2.2.5.3 Microwave and Photonic Reduction

Compared to thermal and chemical reduction processes, microwave and photonic reduction are rapid, chemical-free, and energy efficient.[82] Microwave irradiation has been used as an efficient method to produce exfoliated graphite from graphite intercalation compounds.[105] Chen et al prepared stable reduced GO suspensions by heating the GO suspension in a mixed solution of water and *N,N*-dimethylacetamide with microwave irradiation.[106] They reported that the conductivity of reduced GO was 4 magnitudes higher than that of GO. Furthermore, Zhu et al. reported a rapid production of exfoliated and reduced GO by treating the GO powders in a commercial microwave oven with 1 minute exposure to radiation.[107]

Photonic irradiation has been widely used for sintering printed metal electrodes, which allows a selective heating of the material.[108] Due to the localized heating of the GO, flash irradiation can generate strong temperature gradients in the GO film, which is enough to decompose the oxygen groups, and results in a reduction of GO leading to a conductivity of 1000 Sm^{-1}.[109] Moreover, the GO film can be selectively reduced by employing a photomask, which makes this procedure applicable for direct fabrication of graphene-based electronic devices.

Table 2.2. Summary of reduction methods for graphene oxide.

Methods	Conditions	Time	Conductivity (Sm^{-1})	C/O ratio
Thermal annealing	Rapid heating (> 2000 °C/min) 1050 °C in Argon [85]	30 s	1000-2300	10
	550 °C in Argon or H_2 [89]	-	5×10^3	-
	1100 °C in Argon or H_2 [89]	-	5.5×10^4	-
	1500 °C in Argon [92]	1 h	1.71×10^5	> 1000
	2700 °C in Argon [92]	1 h	5.77×10^5	> 1000
Chemical agents reduction	Hydrazine hydrate at 100 °C [95]	24 h	2400	10.3
	Hydrazine and ammonia solution at 95°C [96]	1 h	~ 7200	~ 8
	Ascorbic acid at 23°C [100]	24 h	800	-
	Hydrazine monohydrate and ammonia solution at 95° [101]	15 min	9960	12.5
	Vitamin C and ammonia solution at 95°C [101]	15 min	7700	12.5
	Aliphatic alcohols at 100 °C [87]	5 days	1019	6.9
	Benzyl alcohol at 100 °C [87]	5 days	4600	30
	Hydroiodic acid at 100 °C [103]	1 h	2.98×10^4	12
	Hydroiodic acid and acetic acid at 40 °C [104]	40 h	3.04×10^4	11.5
Microwave	280 W [107]	1 min	274	2.75
Photonic	Xenon lamp flash in N_2 at frequency of 120 Hz [109]	-	1000	4.23

2.2.6 **Characterizations**

Due to the unique structure and properties of GO, the characterization of GO is interesting and challenging especially in comparison with graphene when it has been reduced. In this section, we will discuss the common experimental techniques that have been used to analyse GO and reduced GO in the literature. For a better understanding of the differences among GO, reduced GO and pristine graphene, the properties of pristine graphene characterized by some tools will also be introduced.

As a powerful and precise technique, solid state ^{13}C nuclear magnetic resonance (NMR) spectroscopy has been used to characterize the chemical structure of GO. By using ^{13}C and ^{1}H NMR, Lerf et al.[77] confirmed the presence of C-OH groups in as-prepared

graphite oxide. Based on this finding, they proposed a structural model for GO, which now is the most well-known and widely accepted model, the Lerf - Klinowski model, as described in the previous section 2.2.4.

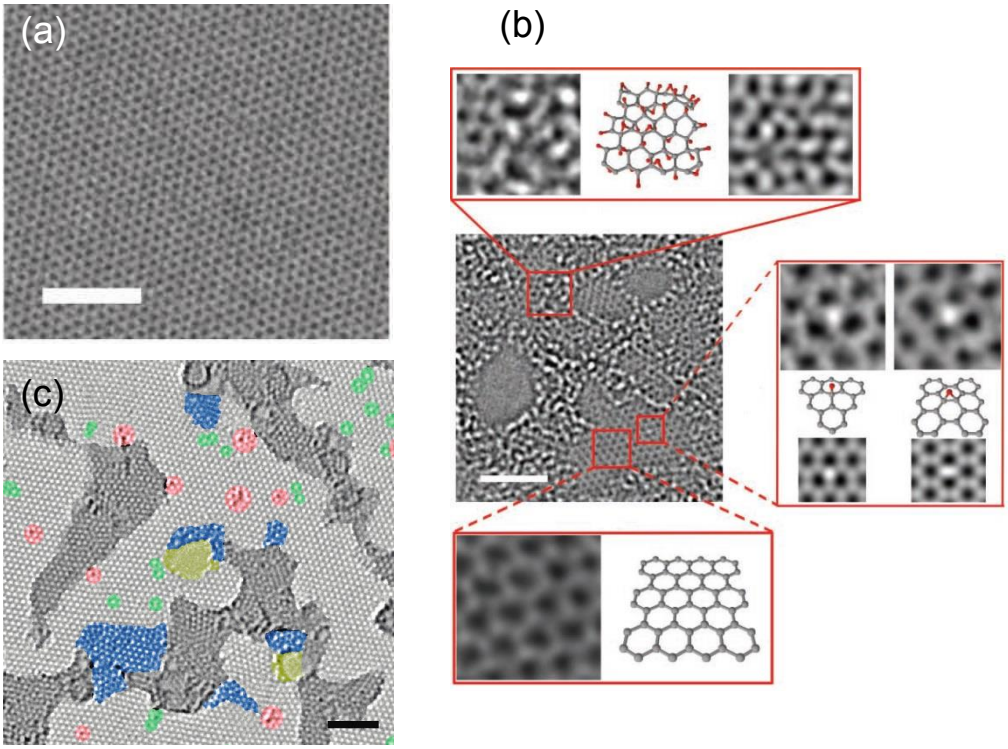

Figure 2.15. (a) HR-TEM images of graphene. (b) Aberration-corrected TEM image of a suspended GO with the atomic structure of different functional group regions. Reprinted from ref. 78. (c) Atomic resolution, aberration-corrected TEM image of a reduced GO membrane with colour added to indicate the different features. Reprinted from ref. 110. The scale bars are 2 nm.

Another powerful method to directly characterize the structure of GO is transmission electron microscopy (TEM). TEM has been considered as a precise tool to identify the number of layers for few-layered graphene that is produced by the solvent phase exfoliation method.[111] Moreover, by using high resolution TEM (HR-TEM) and a fast Fourier transform (FFT) bandpass filter, the atomic structure of graphene, GO and reduced GO can be directly observed (Figure 2.15).[78] The structure of GO and reduced GO is remarkably similar to that of graphene at low magnification TEM. However, using HR-TEM, it is found that the structure of GO consists of holes and functional groups (Figure 2.15b),[78] which can be removed leaving a graphene like sheet with islands in size of between 3 nm and 6 nm (Figure 2.15c).[110] This was matched with the generally accepted structural model of GO proposed by Lerf and Klinowski.[77]

Raman spectroscopy is a convenient and useful method to characterize the crystal quality, layer thickness, mechanical strain, and edge structure of graphene-based materials. Raman fingerprints for single-, bilayer, and multi-layer graphene are the D, G, and 2D (G′) peaks at about 1350 cm^{-1}, 1580 cm^{-1}, and 2700 cm^{-1}, respectively.[56] In single-layer graphene, as shown in Figure 2.16a, a strong 2D peak can be observed, which is about twice the intensity of that of the G peak. With increasing numbers of layers, the intensity of the G peak becomes stronger than the 2D peak. In addition, the 2D peak is shifted to a higher wavenumber and has a different shape. Normally, the quality and layer number of graphene can be determined by the shape, width, and position of the 2D peak.[112] The D peak is normally observed at the graphene edges with strong intensity at armchair but weak intensity at zigzag type edges.[113] The Raman spectrum of graphene oxide and reduced graphene oxide is different from that of either graphite or graphene as shown in Figure 2.16b. The G band is broadened and overlapped with the D band in both GO and reduced GO. The appearance of the D band shows the indication of existing of sp^3 bonding in the GO and the reduced GO due to the defects in the structure.[86]

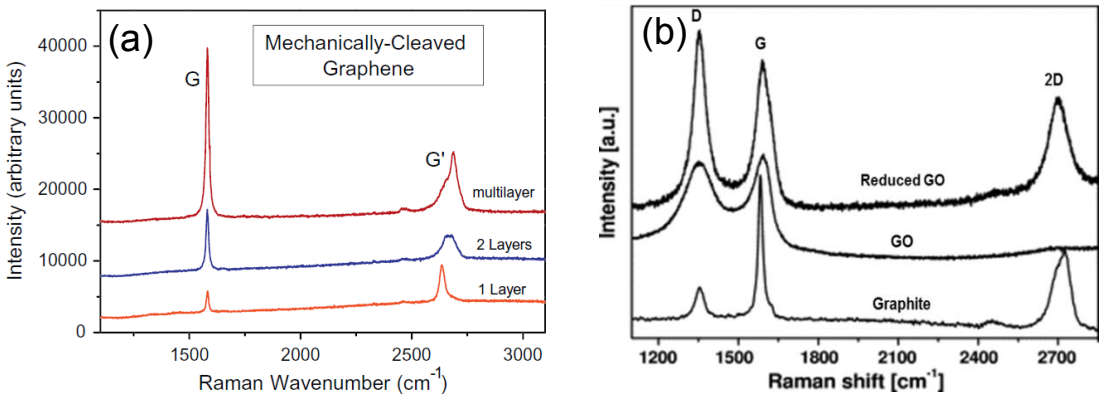

Figure 2.16. (a) Typical Raman spectra of pristine graphene with monolayer, bilayer and multilayer. Reprinted from ref. 114. (b) Raman spectra of graphite, GO and rGO. Reprinted from ref. 115.

Atomic force microscopy (AFM) is one of the most powerful tools for characterizing the 2D nature of graphene-based materials. A single layer of graphene with a thickness of ~ 0.4 nm has been measured by using AFM.[52] The thickness of single-layer graphene is normally reported as between 0.4 and 1.0 nm due to the varying interactions between the AFM tip and graphene or the supporting substrate. As the interlayer spacing in graphite is ~0.335 nm and the detectable resolution that an AFM can obtain ~0.1 nm, AFM is now used routinely for estimating the number of layers of graphene.[114] Recently,

an atomic contrast AFM imaging of graphene has been reported by using inert (carbon monoxide -terminated) and reactive (iridium-terminated) tips.[116] The thickness of GO measured by AFM is around 1 nm.[114] This value is higher than the thickness of graphene due to the presence of oxygen functional groups on GO sheets. After removing the functional group by a reduction procedure, the thickness of obtained reduced GO sheets decreases to ~ 0.37 nm,[117] which is near to that of pristine graphene, as shown in Figure 2.17 a-b. In addition, AFM has also been used for analysing the size distribution of graphene-based flakes, the thickness and surface roughness of deposited graphene-based films.

Scanning electron microscopy (SEM) can provide rapid examination of graphene prepared on various substrates. It can clearly distinguish CVD grown, hexagonally shaped graphene grains on Cu under by contrast due to the conductivity difference between graphene and Cu.[118] SEM is an efficient tool for measuring the lateral size distribution of graphene flakes prepared by the chemical exfoliation method or the oxidation and reduction method.[119] Moreover, SEM is also commonly used to measure the cross-section morphology and thickness of GO and reduced GO papers.[103]

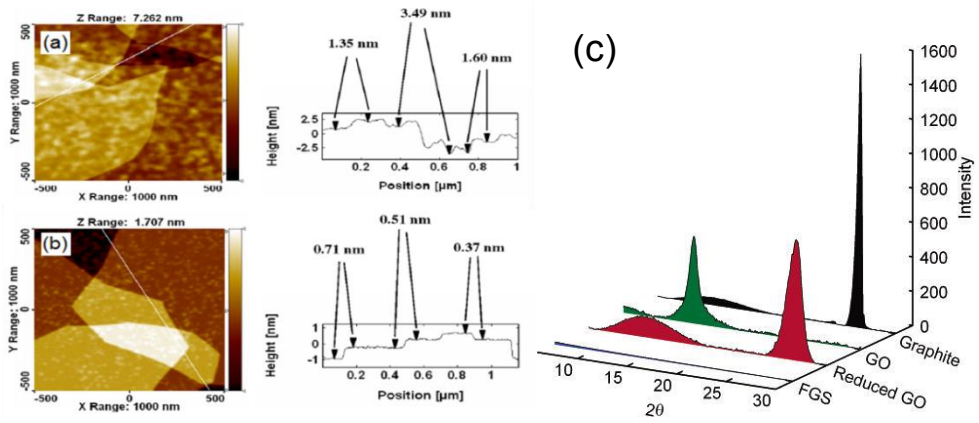

Figure 2.17. AFM images of (a) the as-deposited GO and (b) reduced by the heat treatment at 1000 °C. Reprinted from ref. 117. (c) XRD patterns of graphite, GO, and reduced GO. Reprinted from ref. 84.

X-ray diffraction (XRD) is another technique that can be used to characterize few-layer graphene, graphite oxide and reduced graphite oxide. This is because graphite has a sharp (002) Bragg reflection at 2θ ~26° (using Cu Kα radiation of wavelength 0.154 nm),[114] while this reflection angle in graphite oxide is transferred to a new peak at 2θ ~14° due to the increased layer spacing caused by the existence of functional groups

(~0.7 nm). After heat treatment, the new peak shifts to 2θ ~27° with a broad band to graphite (Figure 2.17c).[84] This tool is now very commonly used for analysing the degree of oxidation of graphite and the recovery ability of reduced GO.

Another powerful, yet complex tool for analysing the electronic structure of graphene is through X-ray photoelectron spectroscopy (XPS).[56] XPS is useful to characterize the doping or functionalizing of graphene, or determining the degree of reduction of GO by analysing the composition and bonding information from the binding energy between different elements.[56] GO material normally shows two overlapped peaks centred near 284 and 286 eV, which are representing the C=C and oxidized carbon bonding respectively.[103] Although XPS is a semi-quantitative analysing technique, it has been frequently used to analyse the C/O ratio in GO and reduced GO.

UV-vis spectroscopy is normally used to analyse the features of the GO dispersion. The GO aqueous dispersion shows two characteristic absorption peaks around 230 and 300 nm, which corresponding to π to π^* transition of C=C bond and n to π^* transition of C=O bond respectively.[65] After reduction, the shoulder peak at 300 nm disappears, while the absorption peak at around 230 nm shifts to around 270 nm.[96]

2.2.7 **Applications in Electronics Deposited by Inkjet Printing**

During the last decade, GO and chemically converted GO have been widely used as a multifunctional material for various applications due to their remarkable properties. The dispersibility of GO in water and organic solvents [120] and the multi-choice availability of reduction strategies makes possible the high yield manufacture of graphene-based functional electronic devices through an environmentally friendly and economically inexpensive solution-based process - inkjet printing. From the literature, it is found that the GO or reduced GO materials deposited by inkjet printing are mainly used as a conductor or sensor layer.

2.2.7.1 As a Conductor

There are two strategies for the use of inkjet printing to obtain reduced GO patterns. The first route is inkjet printing of GO dispersion on the substrate, followed by reducing the GO pattern. Kong et al.[121] reported a graphene electrode fabricated by inkjet printing. In their work, the GO ink was directly printed on a polyimide substrate, and the resulting GO film was further reduced by an infrared heat lamp with a temperature of ~ 200 °C.

The reduced GO film showed a sheet resistance of 0.3 MΩ/□ at a transparency of 45%. Shin et al.[122] reported a highly conductive reduced GO film by inkjet printing, in which the printed GO film was reduced by hydrazine and ammonia vapour at 90 °C. The reduced GO film showed a sheet resistance of ~ 65 Ω/□ after 30 printing repetitions, which can be used as the electrode for wideband dipole-antenna. Recently, Su et al.[123] reported an inkjet-printed graphene film with conductivity of ~ 4.2×10^4 Sm^{-1}. They prepared a mildly oxidized GO film and used HI as the reductant to achieve high conductivity. In addition, the printed graphene pattern was employed as a source/drain/gate electrode for single-wall carbon nanotube field effect transistors, which showed an on/off ratio of 10^4 and mobility of 8 $cm^2 \cdot C^{-1} \cdot s^{-1}$.

The second route for producing printed reduced GO films is obtained by reducing the GO in the solution phase first, then depositing the reduced GO dispersion as the ink. This route always needs a surfactant to prevent aggregation and sedimentation of the ink due to the poor dispersibility of reduced GO sheets in water. Lim et al.[123] reported the use of inkjet-printed reduced GO/polyvinyl alcohol (PVA) electrodes for field effect transistors. In this case, the GO dispersion was first mixed with PVA, and then hydrazine monohydrate was added to reduce the GO. The reduced GO/PVA dispersion was directly printed on a Si/SiO_2 wafer as the electrode. However, the conductivity of the reduced GO/PVA electrode was ~ 1 Sm^{-1}, which was increased to 1000 Sm^{-1} after a further 350 °C heat treatment.

2.2.7.2 As a Sensor Layer

Due to the high available surface area, GO and reduced GO are very promising materials for use as sensor materials for chemical and biological detection. Dua et al.[124] reported an organic vapour sensor based on inkjet-printed reduced GO. Here, the reduced GO was obtained by dispersing the GO powder in an ascorbic acid solution. The reduced GO powder was dispersed in water using Triton-X100 as the surfactant, the dispersion was then printed on a PET substrate. The reduced GO sensor showed a very high sensitivity to various types of organic vapour at the part per billion level. Zhang et al.[125] reported a reduced graphene-polyoxometalate (PTA) composite film through layer-by-layer inkjet printing. The printed GO/PTA film was reduced by a 100 W high-pressure mercury lamp. The test results showed that the reduced GO/PTA composite film had highly electrocatalytic activities for dopamine.

2.3 The New 2D Material: Black Phosphorus

2.3.1 Introduction

Black phosphorus (BP) is the thermodynamically stable form of phosphorus, which shows a layer-by-layer stacked structure of phosphorus atoms, as shown in Figure 2.18. BP was first synthesized in 1914 by Bridgman through conversion from white phosphorus in a cylinder at an elevated temperature of 200 °C and pressure of 1.2 GPa.[126] Although unlike the white and red forms of the phosphorus allotrope, BP is a conductor of electricity and is chemically stable in air in up to 400 °C,[126] it has not attracted much attention by scientists for nearly a century.

Figure 2.18. The chemical structure of few-layer black phosphorus. Reprinted from ref.127.

However, over the past two years, phosphorene, the 2D variant of the layered BP allotrope, has attracted tremendous attention in the research area of 2D materials due to its remarkable semiconducting properties including wide bandgap and high hole mobility.[128, 129] Unlike graphene, which has no bandgap or typical transition metal dichalcogenides (TMDCs) such as MoS_2, which show direct bandgaps only in monolayer form, BP has a direct bandgap from ~ 2 eV (mono-layer) to 0.3 eV (bulk form) depending on its thickness.[130] The mono- or few-layer form of BP has been successfully isolated by micromechanical cleavage and solution phase exfoliation techniques, which has been widely used for producing atomic thick layers from a range of 2D materials. Since the report of successful fabrication and outstanding performance of the few-layer BP field-effect transistor in early 2014,[129, 131] numerous theoretical and experimental research works have been undertaken to predict and find the novel physical, chemical, and mechanical properties of mono and few-layer BP based nano-devices for applications in nanoelectronics, optoelectronics, spintronics, and

photovoltaics.[132] It has also been proposed that BP has the potential applications in lithium ion batteries, gas sensors, humidity sensors, and thermoelectrics.

In this section, we review the recent progress in phosphorene and few-layer BP fabrication, properties, applications, and discuss the potential challenges in the practical applications beyond the laboratory.

2.3.2 **Fabrication of BP**

2.3.2.1 Mechanical Exfoliation

Mechanical cleavage is the simplest way to fabricate atom thick layers of 2D materials, and this has been widely used for preparing small samples of mono- or few- layer graphene and TMDCs. Similar to that of graphene, in the structure of BP (Figure 2.18) the monolayers of phosphorene are stacked together to form layered crystals by weak van der Waals forces, which suggests that it is possible to produce atom thick BP by mechanical cleavage. Liu et al. first reported an atomically thin phosphorene that was exfoliated from a commercial bulk BP crystal by micromechanical cleavage with an adhesive tape.[131] After transfer onto Si/SiO_2 substrates, the sample was cleaned by various organic solvents to remove the tape residue. The BP sheet showed a thickness of ~ 0.85 nm (Figure 2.19), which indicated the presence of single-layer phosphorene. Although the mechanical cleavage method can fabricate high quality mono- and few-layer phosphorene that shows remarkable mobility and optoelectronic properties, this method has low yield and production rate and is hence only used for laboratory research.

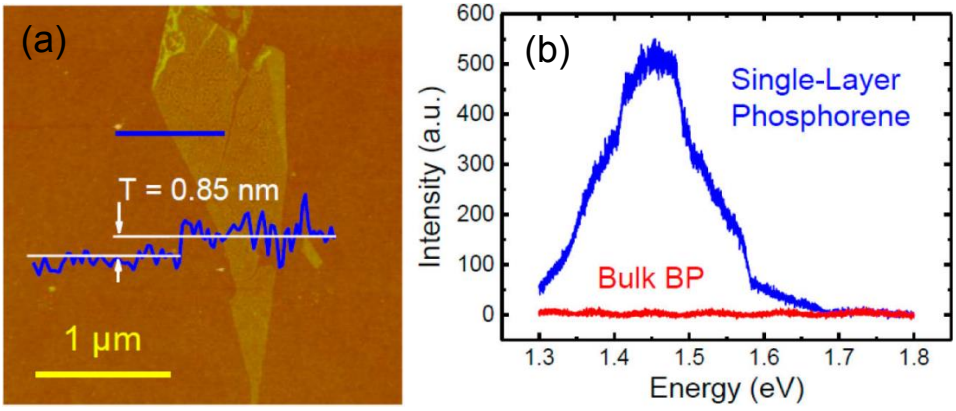

Figure 2.19. (a) AFM image of a single-layer phosphorene by mechanical exfoliation method. (b) Photoluminescence spectra for single-layer phosphorene. Reprinted from ref. 131.

2.3.2.2 Liquid Phase Exfoliation

To produce a large quantity of phosphorene nanosheets, one possible solution is the exfoliation of BP crystal in a liquid phase. The LPE method is a simple method, which has also been widely used for large yield production of graphene and other 2D nanosheets.[133] Normally, layered materials can be well exfoliated and dispersed in a suitable solvent by using high energy ultrasonic waves. When the properties of solvents match the surface energy of 2D materials, the layered crystallites can be break-up to form exfoliated nanosheets by the high energy jets of cavitation bubbles that are generated by ultrasonic waves.[133] After sufficient sonication time, the exfoliated nanosheets are divided to mono- and few-layers by centrifugation process. Moreover, the mean size of the flakes as well as the concentration of the dispersion can be controlled by adjusting the sonication time and centrifugation procedures.[134] A schematic description of the LPE process is shown in Figure 2.20.

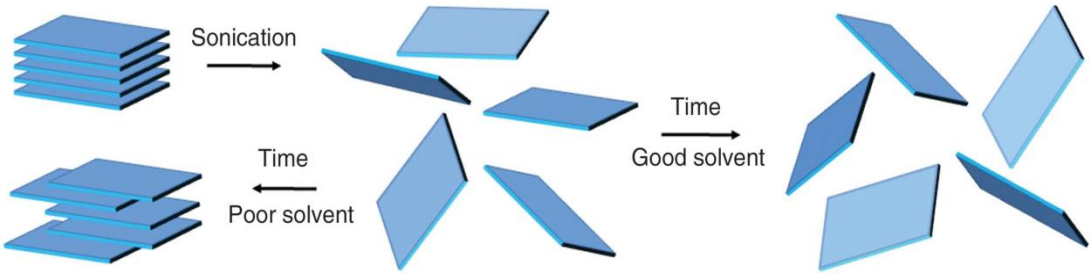

Figure 2.20. The schematic description of the LPE process. Reprinted from ref. 133.

Since the few-layered BP produced by mechanical cleavage has been reported, researchers have also made great effort to employ LPE method to produce large quantity and high quality of phosphorene nanosheets. Brent et al. first reported that using LPE method is a simple and facile route toward the production of few-layer phosphorene.[127] In this paper, they employed methyl-2-pyrrolidone (NMP) as the exfoliation and dispersion solvent, and the exfoliated BP nanosheets showed a thickness of 3.5-5 nm which indicated three to five-layer phosphorene. To find the optimized solvent for BP exfoliation, Kang et al. investigated the concentration of exfoliated BP nanosheets in various solvents, including acetone, chloroform, hexane, ethanol, isopropyl alcohol, dimethylformamide (DMF), and NMP.[135] The results showed that among these solvents, BP exfoliated in NMP displayed the most stable and highest concentration dispersion. Furthermore, Yasaei et al.[136] reported that aprotic and polar solvents, such as DMF and dimethyl sulfoxide (DMSO) are also suitable for exfoliation

of BP to form atomically thin phosphorene nanosheets by sonication. The performance of devices based on these nanosheets indicated that solvent exfoliated BP nanosheets had competitive electrical properties to that of BP flakes obtained by mechanical exfoliated. The high yield production ability of solvent exfoliation opened up new possibility to form BP nanosheets into thin films and composites for large scale applications.

2.3.3 **Applications of BP**

2.3.3.1 Field-Effect Transistors

The field-effect transistor (FET) is the key component for microelectronics. Silicon metal-oxide-semiconductor FETs are widely used in integrated circuits for amplifying or switching electronic signals. However, with the gate length down to 20 nm, it becomes more and more difficult to further fabricate short channels on silicon-based devices due to the short-channel effects and the deteriorating effects of parasitics.[137] Therefore, in recent years, researchers and chipmakers are searching for new materials to replace silicon. Generally, the ideal candidate materials for transistor applications should have high carrier mobility, a high on/off ratio, and low off-state conductance.[132]

Graphene has been considered as the most promising candidate for replacing Si due to its remarkable carrier mobility (2×10^4 $cm^2 \cdot V^{-1}$ s^{-1}),[138] which can be used for high speed and high frequency devices. However, its semimetallic nature, which results in a low on/off switching ratio (< 10), limits its applications in transistors. On the other hand, although 2D TMDCs have bandgaps near 1-2 eV and can obtain a high on/off ratio up to 10^8, their moderate carrier mobility (< 400 $cm^2 \cdot V^{-1}$ s^{-1}) limits their usage for fast operation applications.[139]

Phosphorene is potentially a new candidate material due to its combination of a high carrier mobility and tunable bandgap. It was found that the mobility of few-layer phosphorene was thickness-dependent, which showed the highest mobility of ~ 1000 $cm^2 \cdot V^{-1}$ s^{-1} at room temperature for a thickness of 10 nm.[129] The high mobility feature makes phosphorene-based FETs able to operate at high frequency. Wang et al.[140] reported a BP radio-frequency transistor, with 300 nm channel length, which showed a short-circuit gain cut-off frequency of 12 GHz and a maximum oscillation frequency of 20 GHz. On the other hand, unlike TMDCs materials, which only show a direct

bandgap at monolayer, BP shows a direct bandgap between 0.3 eV (bulk) and 2.0 eV (mono-layer), which ensures that phosphorene-based FETs will have a high current on/off ratio with a factor of 10^4~10^5 at room temperature.[129, 131] This current modulation property of phosphorene-based transistors is much better than that of graphene and approaches to that of TMDCs-based devices. Thus, phosphorene is a promising candidate material for the next generation of high performance microelectronics.

2.3.3.2 Optoelectronic Devices

Due to the property of direct and tunable bandgap, BP is also a very promising semiconductor for optoelectronic applications. As mentioned previously, BP shows a direct bandgap of ~ 0.3 eV in bulk and few-layers and increases to ~ 2.0 eV in monolayer form. This wide range and thickness-dependent bandgap combined with its high mobility allows phosphorene to be used for high speed photodetectors with a range of wavelengths even in the infrared region. Buscema et al. reported a fast and broadband photo-transistor based on few-layer phosphorene, which showed a current on/off ratio > 10^3 with a response time of ~1 ms with the excitation wavelengths from the visible region (640 nm) to near infra region (940 nm).[141] The BP-based transistors that were used for detection of THz-frequency light have been reported recently.[142] Moreover, p-type BP also can be combined with n-type MoS_2 via a van der Waals heterojunction to from high performance p-n diodes.[143] This type of p-n diode showed a maximum photodetection responsivity of 418 mA/W at the wavelength of 633 nm, which is nearly 100 times higher than that of a solely BP-based phototransistor.

2.3.3.3 Chemical Gas/Vapour Sensors

2D materials have been used as promising candidates for gas detectors due to their large surface-to-volume ratio and the correlative charge transfer between the 2D base plane and gas molecules.[144] High performance sensors based on 2D materials such as graphene and MoS_2 have been investigated by both theoretical and experimental works. Generally, in a 2D materials based gas sensor, the gas molecules are adsorbed on the surface of the 2D plane, which induces changes in the resistivity of the plane. Using transport calculations, it has been predicted that monolayer phosphorene can also adsorb gas molecules such as CO, CO_2, NH_3, NO, and NO_2.[144] Further experimental results demonstrated that mechanically exfoliated few-layer phosphorene FETs sensors were able to detect NO_2 down to 5 ppb,[145] which is comparable in sensitivity to that of the

best sensors based on other 2D materials. BP films prepared by solvent exfoliated BP nanosheets also showed a highly selective sensitivity to NO_2 at concentrations as low as 0.1 ppm, which is 20 times higher sensitivity than that of MoS_2 and graphene.[146] Moreover, a NH_3 sensor based on a few-layer BP-based film showed an estimated detection threshold of 80 ppb.[130] Besides, the BP films sensors also showed an ultrasensitive response to humidity in air.[147] Unlike the conventional gas sensors in which the current change is induced by gas adsorption, the current modulation in the BP humidity sensor is caused by the ionic solvation of the phosphorus oxoacids produced on the surface of BP nanosheets when exposed to water molecules. Experimental results showed that the BP nanosheets were degraded under humid air conditions.[148] Thus, the application BP for humidity sensors is arguable because of this permanent property change.

2.3.3.4 Battery Applications

Another promising application for phosphorene is as anodes in advanced batteries due to the high theoretical specific capacity of phosphorus (2596 mAh/g) at the discharge potential range of 0.4 -1.2 V.[149] Theoretical calculation indicated that a phosphorene-based Li-ion battery could exhibit a large average voltage of 2.9 V as well as good electrical conductivity induced by Li-intercalation of phosphorene.[150] It is also predicted that Li atoms can bind strongly with phosphorus atoms in the cationic state. The low energy barrier of monolayer phosphorene along the zigzag direction leading to the speed of Li diffusion in phosphorene is estimated to be 10^2 and 10^4 times faster than that on MoS_2 and graphene at room temperature, respectively.[150] Chen et al. reported a flexible lithium ion battery manufactured using solvent exfoliated few-layer phosphorene as electrodes,[151] which showed a specific capacity of 180 mAh/g at a current density of 100 mA/g. This specific capacity was further increased to the value of 920 mAh/g by using phosphorene-graphene hybrid paper electrodes. By using a chemically bonded phosphorene-graphite composite, Sun et al. reported a high performance Li-Battery with a specific capacity up to 2786 mAh/g at current rate of 0.2 C and 80% capacity retention after 100 cycles.[149]

2.3.4 **Challenges for BP Applications**

Although phosphorene is very promising for both electronic and optoelectronic applications, it is still a challenge to bring phosphorene out of the laboratory. Currently,

almost all phosphorene devices are based on sub-micron lateral dimension few-layer phosphorene nanosheets which are produced by the mechanical cleavage process. To fabricate devices suitable for integrated circuit applications, it is essential to grow wafer-scale size mono- or few layer phosphorene crystals. A possible route is via CVD or epitaxial growth on substrates which have been widely used to fabricate large area graphene and monolayer TMDCs. While the chemical deposition growth strategies for producing monolayer phosphorene have not been successful yet due to its high frangibility, surface exposure to air and the absence of suitable substrates for phosphorene growth.[132] However, the successfully synthesized few-layer phosphorene nanosheets [152] and millimeter size nano-crystalline BP thin film [153] via CVD process provided the possibility for large area phosphorene growth.

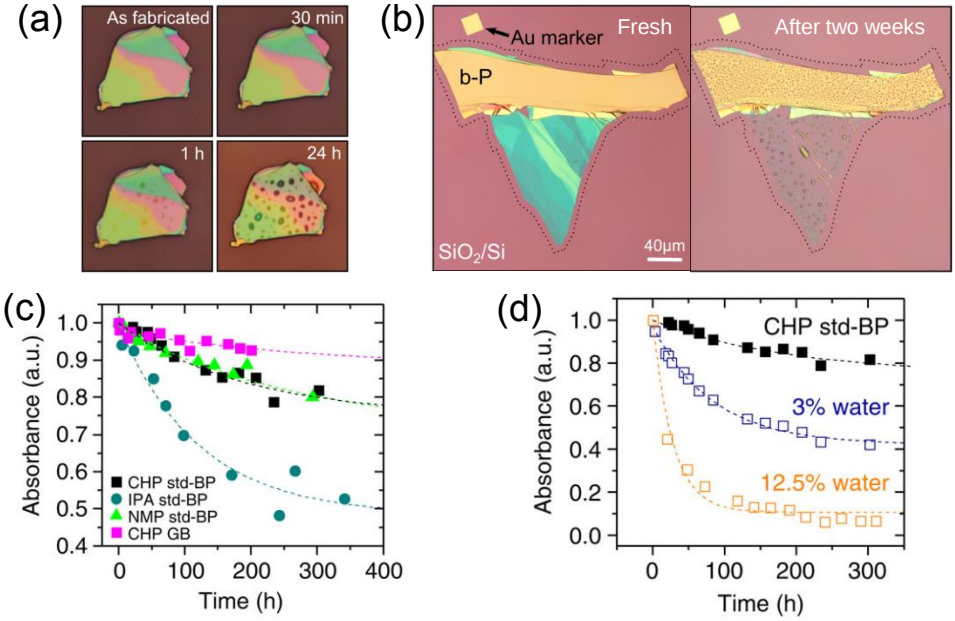

Figure 2.21. (a) Optical images of a same BP nanosheet after exposing in ambient conditions for different time. (b) The comparison of a same BP nanosheet after exfoliation and after two weeks in air. Reprinted from ref. 154. (c) The absorbance of BP dispersion in different solvents over time. (d) The time-dependent absorbance data for BP dispersion with different volume of water added. Reprinted from ref. 130.

Another challenge for the use of phosphorene for practical applications is its instability in ambient conditions. Although bulk BP crystal shows good chemical stability in air and can be heated up to 400 °C without spontaneous ignition,[128] mono- or few-layer phosphorene is found to be unstable in atmospheric environments. Visible drops have been found on the surface of fresh mechanical exfoliated BP flake after exposing in air for 1 h,[154] which kept growing in size with increasing exposure time, as shown in Figure

2.21a. The hydrophilic droplets deteriorate the surface of BP flake, etching away the thinner part of the flakes after longer time exposure to air (Figure 2.21b).[154] The strong affinity of water on the surface of phosphorene greatly influences the performance of the fabricated device. The threshold voltage of the BP FETs occurs shifted after minutes time exposure in air, which eventually degraded after several hours to days exposure.[148] Moreover, the degradation of BP has been also found in few-layer BP exfoliated in solvents. The BP dispersions showed a continuous fall in measured absorbance over time (Figure 2.21c), which indicated the degradation of BP nanosheets.[130] With increasing water volume in the solvent, the degradation rate increased as well (Figure 2.21d).

Theoretical predictions and experimental measurements indicate that the degradation of few-layer phosphorene in ambient air is due to the chemisorption-induced oxidation by water and oxygen.[132] Therefore, to prevent the degradation process, it is critical to avoid the contact between phosphorene and water or oxygen during both the material and device fabrication process. For mechanical exfoliated BP, the whole process can operate in a glove box with N_2 atmosphere. While for solution exfoliated BP, a high boiling point solvent with shell protecting ability can be chosen [130] or else by using a sealed container [135] during the exfoliation process. On the other hand, the device measurement can be operated in a high vacuum environment [129] or after employing an encapsulation and coating layer [155] to isolate the reacting agents.

2.4 **Summary and Conclusions**

In the first part of this chapter, we have summarized and discussed the inkjet printing technique. From the roadmap of development, it is known that inkjet printing has now been applied in manufacturing functional electronic components due to its easy set up and low capital cost. To make functional inks, the properties of inks such as surface tension and viscosity should meet the basic requirement for printable inks. The jetting behaviour of inks is a very complex process, which can be influenced by both the properties of inks and the features of the print-head. The behaviour of drop impacting and spreading on substrates is also very important in determining the final morphology of dried droplets. To obtain a desired and uniform pattern, the influence of the surface energy of substrate and the drop spacing should be considered. In addition, during the

solidification process, the elimination of the coffee ring effect is essential for practical applications.

In the second part, we have reviewed the strategy for manufacturing graphene using the chemical oxidation and reduction route. The presence of functional groups on GO makes it relatively easy to disperse in various solvents forming stable GO inks, which can be further deposited on substrates by inkjet printing. In order to convert the printable GO to a more conductive form, it is necessary to convert it to a form closer to graphene by a reduction process. Chemical routes for this reduction have been reviewed and routes to produce a dramatic increase in electrical conductivity after inkjet printing have been identified.

Finally, we have summarized and discussed the fabrication, applications and challenges of black phosphorus. Similar to graphene, BP can be produced by mechanical and solvent exfoliation process. The high electronic properties in carrier mobility and tunable bandgap as well as the unique structure lead it is promising for a wide range of applications. However, the development of better fabrication method to synthesis large scale phosphorene and finding more efficient strategy to avoid the degradation of thin BP flakes are necessary for practical applications.

Reference

1. Derby, B., Inkjet Printing of Functional and Structural Materials: Fluid Property Requirements, Feature Stability, and Resolution. *Annual Review of Materials Research, Vol 40*, 2010. **40**: p. 395-414.

2. Torrisi, F., Hasan, T., Wu, W.P., Sun, Z.P., Lombardo, A., Kulmala, T.S., Hsieh, G.W., Jung, S.J., Bonaccorso, F., Paul, P.J., Chu, D.P., and Ferrari, A.C., Inkjet-Printed Graphene Electronics. *ACS Nano*, 2012. **6**(4): p. 2992-3006.

3. Tekin, E., de Gans, B.J., and Schubert, U.S., Ink-jet printing of polymers - from single dots to thin film libraries. *Journal of Materials Chemistry*, 2004. **14**(17): p. 2627-2632.

4. Nollet, J.A. and Watson, W., Accompanying an Examination of Certain Phaenomena in Electricity. *Philosophical Transactions*, 1749. **46**: p. 368-397.

5. Savart, F., Mémoire sur la constitution des veines liquides lancees par des orifices circulaires en mince paroi. *Annales de Chimie et de Physique*, 1833. **53**: p. 337.

6. Plateau, M.T., On the recent theories of the constitution of jets of liquid issuing from circular orifices. *Philosophical Magazine Series 4.*, 1856. **12**(79): p. 286-297.

7. Thomson, W., Improvement in recording instruments for the electric telegraph. *British Letters Patent*, 1867, No. 2147.

8. Thomson, W., Recording instruments. *US Patents*, 1897, 588251 A.

9. Rayleigh, F.R.S., On the instability of jets. *Proceedings of the London Mathematical Society,* 1878. **10**(4): p. 4-13.

10. http://www.ecglibrary.com/ecghist.html

11. Sweet, R.G., High Frequency Recording with Electrostatically Deflected Ink Jets. *Review of Scientific Instruments*, 1965. **36**(2): p. 131-136.

12. Cummins, G. and Desmulliez, M.P.Y., Inkjet printing of conductive materials: a review. *Circuit World*, 2012. **38**(4): p. 193-213.

13. Le, H.P., Progress and trends in ink-jet printing technology. *Journal of Imaging Science and Technology*, 1998. **42**(1): p. 49-62.

14. Naiman, M., Sudden steam printer. *US Patents*, 1965, 3179042 A.

15. Kobayashi, H., Koumura, N., and Ohno, S., Liquid recording medium. 1981, *US Patents*. 4243994 A.

16. Vaught, J.L., Cloutier, F.L., Donald, D.K., Meyer, J.D., Tacklind, C.A., and Taub, H.H., Thermal ink jet printer. *US Patents*, 1984, 4490728 A.

17. Hansell, C.W., Jet sprayer actuated by supersonic waves. *US Patents*, 1950, 2512743 A.

18. Brunahl, J. and Grishin, A.M., Piezoelectric shear mode drop-on-demand inkjet actuator. *Sensors and Actuators a-Physical*, 2002. **101**(3): p. 371-382.

19. Zoltan, S.I., Pulsed droplet ejecting system. *US Patents*, 1972, 3683212 A.

20. Smith, P.J., Shin, D.Y., Stringer, J.E., Derby, B., and Reis, N., Direct ink-jet printing and low temperature conversion of conductive silver patterns. *Journal of Materials Science*, 2006. **41**(13): p. 4153-4158.

21. Stemme, N., Arrangement of writing mechanisms for writing on paper with a coloredliquid. *US Patents*, 1972, 3747120 A.

22. Howkins, S.D., Ink jet method and apparatus. *US Patents*, 1984, 4459601 A.

23. Kenneth H. Fischbeck, A.T.W., Shear mode transducer for drop-on-demand liquid ejector. *US Patents*, 1985, 4584590 A.

24. Winston, R., Method of and apparatus for transferring ink. *US Patents*, 1958, 3060429 A.

25. Perelaer, J., Microstructures Prepared via Inkjet Printing and Embossing Techniques. *PhD thesis*, 2009.

26. Magdassi, S., *The Chemistry of Inkjet Inks*. 2009: World Scientific.

27. Creagh, L.T. and McDonald, M., Design and performance of inkjet print heads for non-graphic-arts applications. *MRS Bulletin*, 2003. **28**(11): p. 807-811.

28. Derby, B., Inkjet printing ceramics: From drops to solid. *Journal of the European Ceramic Society*, 2011. **31**(14): p. 2543-2550.

29. Magdassi, S., *Ink requirements and formulations guidelines*, in *The chemistry of inkjet inks*. 2010, World Scientific Publishing: Singapore. p. 19-41.

30. McKinley, G.H. and Renardy, M., Wolfgang von Ohnesorge. *Physics of Fluids*, 2011. **23**(12): p. 127101.

31. *Ohnesorge Number*, in *Encyclopedia of Microfluidics and Nanofluidics*, D. Li, Editor. 2008, Springer US: Boston, MA. p. 1513-1513.

32. Fromm, J.E., Numerical-Calculation of the Fluid-Dynamics of Drop-on-Demand Jets. *Ibm Journal of Research and Development*, 1984. **28**(3): p. 322-333.

33. Reis, N. and Derby, B., Ink jet deposition of ceramic suspensions: Modelling and experiments of droplet formation. *Materials Development for Direct Write Technologies*, 2000. **624**: p. 65-70.

34. Jang, D., Kim, D., and Moon, J., Influence of Fluid Physical Properties on Ink-Jet Printability. *Langmuir*, 2009. **25**(5): p. 2629-2635.

35. Duineveld, P.C., de Kok, M.A., Buechel, M., Sempel, A.H., Mutsaers, K.A.H., van de Weijer, P., Camps, I.G.J., van den Biggelaar, T.J.M., Rubingh, J.E.J.M., and Haskal, E.I., Ink-jet printing of polymer light-emitting devices. *Organic Light-Emitting Materials and Devices V*, 2002. **4464**: p. 59-67.

36. Stow, C.D. and Hadfield, M.G., An Experimental Investigation of Fluid-Flow Resulting from the Impact of a Water Drop with an Unyielding Dry Surface. *Proceedings of the Royal Society of London Series a-Mathematical Physical and Engineering Sciences*, 1981. **373**(1755): p. 419-441.

37. Bhola, R. and Chandra, S., Parameters controlling solidification of molten wax droplets falling on a solid surface. *Journal of Materials Science*, 1999. **34**(19): p. 4883-4894.

38. Derby, B., Additive Manufacture of Ceramics Components by Inkjet Printing. *Engineering*, 2015. **1**(1): p. 113-123.

39. Xu, D., Sanchez-Romaguera, V., Barbosa, S., Travis, W., de Wit, J., Swan, P., and Yeates, S.G., Inkjet printing of polymer solutions and the role of chain entanglement. *Journal of Materials Chemistry*, 2007. **17**(46): p. 4902-4907.

40. Haskal, E.I., Buechel, M., Dijksman, J.F., Duineveld, P.C., Meulenkamp, E.A., Mutsaers, C.A.H.A., Sempel, A., Snijder, P., Vulto, S.I.E., van de Weijer, P., and de Winter, S.H.P.M., 21.1: Ink Jet Printing of Passive-Matrix Polymer Light Emitting Displays. *SID Symposium Digest of Technical Papers*, 2002. **33**(1): p. 776-779.

41. Schiaffino, S. and Sonin, A.A., Molten droplet deposition and solidification at low Weber numbers. *Physics of Fluids*, 1997. **9**(11): p. 3172-3187.

42. Stringer, J. and Derby, B., Limits to feature size and resolution in inkjet printing. *Journal of the European Ceramic Society*, 2009. **29**(5): p. 913-918.

43. Stringer, J. and Derby, B., Formation and Stability of Lines Produced by Inkjet Printing. *Langmuir*, 2010. **26**(12): p. 10365-10372.

44. Soltman, D. and Subramanian, V., Inkjet-printed line morphologies and temperature control of the coffee ring effect. *Langmuir*, 2008. **24**(5): p. 2224-2231.

45. Duineveld, P.C., The stability of ink-jet printed lines of liquid with zero receding contact angle on a homogeneous substrate. *Journal of Fluid Mechanics*, 2003. **477**: p. 175-200.

46. Deegan, R.D., Bakajin, O., Dupont, T.F., Huber, G., Nagel, S.R., and Witten, T.A., Capillary flow as the cause of ring stains from dried liquid drops. *Nature*, 1997. **389**(6653): p. 827-829.

47. Lim, J.A., Lee, W.H., Lee, H.S., Lee, J.H., Park, Y.D., and Cho, K., Self-organization of ink-jet-printed triisopropylsilylethynyl pentacene via evaporation-induced flows in a drying droplet. *Advanced Functional Materials*, 2008. **18**(2): p. 229-234.

48. Chen, S.-P., Chiu, H.-L., Wang, P.-H., and Liao, Y.-C., Inkjet Printed Conductive Tracks for Printed Electronics. *ECS Journal of Solid State Science and Technology*, 2015. **4**(4): p. P3026-P3033.

49. Fukuda, K., Sekine, T., Kumaki, D., and Tokito, S., Profile Control of Inkjet Printed Silver Electrodes and Their Application to Organic Transistors. *ACS Applied Materials & Interfaces*, 2013. **5**(9): p. 3916-3920.

50. Hu, H. and Larson, R.G., Analysis of the effects of Marangoni stresses on the microflow in an evaporating sessile droplet. *Langmuir*, 2005. **21**(9): p. 3972-3980.

51. Geim, A.K. and Novoselov, K.S., The rise of graphene. *Nature Materials*, 2007. **6**(3): p. 183-191.

52. Novoselov, K.S., Geim, A.K., Morozov, S.V., Jiang, D., Zhang, Y., Dubonos, S.V., Grigorieva, I.V., and Firsov, A.A., Electric field effect in atomically thin carbon films. *Science*, 2004. **306**(5696): p. 666-669.

53. Geim, A.K., Graphene: Status and Prospects. *Science*, 2009. **324**(5934): p. 1530-1534.

54. Hecht, D.S., Hu, L.B., and Irvin, G., Emerging Transparent Electrodes Based on Thin Films of Carbon Nanotubes, Graphene, and Metallic Nanostructures. *Advanced Materials*, 2011. **23**(13): p. 1482-1513.

55. Zhu, Y.W., Murali, S., Cai, W.W., Li, X.S., Suk, J.W., Potts, J.R., and Ruoff, R.S., Graphene and Graphene Oxide: Synthesis, Properties, and Applications. *Advanced Materials*, 2010. **22**(35): p. 3906-3924.

56. Weiss, N.O., Zhou, H.L., Liao, L., Liu, Y., Jiang, S., Huang, Y., and Duan, X.F., Graphene: An Emerging Electronic Material. *Advanced Materials*, 2012. **24**(43): p. 5782-5825.

57. Chua, C.K. and Pumera, M., Chemical reduction of graphene oxide: a synthetic chemistry viewpoint. *Chemical Society Reviews*, 2014. **43**(1): p. 291-312.

58. Brodie, B.C., On the Atomic Weight of Graphite. *Philosophical Transactions of the Royal Society of London*, 1859. **149**: p. 249-259.

59. Staudenmaier, L., Verfahren zur Darstellung der Graphitsäure. *Berichte der deutschen chemischen Gesellschaft*, 1898. **31**(2): p. 1481-1487.

60. Hummers, W.S. and Offeman, R.E., Preparation of Graphitic Oxide. *Journal of the American Chemical Society*, 1958. **80**(6): p. 1339-1339.

61. Kovtyukhova, N.I., Ollivier, P.J., Martin, B.R., Mallouk, T.E., Chizhik, S.A., Buzaneva, E.V., and Gorchinskiy, A.D., Layer-by-layer assembly of ultrathin composite films from micron-sized graphite oxide sheets and polycations. *Chemistry of Materials*, 1999. **11**(3): p. 771-778.

62. Zhao, J.P., Pei, S.F., Ren, W.C., Gao, L.B., and Cheng, H.M., Efficient Preparation of Large-Area Graphene Oxide Sheets for Transparent Conductive Films. *ACS Nano*, 2010. **4**(9): p. 5245-5252.

63. Rourke, J.P., Pandey, P.A., Moore, J.J., Bates, M., Kinloch, I.A., Young, R.J., and Wilson, N.R., The Real Graphene Oxide Revealed: Stripping the Oxidative Debris from the Graphene-like Sheets. *Angewandte Chemie-International Edition*, 2011. **50**(14): p. 3173-3177.

64. Wang, S.J., Geng, Y., Zheng, Q.B., and Kim, J.K., Fabrication of highly conducting and transparent graphene films. *Carbon*, 2010. **48**(6): p. 1815-1823.

65. Marcano, D.C., Kosynkin, D.V., Berlin, J.M., Sinitskii, A., Sun, Z.Z., Slesarev, A., Alemany, L.B., Lu, W., and Tour, J.M., Improved Synthesis of Graphene Oxide. *ACS Nano*, 2010. **4**(8): p. 4806-4814.

66. Obata, S., Saiki, K., Taniguchi, T., Ihara, T., Kitamura, Y., and Matsumoto, Y., Graphene Oxide: A Fertile Nanosheet for Various Applications. *Journal of the Physical Society of Japan*, 2015. **84**(12): p. 121012.

67. Peng, L., Xu, Z., Liu, Z., Wei, Y., Sun, H., Li, Z., Zhao, X., and Gao, C., An iron-based green approach to 1-h production of single-layer graphene oxide. *Nature Communications*, 2015. **6**: p. 5716.

68. Zhang, S., Zhu, L.X., Song, H.H., Chen, X.H., Wu, B., Zhou, J.S., and Wang, F., How graphene is exfoliated from graphitic materials: synergistic effect of oxidation and intercalation processes in open, semi-closed, and closed carbon systems. *Journal of Materials Chemistry*, 2012. **22**(41): p. 22150-22154.

69. Pan, S.Y. and Aksay, I.A., Factors Controlling the Size of Graphene Oxide Sheets Produced via the Graphite Oxide Route. *ACS Nano*, 2011. **5**(5): p. 4073-4083.

70. Dimiev, A.M. and Tour, J.M., Mechanism of graphene oxide formation. *ACS Nano*, 2014. **8**(3): p. 3060-3068.

71. Dreyer, D.R., Park, S., Bielawski, C.W., and Ruoff, R.S., The chemistry of graphene oxide. *Chemical Society Reviews*, 2010. **39**(1): p. 228-240.

72. Dreyer, D.R., Todd, A.D., and Bielawski, C.W., Harnessing the chemistry of graphene oxide. *Chemical Society Reviews*, 2014. **43**(15): p. 5288-5301.

73. Hofmann, U. and Holst, R., Über die Säurenatur und die Methylierung von Graphitoxyd. *Berichte der deutschen chemischen Gesellschaft (A and B Series)*, 1939. **72**(4): p. 754-771.

74. Ruess, G., Über das Graphitoxyhydroxyd (Graphitoxyd). *Monatshefte für Chemie und verwandte Teile anderer Wissenschaften*, 1947. **76**(3): p. 381-417.

75. Scholz, W. and Boehm, H.P., Untersuchungen am Graphitoxid. VI. Betrachtungen zur Struktur des Graphitoxids. *Zeitschrift für anorganische und allgemeine Chemie*, 1969. **369**(3-6): p. 327-340.

76. Nakajima, T., Mabuchi, A., and Hagiwara, R., A New Structure Model of Graphite Oxide. *Carbon*, 1988. **26**(3): p. 357-361.

77. Lerf, A., He, H.Y., Forster, M., and Klinowski, J., Structure of graphite oxide revisited. *Journal of Physical Chemistry B*, 1998. **102**(23): p. 4477-4482.

78. Erickson, K., Erni, R., Lee, Z., Alem, N., Gannett, W., and Zettl, A., Determination of the Local Chemical Structure of Graphene Oxide and Reduced Graphene Oxide. *Advanced Materials*, 2010. **22**(40): p. 4467-4472.

79. Szabo, T., Berkesi, O., Forgo, P., Josepovits, K., Sanakis, Y., Petridis, D., and Dekany, I., Evolution of surface functional groups in a series of progressively oxidized graphite oxides. *Chemistry of Materials*, 2006. **18**(11): p. 2740-2749.

80. Wang, Z.W., Shirley, M.D., Meikle, S.T., Whitby, R.L.D., and Mikhalovsky, S.V., The surface acidity of acid oxidised multi-walled carbon nanotubes and the influence of in-situ generated fulvic acids on their stability in aqueous dispersions. *Carbon*, 2009. **47**(1): p. 73-79.

81. Thomas, H.R., Valles, C., Young, R.J., Kinloch, I.A., Wilson, N.R., and Rourke, J.P., Identifying the fluorescence of graphene oxide. *Journal of Materials Chemistry C*, 2013. **1**(2): p. 338-342.

82. Kuila, T., Mishra, A.K., Khanra, P., Kim, N.H., and Lee, J.H., Recent advances in the efficient reduction of graphene oxide and its application as energy storage electrode materials. *Nanoscale*, 2013. **5**(1): p. 52-71.

83. Pei, S.F. and Cheng, H.M., The reduction of graphene oxide. *Carbon*, 2012. **50**(9): p. 3210-3228.

84. McAllister, M.J., Li, J.L., Adamson, D.H., Schniepp, H.C., Abdala, A.A., Liu, J., Herrera-Alonso, M., Milius, D.L., Car, R., Prud'homme, R.K., and Aksay, I.A., Single sheet functionalized graphene by oxidation and thermal expansion of graphite. *Chemistry of Materials*, 2007. **19**(18): p. 4396-4404.

85. Schniepp, H.C., Li, J.L., McAllister, M.J., Sai, H., Herrera-Alonso, M., Adamson, D.H., Prud'homme, R.K., Car, R., Saville, D.A., and Aksay, I.A., Functionalized single graphene sheets derived from splitting graphite oxide. *Journal of Physical Chemistry B*, 2006. **110**(17): p. 8535-8539.

86. Kudin, K.N., Ozbas, B., Schniepp, H.C., Prud'homme, R.K., Aksay, I.A., and Car, R., Raman spectra of graphite oxide and functionalized graphene sheets. *Nano Letters*, 2008. **8**(1): p. 36-41.

87. Dreyer, D.R., Murali, S., Zhu, Y.W., Ruoff, R.S., and Bielawski, C.W., Reduction of graphite oxide using alcohols. *Journal of Materials Chemistry*, 2011. **21**(10): p. 3443-3447.

88. Allen, M.J., Tung, V.C., and Kaner, R.B., Honeycomb Carbon: A Review of Graphene. *Chemical Reviews*, 2010. **110**(1): p. 132-145.

89. Wang, X., Zhi, L.J., and Mullen, K., Transparent, conductive graphene electrodes for dye-sensitized solar cells. *Nano Letters*, 2008. **8**(1): p. 323-327.

90. Valles, C., Nunez, J.D., Benito, A.M., and Maser, W.K., Flexible conductive graphene paper obtained by direct and gentle annealing of graphene oxide paper. *Carbon*, 2012. **50**(3): p. 835-844.

91. Oberlin, A., Carbonization and Graphitization. *Carbon*, 1984. **22**(6): p. 521-541.

92. Rozada, R., Paredes, J.I., Villar-Rodil, S., Martinez-Alonso, A., and Tascon, J.M.D., Towards full repair of defects in reduced graphene oxide films by two-step graphitization. *Nano Research*, 2013. **6**(3): p. 216-233.

93. Eigler, S. and Hirsch, A., Chemistry with Graphene and Graphene Oxide—Challenges for Synthetic Chemists. *Angewandte Chemie International Edition*, 2014. **53**(30): p. 7720-7738.

94. Bai, H., Li, C., and Shi, G.Q., Functional Composite Materials Based on Chemically Converted Graphene. *Advanced Materials*, 2011. **23**(9): p. 1089-1115.

95. Stankovich, S., Dikin, D.A., Piner, R.D., Kohlhaas, K.A., Kleinhammes, A., Jia, Y., Wu, Y., Nguyen, S.T., and Ruoff, R.S., Synthesis of graphene-based nanosheets via chemical reduction of exfoliated graphite oxide. *Carbon*, 2007. **45**(7): p. 1558-1565.

96. Li, D., Muller, M.B., Gilje, S., Kaner, R.B., and Wallace, G.G., Processable aqueous dispersions of graphene nanosheets. *Nature Nanotechnology*, 2008. **3**(2): p. 101-105.

97. Chen, H., Muller, M.B., Gilmore, K.J., Wallace, G.G., and Li, D., Mechanically strong, electrically conductive, and biocompatible graphene paper. *Advanced Materials*, 2008. **20**(18): p. 3557-3561.

98. Qiu, L., Zhang, X.H., Yang, W.R., Wang, Y.F., Simon, G.P., and Li, D., Controllable corrugation of chemically converted graphene sheets in water and potential application for nanofiltration. *Chemical Communications*, 2011. **47**(20): p. 5810-5812.

99. Yang, X.W., Cheng, C., Wang, Y.F., Qiu, L., and Li, D., Liquid-Mediated Dense Integration of Graphene Materials for Compact Capacitive Energy Storage. *Science*, 2013. **341**(6145): p. 534-537.

100. Zhang, J.L., Yang, H.J., Shen, G.X., Cheng, P., Zhang, J.Y., and Guo, S.W., Reduction of graphene oxide via L-ascorbic acid. *Chemical Communications*, 2010. **46**(7): p. 1112-1114.

101. Fernandez-Merino, M.J., Guardia, L., Paredes, J.I., Villar-Rodil, S., Solis-Fernandez, P., Martinez-Alonso, A., and Tascon, J.M.D., Vitamin C Is an Ideal Substitute for Hydrazine in the Reduction of Graphene Oxide Suspensions. *Journal of Physical Chemistry C*, 2010. **114**(14): p. 6426-6432.

102. Zhu, C.Z., Guo, S.J., Fang, Y.X., and Dong, S.J., Reducing Sugar: New Functional Molecules for the Green Synthesis of Graphene Nanosheets. *ACS Nano*, 2010. **4**(4): p. 2429-2437.

103. Pei, S.F., Zhao, J.P., Du, J.H., Ren, W.C., and Cheng, H.M., Direct reduction of graphene oxide films into highly conductive and flexible graphene films by hydrohalic acids. *Carbon*, 2010. **48**(15): p. 4466-4474.

104. Moon, I.K., Lee, J., Ruoff, R.S., and Lee, H., Reduced graphene oxide by chemical graphitization. *Nature Communications*, 2010. **1**: p. 73.

105. Tryba, B., Morawski, A.W., and Inagaki, M., Preparation of exfoliated graphite by microwave irradiation. *Carbon*, 2005. **43**(11): p. 2417-2419.

106. Hassan, H.M.A., Abdelsayed, V., Khder, A.E.R.S., AbouZeid, K.M., Terner, J., El-Shall, M.S., Al-Resayes, S.I., and El-Azhary, A.A., Microwave synthesis of graphene sheets supporting metal nanocrystals in aqueous and organic media. *Journal of Materials Chemistry*, 2009. **19**(23): p. 3832-3837.

107. Zhu, Y.W., Murali, S., Stoller, M.D., Velamakanni, A., Piner, R.D., and Ruoff, R.S., Microwave assisted exfoliation and reduction of graphite oxide for ultracapacitors. *Carbon*, 2010. **48**(7): p. 2118-2122.

108. Wunscher, S., Abbel, R., Perelaer, J., and Schubert, U.S., Progress of alternative sintering approaches of inkjet-printed metal inks and their application for manufacturing of flexible electronic devices. *Journal of Materials Chemistry C*, 2014. **2**(48): p. 10232-10261.

109. Cote, L.J., Cruz-Silva, R., and Huang, J.X., Flash Reduction and Patterning of Graphite Oxide and Its Polymer Composite. *Journal of the American Chemical Society*, 2009. **131**(31): p. 11027-11032.

110. Gomez-Navarro, C., Meyer, J.C., Sundaram, R.S., Chuvilin, A., Kurasch, S., Burghard, M., Kern, K., and Kaiser, U., Atomic Structure of Reduced Graphene Oxide. *Nano Letters*, 2010. **10**(4): p. 1144-1148.

111. Hernandez, Y., Nicolosi, V., Lotya, M., Blighe, F.M., Sun, Z.Y., De, S., McGovern, I.T., Holland, B., Byrne, M., Gun'ko, Y.K., Boland, J.J., Niraj, P., Duesberg, G., Krishnamurthy, S., Goodhue, R., Hutchison, J., Scardaci, V., Ferrari, A.C., and Coleman, J.N., High-yield production of graphene by liquid-phase exfoliation of graphite. *Nature Nanotechnology*, 2008. **3**(9): p. 563-568.

112. Ferrari, A.C., Meyer, J.C., Scardaci, V., Casiraghi, C., Lazzeri, M., Mauri, F., Piscanec, S., Jiang, D., Novoselov, K.S., Roth, S., and Geim, A.K., Raman spectrum of graphene and graphene layers. *Physical Review Letters*, 2006. **97**(18): p. 187401.

113. Casiraghi, C., Hartschuh, A., Qian, H., Piscanec, S., Georgi, C., Fasoli, A., Novoselov, K.S., Basko, D.M., and Ferrari, A.C., Raman Spectroscopy of Graphene Edges. *Nano Letters*, 2009. **9**(4): p. 1433-1441.

114. Young, R.J., Kinloch, I.A., Gong, L., and Novoselov, K.S., The mechanics of graphene nanocomposites: A review. *Composites Science and Technology*, 2012. **72**(12): p. 1459-1476.

115. Wojtoniszak, M., Chen, X.C., Kalenczuk, R.J., Wajda, A., Lapczuk, J., Kurzewski, M., Drozdzik, M., Chu, P.K., and Borowiak-Palen, E., Synthesis, dispersion, and cytocompatibility of graphene oxide and reduced graphene oxide. *Colloids and Surfaces B-Biointerfaces*, 2012. **89**: p. 79-85.

116. Boneschanscher, M.P., van der Lit, J., Sun, Z.X., Swart, I., Liljeroth, P., and Vanmaekelbergh, D., Quantitative Atomic Resolution Force Imaging on Epitaxial Graphene with Reactive and Nonreactive AFM Probes. *ACS Nano*, 2012. **6**(11): p. 10216-10221.

117. Akhavan, O., The effect of heat treatment on formation of graphene thin films from graphene oxide nanosheets. *Carbon*, 2010. **48**(2): p. 509-519.

118. Yu, Q.K., Jauregui, L.A., Wu, W., Colby, R., Tian, J.F., Su, Z.H., Cao, H.L., Liu, Z.H., Pandey, D., Wei, D.G., Chung, T.F., Peng, P., Guisinger, N.P., Stach, E.A., Bao, J.M., Pei, S.S., and Chen, Y.P., Control and characterization of individual grains and grain boundaries in graphene grown by chemical vapour deposition. *Nature Materials*, 2011. **10**(6): p. 443-449.

119. Lin, X.Y., Shen, X., Zheng, Q.B., Yousefi, N., Ye, L., Mai, Y.W., and Kim, J.K., Fabrication of Highly-Aligned, Conductive, and Strong Graphene Papers Using Ultra large Graphene Oxide Sheets. *ACS Nano*, 2012. **6**(12): p. 10708-10719.

120. Paredes, J.I., Villar-Rodil, S., Martinez-Alonso, A., and Tascon, J.M.D., Graphene oxide dispersions in organic solvents. *Langmuir*, 2008. **24**(19): p. 10560-10564.

121. Kong, D., Le, L.T., Li, Y., Zunino, J.L., and Lee, W., Temperature-Dependent Electrical Properties of Graphene Inkjet-Printed on Flexible Materials. *Langmuir*, 2012. **28**(37): p. 13467-13472.

122. Shin, K.Y., Hong, J.Y., and Jang, J., Micropatterning of Graphene Sheets by Inkjet Printing and Its Wideband Dipole-Antenna Application. *Advanced Materials*, 2011. **23**(18): p. 2113-2118.

123. Su, Y., Du, J., Sun, D., Liu, C., and Cheng, H., Reduced graphene oxide with a highly restored π-conjugated structure for inkjet printing and its use in all-carbon transistors. *Nano Research*, 2013. **6**(11): p. 842-852.

124. Dua, V., Surwade, S.P., Ammu, S., Agnihotra, S.R., Jain, S., Roberts, K.E., Park, S., Ruoff, R.S., and Manohar, S.K., All-Organic Vapor Sensor Using Inkjet-Printed Reduced Graphene Oxide. *Angewandte Chemie-International Edition*, 2010. **49**(12): p. 2154-2157.

125. Zhang, H., Xie, A.J., Shen, Y.H., Qiu, L.G., and Tian, X.Y., Layer-by-layer inkjet printing of fabricating reduced graphene-polyoxometalate composite film for chemical sensors. *Physical Chemistry Chemical Physics*, 2012. **14**(37): p. 12757-12763.

126. Bridgman, P.W., Two new modifications of phosphorus. *Journal of the American Chemical Society*, 1914. **36**: p. 1344-1363.

127. Brent, J.R., Savjani, N., Lewis, E.A., Haigh, S.J., Lewis, D.J., and O'Brien, P., Production of few-layer phosphorene by liquid exfoliation of black phosphorus. *Chemical communications*, 2014. **50**(87): p. 13338-13341.

128. Liu, H., Du, Y., Deng, Y., and Ye, P.D., Semiconducting black phosphorus: synthesis, transport properties and electronic applications. *Chemical Society Reviews*, 2015. **44**(9): p. 2732-2743.

129. Li, L.K., Yu, Y.J., Ye, G.J., Ge, Q.Q., Ou, X.D., Wu, H., Feng, D.L., Chen, X.H., and Zhang, Y.B., Black phosphorus field-effect transistors. *Nature Nanotechnology*, 2014. **9**(5): p. 372-377.

130. Hanlon, D., Backes, C., Doherty, E., Cucinotta, C.S., Berner, N.C., Boland, C., Lee, K., Harvey, A., Lynch, P., Gholamvand, Z., Zhang, S., Wang, K., Moynihan, G., Pokle, A., Ramasse, Q.M., McEvoy, N., Blau, W.J., Wang, J., Abellan, G., Hauke, F., Hirsch, A., Sanvito, S., O'Regan, D.D., Duesberg, G.S., Nicolosi, V., and Coleman, J.N., Liquid exfoliation of solvent-stabilized few-layer black phosphorus for applications beyond electronics. *Nature Communications*, 2015. **6**: p. 8563.

131. Liu, H., Neal, A.T., Zhu, Z., Luo, Z., Xu, X.F., Tomanek, D., and Ye, P.D.D., Phosphorene: An Unexplored 2D Semiconductor with a High Hole Mobility. *ACS Nano*, 2014. **8**(4): p. 4033-4041.

132. Kou, L., Chen, C., and Smith, S.C., Phosphorene: Fabrication, Properties, and Applications. *The Journal of Physical Chemistry Letters*, 2015. **6**(14): p. 2794-2805.

133. Nicolosi, V., Chhowalla, M., Kanatzidis, M.G., Strano, M.S., and Coleman, J.N., Liquid Exfoliation of Layered Materials. *Science*, 2013. **340**(6139): p. 1420.

134. O'Neill, A., Khan, U., and Coleman, J.N., Preparation of High Concentration Dispersions of Exfoliated MoS2 with Increased Flake Size. *Chemistry of Materials*, 2012. **24**(12): p. 2414-2421.

135. Kang, J., Wood, J.D., Wells, S.A., Lee, J.H., Liu, X., Chen, K.S., and Hersam, M.C., Solvent exfoliation of electronic-grade, two-dimensional black phosphorus. *ACS Nano*, 2015. **9**(4): p. 3596-3604.

136. Yasaei, P., Kumar, B., Foroozan, T., Wang, C., Asadi, M., Tuschel, D., Indacochea, J.E., Klie, R.F., and Salehi-Khojin, A., High-quality black phosphorus atomic layers by liquid-phase exfoliation. *Advanced Materials*, 2015. **27**(11): p. 1887-1892.

137. Schwierz, F., Graphene Transistors: Status, Prospects, and Problems. *Proceedings of the Ieee*, 2013. **101**(7): p. 1567-1584.

138. Bolotin, K.I., Sikes, K.J., Jiang, Z., Klima, M., Fudenberg, G., Hone, J., Kim, P., and Stormer, H.L., Ultrahigh electron mobility in suspended graphene. *Solid State Communications*, 2008. **146**(9-10): p. 351-355.

139. Wang, Q.H., Kalantar-Zadeh, K., Kis, A., Coleman, J.N., and Strano, M.S., Electronics and optoelectronics of two-dimensional transition metal dichalcogenides. *Nature Nanotechnology*, 2012. **7**(11): p. 699-712.

140. Wang, H., Wang, X.M., Xia, F.N., Wang, L.H., Jiang, H., Xia, Q.F., Chin, M.L., Dubey, M., and Han, S.J., Black Phosphorus Radio-Frequency Transistors. *Nano Letters*, 2014. **14**(11): p. 6424-6429.

141. Buscema, M., Groenendijk, D.J., Blanter, S.I., Steele, G.A., van der Zant, H.S.J., and Castellanos-Gomez, A., Fast and Broadband Photoresponse of Few-Layer Black Phosphorus Field-Effect Transistors. *Nano Letters*, 2014. **14**(6): p. 3347-3352.

142. Viti, L., Hu, J., Coquillat, D., Knap, W., Tredicucci, A., Politano, A., and Vitiello, M.S., Black Phosphorus Terahertz Photodetectors. *Advanced Materials*, 2015. **27**(37): p. 5567-5572.

143. Deng, Y.X., Luo, Z., Conrad, N.J., Liu, H., Gong, Y.J., Najmaei, S., Ajayan, P.M., Lou, J., Xu, X.F., and Ye, P.D., Black Phosphorus-Monolayer MoS2 van der Waals Heterojunction p-n Diode. *ACS Nano*, 2014. **8**(8): p. 8292-8299.

144. Kou, L.Z., Frauenheim, T., and Chen, C.F., Phosphorene as a Superior Gas Sensor: Selective Adsorption and Distinct I-V Response. *Journal of Physical Chemistry Letters*, 2014. **5**(15): p. 2675-2681.

145. Abbas, A.N., Liu, B.L., Chen, L., Ma, Y.Q., Cong, S., Aroonyadet, N., Kopf, M., Nilges, T., and Zhou, C.W., Black Phosphorus Gas Sensors. *ACS Nano*, 2015. **9**(5): p. 5618-5624.

146. Cho, S.Y., Lee, Y., Koh, H.J., Jung, H., Kim, J.S., Yoo, H.W., Kim, J., and Jung, H.T., Superior Chemical Sensing Performance of Black Phosphorus: Comparison with MoS2 and Graphene. *Advanced Materials*, 2016. **28**(32): p. 7020-7028.

147. Yasaei, P., Behranginia, A., Foroozan, T., Asadi, M., Kim, K., Khalili-Araghi, F., and Salehi-Khojin, A., Stable and Selective Humidity Sensing Using Stacked Black Phosphorus Flakes. *ACS Nano*, 2015. **9**(10): p. 9898-9905.

148. Joshua, O.I., Gary, A.S., Herre, S.J.v.d.Z., and Andres, C.-G., Environmental instability of few-layer black phosphorus. *2D Materials*, 2015. **2**(1): p. 011002.

149. Sun, J., Zheng, G.Y., Lee, H.W., Liu, N., Wang, H.T., Yao, H.B., Yang, W.S., and Cui, Y., Formation of Stable Phosphorus-Carbon Bond for Enhanced Performance in Black Phosphorus Nanoparticle-Graphite Composite Battery Anodes. *Nano Letters*, 2014. **14**(8): p. 4573-4580.

150. Li, W.F., Yang, Y.M., Zhang, G., and Zhang, Y.W., Ultrafast and Directional Diffusion of Lithium in Phosphorene for High-Performance Lithium-Ion Battery. *Nano Letters*, 2015. **15**(3): p. 1691-1697.

151. Chen, L., Zhou, G., Liu, Z., Ma, X., Chen, J., Zhang, Z., Ma, X., Li, F., Cheng, H.M., and Ren, W., Scalable Clean Exfoliation of High-Quality Few-Layer Black Phosphorus for a Flexible Lithium Ion Battery. *Advanced Materials*, 2016. **28**(3): p. 510-517.

152. Smith, J.B., Hagaman, D., and Ji, H.F., Growth of 2D black phosphorus film from chemical vapor deposition. *Nanotechnology*, 2016. **27**(21): p. 215602.

153. Li, X.S., Deng, B.C., Wang, X.M., Chen, S.Z., Vaisman, M., Karato, S.I., Pan, G., Lee, M.L., Cha, J., Wang, H., and Xia, F.N., Synthesis of thin-film black phosphorus on a flexible substrate. *2D Materials*, 2015. **2**(3): p. 031002.

154. Castellanos-Gomez, A., Vicarelli, L., Prada, E., Island, J.O., Narasimha-Acharya, K.L., Blanter, S.I., Groenendijk, D.J., Buscema, M., Steele, G.A., Alvarez, J.V., Zandbergen, H.W., Palacios, J.J., and van der Zant, H.S.J., Isolation and characterization of few-layer black phosphorus. *2D Materials*, 2014. **1**(2): p. 025001.

155. Wood, J.D., Wells, S.A., Jariwala, D., Chen, K.S., Cho, E., Sangwan, V.K., Liu, X.L., Lauhon, L.J., Marks, T.J., and Hersam, M.C., Effective Passivation of Exfoliated Black Phosphorus Transistors against Ambient Degradation. *Nano Letters*, 2014. **14**(12): p. 6964-6970.

Chapter 3 Inkjet Printing of High Conductivity Reduced Graphene Oxide Films*

Abstract

In this Chapter, highly conductive reduced graphene oxide (rGO) films with bulk conductivity in excess of 2×10^4 Sm^{-1} have been prepared by inkjet printing a graphene oxide (GO) aqueous ink, with mean flake size 35.9 μm, through a 60 μm inkjet printing nozzle. The printed GO films are reduced to rGO by a low temperature gas phase reduction using HI at temperatures < 100 °C. The conductivity of the printed films increases with increasing number of printed layers to a maximum value with a printed film thickness of about 250 nm. The increase in conductivity with film thickness follows a power law consistent with a percolation model of film conductivity. Individual GO flakes up to 200 μm diameter, considerably larger than the printer nozzle diameter, have been successfully printed with no instances of nozzle blocking or poor printing performance and it is proposed that this is possible via a mechanism of GO sheet folding during drop formation followed by unfolding during drop impact and spreading. Very large GO flakes were produced using a modified Hummer's method and careful control of processing conditions. The original large flake samples were milled ultrasonically to prepare samples with a range of smaller flake sizes. Inks covering a range of mean flake size from 0.68 μm to 35.9 μm were used to probe the influence of flake size on rGO film conductivity and an increase in film conductivity of about 60% was observed over this size range. Hence, there is only a weak influence of interflake contact resistance on the bulk conductivity of rGO films produced with these inks.

---

*This chapter is based on a paper. Pei He, and Brian Derby, 'Inkjet Printing of High Conductivity Reduced Graphene Oxide Films', in preparation. P.H. performed all the experiments. B.D. and P.H. planned the experiments and wrote the paper.

3.1 **Introduction**

Inkjet printing is a promising manufacturing route for the production of large area and low cost flexible electronics.[1-3] Compared to traditional manufacturing techniques, inkjet printing is a versatile manufacturing tool for applications in materials fabrication.[4] It has the following beneficial features: it is a non-contact process, printing is only on demand leading to less wastage of materials, no masks or patterns are required, it has a low process temperature and operates at atmospheric pressure, it is compatible with a large range of flexible and rigid substrates, and is well suited to large area and large scale manufacturing.[5] This makes it attractive for the deposition of a range of ink-based functional materials, including: organic semiconductors,[6] conducting polymers,[7] metal nanoparticles,[8] and carbon nanotubes.[9] Hence inkjet printing has been used to fabricate a range of technologically important electronic components devices, with examples such as transistors,[7, 10] photovoltaic devices,[11, 12] organic light-emitting diodes,[13] sensors,[14] RFID tags,[15] and displays.[16] Despite these device-level advances, the ability to pattern stable devices with low-cost is still an important challenge, especially in the field of printing high conductivity electrodes and interconnects.

The ability to fabricate high conductivity material with long term physical and chemical stability, as well as intrinsic flexibility, is one of the most important requirements for printed electronic devices.[17, 18] Metal nanoparticle inks have been used widely in printed electronics due to their high intrinsic conductivity. However, metal nanoparticle inks are unstable in environmentally friendly solvents, such as deionized water, and there is normally a requirement for organic stabilizers to obtain stable dispersions for printing.[1, 19] Moreover, the high price of the raw materials may also limit them for low-cost applications.[20] Conducting polymers, such as PEDOT:PSS, are regarded as promising conductors for flexible devices due to their high conductivity, cost-effective price, water solubility, and high degree of flexibility. [21] However, there is a key problem that limits the widespread applications of conducting polymers, which is the conductivity of conducting polymers can decrease after extended exposure to moderately elevated temperatures, humidity, or UV light.[18, 22, 23] Although carbon nanotubes (CNTs) demonstrate superb electrical conductivities and could potentially function as conductors for flexible devices,[24] the price of high quality and conductive CNTs is much higher than normal conductors.[18] In addition there is a need to functionalize CNTs or use surfactants to get the required concentration of CNTs in inks.[25]

Recently, graphene, which is a monolayer of sp^2-bonded carbon, has been considered as a potential candidate to replace metallic conductors in printed devices due to its remarkable mechanical, electrical properties. Graphene was first isolated from graphite by micromechanical cleavage,[26] and this form shows the best quality in terms of low defect density, purity, mobility and optical properties. However, mechanical exfoliation is not scalable as a production route for graphene. Several methods have been used for the mass production of graphene including chemical vapour deposition (CVD),[27] epitaxial growth on silicon carbide,[28] chemical synthesis,[29] and liquid phase exfoliation (LPE).[30, 31] Among these, LPE is ideally suited to produce printable graphene inks due to its inexpensive raw materials, the potential for scalability, and low thermal budget.

Graphene inks based on pristine few layer graphene sheets or reduced graphene oxide (rGO) formed by LPE have been inkjet printed for electronic applications, such as transistors,[32] conductive electrodes,[33] chemical sensors,[14] and radio frequency devices.[34] LPE has been successfully used to produce pristine few-layer graphene flakes by sonication in organic solvents [30] or water with the use of surfactants.[35] However, sonication requires relatively long times to break down the source graphite material to few-layer or monolayer graphene, and this also results in a relatively small mean graphene flake size, typically < 1 μm. Most prior works on inkjet printing dispersions of pristine graphene have used solvents derived from those used for LPE. However, the majority of solvents used for high yield LPE of graphene, in particular N-methyl-2-pyrrolidone (NMP), have relatively high boiling points, necessitating elevated temperature heat treatment to ensure solvent removal after printing and limiting its application for large area electronics on flexible polymeric substrates. The poor dispersibility of graphene and rGO in many solvents requires the extensive use of dispersants and surfactants for ink development. The presence of surfactant layers on deposited material flakes after printing may compromise electrical and electronic properties and hence will also require thermal treatment to remove them after printing.

An alternative approach is to develop an ink using exfoliated graphene oxide as the source material for ink development. It is possible to exploit the large number of surface functional groups to promote the dispersion of GO flakes in benign solvents, e.g. water, without the need for surfactants. These inks can be dispensed by inkjet printing to form continuous films that are then reduced by a subsequent thermal or chemical process to form the conductive rGO.[36] It has been generally believed that inks containing small

diameter graphene or other 2D material flakes, such as is produced using conventional LPE, may be beneficial for inkjet delivery allowing for a more stable ink and reducing agglomeration or blocking of the fine nozzles used with inkjet printing. However a small flake size will increase the number of interflake junctions in any conductive pathway in a printed film and the conductivity of a printed film will be governed by both the intrinsic conductivity of the flake material and by the interflake contact resistance. Thus, it is expected that inks containing small graphene flakes will produce printed films with inferior electrical properties to a continuous graphene film and that conductivity should scale with the mean size of the flakes in the ink.

Here, we present a holistic approach to produce highly conductive printed reduced graphene oxide films through liquid phase exfoliation of graphite oxide, ink formulation, inkjet printing, and final reduction. We have produced large GO flakes with average diameter of approximately 36 µm and containing individual flakes up to 200 µm in diameter, using the improved Hummers method. Inks made from dispersions of these flakes can be successfully ejected to form stable droplets through a 60 µm nozzle, which is significantly smaller than the largest GO flakes in suspension. These large flake inks can be used to print stable linear and 2D features after drying. After reduction, the rGO film shows a high conductivity of 2.51×10^4 Sm^{-1} following a post-printing thermal treatment < 100 °C. In addition, we find that the conductivity of the resulting rGO film is only weakly related to the mean size of the GO sheets in the ink.

3.2 Experimental Section

3.2.1 GO Ink Preparation

Synthesis of large size GO sheets. The preparation of GO sheets is based on a modified Hummers' method.[37, 38] In a general procedure, 1.5 g of graphite flakes (grade 9842, Graphexel Ltd., Epping, UK) were dispersed in 200 ml concentrated sulfuric acid (> 95%, > 17.7 mol, Fisher Scientific) using a mechanical stirrer and cooled in an ice bath. Then 1.50 g $KMnO_4$ (Lot # MKBK7079V, Sigma-Aldrich) was added slowly over approximately 20 minutes: the mixture was then allowed to warm to room temperature (with stirring) and left to stir ~ 1 day to consume the oxidizing agent $KMnO_4$ (green colour diminished). The mixture was then cooled in an ice bath and additional $KMnO_4$ (1.50 g) was slowly added. A total of 4 $KMnO_4$ portions were added one by one over 4

days. During the oxidation process, the mixture was continuously stirred at room temperature except during the addition of $KMnO_4$ (~ 20 mins each time). 24 hours after the 4^{th} $KMnO_4$ addition, the mixture became viscous and the graphite was almost fully oxidised to graphite oxide. The viscous mixture was then slowly dispersed into ice-water mixture (600 ml). H_2O_2 solution (35%, ~ 6 ml) was added drop by drop until no effervescence was observed, the mixture turned into a light-yellow suspension and was continuously stirred for 2 hours. The mixture was then centrifuged at 8000 rpm for 30 mins to separate the graphite oxide from the acid solution.

The dark yellow viscous graphite oxide precipitate was redispersed with HCl solution (5%, 600 ml). The mixture was centrifuged at 8000 rpm for 30 minutes. The precipitation was then repeatedly washed with pure water (600 ml) and concentrated via centrifugation (discarding the colourless supernatant) until the pH of the supernatant was about 6 (7 washing cycles). The resulting dark brown-orange viscous GO liquid (about 8 mg/ml) was diluted using deionised water for further application. The final GO dispersion was centrifuged at 3000 rpm for 10 min to remove the unexfoliated graphite oxide before use. These suspensions proved to be highly stable against agglomeration and precipitation and were used as inks for the printing trials.

Preparing different size GO sheets. To break down the lateral size of the GO sheets, the as-prepared GO aqueous solution (~ 2 mg/ml) was subjected to ultrasonic probe sonication (MicrosonXL2000, Misonixlnc., Farmingdale, NY, USA) with a power of 2 W for different treatment times from 10 s to 30 min. The solution was cooled in an ice bath to prevent the temperature rising during the sonication process.

Ink Characterisation. The rheological property of the GO ink was measured using a TA Discovery HR-3rheometer (TA Instruments, New Castle, DE, USA) with a cone-plate geometry (54 μm truncation gap and 60 mm diameter, 2°). After loading the rheometer with ~ 2 ml GO dispersion, the sample was allowed to equilibrate at 25 °C for 20 mins before measurement. The surface tension of the GO ink was performed using a Drop Shape Analyzer DSA100 (KRÜSS GmbH, Hamburg, Germany) with a 1.8 mm diameter syringe needle at 25 °C.

3.2.2 **Inkjet Printing of GO Films**

Prior to printing, the glass substrates were cleaned with ethanol and water in an ultrasonic bath for 15 min. The cleaned substrates were treated with UV-Ozone for 5 min. The as-prepared GO aqueous solution (~ 0.5 mg/ml) was then printed on the glass substrate with different numbers of overprinted layers using an in-house designed and built laboratory scale inkjet printing platform (MPP 1000), equipped with a piezoelectric actuated inkjet printhead of internal diameter 60 μm (MJ-ATP-01-60-8MX, Microfab Technologies Inc., Plano, TX, USA) with drive electronics (JetDrive III, Microfab) interfaced to a PC and controlled in a LabVIEW (National Instruments, Austin, TX, USA) environment. In order to reduce the coffee staining effect,[9] the substrate temperature was set to a temperature of 60 °C during the printing process. The drop spacing was set at 100 μm in both the x- and y- directions.

3.2.3 **Reduction of Printed GO Films**

After printing the GO films were first heated in air at 80 °C for 30 mins. Then the GO films were place in a sealed jar, containing 2.0 ml of HI (55%) and 5.0 ml of acetic acid,[39] and heated in an oil bath at ~ 95 °C for 30 min to reduce the films. The resulting rGO films were then repeatedly washed with ethanol four times to remove residual HI, and dried in air at 80 °C for 1 hour.

3.2.4 **Characterization**

Optical microscopy and POM images were performance with an Olympus BH-2 optical microscope (Olympus, Tokyo, Japan).The structure and morphology of the GO sheets and rGO films were further characterized by scanning electron microscopy (SEM, XL30 FEG-SEM, FEI, Eindhoven, Netherlands) and tapping-mode atomic force microscopy (AFM, Dimension 3100, Veeco Instruments Inc, NY, USA). The SEM images were processed using the software ImageJ to measure the lateral size of the GO sheets. Size distribution data was obtained from measurements of 400 sheets. X-ray diffraction (XRD) patterns from the materials were recorded on a D8 Discover diffractometer (Bruker AXS GmbH, Karlsruhe, Germany), using Cu-kα (λ = 0.154 nm) radiation. The Raman spectra from the GO and rGO films were obtained using a 2000 Raman spectrometer system (Renishaw, Wooton-under-Edge, UK) with a HeNe laser (633 nm excitation). Fourier transform infrared spectroscopy (FTIR) spectra of GO and rGO

films was recorded on a NICOLET 5700 FT-IR system (Thermo Fisher Scientific Inc. MA, USA). X-ray photoelectron spectroscopy (XPS) was performed on a Kratos Axis Ultra DLD XPS spectrometer (Kratos Analytical Ltd, Manchester, UK) with a monochromated Al Kα source (1486.6 eV). Optical transparency of rGO films were measured using a Lambda 25 UV-vis spectrophotometer (Perkin Elmer, Waltham, MA, USA). The water contact angle of GO and rGO films were measured by a Drop Shape Analyzer DSA100 (KRÜSS GmbH, Hamburg, Germany). The sheet resistance of printed rGO films was measured using a four-point-probe station (Jandel Engineering, Linslade, UK) equipped with a 2182A nanovoltmeter and a 6220 current source (Keithley Instruments, Cleveland, OH, USA).

3.3 Results and Discussion

3.3.1 Preparation and Characterization of Large GO Flakes

The process used to prepare rGO films is described in full in the methods section and is schematically illustrated in Figure 3.1. To prepared large size GO flakes, we made the following modifications to the standard method of exfoliating GO: (1) using large diameter graphite powder as the source material (natural graphite flake with a size of 180 – 425 μm), (2) applying the $KMnO_4$, oxidising agent in 4 separate doses over 4 days (as described in the experimental section), and (3) using only mild stirring and shaking during the washing process to avoid the break-up of the GO sheets.

Figure 3.2a-b shows a typical SEM image and the size distribution of the GO sheets used in this study. The average size of the large GO flakes was 35.9 ± 23.2 μm. More than 97% of the GO sheets are larger than 10 μm and individual flakes up to 200 μm in diameter were observed.

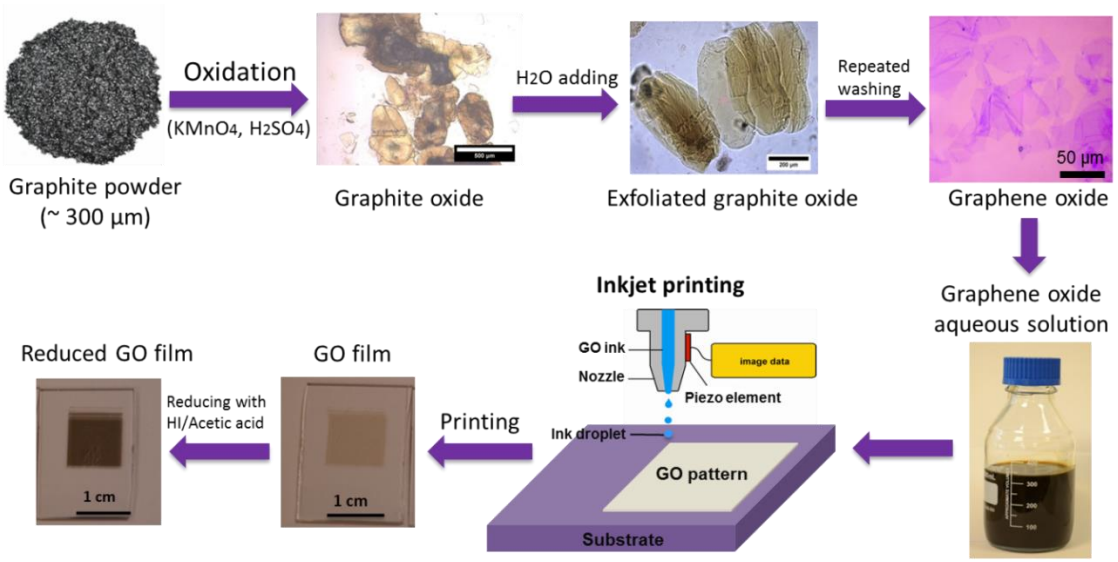

Figure 3.1. Flow chart illustrating the preparation of reduced graphene oxide films using inkjet printing.

Figure 3.2c-e shows SEM, optical microscopy, and AFM images obtained from a single GO sheet of about 50 µm in diameter. Figure 3.2d is a typical SEM image showing an individual large diameter GO sheet deposited on a Si/SiO_2 wafer with folded edges and a wrinkled morphology. The AFM image and height measurements (Figure 3.2 e-f) confirm that it was single GO layer of about 1.0 nm thickness, while the thickness of the fold was around 2.3 nm and the height of the wrinkles ranged from 1 to 4 nm. A number of AFM measurements indicated that most of the GO sheets obtained are 1.0-1.2 nm in thickness even for those with very large lateral dimensions (> 100 µm). Figure 3.2c is an optical microscopy image of the same GO sheet with a lateral size of about 50 µm. The optical imaging proved to be an efficient tool for detecting the number of layers in the GO sheets by the colour change under the same light intensity.[40, 41] Large size individual GO sheets can be easily seen after drop casting on an oxidised Si substrate using optical microscopy (Figure 3.3a). The larger GO sheets are also seen to have defects in the form of folded edges and wrinkles (Figure 3.3b).

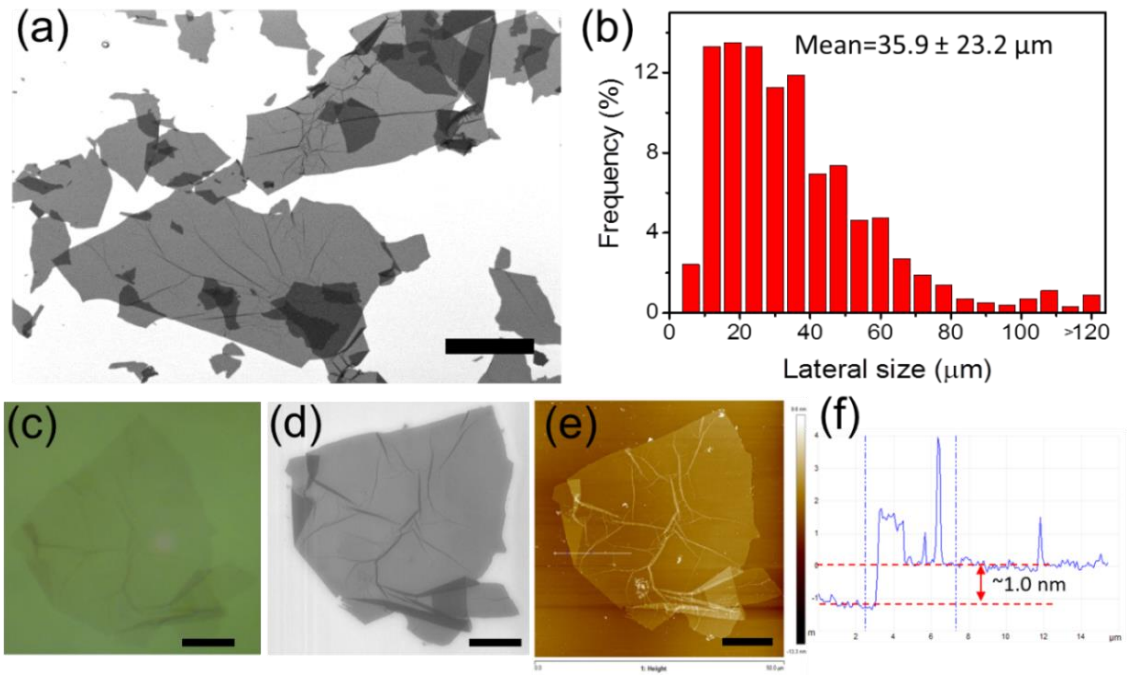

Figure 3.2. (a) Typical SEM image of as-prepared GO sheets deposited on a Si/SiO_2 substrate, and (b) size distribution of GO sheets, the error bar of mean flake size (± 23.2 µm) indicates the standard deviation. (c) Optical microscopy, SEM, and AFM images of the same GO sheet. (f) The height profile shows that the thickness of the GO sheet is around 1.0 nm. Scale bars are 50 µm (a) and 10 µm (c,d,e).

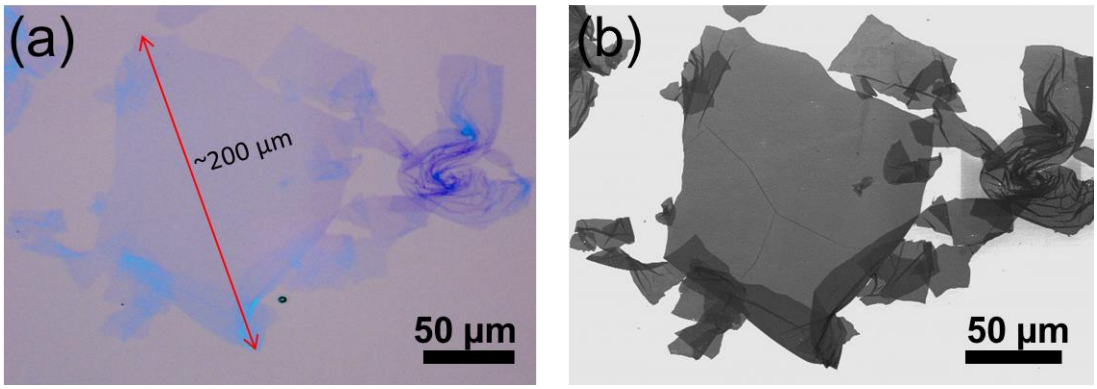

Figure 3.3. (a) Optical microscopy and (b) SEM images of the same area of GO sheets deposited on Si/SiO_2 substrate.

3.3.2 **The Jetting Behaviour of GO Inks**

The GO flakes obtained in water suspension after exfoliation and washing proved to be highly stable against agglomeration and sedimentation over several days. An important parameter for selecting an ink viable for printing is their ability to generate stable droplets. The fluid properties such as viscosity, η, surface tension,γ, density, ρ, and

nozzle diameter, *d*, influence the jettability of the ink and the spreading of the resulting printed drops.[42, 43] An appropriate figure of merit for the suitability of an ink for inkjet printing is the dimensionless grouping:

$$Z = \frac{(\gamma \rho a)^{1/2}}{\eta} \tag{3.1}$$

proposed by Fromm,[44] who proposed that printability was defined by a lower bound defining conditions where viscosity is too great to form drops, Reis and Derby proposed an additional upper bound above which multiple or satellite drops occur in addition to the primary ejected drop;[45] using computational fluid dynamic modelling they suggested a printable range of $10 > Z > 1$. Jang et al. carried out an experimental study using fluid mixtures to vary Z and found a printable range of $14 > Z > 4$ using a printing system similar to that used in our study.[46] A review of experimental data on the printability of particle containing inks by Derby found that there is no actual report of satellite formation for $Z < 15.6$.[47] The viscosity of the GO ink (0.5 mg/ml, mean flake size 35.9 μm) shows highly non-Newtonian shear thinning behaviour with the dynamic viscosity reducing from about 10 Pa.s to 4.32 mPa·s as the shear rate increases from 0.01 - 1000 s^{-1}, as shown in Figure 3.4. Interestingly, due to the large size of GO sheets dispersed, the GO ink shows the rheology behaviour of consistent with a nematic phase even at very low concentration (0.1 mg/ml), which was previously considered to be isotropic phase for GO liquid crystal based on small flakes.[48] The surface tension of the ink was close to that for pure water at 74.1 mNm^{-1} (Table 3.1). Our printer has a nozzle diameter of 60 μm and we take the density of the ink to be ≈ 1000 kgm^{-3}. Using these values in Equation 3.1 gives $Z \approx 15.3$ at a shear rate of 1000 s^{-1}. The inkjet printing drop generation mechanism is expected to occur at a shear rate close to the inverse of the printing frequency, which in this case was 1 kHz. We found that the ink was printable with no evidence for satellite drop formation.

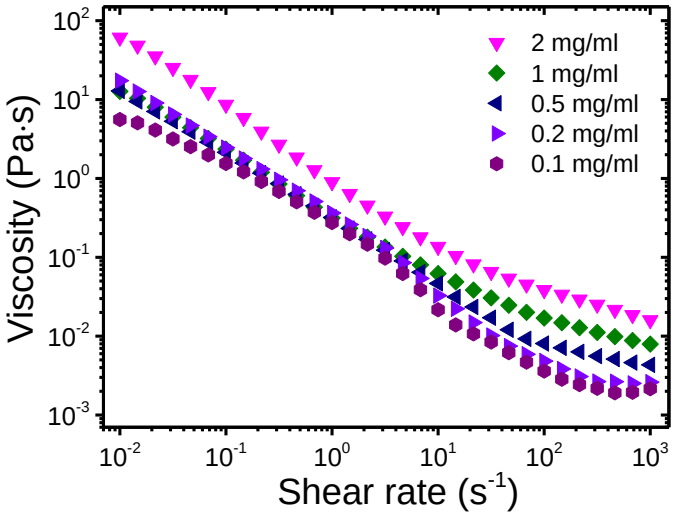

Figure 3.4. Viscosity of the GO aqueous inks with different concentration as a function of shear rate.

Table 3.1. Summary of Properties and Dimensionless Numbers, Z, for GO aqueous inks with different concentration.*

GO concentration (mg/ml)	Viscosity at 1000 s^{-1} (mPa·s)	Surface tension (mN/m)	Figure of merit, *Z* number
0.1	2.16	74.46±0.04	30.4
0.2	2.61	74.77±0.09	25.7
0.5	4.32	74.14±0.16	15.3
1	7.92	74.42±0.06	8.4
2	15.99	72.38±0.36	4.1

*The surface tension for pure H_2O measured in our experiment is 74.56±0.03 mN/m at about 25 °C.

Figure 3.5 shows a sequence of stroboscopic images that capture the drop formation process during the printing of a GO ink containing flakes of the size distribution shown in Figure1b. The drop shows the characteristic elongated tail associated with inkjet drop generation and seen with conventional nanoparticle or solution inks before retracting to a well formed spherical drop in flight, with no satellites, a short distance from the nozzle.[43, 49] This behaviour is similar to that of printing non-Newtonian solutions.[4]

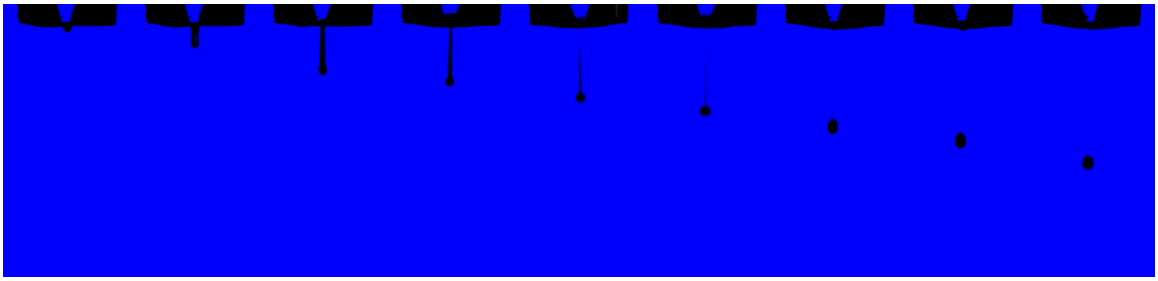

Figure 3.5. Time series showing stroboscopic images of drop formation, using a GO ink containing large mean diameter flakes, close to a 60 µm internal diameter inkjet printer nozzle.

Figure 3.6a shows GO ink drops printed on a Si/SiO_2 substrate using a 60 µm internal diameter printer nozzle and an ink of mean flake diameter of 35.9 µm with the particle size distribution shown in Figure 3.2b. The drops spread to a maximum diameter of 360 ±20 µm on a substrate. The maximum equilibrium spread diameter, d_{eqm}, is related to the diameter of a spherical drop in flight, d_0, by the contact angle, θ, with:[50]

$$\frac{d_{eqm}}{d_0} = \sqrt[3]{\frac{8}{\tan\frac{\theta}{2}\left(3+\tan^2\frac{\theta}{2}\right)}} \tag{3.2}$$

In our experiments, the equilibrium contact angle of GO droplets on Si/SiO_2 was measured from 7.5 to 11.8 degree with a mean value of 9.6° ±1.4° (standard deviation). Thus, from Equation 3.2 the mean diameter of drops in flight were calculated from about 105 to 122 µm with a mean value of 114 ± 6 µm (volume = 7.76×10^{-13} m^3 or 0.77 nL). Figure 3.6b-c confirms that a large proportion of the flakes are > 30 µm diameter. We have found that GO flakes with diameters in the range 70 - 150 µm, significantly greater than the printer nozzle diameter, can be efficiently passed through a 60 µm diameter printer nozzle to generate printable droplets without any clogging. By adjusting the actuating pulse for the inkjet droplet generator, it is possible to vary the volume (and hence diameter) of the ejected drop.[51] Figure 3.6d shows an image of an ultra-large GO flake that was deposited within a printed drop of approximately 47 µm diameter in flight, the dotted line indicates the maximum equilibrium diameter that the drop has spread. The ultra-large GO flake in the image has a diameter significantly greater than both the nozzle diameter and the diameter of the spherical drop generated at the nozzle. Thus the flake must fold or roll-up within the ink during drop generation and unfold after drop impact and subsequent spread to equilibrium.

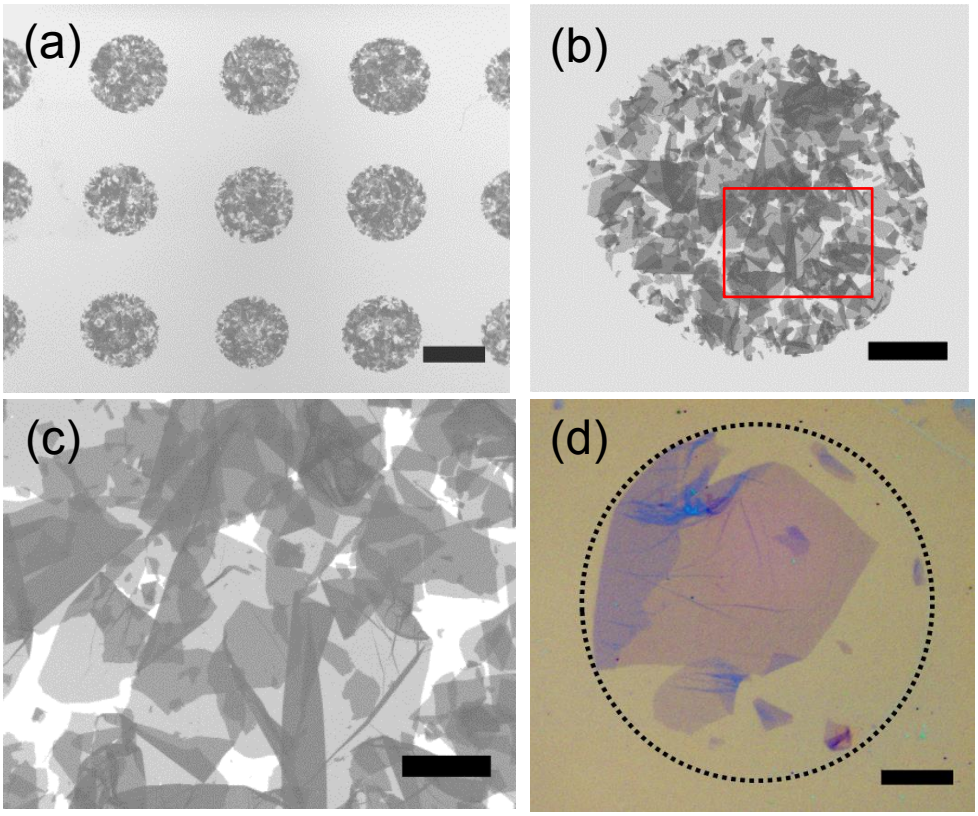

Figure 3.6. (a) SEM image of printed GO ink droplets on Si/SiO_2 substrate. (b) SEM image of a printed GO droplet and (c) the magnified SEM image of the red area. (d) Optical image of a printed drop (47 µm diameter in flight) with a partially folded large GO flake after drying. The dashed line indicates the location of the drop contact line after printing. Scale bars are 300 µm (a), 100 µm (b), 30 µm (c, d).

It is clear that the large printed flakes show similar fold and wrinkle densities as with the smaller flakes and also on comparison with unprinted large flakes (Figure 3.3), despite the deformation they must undergo to reside within a spherical drop produced by the printer. It is notable that stroboscopic imaging of the drop generation process always showed well-formed spherical drops, indicating that all GO flakes must be contained within the drop (Figure 3.2). The printing nozzle used in this study comprises a long glass capillary with a drawn fine nozzle at its end, as shown in Figure 3.7. The images of GO ink in the nozzle shown in Figures 3.8a-b indicate that the fluid flow in the inkjet printer capillary aligns the GO flakes prior to drop formation through the action of the radial velocity gradient. The alignment of GO sheets complies with the flowing direction under printing, and the polarized optical microscopy (POM) images show more uniform during and after printing, as shown in Figure 3.9. The highly bending stiffness of the high aspect ratio GO flakes allows them to deform to lie along stream lines of constant fluid velocity at a constant radial position within the tube

(Figure 3.8c-d). The bending stiffness is defined at *EI*, where *E* is Young's modulus and *I* is the second moment of area. For a plate of rectangular area radium of thickness, *h*, and width, *b*, $I=bh^3/12$. Thus the bending stiffness is propertied the third power of flake thickness, for example, a single atom large flake will be 1000× less stiff than a 10 atom large flake. This is a similar mechanism to the alignment of large GO fibres during wet spinning, albeit at a higher flake concentration.[52-54] In all cases with this ink, the printed drops dry to a uniform flat profile without any segregation during drying, i.e. the ink does not display the circular drying profile known as a coffee ring or coffee stain.[55]

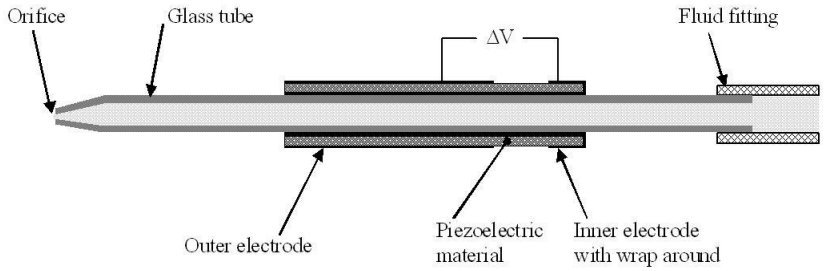

Figure 3.7. Cross section of the inkjet printer drop generation device showing a long glass capillary drawn to a nozzle opening of 60 µm diameter. Image supplied by Microfab, Plano TX, USA.

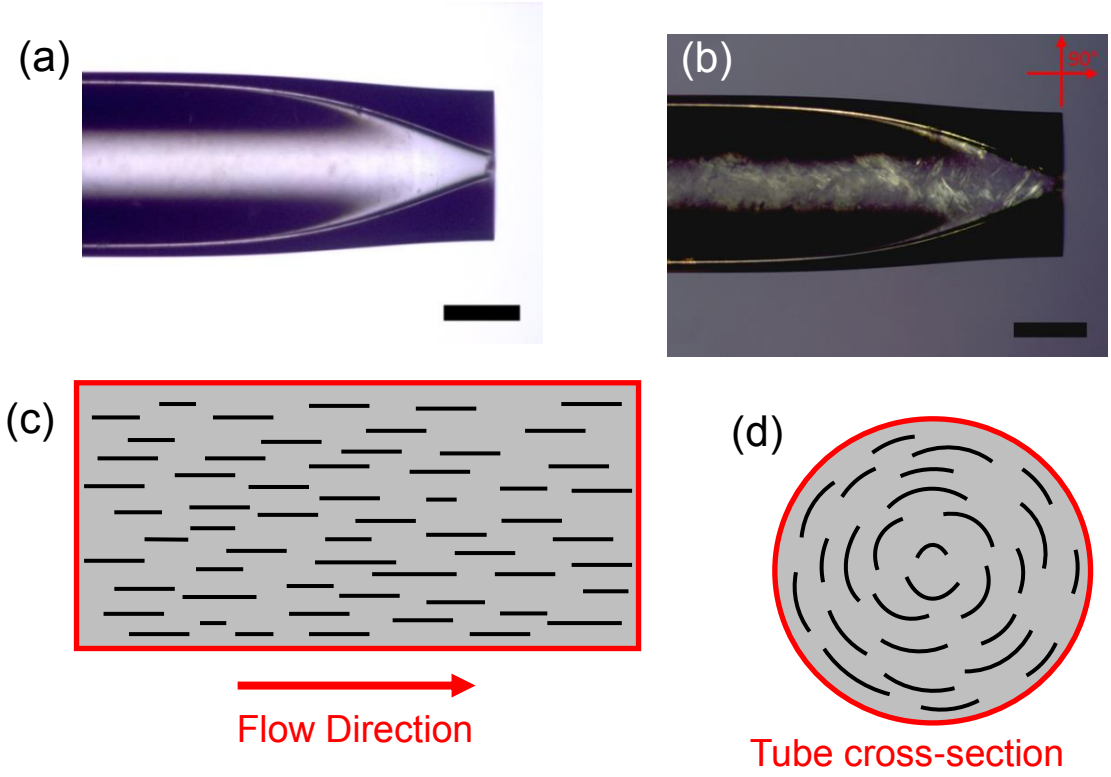

Figure 3.8. Optical microscopy (a) and POM (b) images of GO inks in the printer nozzle. (c) Schematic illustration of the alignment of 2D GO flakes parallel to the fluid flow direction within the capillary of the inkjet printer through the action of the radial variation of the flow

velocity. (d) Cross-section of the capillary showing the proposed bending of the GO flakes to follow stream lines of constant velocity. Scale bars are 300 µm (a, b).

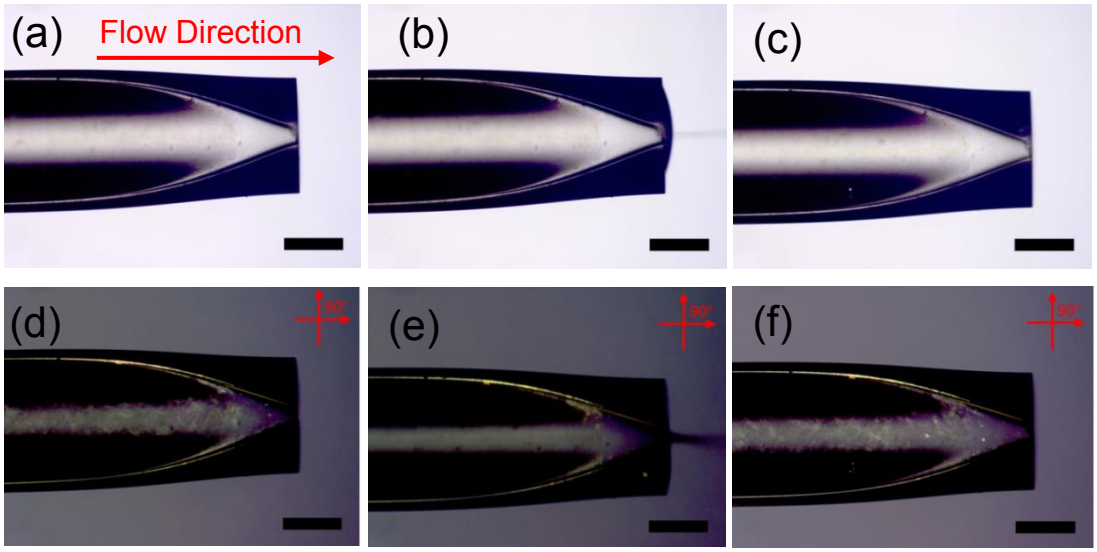

Figure 3.9. Optical microscopy (a-c) and polarized optical microscopy (d-f) images of GO inks in the printer nozzle with different state: ink loading (a, d), printing ongoing (b, e), and stop ink-jetting (c, f). All scale bars are 300 µm.

3.3.3 **Inkjet Printing GO and rGO Films**

GO films (1cm ×1cm) with different thickness values were printed on glass substrates by varying the number of repeated printing passes. The printed GO films were reduced in the presence of HI and acetic acid vapour. Figure 3.10a shows images of the printed films with different numbers of printed repetitions after reduction. The colour of the films changes from near transparency to dark black and the transmittance of film decreased with increased film thickness (Figure 3.10b), which is due to the light absorption of the resulting rGO sheets.[56]

XRD was used to characterize bulk structural changes within the inkjet-printed films on glass substrates after reduction to rGO, as shown in Figure 3.11a. A typical broad peak near 9.78 ° (*d*-spacing ~ 9.04 Å) was observed for the GO film. Compared with the printed GO film, the peak of the rGO film showed a noticeable shift to higher 2θ angles (24.11°, *d*-spacing ~3.69 Å) and was narrower than that of hydrazine reduced GO (23-24°, *d*-spacing 3.7-3.8 Å).[57] This suggests that both GO and rGO films are well ordered with 2-dimensional sheets and the reduction process decreased the average interlayer spacing of the rGO film. Figure 3.11b presents the Raman spectra obtained from

graphite powder, the GO film and the rGO film on glass substrates using 633 nm laser irradiation. The G-band peak of GO film (1594 cm^{-1}) was up-shifted compared with that of graphite powder (1581 cm^{-1}). The G-band peak of rGO film shifted to 1589 cm^{-1}, which is attributed to the recovery of the hexagonal network of carbon atoms with defects. The I_D/I_G ratio of the rGO film notably increased, indicating that the reduction process changed the structure of GO.[39] The intensity of the 2D-band peak of the rGO film is stronger that of the GO film, indicating a better graphitization in the rGO.[31]

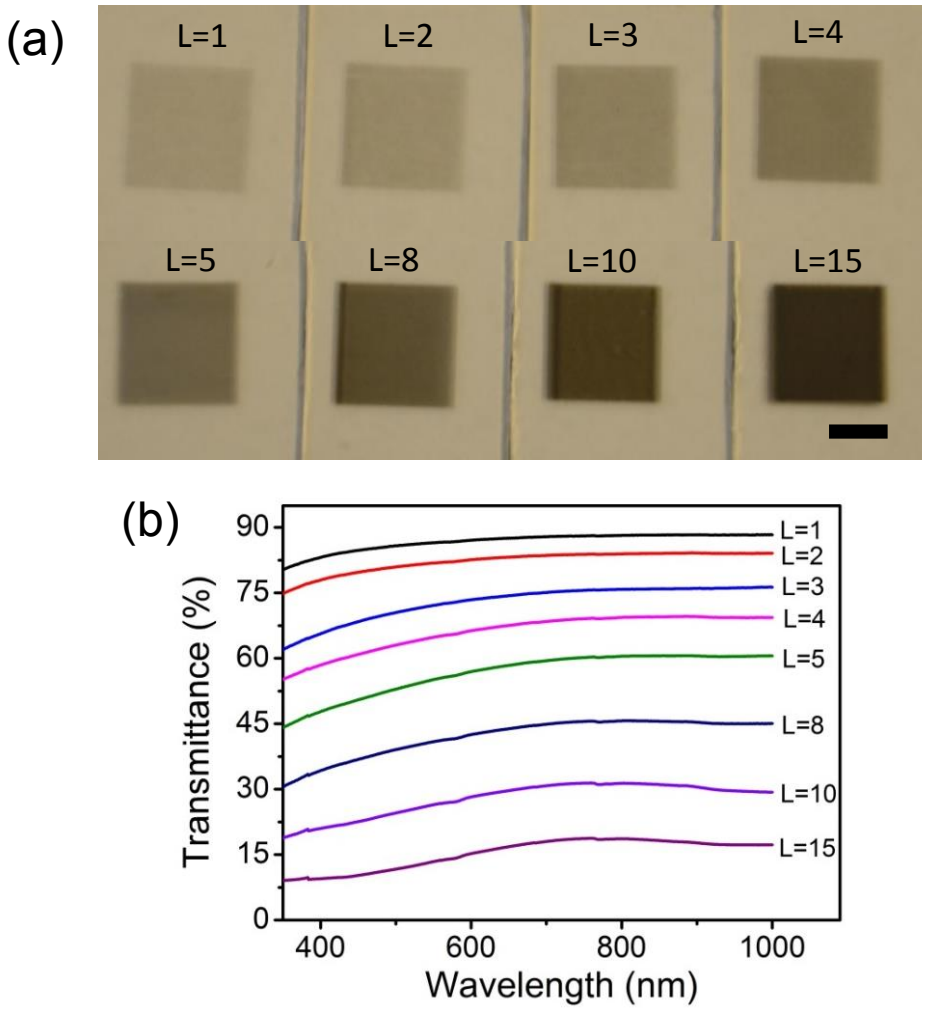

Figure 3.10. (a) Photograph of printed rGO films for different number of printed repetitions. Scale bar is 5mm. (b) Transmittance spectra of printed rGO films for different number of printed repetitions.

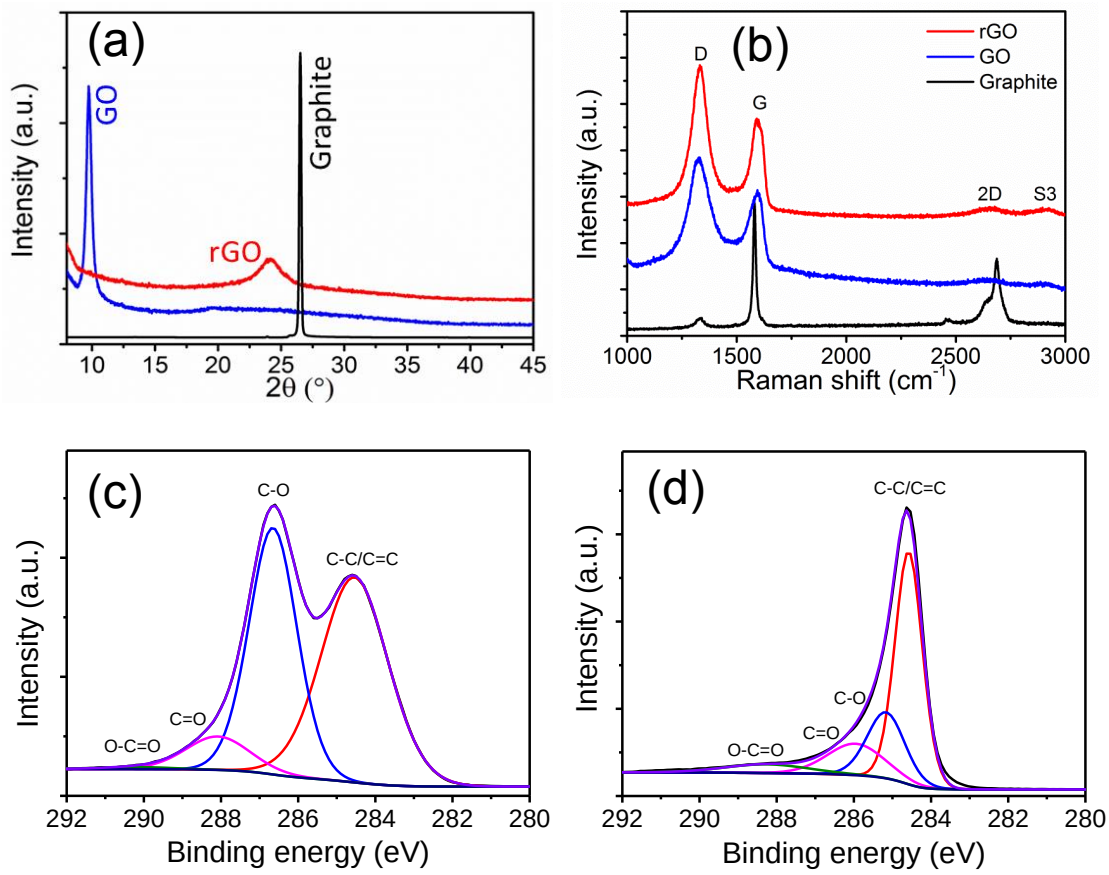

Figure 3.11. (a) X-ray diffraction patterns of graphite powder (black), printed GO (blue) and rGO (red) films on glass substrates. The 2θ angles of the XRD peaks (*d*-spacing) of GO and rGO shifted from 9.78° (*d*-spacing ~ 9.04 Å) to 24.11° (*d*-spacing ~3.69 Å) after reduction. (b) Raman spectra of graphite, GO, and rGO. XPS spectra of GO (c) and rGO (d) films.

The chemical structure and composition change from GO to rGO after exposure to HI was further investigated using XPS. Figure 3.11c and d show the C1s spectra of printed GO and rGO films. In general, the GO signal exhibits two separated peaks at 284.5 eV, corresponding to sp^2 carbon components and at 286.6 eV, corresponding to C-O single bond components of hydroxyl and 1.2-expoxide functionalities. The broad small shoulder at approximately 288 - 299 eV corresponds to C=O double bond components of carboxyl and ketone functionalities.[57] These peaks in the rGO spectrum were notably decreased, suggesting the efficient removal of oxygen functional groups by the reduction process. However, the spectrum still shows small peaks in that region due to residual of oxygen functionalities. In addition, the evidence of reduction of the GO film was further assessed by its hydrophobicity. The water contact angles on the GO and rGO films were measured as 28.4° and 79.2°, respectively using the sessile drop method,

shown in Figure 3.12. The increase in contact angle with film reduction is consistent with the removal of oxygen functional groups from the surface.[39]

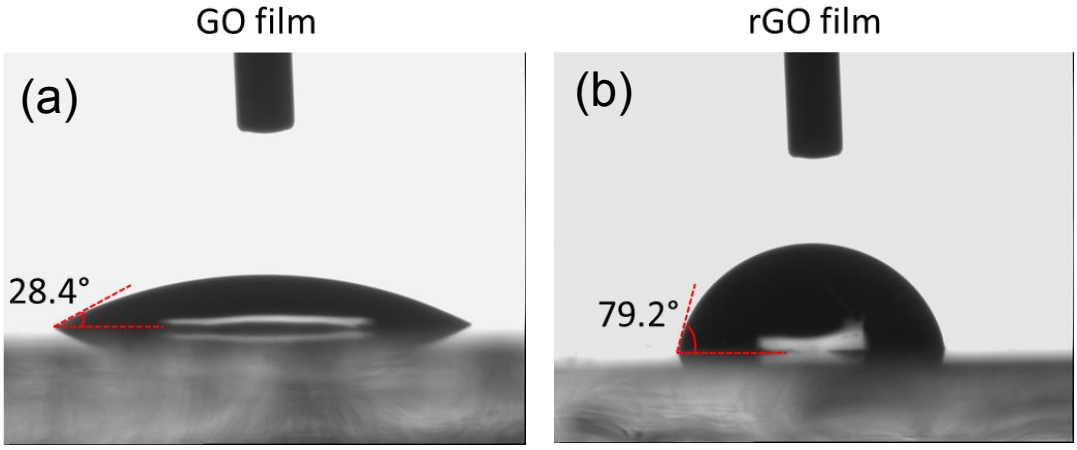

Figure 3.12. Water contact angle of printed GO (a) and rGO (b) films on glass substrates.

Figure 3.13a-d shows AFM images of rGO films with different printing repetitions. It can be seen that the thickness of the first printed layer is about 8.7 nm, and this increases approximately linearly with increasing numbers of printed repetitions to about 470 nm after 60 layers (Figure 3.13f). The average surface roughness increases from 1.7 nm to about 32 nm and after a few passes remains at approximately 7% of the film thickness, as shown in Figure 3.13e. The increased surface roughness is mainly caused by wrinkling of the GO film. It has been proposed that wrinkling occurs during solvent evaporation, when there is a transition between the electrostatic repulsion that separates the flakes in solution to the van der Waals attraction between the previously deposited layer and depositing layer.[58] Since the GO sheets are deposited together one on top of another, the wrinkling can become serious with increased printing repetitions because the substrate surface is no longer flat due to the presence of the GO sheets deposited previously.[59]

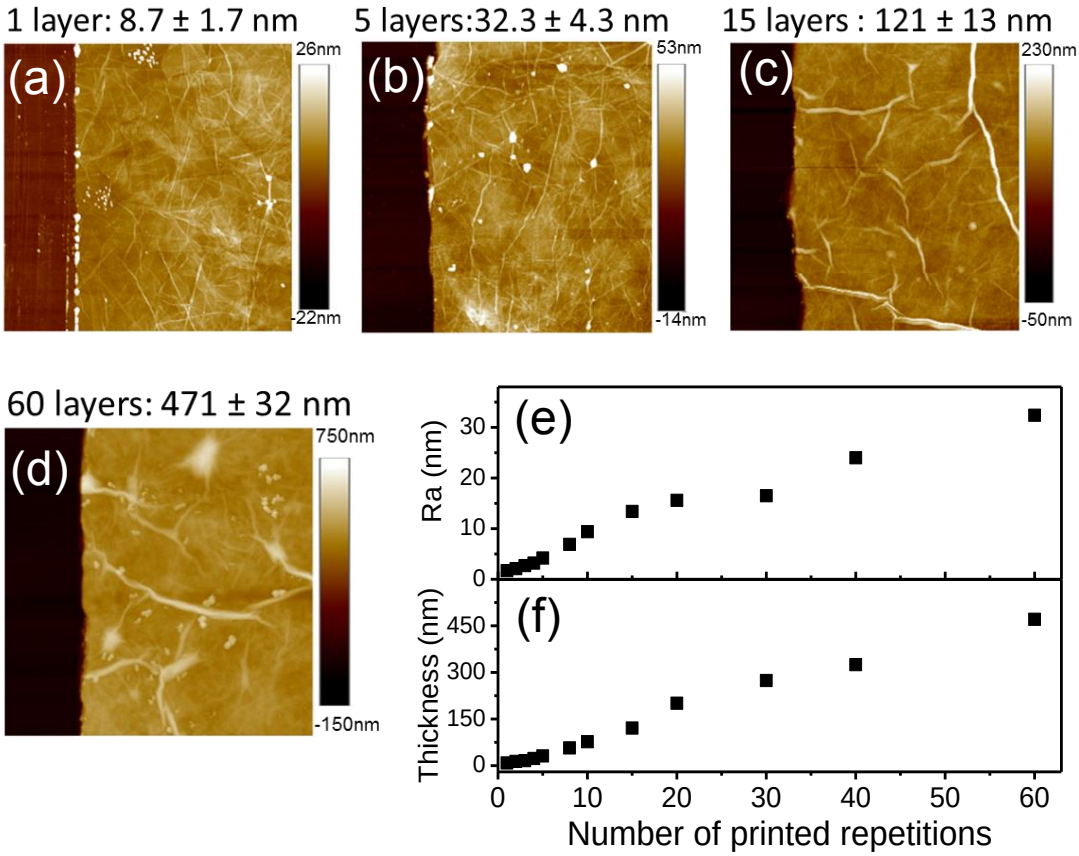

Figure 3.13. Typical AFM images of printed rGO films with different printing repetitions: 1 layer, 5 layers, 15 layers, and 60 layers. (e) Film surface roughness and film thickness (f) of the inkjet-printed rGO films as a function of the number of printed repetitions.

The sheet resistance of the films, measured after reduction to rGO, is plotted as a function of number of printing repetitions in Figure 3.14a. The sheet resistance decreases from 4.64×10^4 to 109 Ω/□. These resistance values are much lower than previous reported for inkjet printed graphene films fabricated using low temperature thermal treatment (see Table 3.3). Figure 3.14b combines the sheet resistance data with the measured film thickness to indicate how the DC conductivity of the printed films changes with increasing number of printed layers. The conductivity increases with film thickness up to a maximum value of 2.51×10^4 Sm^{-1} at a thickness of 250 nm; above this thickness there is a small decrease in conductivity but it remains close to 2×10^4 Sm^{-1}.

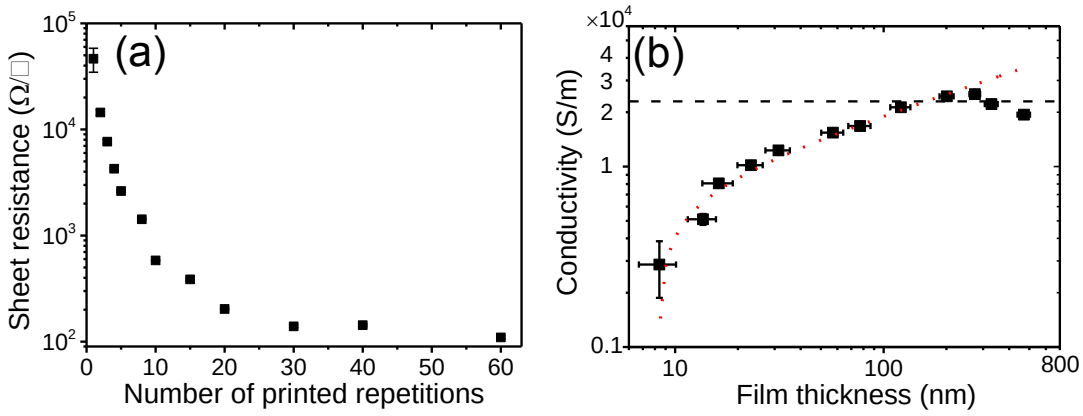

Figure 3.14. (a) Sheet resistance of the inkjet-printed rGO films as a function of the number of printed repetitions. (b) Film electrical conductivity plotted as a function of film thickness.

A similar behaviour of a non-linear increase of film conductivity with increasing surface coverage of discrete overlapping conducting units has been observed previously with inkjet-printed graphene patterns [32, 60] and silver nanowires.[61] For a network of overlapping elongated conductors, the conductivity normally follows a percolation law

$$\sigma_{DC} \propto (N_A - N_{Ac})^{\alpha} \tag{3.3}$$

where N_A is the number of conducting rods per unit area, $N_{A.c}$ is the percolation threshold (the coverage at which at least one conducting pathway spans the specimen) and α is an exponent.[62] In our work, the relation between printed film thickness and conductivity can be represented by a similar empirical power-law relation,

$$\sigma_{DC} \propto (t - t_c)^{n} \tag{3.4}$$

where t_c is the thickness associated with the percolation threshold, and n is an exponent. Fitting data in Figure 3.14b to Eq. (3.4) (red dashed line) yields t_c = 8.4 nm and n = 0.38. This threshold thickness is intermediate to the measured thickness of one and two printed layers. This suggests that printing a single layer of the rGO film will not be sufficient to generate a continuous conductive network. Although the value of n is much lower than the observed universal percolation exponent of 1.3,[63] such a low exponent value is similar to that reported for inkjet-printed pristine graphene conductive films, where n = 0.32.[60] The film conductivity reaches a peak value at a thickness ≈ 250 nm, above which a small decrease is observed; this is possibly due to the increased difficulty in reducing thick GO films by the gaseous reducing agent used. The bulk conductivity (thickness independent conductivity) of the rGO film is ~ 2.51 × 10^4 Sm^{-1}, which is higher than that obtained from inkjet-printed graphene and rGO films reported previously, as shown in Table 3.3.[60, 64-66] The high conductivity of the rGO films

observed here is possibly due to the use of larger size GO sheets than in previous studies.

3.3.4 **The Influence of GO Flake Size to the Conductivity of Printed rGO Films**

To further investigate the effect of flake size on the conductivity of rGO films, we prepared a range of GO dispersions in water with different lateral sheet sizes. These were obtained through using different sonication times with a starting suspension of the large size GO flake used earlier. From the size distribution data displayed in Figure 3.15, it is clear that the mean size of the GO sheets decreases with increasing sonication time (as shown in Table 3.2). The mean size of the GO sheets decreased from 35.9 ± 23.2 to 21.7±15.8 μm after 10 s sonication treatment. The fraction of GO sheets with size smaller than 10 μm increased from 2.4% to 9.5% after 10 s sonication, and no GO sheets larger than 100 μm are found after 10s sonication, showing that large size GO sheets are easily to broken down by sonication. Notably, the variance of GO sheets for 30 s, 2 min, and 5 min treatment samples is larger than the mean size because the powder size distribution in the solvent is not symmetrical for probe sonication. This non-uniform size distribution of sonicated GO sheets has been observed in previous reports in the literature.[52] With increasing sonication time to 30 min, almost all the GO sheets have broken down to small sizes < 2 μm. Moreover, the rheological behaviour of GO inks with mean flake size larger than 1.8 μm exhibited yield values with flow curves that are similar to those of a non-Newtonian liquid (pseudoplastic fluids or thixotropic fluids), as shown in Figure 3.16. This phenomenon indicates that the fluid moves more freely with high rates of deformation caused by an increasing shear rate.[52] Whereas, when the GO flake size is smaller than 0.95 μm, the rheological behaviour of GO inks shows behaviour similar to Newtonian liquids.

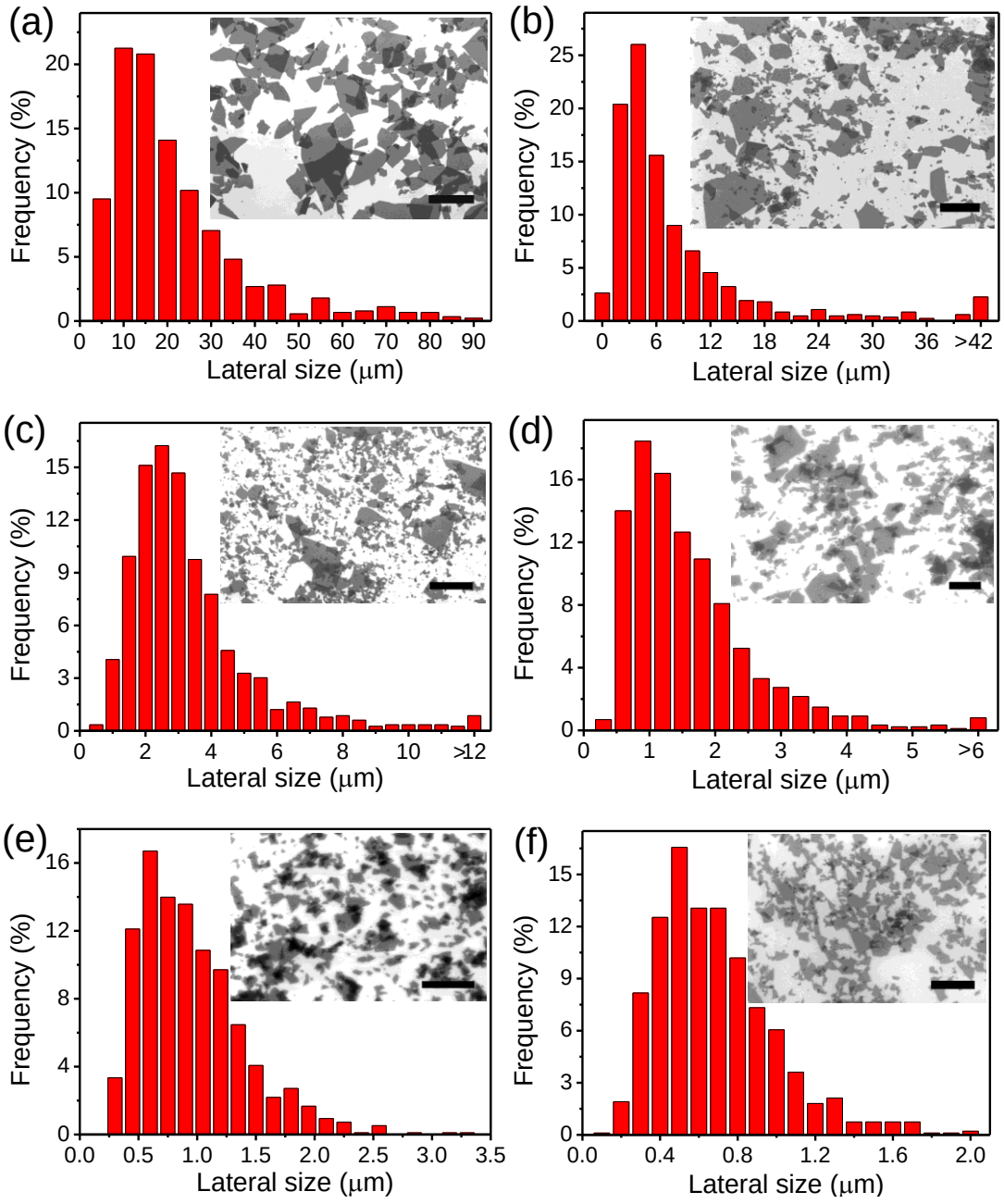

Figure 3.15. Lateral size distributions of GO sheets of different size groups with sonication time: (a) 10 s, (b) 30 s, (c) 2 min, (d) 5 min, (e) 20 min, and (f) 30 min. Inset shows the SEM images used for size distribution measurements. Scale bars are (a) 50 μm, (b, c) 20 μm, (d, e) 5 μm, and (f) 3 μm.

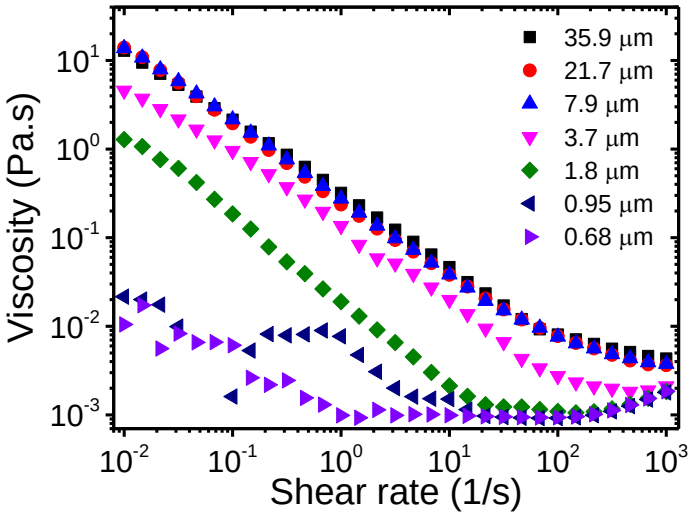

Figure 3.16. Rheological behaviour of the GO aqueous inks with different mean flake size as a function of shear rate.

Table 3.2. Lateral flake size and viscosity of GO inks treated with different sonication time.

	Tip sonication time						
	no	10 s	30 s	2 min	5 min	20 min	30 min
Mean sheet size (μm)	35.9	21.7	7.1	3.7	1.8	0.95	0.68
Standard deviation (μm)	23.2	15.8	9.0	3.8	4.3	0.45	0.31

To obtain the conductivity of rGO films with different sizes of flakes, we printed GO films based on our previous GO dispersions using a procedure similar to that for the large GO flake ink. It was noticed that inks with mean GO flake size < 1 μm showed coffee rings after drying and inks with mean flake size only slightly larger than 1 μm showed partial flake segregation, as shown in Figure 3.17. The mechanism of this phenomenon will be comprehensively investigated in Chapter 4. We measured the conductivity of the printed GO films after reduction to rGO. We found that the transition to the constant bulk conductivity occurred at a critical thickness in the range 200 - 300 nm for all the rGO films of different mean flake size.

Figure 3.18a shows the DC bulk conductivities of printed rGO films as a function of GO sheet lateral size. The conductivity of the rGO films shows a consistent rise with increasing lateral dimension of the GO sheets. The bulk conductivity increases from 1.53×10^4 to 2.48×10^4 Sm^{-1} as the mean diameter of the GO sheets increases from 0.68

to 35.9 µm. It is likely that the reason for this increase in conductivity is the relatively high resistance of inter-sheet contacts, which is much greater than the in plane resistance of graphene flakes, as reported in the literature.[67] For an edge-to-edge continuous conductive film from networks of reduced GO sheets, the larger GO sheets should give a lower number of inter-sheet junctions compared to the small size GO sheets within a fixed channel length.[68] However, the data in Figure 18a shows a relatively small increase in conductivity with increasing flake size; the conductivity increasing by a factor of approximately 1.6 as the flake size increases from 0.68 µm to 35.9 µm (a factor of 53). This relationship can be described by a power law with the conductivity, σ, proportional to the flake diameter, d^n, where the exponent n is approximately 1/9, indicating a very weak dependency on flake size. These data indicate that the effect of inter-flake contact resistance on sheet resistance in these rGO films is relatively small.

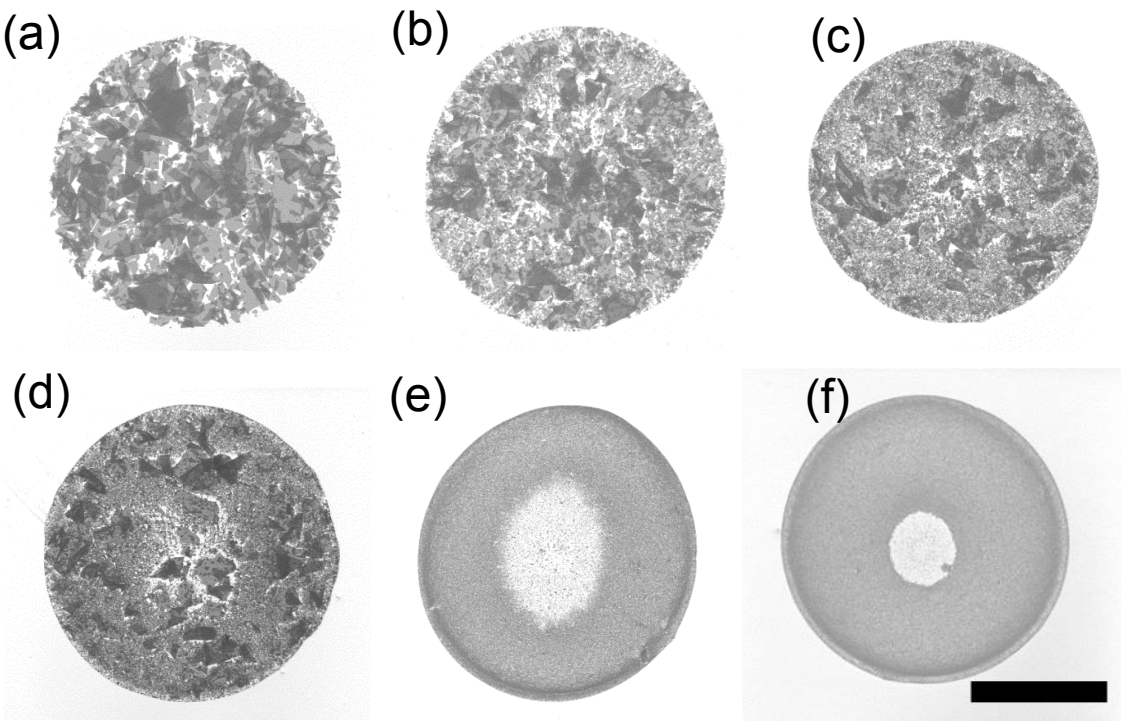

Figure 3.17. SEM images of printed GO droplets with different mean flake size: (a) 21.7±15.8, (b) 7.1±9.0. (c) 3.7±3.8, (d) 1.8±4.3, (e) 0.95±0.45, and (f) 0.68±0.31 µm. The scale bar is 200 µm.

Table 3.3. Comparison of inkjet-printed graphene and rGO patterns from literatures.

Graphene type	Solvents used	Highest process temperature (°C)	Flake size (μm)	Conductivity (Sm^{-1})	Ref.
Lithium-THF expanded graphite	Isopropanol/n-butanol	50	> 1	1×10^3	69
NMP exfoliated graphene	NMP	70	~ 0.04-0.6	3×10^3	60
NMP exfoliated graphene	NMP/ Ethylene Glycol	170	~ 0.3-1	1×10^2	32
Ethanol and EC exfoliated graphene	Cyclohexanone/ terpineol	250	~ 0.05	2.5×10^4	70
Supercritical CO_2 exfoliated graphene	Cyclohexanone with EC	300	0.03-0.1	9.24×10^3	71
DMF exfoliated graphene	Terpineol/ethanol	400	0.1-0.5	3.4×10^3*	66
Ethanol and EC exfoliated graphene	Cyclohexanone/ terpineol	NA (intense pulsed light annealing)	~ 0.1	2.56×10^4	72
rGO by ascorbic acid	H_2O	80	NA	1.5×10^3	14
rGO by HBr acid	H_2O/ propylene glycol	80	NA	4×10^3	73
rGO by N_2H_4 and NH_3 vapour	H_2O	90	NA	3.5×10^4*	34
rGO by N_2H_4 and NH_3 vapour	H_2O	90	NA	5.5×10^3	65
rGO by hydrazine fumes	H_2O	100	0.54	8.8×10^3	74
			2.2	1.6×10^4	
rGO by HI vapour	H_2O	100	< 2	4.2×10^4 ** 4×10^3 **	33
rGO by IR heat lamp	H_2O	200	~ 0.53	8×10^2*	75
rGO by hydrazine	DMF/ H_2O	350	NA	1×10^3	76
rGO by heating	H_2O	400	< 0.4	8.7×10^2	64
rGO by HI and acetic acid vapour	**H_2O**	**95**	**35.9 ± 23.2**	**2.51×10^4**	**Our work**

* Data refers from reference 59

**4.2×10^4 Sm^{-1} made from weakly oxidized GO, 4×10^3 Sm^{-1} made from reference GO.

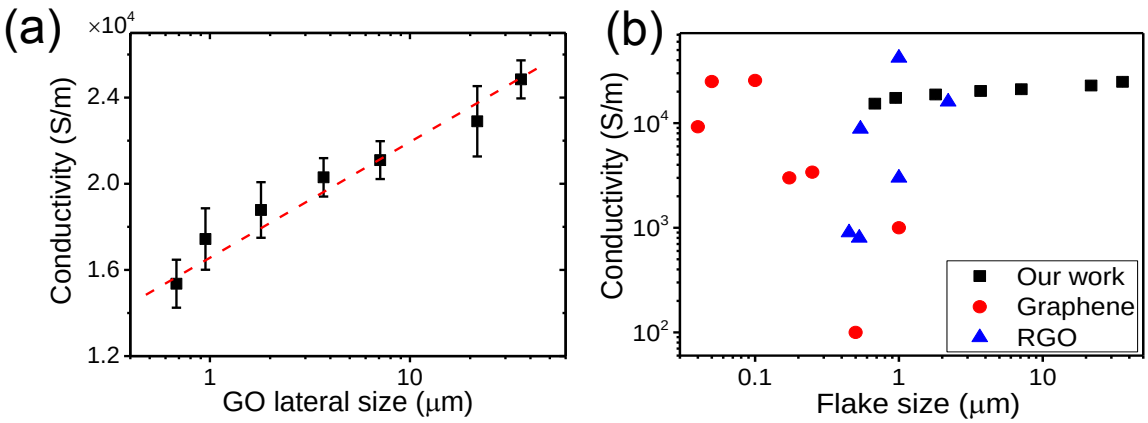

Figure 3.18. (a) Electrical conductivities of printed rGO films as a function of GO sheets mean lateral size. (b) Comparison of electrical conductivity of inkjet-printed graphene and rGO patterns taken from the literature. Detail data of these references is shown in the Table 3.

The electrical conductivity of inkjet-printed patterns made from graphene and reduced GO with different flake size are compared between our work and earlier reports in the literature in Figure 3.18b. The maximum conductivity observed for printed pristine graphene patterns tends to be ~ 2.5×10^4 Sm^{-1},[70, 72] and the highest conductivity of printed rGO film is close to 4.2×10^4 Sm^{-1},[33] while most papers report values lower than 1.0×10^4 Sm^{-1}.[14, 32, 60, 64-66, 69, 71, 73, 75, 76] However, most previous studies on inkjet-printed graphene or rGO conductive patterns have used inks with flake size < 1 μm because of the belief that larger flake size inks will lead to blocked printer nozzles. However, from our results, it is clear that this perceived size limitation is not necessarily applicable for inks based on graphene and its derivatives and that this observation may also apply to other 2D materials because of the unique flexibility of these atom thick sheets.[77] This will be a great advantage for inkjet printing highly conductive graphene patterns. Finally we note that although our printed rGO films will contain higher defect densities and hence lower intrinsic electrical properties than available through solvent exfoliated pristine graphene, the significantly larger flake size, ease of ink formulation and lower temperature thermal processing gives this production route significant potential benefits for use with polymer substrates for flexible and stretchable electronics.

3.4 Conclusions

In this Chapter, highly conductive rGO films has been successfully prepared by inkjet printing large GO flakes prior to a gas phase reduction using HI vapour. The highest conductivity films were prepared using a GO ink with mean flake size 35.9 μm

dispensed through a 60 µm diameter inkjet printer nozzle. This ink was found to contain a significant proportion of flakes with diameter greater than the printer nozzle and flakes with size > 200 µm were observed in the printed deposit. The capability of dispensing GO flakes larger than the printer nozzle contradicts the stated belief in much of the literature that the particles in an ink must be significantly smaller than the diameter of the printer nozzle to prevent blockage during printing. We conclude that this observation can only be explained if the GO flakes undergo considerable folding or crumpling during drop formation and subsequently unfold after drop impact and spreading. It is notable that the large sized flakes show no greater incidence of folding or wrinkling after printing when compared with smaller flakes in the same ink. The conductivity of rGO film increases with layer thickness to a stable value of around 2.4×10^4 Sm^{-1} when the thickness of rGO film exceeded 250 nm. The conductivity of the rGO films is a weak function of the mean flake size in the GO inks prior to printing and reduction with there being a 60% improvement in film conductivity as the mean flake size increases from < 0.6 µm to > 35 µm. This result indicates that the interflake contact resistance between the rGO flakes has a relatively small influence on the conductivity of a thick printed film. These results demonstrate that it is possible to produce highly conductive inkjet-printed films using an ink prepared from large area GO flakes dispersed in water. The HI gaseous phase reduction process we have used requires a thermal treatment at temperatures < 100 °C, hence this processing route is compatible with many flexible polymeric substrates.

References

1. Singh, M., Haverinen, H.M., Dhagat, P., and Jabbour, G.E., Inkjet Printing-Process and Its Applications. *Advanced Materials*, 2010. **22**(6): p. 673-685.

2. Cummins, G. and Desmulliez, M.P.Y., Inkjet printing of conductive materials: a review. *Circuit World*, 2012. **38**(4): p. 193-213.

3. Park, S., Vosguerichian, M., and Bao, Z., A review of fabrication and applications of carbon nanotube film-based flexible electronics. *Nanoscale*, 2013. **5**(5): p. 1727-1752.

4. Derby, B., Inkjet Printing of Functional and Structural Materials: Fluid Property Requirements, Feature Stability, and Resolution. *Annual Review of Materials Research, Vol 40*, 2010. **40**: p. 395-414.

5. de Gans, B.J., Duineveld, P.C., and Schubert, U.S., Inkjet printing of polymers: State of the art and future developments. *Advanced Materials*, 2004. **16**(3): p. 203-213.

6. Lim, J.A., Lee, W.H., Lee, H.S., Lee, J.H., Park, Y.D., and Cho, K., Self-organization of ink-jet-printed triisopropylsilylethynyl pentacene via evaporation-induced flows in a drying droplet. *Advanced Functional Materials*, 2008. **18**(2): p. 229-234.

7. Sirringhaus, H., Kawase, T., Friend, R.H., Shimoda, T., Inbasekaran, M., Wu, W., and Woo, E.P., High-resolution inkjet printing of all-polymer transistor circuits. *Science*, 2000. **290**(5499): p. 2123-2126.

8. Tang, W., Feng, L.R., Zhao, J.Q., Cui, Q.Y., Chen, S.J., and Guo, X.J., Inkjet printed fine silver electrodes for all-solution-processed low-voltage organic thin film transistors. *Journal of Materials Chemistry C*, 2014. **2**(11): p. 1995-2000.

9. Wang, T.M., Roberts, M.A., Kinloch, I.A., and Derby, B., Inkjet printed carbon nanotube networks: the influence of drop spacing and drying on electrical properties. *Journal of Physics D-Applied Physics*, 2012. **45**(31): p. 315304.

10. Sou, A., Jung, S., Gili, E., Pecunia, V., Joimel, J., Fichet, G., and Sirringhaus, H., Programmable logic circuits for functional integrated smart plastic systems. *Organic Electronics*, 2014. **15**(11): p. 3111-3119.

11. Eggenhuisen, T.M., Galagan, Y., Biezemans, A.F.K.V., Slaats, T.M.W.L., Voorthuijzen, W.P., Kommeren, S., Shanmugam, S., Teunissen, J.P., Hadipour, A., Verhees, W.J.H., Veenstra, S.C., Coenen, M.J.J., Gilot, J., Andriessen, R., and Groen, W.A., High efficiency, fully inkjet printed organic solar cells with freedom of design. *Journal of Materials Chemistry A*, 2015. **3**(14): p. 7255-7262.

12. Jung, S., Sou, A., Banger, K., Ko, D.H., Chow, P.C.Y., McNeill, C.R., and Sirringhaus, H., All-Inkjet-Printed, All-Air-Processed Solar Cells. *Advanced Energy Materials*, 2014. **4**(14): p. 1400432.

13. Chang, S.C., Liu, J., Bharathan, J., Yang, Y., Onohara, J., and Kido, J., Multicolor organic light-emitting diodes processed by hybrid inkjet printing. *Advanced Materials*, 1999. **11**(9): p. 734-737.

14. Dua, V., Surwade, S.P., Ammu, S., Agnihotra, S.R., Jain, S., Roberts, K.E., Park, S., Ruoff, R.S., and Manohar, S.K., All-Organic Vapor Sensor Using Inkjet-Printed Reduced Graphene Oxide. *Angewandte Chemie-International Edition*, 2010. **49**(12): p. 2154-2157.

15. Yang, L., Zhang, R.W., Staiculescu, D., Wong, C.P., and Tentzeris, M.M., A Novel Conformal RFID-Enabled Module Utilizing Inkjet-Printed Antennas and Carbon Nanotubes for Gas-Detection Applications. *Ieee Antennas and Wireless Propagation Letters*, 2009. **8**: p. 653-656.

16. Forrest, S.R., The path to ubiquitous and low-cost organic electronic appliances on plastic. *Nature*, 2004. **428**(6986): p. 911-918.

17. Gordon, R.G., Criteria for choosing transparent conductors. *MRS Bulletin*, 2000. **25**(8): p. 52-57.

18. Hecht, D.S., Hu, L.B., and Irvin, G., Emerging Transparent Electrodes Based on Thin Films of Carbon Nanotubes, Graphene, and Metallic Nanostructures. *Advanced Materials*, 2011. **23**(13): p. 1482-1513.

19. Luechinger, N.A., Athanassiou, E.K., and Stark, W.J., Graphene-stabilized copper nanoparticles as an air-stable substitute for silver and gold in low-cost ink-jet printable electronics. *Nanotechnology*, 2008. **19**(44): p. 445201.

20. Li, L.H., Guo, Y.Z., Zhang, X.Y., and Song, Y.L., Inkjet-printed highly conductive transparent patterns with water based Ag-doped graphene. *Journal of Materials Chemistry A*, 2014. **2**(44): p. 19095-19101.

21. Kim, Y.H., Sachse, C., Machala, M.L., May, C., Muller-Meskamp, L., and Leo, K., Highly Conductive PEDOT:PSS Electrode with Optimized Solvent and Thermal Post-Treatment for ITO-Free Organic Solar Cells. *Advanced Functional Materials*, 2011. **21**(6): p. 1076-1081.

22. Nardes, A.M., Kemerink, M., de Kok, M.M., Vinken, E., Maturova, K., and Janssen, R.A.J., Conductivity, work function, and environmental stability of PEDOT : PSS thin films treated with sorbitol. *Organic Electronics*, 2008. **9**(5): p. 727-734.

23. Vitoratos, E., Sakkopoulos, S., Dalas, E., Paliatsas, N., Karageorgopoulos, D., Petraki, F., Kennou, S., and Choulis, S.A., Thermal degradation mechanisms of PEDOT:PSS. *Organic Electronics*, 2009. **10**(1): p. 61-66.

24. Gu, H. and Swager, T.M., Fabrication of Free-standing, Conductive, and Transparent Carbon Nanotube Films. *Advanced Materials*, 2008. **20**(23): p. 4433-4437.

25. Mirri, F., Ma, A.W.K., Hsu, T.T., Behabtu, N., Eichmann, S.L., Young, C.C., Tsentalovich, D.E., and Pasquali, M., High-Performance Carbon Nanotube Transparent Conductive Films by Scalable Dip Coating. *ACS Nano*, 2012. **6**(11): p. 9737-9744.

26. Novoselov, K.S., Geim, A.K., Morozov, S.V., Jiang, D., Zhang, Y., Dubonos, S.V., Grigorieva, I.V., and Firsov, A.A., Electric field effect in atomically thin carbon films. *Science*, 2004. **306**(5696): p. 666-669.

27. Huang, P.Y., Ruiz-Vargas, C.S., van der Zande, A.M., Whitney, W.S., Levendorf, M.P., Kevek, J.W., Garg, S., Alden, J.S., Hustedt, C.J., Zhu, Y., Park, J., McEuen, P.L., and Muller, D.A., Grains and grain boundaries in single-layer graphene atomic patchwork quilts. *Nature*, 2011. **469**(7330): p. 389-392.

28. Emtsev, K.V., Bostwick, A., Horn, K., Jobst, J., Kellogg, G.L., Ley, L., McChesney, J.L., Ohta, T., Reshanov, S.A., Rohrl, J., Rotenberg, E., Schmid, A.K., Waldmann, D., Weber, H.B., and Seyller, T., Towards wafer-size graphene layers by atmospheric pressure graphitization of silicon carbide. *Nature Materials*, 2009. **8**(3): p. 203-207.

29. Cai, J.M., Ruffieux, P., Jaafar, R., Bieri, M., Braun, T., Blankenburg, S., Muoth, M., Seitsonen, A.P., Saleh, M., Feng, X.L., Mullen, K., and Fasel, R., Atomically precise bottom-up fabrication of graphene nanoribbons. *Nature*, 2010. **466**(7305): p. 470-473.

30. Hernandez, Y., Nicolosi, V., Lotya, M., Blighe, F.M., Sun, Z.Y., De, S., McGovern, I.T., Holland, B., Byrne, M., Gun'ko, Y.K., Boland, J.J., Niraj, P., Duesberg, G., Krishnamurthy, S., Goodhue, R., Hutchison, J., Scardaci, V., Ferrari, A.C., and Coleman, J.N., High-yield production of graphene by liquid-phase exfoliation of graphite. *Nature Nanotechnology*, 2008. **3**(9): p. 563-568.

31. Tung, V.C., Allen, M.J., Yang, Y., and Kaner, R.B., High-throughput solution processing of large-scale graphene. *Nature Nanotechnology*, 2009. **4**(1): p. 25-29.

32. Torrisi, F., Hasan, T., Wu, W.P., Sun, Z.P., Lombardo, A., Kulmala, T.S., Hsieh, G.W., Jung, S.J., Bonaccorso, F., Paul, P.J., Chu, D.P., and Ferrari, A.C., Inkjet-Printed Graphene Electronics. *ACS Nano*, 2012. **6**(4): p. 2992-3006.

33. Su, Y., Du, J., Sun, D., Liu, C., and Cheng, H., Reduced graphene oxide with a highly restored π-conjugated structure for inkjet printing and its use in all-carbon transistors. *Nano Research*, 2013. **6**(11): p. 842-852.

34. Shin, K.Y., Hong, J.Y., and Jang, J., Micropatterning of Graphene Sheets by Inkjet Printing and Its Wideband Dipole-Antenna Application. *Advanced Materials*, 2011. **23**(18): p. 2113-2118.

35. De, S., King, P.J., Lotya, M., O'Neill, A., Doherty, E.M., Hernandez, Y., Duesberg, G.S., and Coleman, J.N., Flexible, Transparent, Conducting Films of Randomly Stacked Graphene from Surfactant-Stabilized, Oxide-Free Graphene Dispersions. *Small*, 2010. **6**(3): p. 458-464.

36. Le, L.T., Ervin, M.H., Qiu, H., Fuchs, B.E., and Lee, W.Y., Graphene supercapacitor electrodes fabricated by inkjet printing and thermal reduction of graphene oxide. *Electrochemistry Communications*, 2011. **13**(4): p. 355-358.

37. Hummers, W.S. and Offeman, R.E., Preparation of Graphitic Oxide. *Journal of the American Chemical Society*, 1958. **80**(6): p. 1339-1339.

38. Dimiev, A., Kosynkin, D.V., Alemany, L.B., Chaguine, P., and Tour, J.M., Pristine graphite oxide. *Journal of the American Chemical Society*, 2012. **134**(5): p. 2815-2822.

39. Moon, I.K., Lee, J., Ruoff, R.S., and Lee, H., Reduced graphene oxide by chemical graphitization. *Nature Communications*, 2010. **1**: p. 73.

40. Gudarzi, M.M., Moghadam, M.H.M., and Sharif, F., Spontaneous exfoliation of graphite oxide in polar aprotic solvents as the route to produce graphene oxide - organic solvents liquid crystals. *Carbon*, 2013. **64**: p. 403-415.

41. Jung, I., Rhyee, J.S., Son, J.Y., Ruoff, R.S., and Rhee, K.Y., Colors of graphene and graphene-oxide multilayers on various substrates. *Nanotechnology*, 2012. **23**(2): p. 025708.

42. Derby, B. and Reis, N., Inkjet printing of highly loaded particulate suspensions. *MRS Bulletin*, 2003. **28**(11): p. 815-818.

43. Derby, B., *Inkjet Printing of Functional and Structural Materials: Fluid Property Requirements, Feature Stability, and Resolution*, in *Annual Review of Materials Research, Vol 40*. 2010. p. 395-414.

44. Fromm, J.E., Numerical-Calculation of the Fluid-Dynamics of Drop-on-Demand Jets. *Ibm Journal of Research and Development*, 1984. **28**(3): p. 322-333.

45. Reis, N. and Derby, B., *Ink jet deposition of ceramic suspensions: Modelling and experiments of droplet formation*, in *Solid Freeform and Additive Fabrication-2000*. 2000. p. 117-122.

46. Jang, D., Kim, D., and Moon, J., Influence of Fluid Physical Properties on Ink-Jet Printability. *Langmuir*, 2009. **25**(5): p. 2629-2635.

47. Derby, B., Inkjet printing ceramics: From drops to solid. *Journal of the European Ceramic Society*, 2011. **31**(14): p. 2543-2550.

48. Xu, Z. and Gao, C., Aqueous Liquid Crystals of Graphene Oxide. *ACS Nano*, 2011. **5**(4): p. 2908-2915.

49. Martin, G., D., Hoath, S.D., and Hutchings, I.M., Inkjet printing - the physics of manipulating liquid jets and drops. *Journal of Physics: Conference Series*, 2008. **105**: p. 012001.

50. Stringer, J. and Derby, B., Formation and Stability of Lines Produced by Inkjet Printing. *Langmuir*, 2010. **26**(12): p. 10365-10372.

51. Reis, N., Ainsley, C., and Derby, B., Ink-jet delivery of particle suspensions by piezoelectric droplet ejectors. *Journal of Applied Physics*, 2005. **97**(9): p. 094903.

52. Jalili, R., Aboutalebi, S.H., Esrafilzadeh, D., Konstantinov, K., Razal, J.M., Moulton, S.E., and Wallace, G.G., Formation and processability of liquid crystalline dispersions of graphene oxide. *Materials Horizons*, 2014. **1**(1): p. 87-91.

53. Xu, Z. and Gao, C., Graphene chiral liquid crystals and macroscopic assembled fibres. *Nature Communications*, 2011. **2**.

54. Xu, Z., Sun, H., Zhao, X., and Gao, C., Ultrastrong Fibers Assembled from Giant Graphene Oxide Sheets. *Advanced Materials*, 2013. **25**(2): p. 188-193.

55. Deegan, R.D., Bakajin, O., Dupont, T.F., Huber, G., Nagel, S.R., and Witten, T.A., Capillary flow as the cause of ring stains from dried liquid drops. *Nature*, 1997. **389**(6653): p. 827-829.

56. Wang, X., Zhi, L.J., and Mullen, K., Transparent, conductive graphene electrodes for dye-sensitized solar cells. *Nano Letters*, 2008. **8**(1): p. 323-327.

57. Park, S., An, J., Potts, J.R., Velamakanni, A., Murali, S., and Ruoff, R.S., Hydrazine-reduction of graphite- and graphene oxide. *Carbon*, 2011. **49**(9): p. 3019-3023.

58. Zheng, Q.B., Ip, W.H., Lin, X.Y., Yousefi, N., Yeung, K.K., Li, Z.G., and Kim, J.K., Transparent Conductive Films Consisting of Ultra large Graphene Sheets Produced by Langmuir-Blodgett Assembly. *ACS Nano*, 2011. **5**(7): p. 6039-6051.

59. Cote, L.J., Kim, F., and Huang, J.X., Langmuir-Blodgett Assembly of Graphite Oxide Single Layers. *Journal of the American Chemical Society*, 2009. **131**(3): p. 1043-1049.

60. Finn, D.J., Lotya, M., Cunningham, G., Smith, R.J., McCloskey, D., Donegan, J.F., and Coleman, J.N., Inkjet deposition of liquid-exfoliated graphene and MoS2 nanosheets for printed device applications. *Journal of Materials Chemistry C*, 2014. **2**(5): p. 925-932.

61. Finn, D.J., Lotya, M., and Coleman, J.N., Inkjet Printing of Silver Nanowire Networks. *Acs Applied Materials & Interfaces*, 2015. **7**(17): p. 9254-9261.

62. De, S., King, P.J., Lyons, P.E., Khan, U., and Coleman, J.N., Size Effects and the Problem with Percolation in Nanostructured Transparent Conductors. *ACS Nano*, 2010. **4**(12): p. 7064-7072.

63. De, S. and Coleman, J.N., The effects of percolation in nanostructured transparent conductors. *MRS Bulletin*, 2011. **36**(10): p. 774-781.

64. Huang, L., Huang, Y., Liang, J.J., Wan, X.J., and Chen, Y.S., Graphene-based conducting inks for direct inkjet printing of flexible conductive patterns and their applications in electric circuits and chemical sensors. *Nano Research*, 2011. **4**(7): p. 675-684.

65. Shin, K.Y., Hong, J.Y., and Jang, J., Flexible and transparent graphene films as acoustic actuator electrodes using inkjet printing. *Chemical Communications*, 2011. **47**(30): p. 8527-8529.

66. Li, J., Ye, F., Vaziri, S., Muhammed, M., Lemme, M.C., and Ostling, M., Efficient inkjet printing of graphene. *Advanced Materials*, 2013. **25**(29): p. 3985-3992.

67. Nirmalraj, P.N., Lutz, T., Kumar, S., Duesberg, G.S., and Boland, J.J., Nanoscale Mapping of Electrical Resistivity and Connectivity in Graphene Strips and Networks. *Nano Letters*, 2011. **11**(1): p. 16-22.

68. Wang, S., Ang, P.K., Wang, Z.Q., Tang, A.L.L., Thong, J.T.L., and Loh, K.P., High Mobility, Printable, and Solution-Processed Graphene Electronics. *Nano Letters*, 2010. **10**(1): p. 92-98.

69. Arapov, K., Abbel, R., de With, G., and Friedrich, H., Inkjet printing of graphene. *Faraday Discussions*, 2014. **173**(0): p. 323-336.

70. Secor, E.B., Prabhumirashi, P.L., Puntambekar, K., Geier, M.L., and Hersam, M.C., Inkjet Printing of High Conductivity, Flexible Graphene Patterns. *Journal of Physical Chemistry Letters*, 2013. **4**(8): p. 1347-1351.

71. Gao, Y.H., Shi, W., Wang, W.C., Leng, Y.P., and Zhao, Y.P., Inkjet Printing Patterns of Highly Conductive Pristine Graphene on Flexible Substrates. *Industrial & Engineering Chemistry Research*, 2014. **53**(43): p. 16777-16784.

72. Secor, E.B., Ahn, B.Y., Gao, T.Z., Lewis, J.A., and Hersam, M.C., Rapid and Versatile Photonic Annealing of Graphene Inks for Flexible Printed Electronics. *Advanced Materials*, 2015. **27**(42): p. 6683-6688.

73. Rogala, M., Wlasny, I., Dabrowski, P., Kowalczyk, P.J., Busiakiewicz, A., Kozlowski, W., Lipinska, L., Jagiello, J., Aksienionek, M., Strupinski, W., Krajewska, A., Sieradzki, Z., Krucinska, I., Puchalski, M., Skrzetuska, E., and Klusek, Z., Graphene oxide overprints for flexible and transparent electronics. *Applied Physics Letters*, 2015. **106**(4): p. 041901.

74. Kim, H., Jang, J.I., Kim, H.H., Lee, G.W., Lim, J.A., Han, J.T., and Cho, K., Sheet Size-Induced Evaporation Behaviors of Inkjet-Printed Graphene Oxide for Printed Electronics. *ACS Appl Mater Interfaces*, 2016. **8**(5): p. 3193-9.

75. Kong, D., Le, L.T., Li, Y., Zunino, J.L., and Lee, W., Temperature-Dependent Electrical Properties of Graphene Inkjet-Printed on Flexible Materials. *Langmuir*, 2012. **28**(37): p. 13467-13472.

76. Lim, S., Kang, B., Kwak, D., Lee, W.H., Lim, J.A., and Cho, K., Inkjet-Printed Reduced Graphene Oxide/Poly(Vinyl Alcohol) Composite Electrodes for Flexible Transparent Organic Field-Effect Transistors. *Journal of Physical Chemistry C*, 2012. **116**(13): p. 7520-7525.

77. Zheng, J., Zhang, H., Dong, S., Liu, Y., Nai, C.T., Shin, H.S., Jeong, H.Y., Liu, B., and Loh, K.P., High yield exfoliation of two-dimensional chalcogenides using sodium naphthalenide. *Nature Communications*, 2014. **5**: p. 2995.

Chapter 4 Controlling the "Coffee Ring" Effect with Graphene Oxide Inks*

Abstract

This chapter describes an investigation of the coffee ring (or coffee stain) effect that is observed during the drying of droplets of graphene oxide aqueous inks. In particular it studies the influence of ink composition, drop size, substrate composition and environmental conditions. Eight GO inks with mean flake size ranging from 0.68 to 35.9 μm were prepared. It was found the coffee ring effect for GO drops was weakening when the contact angle of Si/SiO_2 substrates increased from 10.6° (UV-Ozone-treated) to 79.9° (HMDS treated). However, the surface morphology of dried drops on HMDS-treated substrates was observed non-uniform. By further investigating the evaporation dynamics and flake transport mechanism in a drying GO drops, it was observed that the coffee ring effect can be modified by changing the GO flake size, substrate temperature and drop size. Firstly, the influenced of mean flake size on the shape of inkjet-printed droplets on UV-Ozone treated substrates was studied. It was found that the, with large printed drops with diameter around 340 μm, the coffee ring effect was supressed when the flake size was larger than 10.3 μm. When the substrate temperature was increased to 40 and 50 °C, the coffee ring effect for drops with flake size > 5.97 and 3.68 μm, respectively. However, for flake size < 3.68 μm, the coffee ring effect was observed even when with the temperature at 60 °C. Finally, it was observed that the coffee ring effect weakened with drop size decrease such that dried drops with diameter of 30 μm showed uniform dried deposits with mean flake size of 1.58 μm.

---

*This chapter is based on a paper. Pei He, and Brian Derby, 'Controlling the "Coffee Ring" Effect with Graphene Oxide Inks', in preparation. P.H. performed all the experiments. B.D. and P.H. planned the experiments and wrote the paper.

4.1 Introduction

When a liquid sessile drop of liquid containing suspended particles dries on a solid surface, it may leave a ring-like structure around the periphery of the drop after completion of liquid evaporation. This phenomenon is commonly known as the coffee ring [1] and is observed in systems with diverse constituents, ranging from nanoparticles, to colloids and molecules in solution.[2] A mechanism for the coffee-ring effect (CRE) was first developed by Deegan et al.,[1] who proposed that the dispersed materials in the droplet are transported to the contact line of the drop by radial flow generated during the evaporating process when the contact line is pinned. The mechanism of CRE induced by capillary flow was further developed and explained by Fisher[3] and Larson,[4, 5] who used lubrication theory and numerical solutions of the fluid transport equations to model the flow field within evaporating droplets. Further investigations by other workers showed that numerous parameters can affect the morphology of the final pattern of dried deposits in this complex process, including: Marangoni flow,[6] drying conditions,[7] particle-interface interactions,[8] particle-particle interactiosn,[2] surface tension and the constituents of the solvents,[9] as well as the surface properties of substrates.[10, 11] Although the ubiquitous nature of the CRE makes it hard to avoid, achieving morphology uniformity from evaporated drops is critical in many practical applications, such as graphics inkjet printing,[12] micro-arrays,[13] coatings,[14] biosensors,[15] and the self-assembly of particles.[16]

Many techniques have been developed to suppress or control the CRE. The most common strategy to obtain uniform depositions is to weaken the outward radial flow within an evaporating drop. Examples of methods proposed to control the CRE include: using cooled substrates,[7] increasing environment humidity,[17] reducing the droplet size,[18] introducing UV sensitive cationic surfactant,[19] and utilizing sol-gel transition[20] and depletion flocculation.[21] Another approach to reduce or eliminate the CRE is through promoting an inward Marangoni flow, which is driven by local changes in surface tension, by using co-solvents,[9] polymers in solution,[22] and surfactants.[23] Recently, Yodh et al, proposed that the CRE can be suppressed by using high aspect ratio particles instead of spherical particles.[2] A uniform distribution of ellipsoids was predicted when the aspect ratio of anisotropic particles is greater than 1.5. However, the authors ignored the effect of particle-particle and particle-substrate interaction forces during the evaporation process.[24] A number of experiments have reported findings that contradict

Yodh's predictions with the observation of a clear ring of solute after drying sessile drops containing rod-like colloids with aspect ratio in the range 4 - 15.[24] Nanotubes with high aspect ratio have also been reported to show a CRE from inkjet-printed droplets.[25]

Several groups have reported using inkjet printing technique to deposit graphene dispersions for electronic applications.[33-38] During drying of droplets, inks containing 2D materials such as graphene or graphene oxide (GO) show a behaviour similar to that observed during the drying of inks made from nanoparticles or nanotubes, i.e. they show a clear CRE with the dried 2D flakes arranged at the contact line of the dried droplets forming a characteristic ring-like structure.[33, 37] Although the CRE can be suppressed by using a combination of two solvents[34, 38] or adding surfactant and a high boiling point solvent,[36] the harsh post-treatment condition required and restrictions to the use of some organic solvents limits these mitigating techniques for large area applications.

This chapter will explore the influence of parameters such as contact angle, particle size, temperature, and drop size on the final morphology and shape of dried droplets of a GO ink. GO inks with a range of mean flake size were obtained by ultrasonically milling inks with very large flake size for a range of process times, with increasing sonication time leading to a smaller mean flake size. GO inks of the initial large flake size were obtained using a modified Hummers' method to produce GO dispersions with mean flake size 35.9 μm, as described in Chapter 3. This method allowed us to produce a range of GO inks with mean flake size ranging from 0.68 to 35.9 μm. The GO suspensions are highly stable against sedimentation in deionised water and these were then used, after appropriate dilution, directly as inks in this study.

Droplets of GO ink were deposited onto the substrates with different equilibrium contact angles for sessile drops of the ink, which were prepared by treating Si/SiO_2 substrates with UV-Ozone (10.6 °) and HMDS (79.9 °). Although, no CRE was observed with drops drying on hydrophobic surfaces, the edge of dried drop was non-uniform due to the aggregation of GO flakes. The evaporation dynamics and flake transport mechanisms during drop drying have been further investigated. We found the presence of the CRE is influenced by the GO flake size, the sessile drop size and the substrate temperature. Inks with GO flake size > 10.3 μm did not show a CRE when drops with a contact diameter of ~ 340 μm dried. The critical flake size for CRE

suppression decreases as the substrate (drying) temperature increases. A decrease in the critical flake size was also observed when smaller drop diameters were used in the drying experiments. These observations are shown to be consistent with a model that compares characteristic time constants for flake aggregation and for drop drying.

4.2 Experimental Section

GO ink preparation. The preparation of the GO sheets is based on a modified Hummers' method.[39] Briefly, nature graphite flakes (1.5 g, grade 9842, Graphexel Ltd., Epping, UK) were dispersed in concentrated sulfuric acid (200 ml, > 95%, > 17.7 mol, Fisher Scientific) by stirring in an ice bath. Then a total of 6.0 g $KMnO_4$ (Lot # MKBK7079V, Sigma-Aldrich) were added at 24 hour intervals over 4 days (1.5 g each time). Full experimental procedures have been described in Chapter 3, section 3.2.1. The as-prepared GO dispersion was diluted to about 0.5 mg/mL for further use.

The initial GO ink was termed "GO-0". The ink "GO-1" were prepared by centrifuging the GO-0 ink at 3000 rpm for 15 min. To further obtain GO sheets with small size, the GO-0 inks were treated by probe sonication (MicrosonXL2000, Misonixlnc., Farmingdale, NY, USA) for periods of 2s, 5s, 2 min, 3 min, 5 min and 30 min and these inks were termed "GO-2", "GO-3", "GO-4", "GO-5", "GO-6", and "GO-7", respectively.

Surface energy modification of substrates. Prior to modification, the Si/SiO_2 substrates were cleaned with ethanol and water by ultrasonication for 15 mins, then dried with a pressurised nitrogen cleaning gun. To make a hydrophilic surface, the Si/SiO_2 substrates were treated with UV-Ozone (Zone SEM) at a low vacuum for 5 min. The hydrophobic surface was prepared by applying a self-assembled monolayer (SAM) coating the Si/SiO_2 substrates with hexamethyldisilazane (HMDS, Sigma-Aldrich) vapour in a sealed flask for 30 min.

Deposition of large GO droplets. Briefly, the cleaned and UV-Ozone treated Si/SiO_2 substrates were placed on an Ultra-Microbalances weighing system (XPR2, Mettler-Toledo Ltd, Leicester, U.K). Then the GO droplets with volume from 0.25 to 2 µL were dropped on the Si/SiO_2 substrates through a micropipette. The real time mass of the GO droplets was record by a Nikon D7000camera (Nikon U.K. Limited).

Deposition of GO droplets by Inkjet printing. Prior to printing, the Si/SiO_2 substrates, which were cleaned as described above, were treated with UV-Ozone for 5 min. GO aqueous inks with a concentration of ~ 0.5 mg/mL were deposited onto the substrates by inkjet printing. An in-house designed and built laboratory inkjet printer (MPP 1000) was equipped with drive electronics (JetDrive III, Microfab, Plan, TX, USA) interfaced to a PC and controlled in a LabVIEW (National Instruments, Austin, TX, USA) system. The dried droplets with diameter of 150 – 370 μm were printed by the nozzles with diameter of 30 (Part #: MJ-AT-01-30-8MX) and 60 μm (Part #: MJ-AT-01-60-8MX), respectively. For ejecting small droplets (< 80 μm), a Dimatix inkjet printer (DMP 2800, Fujifilm Dimatix, Santa Clara, CA, USA) integrated with a 10 pL cartridge (Part #: DIMATIX DMC-11610) was used.

Characterization. The viscosity of the GO inks were measured using a TA Discovery HR-3rheometer (TA Instruments, New Castle, DE, USA) with a cone-plate geometry (60 mm diameter, 2°).The surface tension and contact angle of GO inks were measure by a Drop Shape Analyser DSA100 (KRÜSS GmbH, Hamburg, Germany). Images of dried GO droplets were captured using an Olympus BH-2 optical microscope (Olympus, Tokyo, Japan). The morphology and structure of the GO sheets and GO droplets were characterized by scanning electron microscopy (SEM, XL30 FEG-SEM, FEI, Eindhoven, Netherlands) and atomic force microscopy (AFM, Dimension 3100, Bruker Billerica, MA, USA). The size distribution of GO sheets was calculated from SEM images by the software ImageJ (NIH, Bethesda, MA, USA).

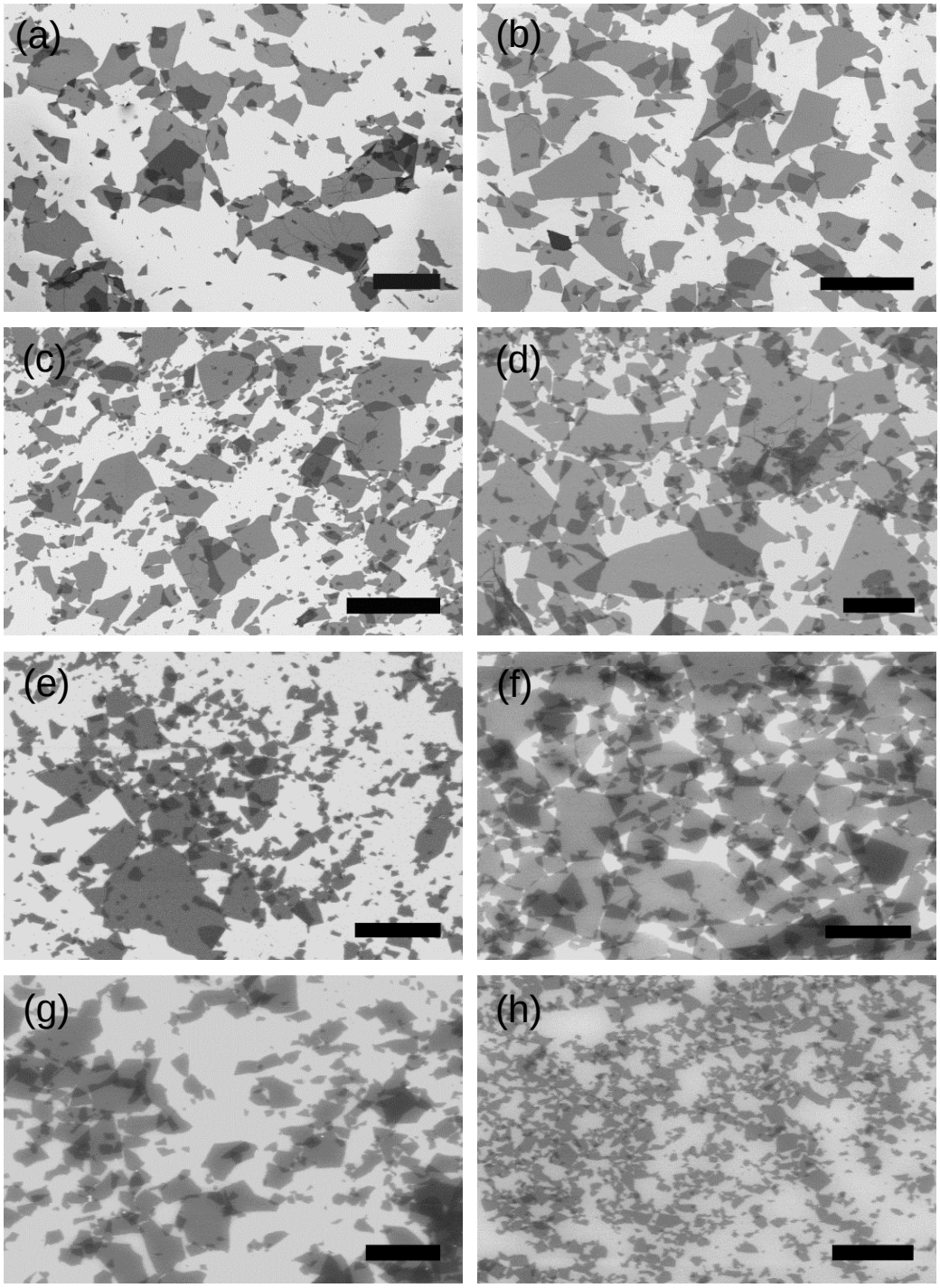

Figure 4.1. SEM images of GO sheets dried on Si/SiO_2 substrates with different mean lateral flake size: GO-0 (a), GO-1 (b), GO-2 (c), GO-3 (d), GO-4 (e), GO-5 (f), GO-6 (g), and GO-7 (h). All scale bars are at 100 μm (a, b), 50 μm (c), 15 μm (d, e), and 5μm (f, g, h).

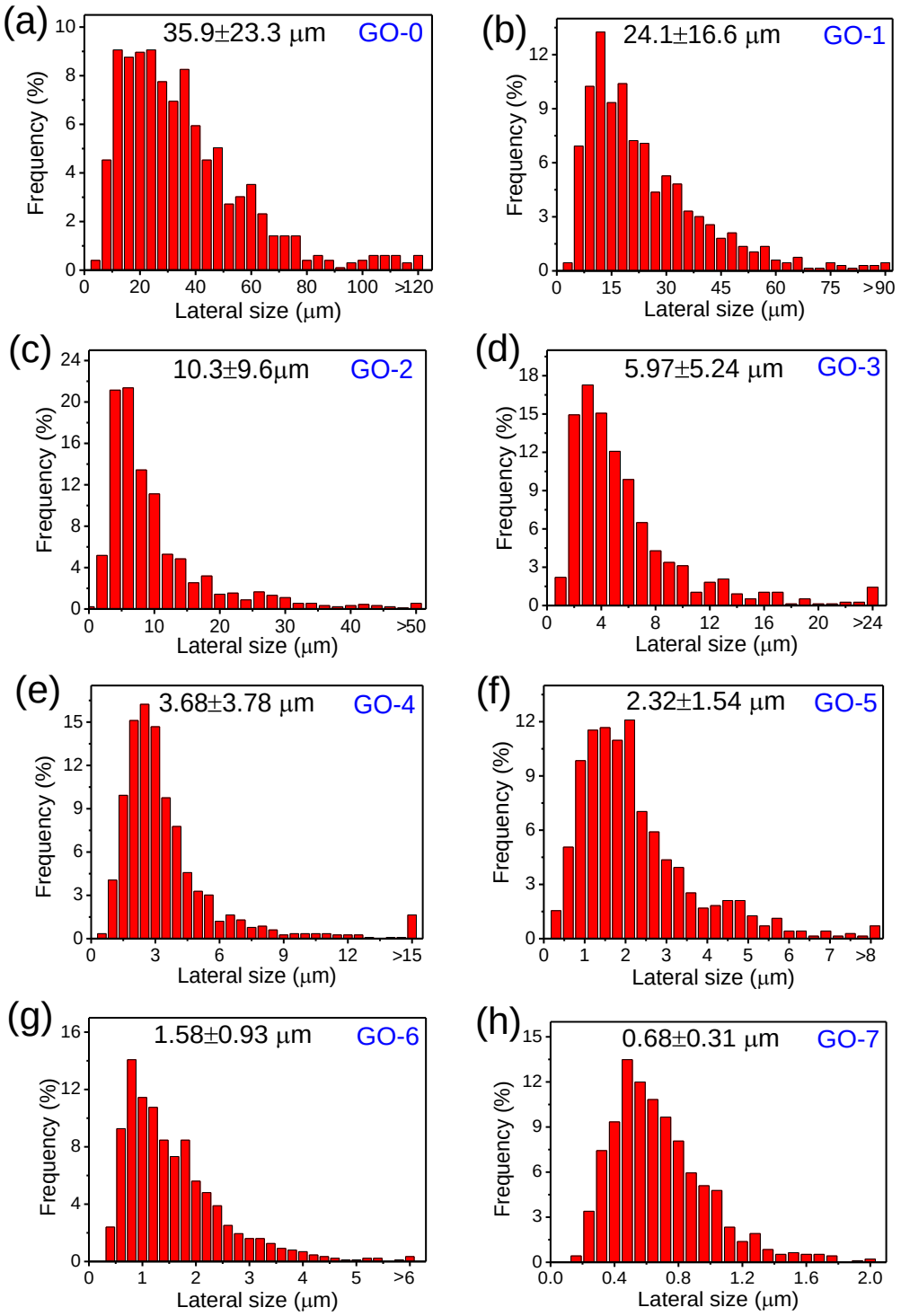

Figure 4.2. Lateral size distribution of GO sheets dried on Si/SiO_2 substrates with different mean lateral flake size: GO-0: 35.9±23.2 (a), GO-1: 24.1±16.6 (b), GO-2: 10.3±9.6 (c), GO-3: 5.97±5.24 (d), GO-4: 3.68±3.78 (e), GO-5: 2.32±1.54 (f), GO-6: 1.58±0.93 (g), and GO-7: 0.68±0.31 μm (h).

4.3 Results and Discussions

4.3.1 The Preparation and Characterization of GO Flakes

The GO flakes were synthesized as described in the experimental section. To obtain monolayer GO sheets of large flake size, a natural graphite powder with mean flake size of about 300 μm was used. Figure 4.1a shows a SEM image of as-prepared GO sheets deposited on a Si/SiO_2 substrate. It can be seen that the size of GO sheets ranged from several μm to ~200 μm. The wide size distribution of the GO sheets is believed to be derived from the existing of small size of the starting graphite powder and the break-down of the graphite flakes during the oxidization process. ImageJ software was used to analyse the SEM images to obtain the lateral size of individual GO sheets. Figure 4.2a shows the size distribution of GO sheets determined by measuring more than 400 individual GO sheets from at least five SEM images. The GO sheets show a mean size of 35.9 ± 23.2 μm and > 95% of flakes are larger than 10 μm. Figure 4.3 shows images of a GO sheet taken using optical microscopy, SEM, and AFM obtained from the same area on a Si/SiO_2 substrate. It can be seen that the size of the large GO sheet is around 70 μm. The overlaps, folds, and wrinkles of GO sheets, which are the three main morphology features of the two dimensional flakes, can be seen clearly. The height profile of an individual GO sheet, as shown in Figure 4.3d, is about 1.07 nm, which confirms that the GO sheet is monolayer.

To obtain GO sheets with smaller size, the initial GO-0 ink was first centrifuged at 3000 rpm for 15 min to remove the ultra-large flakes, the supernatant after centrifuging is the GO-1 ink. Figure 4.1b shows the typical SEM image of GO sheets from the GO-1 ink. The sheet size of GO-1 ink ranged up to about 120 μm in size, as shown in Figure 4.2b. The mean flake size of the GO-1 ink is 24.1±16.6 μm with ~ 85.7% of sheets larger than 10 μm. Further reduction of the size of the GO sheets was obtained by applying tip sonication to the ink for different treatment times as described in the experimental section. Figure 4.2c-h shows SEM images of GO sheets from the GO-2, GO-3, GO-4, GO-5, GO-6, and GO-7 inks, respectively. Note that the tip sonication process, compared to the centrifugation process, efficiently breaks down the GO sheets to smaller sizes even after a few seconds. The mean flake size of GO-2 ink, sonicated with 2s, is 10.3 ± 9.6 μm, as shown in Figure 4.2c. It can be seen that the flake size ranged

from hundreds of nm up to about 80 μm, this shows a much larger size range than the original ink due to the non-uniform break-down energy distribution for the tip sonication process.[40] The longer the sonication time, the smaller the flake size generated. Figure 4.2d-h show the mean flake size of GO-3, GO-4, GO-5, GO-6, and GO-7 ink are 5.97 ± 5.24, 3.68 ± 3.78, 2.32 ± 1.54, 1.58 ± 0.93, and 0.68 ± 0.31 μm, respectively. Noticeably, with increasing sonication time, the size distribution of GO sheets is becoming more like a Poisson distribution since the large flakes are more liable to fracture by ultrasonic excitation.

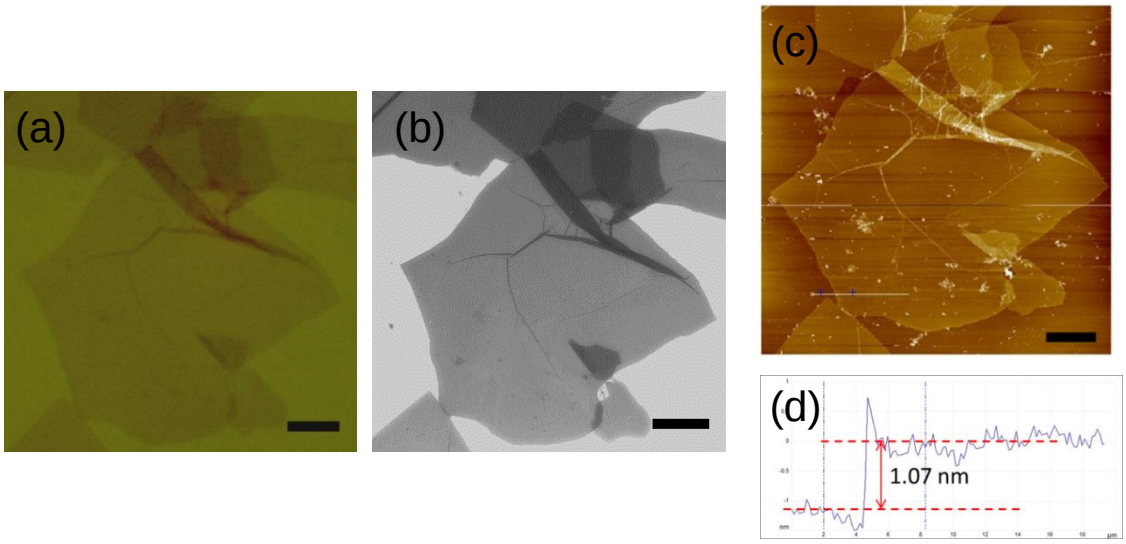

Figure 4.3. Images of GO sheets on a Si/SiO_2 substrate taken by (a) optical microscopy, (b) SEM, and (c) AFM, and the corresponding height profiles for the indicated line shown in (d). Scale bar corresponds to 10 μm on all images.

4.3.2 The Influence of Contact Angle during Droplet Drying

During the evaporation of a sessile droplet on a solid substrate, it is known that the solvent molecules at the periphery of the droplet have a higher evaporation rate than the solvent molecules at the centre. When a droplet containing solute or dispersed solids dries and the contact line is pinned, the solute or solids will move from the centre of the droplet to the edge driven by an outward capillary flow,[1] ,which generated by the evaporation rate difference between the centre and the edge of the droplet, as shown in Figure 4.4.

In order to investigate the influence of contact angle on the evaporation of a sessile droplet and any resulting CRE, the GO ink droplets were deposited onto UV-Ozone

treated Si/SiO_2 substrates, pristine Si/SiO_2 substrates, and HMDS treated Si/SiO_2 substrates. Figure 4.4 shows the contact angle of GO aqueous ink on Si/SiO_2 substrates with different treatment method. The contact angle of the GO droplet on the pristine Si/SiO_2 substrate was 57.3°, whereas the contact of GO droplets are 10.6° and 79.9° for UV-Ozone and HMDS-treated Si/SiO_2 substrates.

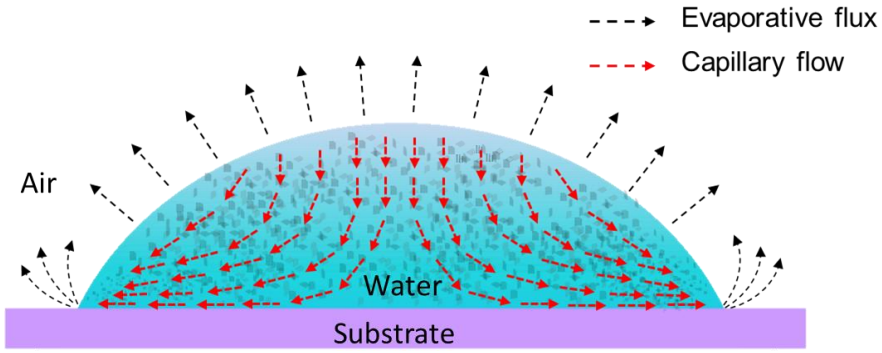

Figure 4.4. Schematic diagram of the evaporation process of a water droplet on a solid substrate.

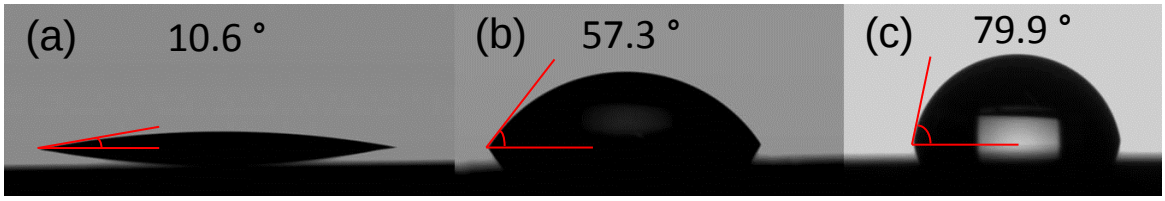

Figure 4.5. The contact angle of the GO aqueous ink on Si/SiO_2 substrates with different treatment: (a) UV-Ozone treated: 10.6 °, (b) pristine: 57.3 °, and (c) HMDS treated: 79.9 °.

Figure 4.6 shows optical images of dried droplets of GO inks with different mean flake size on Si/SiO_2 substrates with different contact angle. It can be seen that the dried droplets on the low contact angle UV-Ozone treated Si/SiO_2 substrates leave patterns with a uniform outline, whereas the outline of dried droplets on the pristine and HMDS-treated Si/SiO_2 substrates is non-uniform. The red arrows indicate drying tracks left by the moving contact line as the droplet shrinks. It is worth mentioning that, for the GO-0 with a mean size of 35.9±23.2 μm, the dried pattern shows a uniform cap-like structure on UV-Ozone treated substrate, whereas the morphology of dried droplets on the pristine (Figure 4.6b) and HMDS-treated (Figure 4.6c) substrates show a strong striped surface due to wrinkles on the GO flakes that form during drying. As the mean flake size decreases to 3.68 ± 3.78 μm, the dried patterns show a slight CRE at the edge. A strong CRE was observed with a GO droplet of the ink containing small flakes (1.58±0.93 μm) deposited on UV-Ozone treated substrate, as shown in Figure 4.6g.

Therefore, from the data shown in Figure 4.6, it can be seen that the shape of a drying GO aqueous ink droplet is affected by both the contact angle and the size of the GO sheets in the ink.

Flake size (μm)	Contact angle		
	10.6°	57.3°	79.9°
35.9±23.3	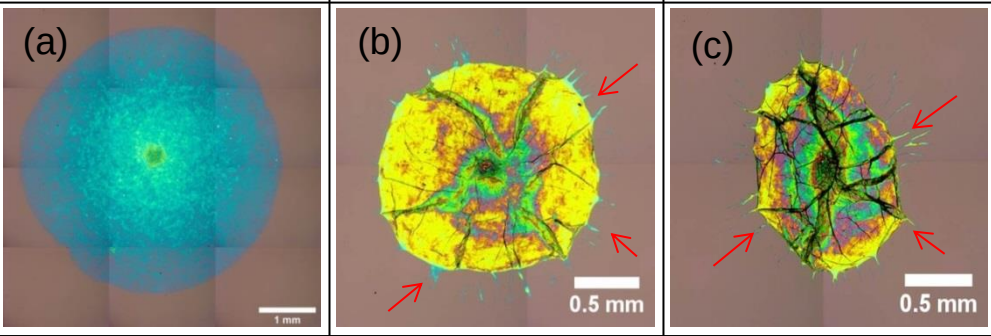		
2.32±1.32	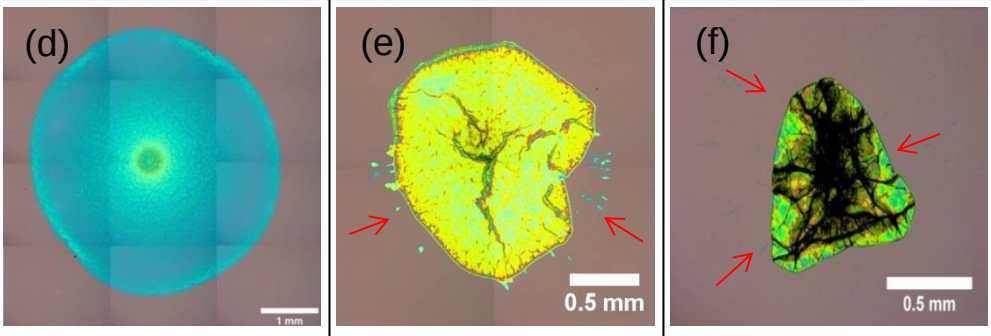		
0.68±0.31	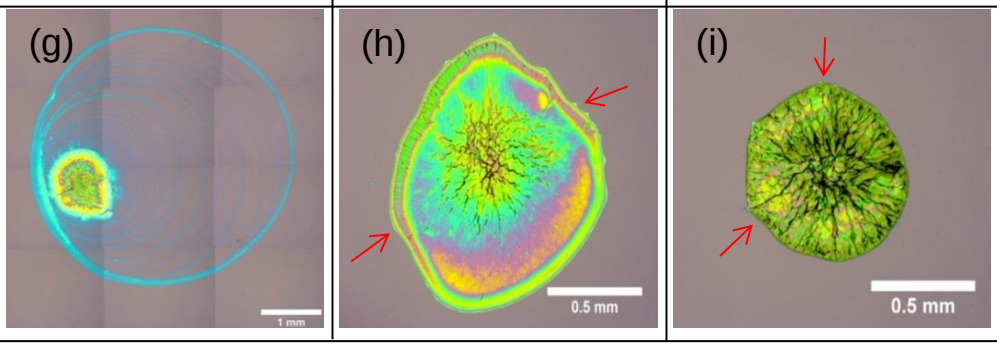		

Figure 4.6. Optical microscopy images of drying droplets prepared from GO-0 (a-c), GO-5 (d-f), and GO-7 (g-i) inks on Si/SiO_2 substrates with different contact angle: (a, d, g) UV-Ozone treated, (b, e, h) pristine, and (c, f, i) HMDS treated.

4.3.3 The Evaporation Dynamics and Flake Transport in a Drying GO Drop

4.3.3.1 Drop Evaporation

To control the final shape of GO droplets after solvent evaporating, it is important to understand the drying process of GO drops. In our experiments, we will focus on the drying of GO droplets on UV-treated Si/SiO_2 substrates. In this case, the contact angle

is about 10°, which means the maximum height of the spreading droplet is much smaller than its diameter. As the concentration of GO in the ink is only 0.5 mg/ml, we assume that the shape of droplet is not affected by the GO flakes.

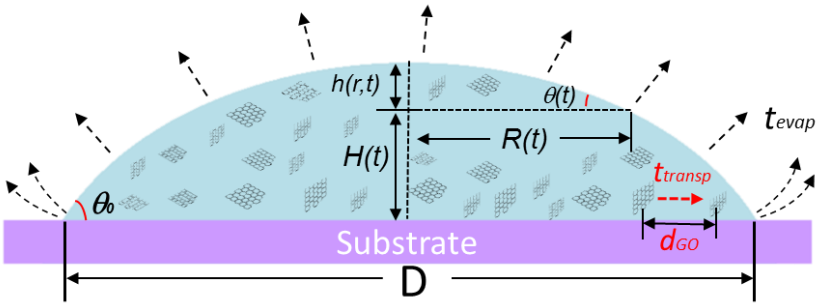

Figure 4.7. A schematic representation of a GO droplet drying on a solid substrate.

Figure 4.7 shows a schematic of the process of GO droplet drying. Popov proposed an evaporation model for a drying droplet with constant contact diameter, assuming transport control by atmospheric diffusion.[41] From this the droplet evaporation rate, dV_d/dt, and the evaporation time, t_{evap}, can be expressed as:

$$\frac{dV_d}{dt} = -\frac{2D_v(c_0-c_\infty)D}{\rho_L} \tag{4.1}$$

$$t_{evap} = \frac{\pi\rho_L\theta_0}{16D_V(c_0-c_\infty)}\left(\frac{D}{2}\right)^2 \tag{4.2}$$

where V_d is the drop volume; ρ_L is the density of water; θ_0 is the initial contact angle; D_V is the molecular diffusion coefficient of the vapour in air; c_0 is the density of the saturated vapour just above the liquid-air interface; c_∞ is the ambient vapour density; and D is the spherical cap diameter. The value of c_0-c_∞, D_V, and ρ_L can be calculated from [18]

$$c_0-c_\infty = \left[\frac{M_w P_{vs}}{R_g(273.3+T)}\right](1-RH) \tag{4.3a}$$

$$D_V = 21.6\times10^{-6}\times(1+0.0071\,T) \tag{4.3b}$$

$$\rho_L = 1000-0.0067\times(T-3.98)^2+5.2\times10^{-7}\times(T-3.98)^4 \tag{4.3c}$$

$$P_{vs} = 610.7\times 10^{\frac{7.5T}{237.3}+T} \tag{4.3d}$$

where M_w is the molar mass of water (18.0152); P_{vs} is the saturation water vapour pressure; R_g is the ideal gas constant; T is the substrate temperature in degree Celcius

(°C); and *RH* the relative humidity level. From Equation 4.2-4.3, it can be seen that the time scale of the droplet evaporation is influenced by the droplet contact angle, substrate temperature, relative humidity, and the spherical cap diameter. The contact angle, spherical cap diameter and the volume of a sessile droplet (V_d) are related by [42]

$$V_d = f(\theta)\left(\frac{D}{2}\right)^3 \tag{4.4a}$$

$$f(\theta) = \frac{\pi}{3}\frac{2-3\cos\theta+\cos^3\theta}{\sin^3\theta} \tag{4.4b}$$

$$t_{evap} = \frac{\pi\rho_L\theta_0}{16D_V(c_0-c_\infty)(f(\theta))^{2/3}} V_d^{2/3} \tag{4.5}$$

For droplet drying with constant angle and environment condition (constant temperature and relative humidity), Equation 4.5 shows that the complete evaporation time of the droplet shows a linear increase with $V_d^{2/3}$.

To investigate the drying process, we measured the continuous weight change of GO droplets with evaporation time, as shown in Figure 4.8a. The experimental data shows the decrease in weight of GO ink droplets with different initial volumes on UV-Ozone treated Si/SiO_2 substrates ($\theta_0 \sim 10°$) under the same environment condition (*T*: 23.5 °C, *RH*: 37.3%). Note that the weight for all droplets decreases linearly with time at the initial evaporation stage. Since the evaporation rate relies only on the diameter of the droplet, this linear region indicates that the droplet remained pinned throughout this time scale. As the density of fluid, ρ_L, is constant, thus Equation 4.1 can be written as weight, W_d, loss rate:

$$\frac{dW_d}{dt} = -2D_v(c_0-c_\infty)D \tag{4.6}$$

It can be seen from Figure 4.8a that the rate of decrease in the weight of a drop can be approximated as a linear function for the majority of the drying time, which indicates that the drop was pinned over this time scale. Here, the t_{evap} can be expressed as the time at which the free surface of the liquid phase becomes flat and all the flakes become part of the deposit phase.[41] Before t_{evap} the surface of droplet is convex, after t_{evap} it becomes concave and bows inward until the droplet fully dry. Thus the total drying time is generally longer than t_{evap}. This is because the diameter of droplet at the end of drying process is not as the same as the initial diameter, but rather the diameter of the ring at depinning. This depinning time, t_{dep}, depends on the initial concentration of the solute.[41]

In our experiment, as shown in Table 4.1, the ratio of t_{dep} and t_{evap}, t_{dep}/t_{evap}, is about 0.69, which is within the range of 0.4-0.8 as reported in previous work.[41]

Figure 4.8b shows the fitted weight loss rate with increasing drop diameter. Notice that the weight loss rate increases with increasing drop diameter. The weight loss rate for 0.25, 0.5, 1.0, 1.5 and 2.0 µL droplets, which show dimeter of 2.961, 3.633, 4.653, 5.293, and 6.142 mm, are 2.05, 2.48, 3.23, 3.58, and 4.19 µg/s, respectively. The data shows a good fit with the calculated data from Equation 4.6, which means the effect of GO flakes during the fluid drying process can be ignored. The summary data of droplets information, experimental and calculated weight loss rate is shown in Table 4.1.

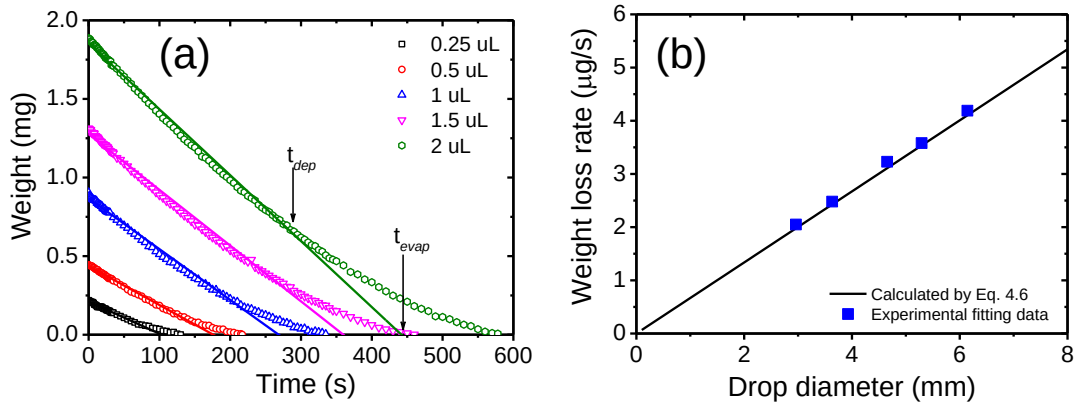

Figure 4.8. (a) The weight of GO droplets with different volume (0.25, 0.5, 1, 1.5, and 2 µL) vs. time deposited on UV-Ozone treated Si/SiO_2 substrates ($\theta_0 \sim 10°$) evaporating at temperature of 23.5 °C and relative humidity of 37.3%. The solid lines indicate the fitted evaporation rate with pinned contact lines. (b) The weight loss rate of droplets as a function of drop diameter. The scattered square data is the slope value of fitting lines in (a). The black solid line indicates the calculated data by Equation 4.6.

Table 4.1. Summary of experimental and calculated value of weight loss rate by Equation 4.6.

Drop volume (µL)	**Initial weight (mg)**	**Drop diameter (mm)**	***dW*$_d$*/dt* (µg/s)**		t_{evap} **(s)**	t_{dep} **(s)**	t_{dep}/t_{evap}
			Experimental	***Calculated***			
0.25	0.215	2.961	2.05	1.98	442	295	0.67
0.5	0.443	3.633	2.48	2.43	359	250	0.69
1.0	0.884	4.653	3.23	3.11	269	190	0.70
1.5	1.309	5.293	3.58	3.53	176	125	0.71
2.0	1.882	6.142	4.19	4.10	103	70	0.68

The weight of the droplet during evaporation, W_e, normalized by the initial weight, W_0, versus the droplet evaporation time from deposition, t_d, normalized by the full

evaporation time, t_f, is plotted in Figure 4.9a. Interestingly, the change of weight ratio, W_e/W_0, for all droplets with normalized time, t_d/t_f, shows almost the same trend, which further indicates that the evaporation process for droplets with different volume is the same. Moreover, since each droplet was deposited on the substrate with the same contact angle, temperature, and environment humidity level, we assumed the evaporation time is only related to the initial drop volume, thus the Equation 4.5 can be written as

$$t_{evap} \propto V_d^n \tag{4.7}$$

Figure 4.9b shows the fully evaporation time of droplets as a function of droplet volume deposited on the UV-Ozone treated Si/SiO_2 substrates. The drop volume was converted from the droplet weight using a measured GO ink density (0.981 ± 0.005 g/cm^3). It can be seen that the evaporation time decreases linearly with reducing drop volume on the log-log scale. By fitting the data with Equation 4.7, we get

$$t_{evap}=0.03804\ V_d^{0.667} \tag{4.8}$$

with a linear regression coefficient, R^2, of 0.9815, as shown in Figure 4.9b (the red line). The fitted value, 0.03804, is also very close to the calculated value by Equation 4.5, which is 0.03837 at the contact angle of 10 °. Moreover, for a constant drying condition, we assumed that the drying behaviour of droplets is the transport of water vapour by atmospheric diffusion applying even though the volume decreases by 2-3 orders of magnitude. Thus, by expanding the drop volume to the range for normal inkjet-printed droplets ($10 \sim 10^3$ pL), it can be predicted that the evaporation time for printed droplets is in the range of 0.18 to 3.8 s.

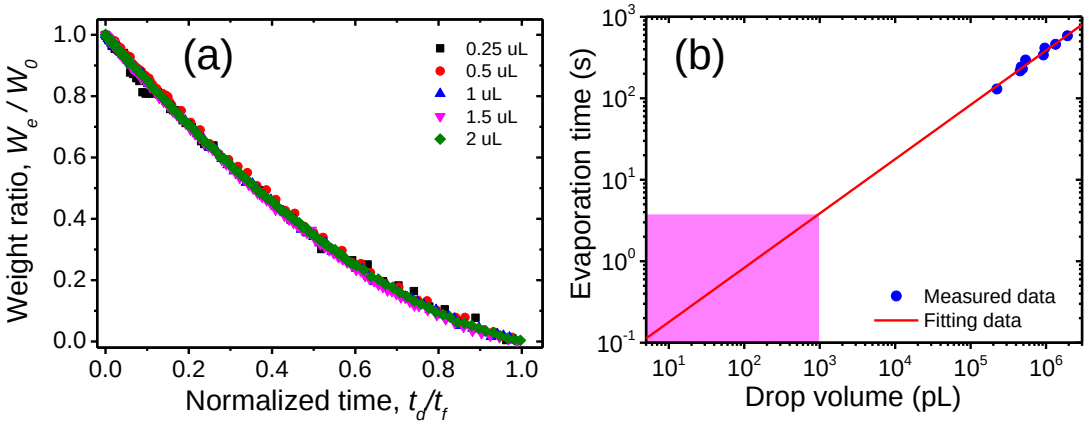

Figure 4.9. (a) The droplet weight ratio, W_e/W_0, as a function of normalized drying time, t_d/t_f, for different volume of deposition droplets. (b) The fully evaporation time of droplets as a function of droplet volume deposited on the UV-Ozone treated Si/SiO_2 substrates ($\theta_0 \sim 10°$) at temperature of 23.5 °C and relative humidity of 37.3%. The red line is fitted by $t \propto V_d^n$. The magenta area indicates the evaporation range for printed droplets, which have volume lower than 1 nL.

4.3.3.2 Flake Transport

Equations 4.1 - 4.8 assume that the drying of drops is controlled by diffusional transport of water vapour and that this behaviour fits our observations for the drying of mL droplets and is reasonably extrapolated to the < nL drops appropriate for inkjet printing. The final shape of a drying droplet containing solute is believed to be related to both the evaporation process and the GO flake diffusion process during solvent evaporation. In particular, current models for the onset of the CRE focus on the role of solute deposition in controlling the pinning of the contact line.[18, 43] In order for the contact line to be pinned, there must be a deposit of particles at the line to provide a pinning force and the onset of the CRE is controlled by the relative timescale for the formation of the pinning deposit and the timescale for the retraction of the contact line. Shen et al[18] proposed that the appropriate time constants are the time taken for a drop to evaporate and the time for drops to agglomerate by random diffusional processes. Gorr et al [43] proposed a slightly different approach by comparing the velocity of particle transport through the radial capillary (advective) flow and the counter diffusional flow driven by consequent excess particle concentration near the contact line through use of the dimensionless Peclet number. However, both these studies used particle suspensions that were very different in size and shape than the GO suspensions used in this study with Shen using ~100 nm

diameter polystyrene spheres [18] and Gorr using lysozyme molecules, which are ellipsoids of major axis diameter ~10 nm.[43]

Thus, to understand the mechanism of formation of the shape during drying process, it is necessary to understand the mechanisms for the transport of GO flakes to the contact line region by the outward capillary flow and the GO flake diffusion coefficient. In the case of GO droplet evaporation, it is proposed that there are two important length scales that are central to the formation of the coffee ring structure during drying. The first length scale is related the transport length of individual GO flake, d_{transp}, which indicates the displacement of GO flakes from the inner region of the droplet to the contact line over the evaporation time. The second length scale is related the distribution of GO flakes in solution, denoted as d_{GO}, which indicates the mean distance between two adjacent GO flakes in the droplet. Generally, if the contact line is pinned, there will be an outward radial transport of GO driven by the radial capillary flow, as shown in Figure 4.10. However, if the diffusion length is larger than the mean distance, the adjacent GO flakes will impact to each other, which facilitates the possibility of flocculation through stacking of the flakes, pinning the contact line to form the coffee ring structure. To quantify the competition between these two length scales, a dimensionless number, C_L, is defined as

$$C_L = \frac{d_{transp}}{d_{GO}} \tag{4.9}$$

When $C_L < 1$, the GO flakes are separated too great a distance for transport, and the flakes will be deposited at their initial distribution. Whereas, when $C_L > 1$, the GO flakes can interact and are more likely to stack, accelerating the formation of a coffee ring.

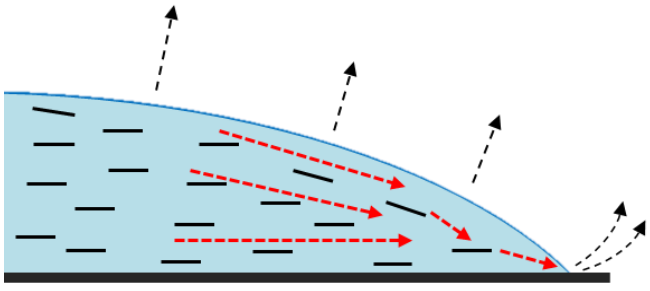

Figure 4.10. A schematic diagram showing the movement of GO flakes during droplet drying.

To understanding the formation of a coffee ring using the parameter C_L, it is necessary to indicate both d_{transp} and d_{GO} by using the parameters of the GO ink droplet and the evaporation conditions. It is assumed that the GO sheets are homogeneously distributed

in the droplet, so that the mean distance between two adjacent GO sheets in the ink droplet can be calculated as

$$d_{GO}=\sqrt[3]{V_d/N} \tag{4.10}$$

where V_d is the volume of the droplet and N is the number of GO sheets within the droplet.

For a sessile drop, it is assumed that all of individual GO flakes have the same parameters of density and thickness, hence the relationship between V_d and N can be expressed as

$$C_{GO}V_d = N\rho_{GO}h\pi\left(\frac{L}{2}\right)^2 \tag{4.11}$$

where C_{GO} is the concentration of GO in the inks, ρ_{GO} is the density of GO flakes, and h is the thickness of the GO sheets. Thus Equation 4.9 can be rewritten as

$$d_{GO}=\left(\frac{\rho_{GO}h\pi L^2}{4\,C_{GO}}\right)^{1/3} \tag{4.12}$$

According to the Einstein diffusion equation, the mean transport length of GO flakes over the evaporation time can be expressed as [18]

$$d_{transp}=\left(2D_{GO}t_{transp}\right)^{1/2} \tag{4.13}$$

where D_{GO} is the diffusion coefficient of GO sheets, given by the modified Stokes-Einstein law used for the diffusion of plates and rods in suspension [44, 45]

$$D_{GO} = \frac{k_B(273.16+T)(lnP+C_t)}{3\pi\eta L} \tag{4.14a}$$

$$C_t=0.312+0.565/P-0.100/P^2 \tag{4.14b}$$

$$\eta =2.414\times10^{-5}\times10^{247.8/(T+133.16)} \tag{4.14c}$$

k_B is the Boltzmann constant, η is the viscosity of the solvent, and P is the aspect ratio of GO sheets given by L/h. The t_{transp} in Equation 4.13 is the transport time of GO flakes during the drying process. For GO flakes near the initial contact line, the value of t_{transp} is equal to t_{dep}, while for GO flakes near the centre of drop, the value of t_{transp} is approximately equal to t_{evap}. According to previous experimental observations,[18] if the adjacent GO flake cannot be stacked before the evaporation time reaches t_{dep}, the

contact line of the drop starts to recede and move the GO flakes inward. Therefore, the time required for the coffee ring to form depends on t_{dep}. By combining Equation 4.9, 4.12, and 4.13, Equation 4.9 can be expressed as

$$C_L = \sqrt{\frac{A\pi\rho_L\theta_0 D^2}{32D_V(c_0-c_\infty)}}\frac{\sqrt{D_{GO}}}{d_{GO}} \tag{4.15}$$

Here, A is a characteristic coefficient representing the value of t_{dep}/t_{evap}. It can be seen from Equation 4.15 that, excepting the intrinsic parameter of the solvent (e.g., vapour pressure and molar mass) and GO flakes (e.g., density and thickness), the value of C_L is influenced by serval parameters, including drop contact angle, drop spherical cap diameter, substrate temperature, ink concentration, and mean flake size of the GO.

4.3.4 Flake Size and Temperature Dependency in the CRE of Droplets

In order to investigate the influence of GO flake size to the coffee ring effect, GO inks with different values of mean flake size (GO-0: 35.9±23.2, GO-1: 24.1±16.6, GO-2: 10.3±9.6, GO-3: 5.97±5.24, GO-4: 3.68±3.78, GO-5: 2.32±1.54, GO-6: 1.58±0.93, and GO-7: 0.68±0.31 μm) were inkjet-printed onto UV-Ozone treated Si/SiO_2 substrates. All the GO inks were deposited using a printing nozzle with diameter 60 μm and the temperature of the substrate was set to 30 °C. It was expected that the size of particles in an ink should be less than 1/20 of the nozzle diameter to avoid nozzle clogging during printing. However, no clogging problems were observed even for printing of GO-0 ink, which has mean size of 35.9±23.2 μm with large size up to 200 μm. This remarkable printing property of GO inks is down to the unique property of GO sheets, which can be aligned and folded by the capillary force in the nozzle tube. More details have been discussed in chapter 3.

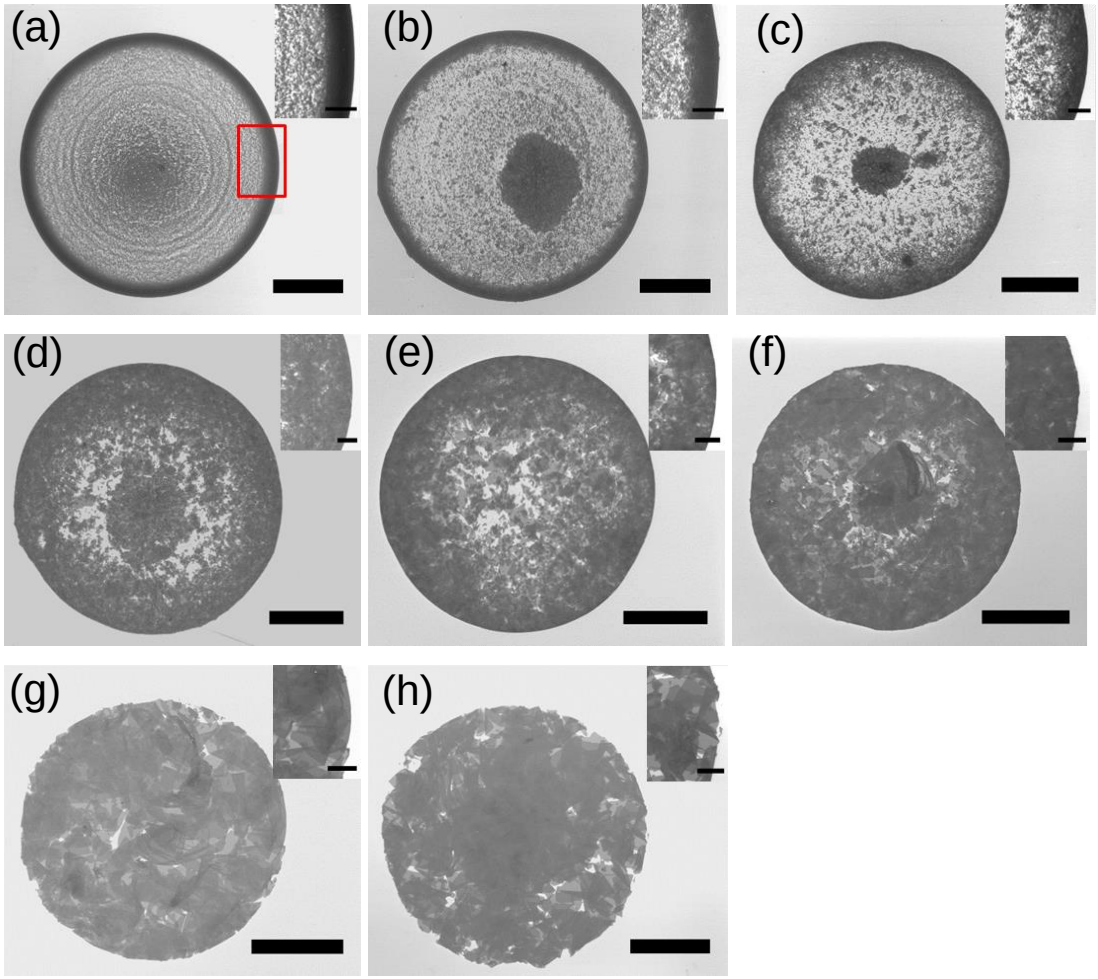

Figure 4.11. SEM images of printed GO droplets on Si/SiO_2 substrates after water evaporation at 30 °C prepared from GO inks with different flake size: (a) GO-7: 0.68±0.31, (b) GO-6: 1.58±0.93, (c) GO-5: 2.32±1.54, (d) GO-4: 3.68±3.78, (e) GO-3: 5.97±5.24, (f) GO-2: 10.3±9.6, (g) GO-1: 24.1±16.6, and (h) GO-0: 35.9±23.2 µm. All scale bars are 100 µm. Inset show the magnified SEM images collected at the edge of the droplets (red rectangle area). All scale bars are 20 µm.

Figure 4.11 shows the SEM images of printed GO droplets on Si/SiO_2 substrates after drying prepared from inks with different GO mean flake size. Droplets of GO inks containing the smallest flake size (GO-7: 0.68 ± 0.31 µm), as shown in Figure 4.11a, leave a clear ring-like dried deposit on the substrate after evaporation. The magnified image (inset image in Figure 4.11a) shows that most of the GO flakes have segregated to the edge of the ring, close to the maximum spread contact line, indicating an outward radial movement of GO flakes during drying. Inside the pronounced outer coffee ring there are a series of faint concentric subsidiary rings that track the final stages of liquid evaporation. As the mean GO flake size in the ink increases, the inner limit of the coffee

ring moves gradually towards the centre of the drying drop and the region towards the drop centre becomes less depleted in GO flakes (Figure 4.9b-h). When the GO had a mean flake size of 10.3±9.6 µm (Figure 4.11f) there is almost complete uniform coverage of GO sheets after drying and this is seen with all inks of larger mean GO flake size. We define the distance between the inner and outer radius of the coffee ring as the ring width (*w*). Figure 4.12 shows a plot of the ring width normalised by the drop spread radius, *R*, as a function of GO flake size. It can be seen that the *w/R* value for droplets with flake size smaller than 1.58 µm is constant at about 0.1 and for a flake size > 10 µm *w/R* is constant at 1, indicating and absence of the CRE. Between these two limits there is a transition region where the CRE reduces in intensity before being eliminated.

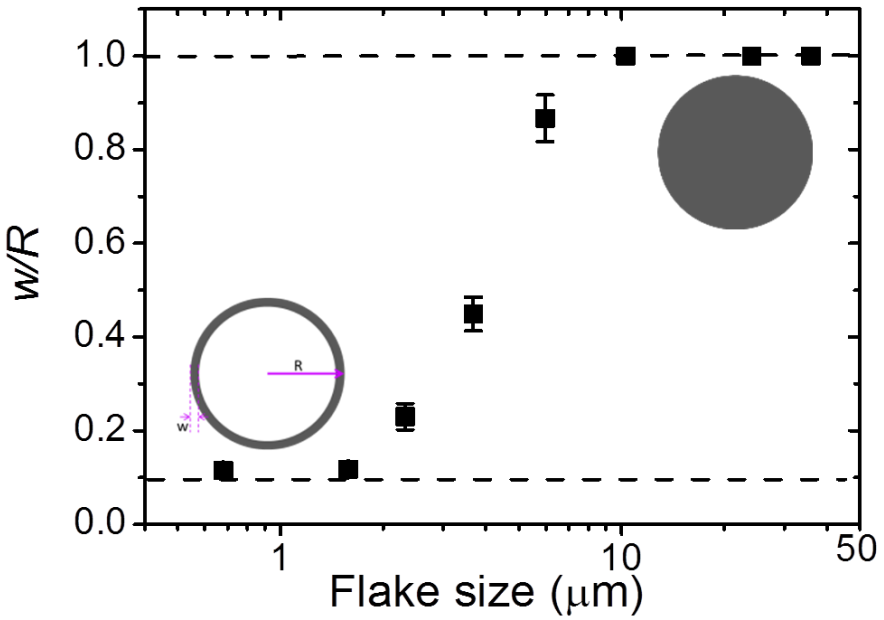

Figure 4.12. Width of the ring (*w*) normalized by the droplets radius (*R*) as a function of the lateral size of GO flakes at 30 °C. Insert shows the schematic illustration of a "coffee ring" like and a disk-like droplet.

In order to investigate the critical flake size, L_C, defined as the smallest mean flake size to achieve *w/R* = 1.0, it is necessary to understand the relationship between the mean flake size *L* and C_L. The drying droplets were inkjet-printed using identical jetting parameters and environmental condition (~ 50% relative humidity). The mean spread diameter of the printed droplets presented in Figure 4.11 is 338±24 µm. Note that the diameter of droplets made using inks with large GO flakes are smaller than the droplets containing small flakes. This can be explained by the higher viscosity and smaller

volume of fluid ejected from nozzle with large flakes (Figure 3.16). The measured results showed that all the GO inks have similar contact angle at around 10°.

Figure 4.13 shows the dependence of C_L with the mean lateral size of GO flakes calculated from Equation 4.15. The data and constant values that used to compute C_L are shown in Table 4.2, note that the C_L reduces with increasing in GO flake size. The computed L_C (C_L=1) is about 2.25 µm. Comparing with the experiment observation, it shows the droplet with GO flake size < 2.25 µm showed a strong coffee ring. However, for droplets with mean flake size at 5.97±5.24 (ink GO-3) and 3.68±3.78 (ink GO-4) µm, droplets with a partially formed coffee ring have been observed. This difference can be explained by the non-uniform size distribution of GO flakes disrupted by the sonication process, which ink GO-3 and ink GO-4 have a size fraction of 30.7% and 13.4% less than 2.2 µm, respectively, as shown in Figure 4.2.

Table 4.2. Physical constants and data used to compute C_L from Equation 4.15.

Symbol	Physical Parameter	Value	Unit & Specification
R_g	Ideal gas constant	8.3144	J mol^{-1} K^{-1}
P	Pressure	101.3×10^{3}	Pa
M_w	Molar mass of water	18.0152	g mol^{-1}
k_B	Boltzmann constant	1.380×10^{-23}	J K^{-1}
D	Drop diameter	3.38×10^{-4}	m
θ_0	Contact angle of droplets	10	°
RH	Relative humidity	50%	-
C_{GO}	Concentration of GO ink	0.5	g L^{-1}
h	Thickness of GO flakes	1×10^{-9}	m
ρ_{GO}	Density of GO	2.2×10^{3}	kg m^{-3}
A	t_{dep}/t_{evap}	0.69	-

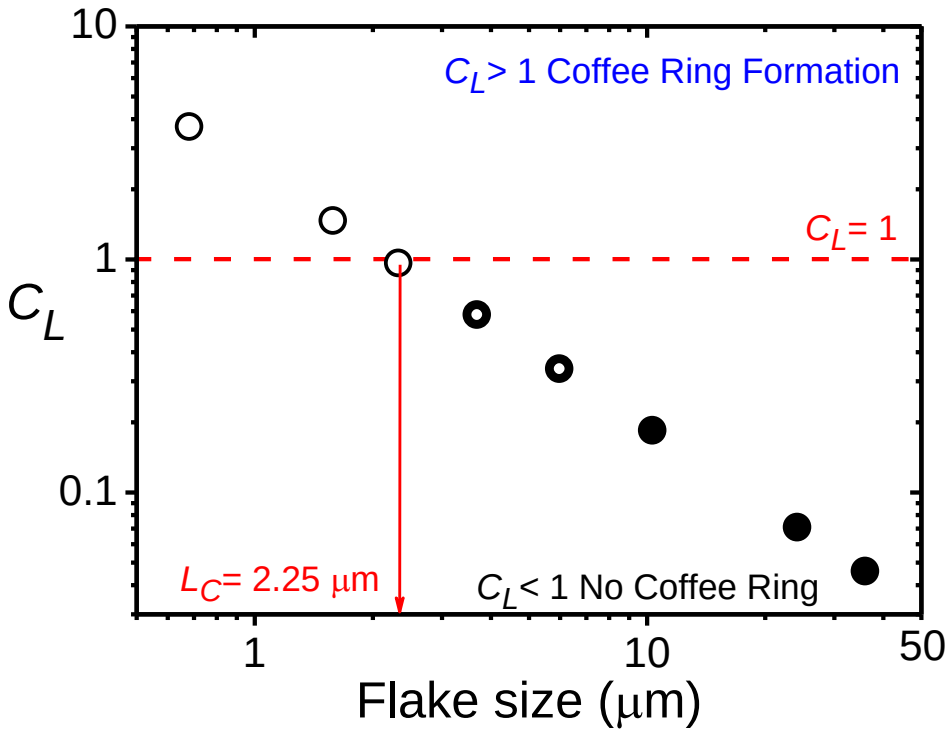

Figure 4.13. The dependence of C_L with the mean GO flake size. The red dotted line demonstrates when C_L =1 ($d_{transp} = d_{GO}$). When C_L > 1, the d_{transp} is larger than the d_{GO}, a coffee ring structure is formed by the stacking of GO flakes. Whereas C_L < 1, the transport length of GO flakes have insufficient distance to impact, and the flakes will deposit on the surface near to initial distribution.

To further investigate the influence of temperature to the final shape of drying drop, the GO inks were inkjet-printed on the substrates with temperature in the range of 20-60 °C. Figure 4.14 shows SEM image maps for the drying droplets with increasing substrate temperature and GO flake size. It is noticed that the shape of the droplets becomes more uniform with increasing substrate temperature for all sizes of the GO flakes. This is believed to be caused by the reduced time for graphene flake transport that results from the increased solvent evaporation rate with increasing temperature. Thus the reduced transport distance will decrease the possibility of GO flake stacking during evaporation with a consequent reduction in any coffee ring. Although GO inks with flake size of 10.3, 5.97, and 3.68 μm show a coffee ring after drying at 20 °C, the width of the ring increases as the drying temperature increased to 30, 40, and 50 °C, respectively. However, when the GO flake size is 2.32 μm or smaller the coffee ring effect is observed at all temperatures up to 60 °C.

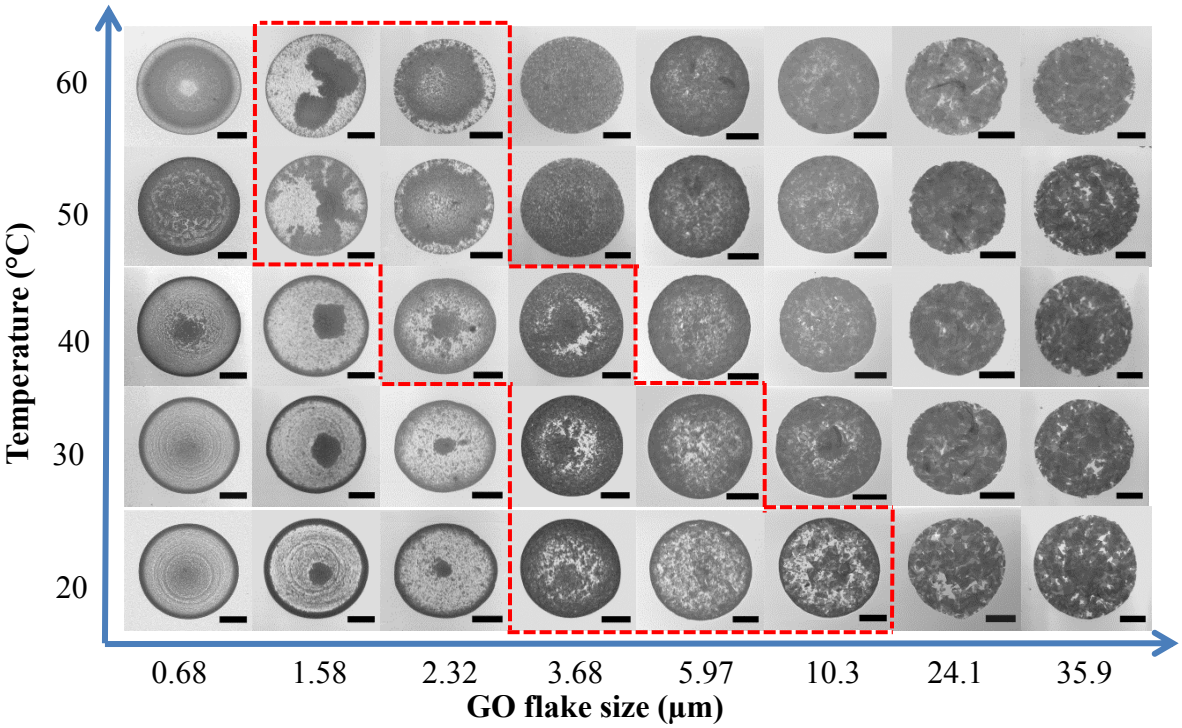

Figure 4.14. SEM image maps for printed droplets in rows with increasing substrate temperature and in columns from left to right with increasing mean GO flake size. The dotted block area indicates the droplets with partly coffee ring. All scale bars are 100 µm.

The onset of coffee ring formation was further controlled by the substrate temperature and the GO flake size, as shown in Figure 4.15. If we assumed the other drying condition (e.g., contact angle and relative humidity) and drop diameter are the same for all droplets studied, then the value of the mean flake size that leads to C_L =1 (the onset of coffee ring formation) as a function of temperature can be calculated using Equation 4.15. The locus of the predicted critical GO flake size that defines the coffee ring transition as a function of temperature is plotted on Figure 4.15 (red line), superimposed on the experimental data from Figure 4.14. At high temperature there is a good correspondence between the predicted onset of coffee ring formation and experimental observation but at lower temperature the model diverges. This may be explained by the smaller spread drop size of the GO inks at larger aspect ratios, which leads to a dependence of the contact angle on flake size, an effect that is not captured in Equation 4.15.

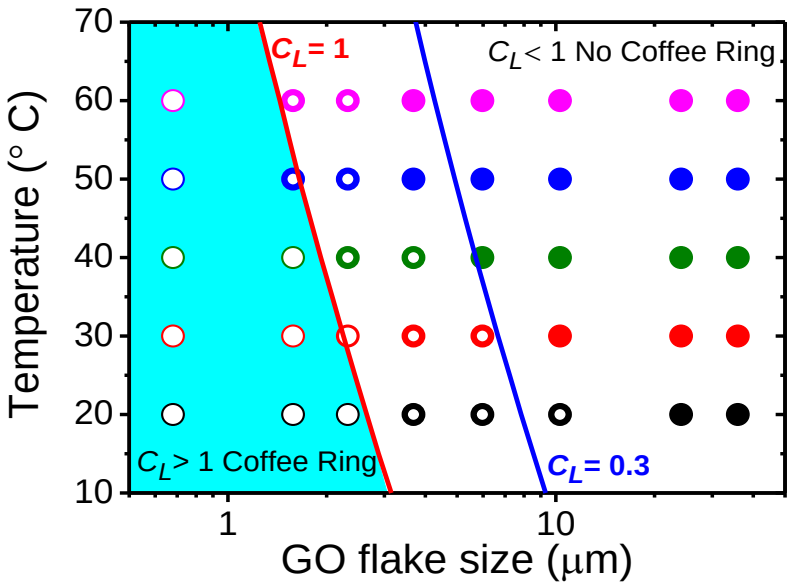

Figure 4.15. Shape map of drying droplets defined by the substrate temperature and the mean flake size. The red line indicates the onset of coffee ring formation (C_L =1) at different temperature. The cyan area is the calculated distribution area with coffee ring. The blue line represents the onset of C_L =0.3. The open circles indicate that a coffee ring was observed (C_L > 1 = Equation 4.15) after drying the droplets, the half open circles indicate partly coffee ring structure, and the solid circles indicate the absence of a coffee ring (C_L<1).

4.3.5 Drop Size Dependency for Coffee-Ring Effect in Printed Droplets

In order to investigate the effect of drop size on the morphology of dried GO droplets, printer heads with nozzle diameters of of 21 (Dimatix DMP 2800 inkjet printer with a 10 pL cartridge), 30, and 60 µm (MPP 1000 Printer with Microfab 30 and 60 mm nozzles respectively) were selected. The droplets were deposited on UV-treated Si/SiO_2 substrates at 30 °C. Four GO inks with mean flake size of 0.68, 1.58, 2.32, and 3.68 µm were used.

As shown in Figure 4.16, the coffee ring becomes weaker with decreasing droplet size for all inks with each of the inks with different mean GO flake size. For flake size of 0.68 µm (left column), Droplets with spread diameter of ~370 and 170 µm (generated by 60 and 30 µm nozzles respectively) show a well defined ring structure after drying, whereas when the drop size decreases to 70 µm (ejected from the 21 µm nozzle), the ring structure becomes weak. Further reducing the drop size to 35 µm results in only a weak ring developing. The ring factor value of *w/R* for droplets with diameter of about 370, 170, 70, and 35 µm are 0.106, 0.086, 0.073 and 0.068, respectively. On increasing

the GO flake size to 1.58 µm (middle left column in Figure 4.16) coffee ring effect is retained with the 358, 185, and 78 µm diameter drops, however a uniform distribution of GO flakes was observed for the 30 µm drop. Further increasing flake size to 2.32 µm (middle right column) shows a coffee ring effect for all droplets, but it is weaker than with the mall flake size inks. Finally, for inks with a flake size of 3.68 µm, a uniform structure was observed at a spread drop size of 75 µm. Note that because the concentration of GO in the ink is only 0.5 mg/ml (0.23% in volume fraction), the shape of dried droplet cannot be fully covered by GO flakes after drying even for a uniformly distributed pattern. Moreover, for droplets with similar size, ejecting from the same nozzle, increasing the flake size shows a weakening in the CRE, which represents the same trend as seen with previous results.

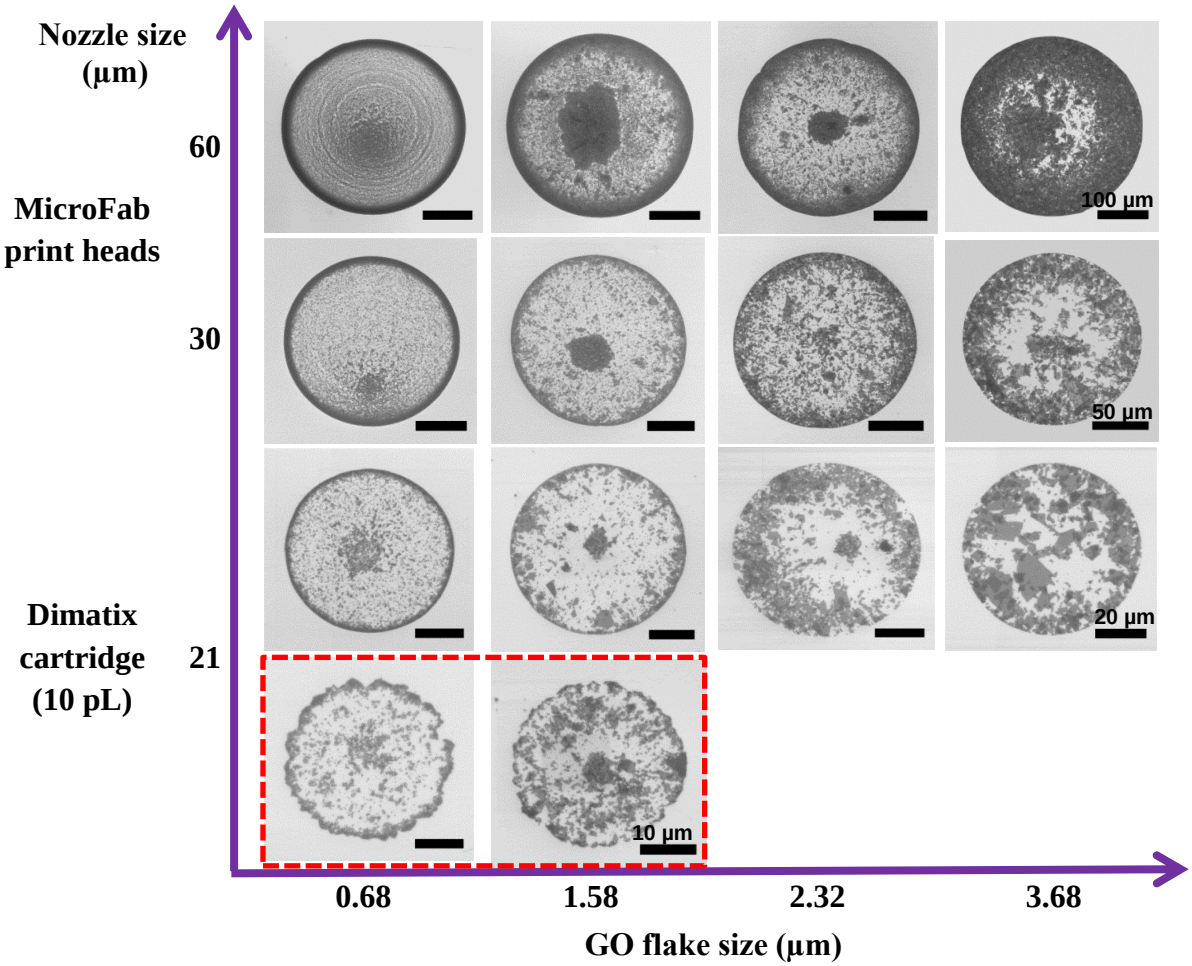

Figure 4.16. SEM image maps for printed droplets with different drop size. The ordinate represents the diameter of printer nozzles which manufactured from Microfab (30 and 60 µm) and Dimatix (10 pL cartridge, 21 µm). The abscissa indicates the mean flake size of GO inks used for droplets. Red dashed box shows the small droplets (~ 30 µm) generated form modified wavelength of voltage during printing.

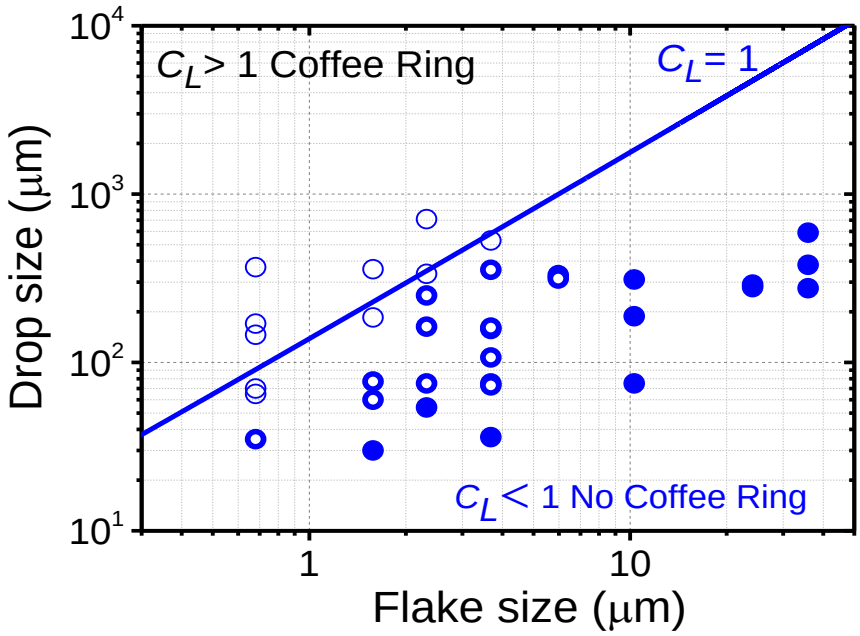

Figure 4.17. Plot of drying droplets defined by the mean flake size and the diameter of sphere cap droplets. The blue line indicates the drop diameter as a function of the flake size at C_L=1. It assumed the contact angle for all droplets is 10°, the substrate temperature is set to 30 °C, and the relative humidity is constant at 50% during printing process. The open circles indicate the coffee ring effect (C_L > 1) for the drying droplets observed in experiments, the half open circles indicate partly coffee ring structure, and the solid circles indicate the drying droplets without coffee ring effect (C_L < 1).

Figure 4.17 summarizes the experimental results for printed droplets with different drop diameter and GO flake size. It is clear that the value of C_L=1 separates to coffee ring and non-coffee ring data reasonably consistently. However, some droplets that show the CRE or a partly CRE are located in the non-coffee ring area as defined by C_L. This may be explained by the difference between calculated value and experiment value of environmental conditions during printing process, such as environmental humidity, and the non-uniform size distribution of GO flakes generated by sonication process.

4.4 Conclusions

In this chapter, we have shown that the CRE of GO droplets can be controlled by the size of GO flakes, the substrate temperature, and the drop size. Under the conditions of this study, we observed a critical length related to GO flake size, *Lc*, for well-controlled coffee ring formation. The CRE is observed when the mean flake size is below the critical value. This critical length can be estimated by the competition between two length scales that relate to the diffusion of GO flakes during the evaporation process and

the distribution of GO flakes within the droplet. The boundary condition for coffee ring formation can be defined by a dimensionless value, C_L. When $C_L > 1$, a coffee ring structure is formed by the stacking of GO flakes, whereas $C_L < 1$, the flakes will deposit on the surface near to initial distribution and a uniform morphology occurs. Our experimental results show that with printed drops of diameter around 340 µm, the CRE is suppressed when the GO flake size larger than 10.3 µm. Moreover, it was observed that the CRE weakens when the drop size decreases. The critical drop size, which indicates the smallest drop size for coffee ring formation, increased with increasing GO flake size. All these findings can serve as a guideline to understand the flake transportation behaviour of 2D flakes within printed droplets.

References

1. Deegan, R.D., Bakajin, O., Dupont, T.F., Huber, G., Nagel, S.R., and Witten, T.A., Capillary flow as the cause of ring stains from dried liquid drops. *Nature*, 1997. **389**(6653): p. 827-829.

2. Yunker, P.J., Still, T., Lohr, M.A., and Yodh, A.G., Suppression of the coffee-ring effect by shape-dependent capillary interactions. *Nature*, 2011. **476**(7360): p. 308-311.

3. Fischer, B.J., Particle convection in an evaporating colloidal droplet. *Langmuir*, 2002. **18**(1): p. 60-67.

4. Hu, H. and Larson, R.G., Evaporation of a sessile droplet on a substrate. *Journal of Physical Chemistry B*, 2002. **106**(6): p. 1334-1344.

5. Hu, H. and Larson, R.G., Analysis of the microfluid flow in an evaporating sessile droplet. *Langmuir*, 2005. **21**(9): p. 3963-3971.

6. Hu, H. and Larson, R.G., Marangoni effect reverses coffee-ring depositions. *Journal of Physical Chemistry B*, 2006. **110**(14): p. 7090-7094.

7. Soltman, D. and Subramanian, V., Inkjet-printed line morphologies and temperature control of the coffee ring effect. *Langmuir*, 2008. **24**(5): p. 2224-2231.

8. Dugyala, V.R. and Basavaraj, M.G., Control over Coffee-Ring Formation in Evaporating Liquid Drops Containing Ellipsoids. *Langmuir*, 2014. **30**(29): p. 8680-8686.

9. Lim, J.A., Lee, W.H., Lee, H.S., Lee, J.H., Park, Y.D., and Cho, K., Self-organization of ink-jet-printed triisopropylsilylethynyl pentacene via evaporation-induced flows in a drying droplet. *Advanced Functional Materials*, 2008. **18**(2): p. 229-234.

10. Dou, R. and Derby, B., Formation of Coffee Stains on Porous Surfaces. *Langmuir*, 2012. **28**(12): p. 5331-5338.

11. Yan, Q., Gao, L., Sharma, V., Chiang, Y.M., and Wong, C.C., Particle and Substrate Charge Effects on Colloidal Self-Assembly in a Sessile Drop. *Langmuir*, 2008. **24**(20): p. 11518-11522.

12. Park, J. and Moon, J., Control of colloidal particle deposit patterns within picoliter droplets ejected by ink-jet printing. *Langmuir*, 2006. **22**(8): p. 3506-3513.

13. Pirrung, M.C., How to make a DNA chip. *Angewandte Chemie-International Edition*, 2002. **41**(8): p. 1277-1289.

14. Bigioni, T.P., Lin, X.M., Nguyen, T.T., Corwin, E.I., Witten, T.A., and Jaeger, H.M., Kinetically driven self assembly of highly ordered nanoparticle monolayers. *Nature Materials*, 2006. **5**(4): p. 265-270.

15. Wen, J.T., Ho, C.M., and Lillehoj, P.B., Coffee Ring Aptasensor for Rapid Protein Detection. *Langmuir*, 2013. **29**(26): p. 8440-8446.

16. Cai, Y. and Newby, B.M.Z., Marangoni flow-induced self-assembly of hexagonal and stripelike nanoparticle patterns. *Journal of the American Chemical Society*, 2008. **130**(19): p. 6076-6077.

17. Fukuda, K., Sekine, T., Kumaki, D., and Tokito, S., Profile Control of Inkjet Printed Silver Electrodes and Their Application to Organic Transistors. *Acs Applied Materials & Interfaces*, 2013. **5**(9): p. 3916-3920.

18. Shen, X.Y., Ho, C.M., and Wong, T.S., Minimal Size of Coffee Ring Structure. *Journal of Physical Chemistry B*, 2010. **114**(16): p. 5269-5274.

19. Anyfantakis, M. and Baigl, D., Dynamic photocontrol of the coffee-ring effect with optically tunable particle stickiness. *Angewandte Chemie International Edition*, 2014. **53**(51): p. 1-6.

20. Talbot, E.L., Yang, L.S., Berson, A., and Bain, C.D., Control of the Particle Distribution in Inkjet Printing through an Evaporation-Driven Sol-Gel Transition. *ACS Applied Materials & Interfaces*, 2014. **6**(12): p. 9572-9583.

21. Talbot, E.L., Yow, H.N., Yang, L., Berson, A., Biggs, S.R., and Bain, C.D., Printing small dots from large drops. *ACS Appl Mater Interfaces*, 2015. **7**(6): p. 3782-90.

22. Cui, L.Y., Zhang, J.H., Zhang, X.M., Huang, L., Wang, Z.H., Li, Y.F., Gao, H.N., Zhu, S.J., Wang, T.Q., and Yang, B., Suppression of the Coffee Ring Effect by Hydrosoluble Polymer Additives. *ACS Applied Materials & Interfaces*, 2012. **4**(5): p. 2775-2780.

23. Still, T., Yunker, P.J., and Yodh, A.G., Surfactant-Induced Marangoni Eddies Alter the Coffee-Rings of Evaporating Colloidal Drops. *Langmuir*, 2012. **28**(11): p. 4984-4988.

24. Dugyala, V.R. and Basavaraj, M.G., Evaporation of Sessile Drops Containing Colloidal Rods: Coffee-Ring and Order-Disorder Transition. *Journal of Physical Chemistry B*, 2015. **119**(9): p. 3860-3867.

25. Wang, T.M., Roberts, M.A., Kinloch, I.A., and Derby, B., Inkjet printed carbon nanotube networks: the influence of drop spacing and drying on electrical properties. *Journal of Physics D-Applied Physics*, 2012. **45**(31): p. 315304.

26. Zhuang, X., Mai, Y., Wu, D., Zhang, F., and Feng, X., Two-dimensional soft nanomaterials: a fascinating world of materials. *Advanced Materials*, 2015. **27**(3): p. 403-27.

27. Novoselov, K.S., Geim, A.K., Morozov, S.V., Jiang, D., Zhang, Y., Dubonos, S.V., Grigorieva, I.V., and Firsov, A.A., Electric field effect in atomically thin carbon films. *Science*, 2004. **306**(5696): p. 666-669.

28. Zheng, Q., Li, Z., Yang, J., and Kim, J.-K., Graphene oxide-based transparent conductive films. *Progress in Materials Science*, 2014. **64**(0): p. 200-247.

29. Lotya, M., Hernandez, Y., King, P.J., Smith, R.J., Nicolosi, V., Karlsson, L.S., Blighe, F.M., De, S., Wang, Z.M., McGovern, I.T., Duesberg, G.S., and Coleman, J.N., Liquid Phase Production of Graphene by Exfoliation of Graphite in Surfactant/Water Solutions. *Journal of the American Chemical Society*, 2009. **131**(10): p. 3611-3620.

30. Eda, G. and Chhowalla, M., Chemically Derived Graphene Oxide: Towards Large-Area Thin-Film Electronics and Optoelectronics. *Advanced Materials*, 2010. **22**(22): p. 2392-2415.

31. Hernandez, Y., Nicolosi, V., Lotya, M., Blighe, F.M., Sun, Z.Y., De, S., McGovern, I.T., Holland, B., Byrne, M., Gun'ko, Y.K., Boland, J.J., Niraj, P., Duesberg, G., Krishnamurthy, S., Goodhue, R., Hutchison, J., Scardaci, V., Ferrari, A.C., and Coleman, J.N., High-yield production of graphene by liquid-phase exfoliation of graphite. *Nature Nanotechnology*, 2008. **3**(9): p. 563-568.

32. Paredes, J.I., Villar-Rodil, S., Martinez-Alonso, A., and Tascon, J.M.D., Graphene oxide dispersions in organic solvents. *Langmuir*, 2008. **24**(19): p. 10560-10564.

33. Torrisi, F., Hasan, T., Wu, W.P., Sun, Z.P., Lombardo, A., Kulmala, T.S., Hsieh, G.W., Jung, S.J., Bonaccorso, F., Paul, P.J., Chu, D.P., and Ferrari, A.C., Inkjet-Printed Graphene Electronics. *ACS Nano*, 2012. **6**(4): p. 2992-3006.

34. Li, J., Ye, F., Vaziri, S., Muhammed, M., Lemme, M.C., and Ostling, M., Efficient inkjet printing of graphene. *Advanced Materials*, 2013. **25**(29): p. 3985-3992.

35. Lim, S., Kang, B., Kwak, D., Lee, W.H., Lim, J.A., and Cho, K., Inkjet-Printed Reduced Graphene Oxide/Poly(Vinyl Alcohol) Composite Electrodes for Flexible Transparent Organic Field-Effect Transistors. *Journal of Physical Chemistry C*, 2012. **116**(13): p. 7520-7525.

36. Su, Y., Du, J., Sun, D., Liu, C., and Cheng, H., Reduced graphene oxide with a highly restored π-conjugated structure for inkjet printing and its use in all-carbon transistors. *Nano Research*, 2013. **6**(11): p. 842-852.

37. Eom, D.S., Chang, J., Song, Y.W., Lim, J.A., Han, J.T., Kim, H., and Cho, K., Coffee-Ring Structure from Dried Graphene Derivative Solutions: A Facile One-Step Fabrication Route for All Graphene-Based Transistors. *Journal of Physical Chemistry C*, 2014. **118**(46): p. 27081-27090.

38. Rogala, M., Wlasny, I., Dabrowski, P., Kowalczyk, P.J., Busiakiewicz, A., Kozlowski, W., Lipinska, L., Jagiello, J., Aksienionek, M., Strupinski, W., Krajewska, A., Sieradzki, Z., Krucinska, I., Puchalski, M., Skrzetuska, E., and Klusek, Z., Graphene oxide overprints for flexible and transparent electronics. *Applied Physics Letters*, 2015. **106**(4): p. 041901.

39. Dimiev, A., Kosynkin, D.V., Alemany, L.B., Chaguine, P., and Tour, J.M., Pristine graphite oxide. *Journal of the American Chemical Society*, 2012. **134**(5): p. 2815-2822.

40. Han, J.T., Jang, J.I., Kim, H., Hwang, J.Y., Yoo, H.K., Woo, J.S., Choi, S., Kim, H.Y., Jeong, H.J., Jeong, S.Y., Baeg, K.J., Cho, K., and Lee, G.W., Extremely efficient liquid exfoliation and dispersion of layered materials by unusual acoustic cavitation. *Scientific Reports*, 2014. **4**: p. 5133.

41. Popov, Y.O., Evaporative deposition patterns: Spatial dimensions of the deposit. *Physical Review E*, 2005. **71**(3): p. 036313.

42. Stringer, J. and Derby, B., Formation and Stability of Lines Produced by Inkjet Printing. *Langmuir*, 2010. **26**(12): p. 10365-10372.

43. Gorr, H.M., Zueger, J.M., and Barnard, J.A., Characteristic Size for Onset of Coffee-Ring Effect in Evaporating Lysozyme-Water Solution Droplets. *Journal of Physical Chemistry B*, 2012. **116**(40): p. 12213-12220.

44. Cassagnau, P., Linear viscoelasticity and dynamics of suspensions and molten polymers filled with nanoparticles of different aspect ratios. *Polymer*, 2013. **54**(18): p. 4762-4775.

45. Ortega, A. and de la Torre, J.G., Hydrodynamic properties of rodlike and disklike particles in dilute solution. *Journal of Chemical Physics*, 2003. **119**(18): p. 9914-9919.

Chapter 5 Response, Degradation and Recovery of Few Layer Black Phosphorus Devices in Humid Atmospheres*

Abstract

This chapter investigates the interaction between black phosphorus (BP) nanometre thickness flakes and humid atmospheres using an inkjet printed sensor. This is highly responsive to changes in humidity with a response time of a few seconds and the effect is reproducible. Impedance spectroscopy shows a three orders of magnitude change in both resistance and capacitance of an equivalent circuit as a function of relative humidity (RH) in the range from 11% -> 95%. Long term exposure to humid air (RH > 11%) leads to a significant chemical change to the BP films, with Fourier transform infra-red spectroscopy (FTIR) indicating partial hydrolysis of the BP to form phosphate and phosphonate ions. However, exposure to dry air (RH < 4%) shows no significant change in the FTIR spectrum after 7 days exposure. X-Ray photoemission spectroscopy (XPS) results also show that exposure to low levels of humidity do not further oxidise BP. Low temperature heat treatment of BP films under dry conditions after exposure to elevated RH leads to a partial recovery of the impedance response and reversion to a chemical state similar to that before exposure to a humid environment. The recovery of BP properties is most complete after exposure to lower humidity environments (RH < 11%), although exact replication of the original impedance response and FTIR spectrum was not possible. Thus BP is rapidly degraded through oxidation by humid air but the oxidation process occurs at a much decreased rate in dry atmospheres.

---

*This chapter is based on a paper. Pei He, Jack R. Brent, Andrew G. Thomas, Christopher A. Muryn, David J. Lewis, Paul O'Brien and Brian Derby, 'Response, Degradation and Recovery of Few Layer Black Phosphorus Devices in Humid Atmospheres', in preparation. J.R.B. prepared BP inks and AFM image of BP flakes. P.H. performed the sensor device, device characterization and FTIR analysis. A.G.T. and C.A.M. performed the XPS analysis. B.D., P.H., D.J.L., and P.O.B. planned the experiments and wrote the paper.

5.1 **Introduction**

Since the discovery of the remarkable electric properties of one-atom thick two dimensional (2D) graphene,[1] a number of other2D materials have been isolated, including hexagonal boron nitride (h-BN) and several transition metal dichalcogenides (TMDC). These have a number of potential applications in electronics, sensing, and photovoltaic cells, due to their remarkable optoelectronic and structural properties. Recently, phosphorene, a new member of the 2D layered material family, has been isolated.[2, 3] Phosphorene is the 2D structural analogue of the layered black phosphorus (BP) structure. BP is an allotrope of phosphorus, first identified in 1914.[4] Unlike semi-metallic graphene, which has no appreciable bandgap in its pristine form, BP is a direct semiconductor whose band gap may be tuned in energy according to the thickness of the crystal, similar to the effect observed in (indirect band gap) few-layer MoS_2.[5] Bulk black phosphorus has a band gap of ~ 0.3 eV and monolayer phosphorene ~ 2.0 eV.[3, 6] In addition, the carrier mobility of few-layer BP can be up to 600 $cm^2V^{-1}s^{-1}$ at room temperature (increasing to 1000 $cm^2 \cdot V^{-1}s^{-1}$ at 120 K),[7] and there is considerable anisotropy of mobility within the *a-b* crystal plane.[3] In contrast, the n-type carrier mobility of MoS_2 is about 200 $cm^2V^{-1}s^{-1}$, with typically wide band gaps of ~ 2 eV.[8] Thus phosphorene has an intermediate carrier mobility and band gap between graphene and MoS_2. These desirable electronic properties make phosphorene and few-layered BP attractive semiconductors for high-performance electronics and optoelectronics applications.

Phosphorene or few-layer BP nanosheets, obtained by mechanical exfoliation, have been used to create a variety of useful electronic devices. Field-effect transistors (FETs) based on mechanically exfoliated few-layered BP display current on/off ratios in the range ~ 10^4 - 10^5 and carrier mobility up to ~ 200 – 1000 $cm^2V^{-1}s^{-1}$.[7, 9, 10]A number of devices have been fabricated from mechanically exfoliated BP including: radio frequency transistors,[11] gas sensors,[12] terahertz photodetectors,[13] and functional composite lasers.[14] Although few-layer BP shows outstanding electronic properties, mechanical exfoliation is inherently unscalable, and is generally used to demonstrate rather than enabling the production of 2D materials. Chemical vapour deposition (CVD) is a promising method for the thin film deposition 2D materials, but there has been little progress in the synthesis of mono- or few layer BP by CVD to date.

Another method used to obtain large quantities of 2D materials is by top-down processes based on liquid phase exfoliation (LPE) of the bulk layered crystals in appropriate solvents, where ultrasonic excitation is used to force the layered crystals apart to form monolayer and few-layer atomic crystals. The LPE method has been successfully used for producing of 2D materials including TMDCs (MoS_2, WS_2, $MoSe_2$, $MoTe_2$, $TaSe_2$, $NbSe_2$, $NiTe_2$), h-BN, bismuth telluride (Bi_2Te_3) and graphene.[15-18] We have recently demonstrated that liquid exfoliation of BP in *N*-methyl-2-pyrollidone (NMP) is a simple and facile route toward the production of few-layer phosphorene.[19] We have also shown that a similar method can be used to produce 2D SnS from the related herzenbergite structure.[20] Much smaller few layer BP quantum dots have also been produced through LPE with NMP.[21] Polar aprotic solvents such as dimethylformamide (DMF) and dimethyl sulfoxide (DMSO) have also been used to produce uniform and stable BP dispersions.[22] FETs based on solvent-exfoliated BP nanosheets exhibited ambipolar behaviour with current on/off ratios and mobility up to ~ 10^4 and ~ 50 $cm^2 V^{-1}s^{-1}$, respectively, which is comparable to mechanically exfoliated few-layer BP flakes.[23] Hence LPE provides a route for large area or flexible BP devices on appropriate substrates.

It has been reported that both mechanically cleaved and LPE derived few-layer BP nanosheets easily degrade to oxidized phosphorus compounds under ambient conditions, due to reactions between the BP nanosheets and water or oxygen in the atmosphere.[23-26] A similar reactivity had also been reported in earlier studies of bulk BP crystals.[27] For solvent exfoliated BP, this process accelerates when the BP flake thickness decreases,[28] with the degradation starting at the edges of the flakes and the aqueous medium becoming acidic over periods of time due to the formation of phosphate and phosphonate ions. However thicker BP nanosheets have been reported to show little degradation with time, suggesting that an oxidized overlayer could act as a barrier to protect nanosheets.[29] BP dispersions have also been observed to become acidic over periods of time stored in the open atmosphere due to the formation of phosphate and phosphonate ions.[28] However, the exact mechanism for the degradation of few-layer BP in the presence of water molecules or oxygen is still unclear. In particular the relationship between the mechanisms that lead to the high sensitivity of the electrical properties of BP nanosheets to water vapour,[29] and those that are reported to cause material degradation remain uninvestigated.

In this chapter, we demonstrate that BP can be exfoliated by ultrasonication in the volatile solvent acetonitrile (CH_3CN), to give few-layer BP nanosheets suspensions usable as an ink. We show that these can be directly inkjet-printed onto substrates to form continuous patterns and that such patterns can be combined with inkjet-printed silver nanoparticle electrodes to produce fully-printed BP devices. Inkjet printing provides an economical way to achieve additive patterning and direct writing of inks with potential scalability for large area deposition of materials.[30] The effective use of inkjet printing as a way to deploy 2D materials has already been demonstrated for graphene [31-34] and MoS_2.[34-36] The electrical performance of the printed BP device structures in the presence of controlled atmospheric humidity has been probed using impedance spectroscopy and the physical principles modelled by the use of equivalent circuits to describe the observed behaviour is discussed. The interpretation of these data is supported by a parallel study of the chemical changes in BP flakes using FTIR and XPS under near atmospheric pressure conditions.

5.2 Experimental Section

5.2.1 Few-Layer BP Ink Preparation and Characterization

BP powder was purchased from Smart Elements (Vienna, Austria). Acetonitrile was purchased from Sigma-Aldrich (Dorset, wood, UK) and degassed before use. Generally, BP (75 mg, 2.42 mmol) was added to acetonitrile (15 ml). The vial was sealed with parafilm© and ultrasonicated in an Elmasonic P 70H ultrasonic bath - 820 W across four horns (Elma Schmidbauer, Singen, Germany). The bath was operated at 37 kHz frequency and 30% power for 24 h. The reaction temperature was maintained below 30 °C throughout the reaction using a home-made water-cooling coil. Upon completion of the reaction the dispersions were centrifuged (822 series benchtop centrifuge, Centurion Scientific, Chichester, UK) at a rate of 1500 rpm (RCF ~ 180 g) for 45 min to remove unexfoliated material. The top 10 ml of the dispersions was removed for inkjet printing and further analysis. Samples for analysis by atomic force microscopy were prepared by spin-coating a small portion of the dispersion onto 300 nm Si/SiO_2 substrates at 6000 rpm.

5.2.2 Inkjet Printing

Silver electrode patterns were printed on glass substrates using a commercial Dimatix Material Printer (DMP 2800, Dimatix-Fujifilm Inc., Santa Clara, CA, USA) with a 10

pL cartridge (DMC-11610) loaded with a commercially silver nanoparticle ink. During the printing, the drop spacing was set to 30 μm and the temperature of substrate was set to 50 °C. The samples were then annealed on a hot plate at 150 °C for 30 minutes.

The BP films were printed by an in-house designed and built laboratory scale inkjet printing platform (MPP 1000). This comprises an *x-y* table with a positional accuracy of 3μm (Micromech Systems, Braintree, UK), equipped with a piezoelectric actuated inkjet print head of internal diameter 60 μm (MJ-ATP-01-60-8MX, Microfab Technologies Inc., Plano, TX, USA) with drive electronics (JetDrive III, Microfab) interfaced to a PC and controlled in a LabVIEW (National Instruments, Austin, TX, USA) environment. All samples were printed on the silver electrode pattern with a drop spacing 100 μm. The devices were then dried in a tubular furnace in a N_2 atmosphere (300 sccm), at 80 °C for 1 h.

5.2.3 **Characterization Methods**

The morphology of the BP nanosheets and films were characterized by scanning electron microscopy (SEM) (XL30 FEG-SEM, FEI, Eindhoven, Netherlands). Raman spectroscopy was conducted to analyse the crystalline structure of BP nanosheets using a 2000 Raman spectrometer system (Renishaw, Wooton-under-Edge, UK) with a HeNe laser (633 nm excitation). FTIR spectra of the BP film was recorded on a NICOLET 5700 FT-IR system (Thermo Fisher Scientific Inc., Waltham, MA, USA). We used drop casting of the BP ink to form a BP film on the NaCl crystal of the FTIR spectrometer. The UV-Vis absorbance of the BP inks was measured using a Lambda 25 UV-vis spectrophotometer in a quartz cuvette (Perkin Elmer, Waltham, MA, USA).

The inkjet-printed BP film was investigated using near-ambient pressure XPS (NAP-XPS) using a custom built Specs instrument. The sample is analysed using a SPECS Focus 500 monochromated- Al Kα source (photon energy 1486.6 eV), and photoemitted electrons are detected using the SPECS 150 mm Phoibos 150 NAP analyser, fitted with a three-stage, differentially pumped electrostatic lens that allows working pressures up to 25 mbar and a 44° acceptance angle. The sample is placed in a specially built near ambient pressure cell and XPS spectra recorded in a normal emission geometry.[37] The sample was cooled to around 273 K during NAP-XPS measurements. Samples are referenced on the binding energy scale to the position of the Au $4f_{7/2}$ peaks of the substrate at 84 eV. Binding energies are quoted ±0.1 eV. Spectra were analysed and

peak fitting carried out using the CASA XPS software package. XPS spectra were recorded from the as presented sample in ultra-high vacuum (10^{-10} mbar, with the sample in 2 mbar water vapour (corresponding to ca 30 % relative humidity (RH) at the sample surface with the sample at 273 K), and again following evacuation of the NAP cell back to a pressure $< 1 \times 10^{-8}$ mbar.

5.2.4 **Sensor Measurements**

The moisture sensing properties were measured by exposing the BP devices to various relative humidity (RH) levels. To set up different RH environments, saturated aqueous of LiCl, CH_3COOK, $CaCl_2$, K_2CO_3, NaBr, $CuCl_2$, NaCl, KCl and K_2SO_4 were placed in airtight glass vessels at a temperature of 20 °C, which yielded atmospheres with RHs of 11%, 23%, 33%, 43%, 57%, 67%, 75%, 85%, and 97%.[38] The capacitance response of the BP sensors was measured using a Portable Electrochemical Interface & Impedance Analyser (Ivium Technologies B.V., Netherlands) over a frequency range of 10 Hz to 1 MHz with testing voltage of 0.5 V and temperature of 20 °C. The AC conductance measurements were carried out by a Frequency Response Analyzer LCR meter (PSM1735, Newtons4th Ltd, UK) at 100 Hz and 1 kHz with a bias voltage of 0.5V.

5.3 **Results and Discussions**

5.3.1 **Device Printing**

Liquid phase exfoliation in acetonitrile was used to produce copious quantities of BP nanosheets as a stable dispersion. Acetonitrile has been previously reported as suitable for dispersing graphene.[39] Acetonitrile is a suitable solvent for inkjet printing. It has a boiling point of 82 °C, hence allowing solvent removal at low temperatures after printing. NMP, by comparison, has a boiling point of 202 °C, which requires a high temperature (>150 °C) to successfully remove the solvent. Atomic force microscopy (AFM) measurements of the exfoliated BP flakes found a mean height of 8.5 nm and a mean flake diameter of 155 nm (Figure 5.1b). Previous studies have assumed a layer spacing of 0.9 nm for BP,[9, 22] which indicates a mean flake thickness of approximately 10 atomic layers. We note that although this is thicker than the reported mean flake thickness achievable through exfoliation in NMP, it is thinner than flakes produced by the exfoliation of BP in other solvents, e.g. dimethylformamide (DMF) and dimethyl sulfoxide (DMSO).[22] Figure 5.2a shows a stable dispersion of exfoliated BP in acetonitrile after centrifugation. Ink concentration was estimated using the optical

absorption (Figure 5.1a) coefficient at 465 nm (α = 1500 $Lg^{-1}m^{-1}$) [28] to be ~0.67 mg mL^{-1}. The BP ink was found to be stable for more than one week, without any visible sedimentation by visual inspection.

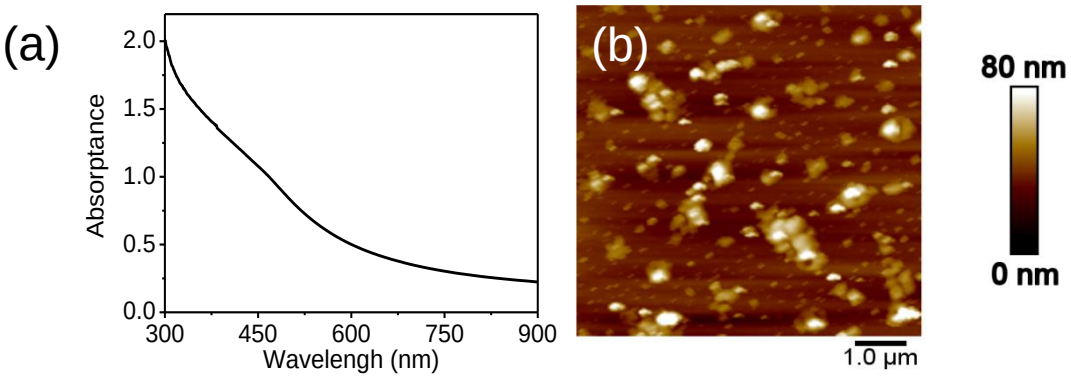

Figure 5.1. (a) Absorption of the BP ink in MeCN after 10 × dilution. (b) AFM image of few-layer BP flakes coated on Si/SiO_2 substrates. AFM data shows mean height = 8.5 nm, up to maximum of 100.8 nm. The average flake length is 155.1 nm from a minimum of 44.07 nm to maximum of 1146.0 nm (N = 239).

Figure 5.2b shows a representative Raman spectrum from a BP flake. Four Raman modes are observed at ~362, ~439, ~466, and ~520 cm^{-1}, which correspond to the A_g^1 (out-of-plane mode), B_{2g} and A_g^2 (in-plane modes) for BP and the TO mode for the silicon substrate, respectively.[23] The positions of these peaks are consistent with the signature Raman spectrum of crystalline BP nanosheets, indicating that the BP flakes are crystalline after solvent exfoliation.[25] SEM images (Figures 5.2c and d) show that the individual BP flakes range in diameter from tens of nm to about 1 µm both in the centre and the edge of a printed droplet. The device was fabricated by inkjet printing the BP ink onto an interdigitated pair of Ag electrodes previously deposited by inkjet printing (Figure 5.2e). SEM images of the printed BP film show that it is continuous (Figure 5.2f). The thickness of the BP film after 15 printing passes was determined to be approximately 640 ± 150 nm by AFM (Figure 5.3).

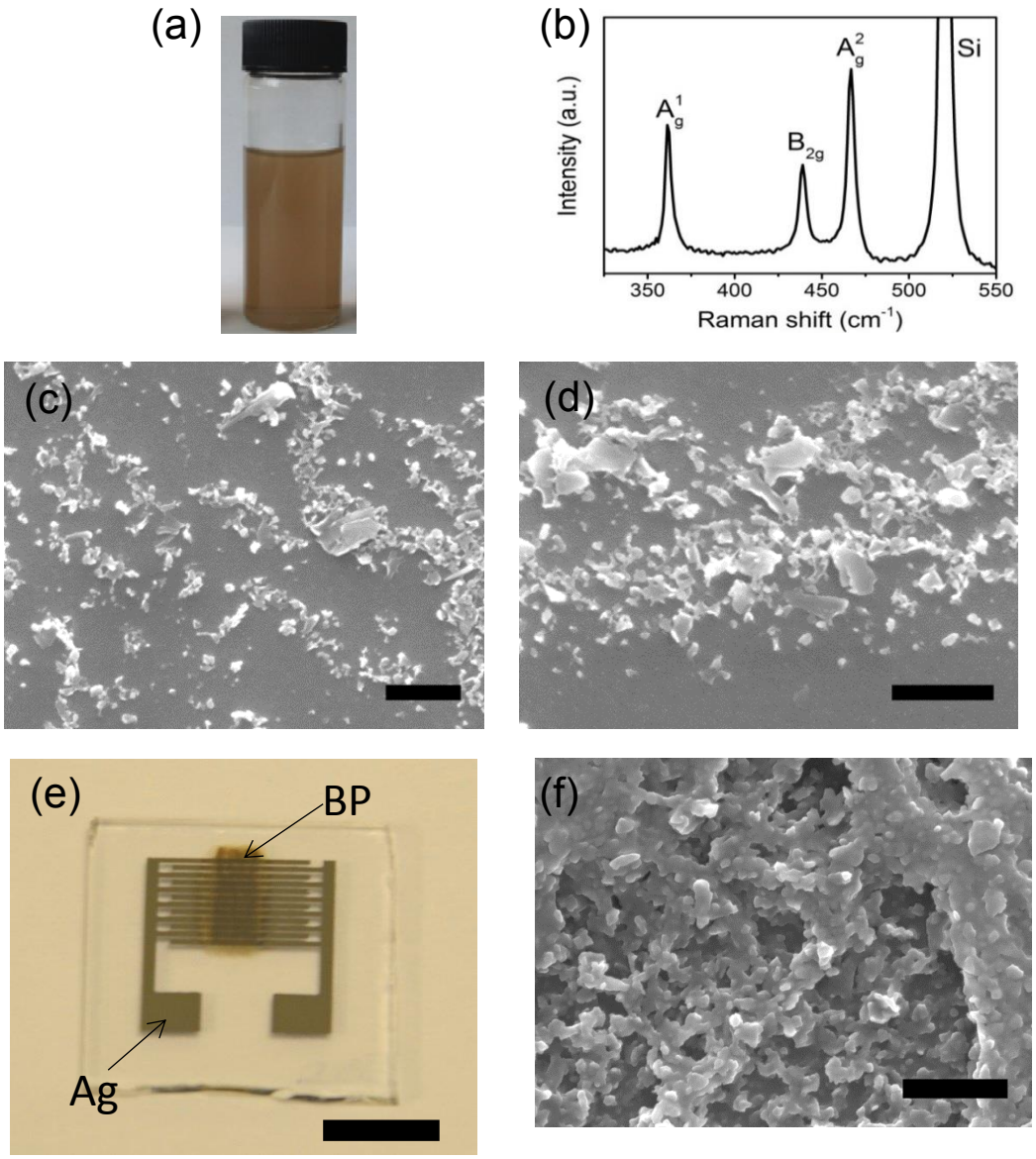

Figure 5.2. (a) Dispersion of exfoliated BP in acetonitrile. (b) Typical Raman spectrum obtained from the BP ink deposited on a 300 nm Si/SiO_2 substrate. (c) Magnified SEM image of the central area of the drop, scale bar 1 µm. (d) Magnified SEM image of the ring area of the drop, scale bar 1 µm. (e) Inkjet-printed BP device with silver electrodes on glass substrate, scale bar 0.5 cm. (f) SEM image of the printed BP film, scale bar 1 µm.

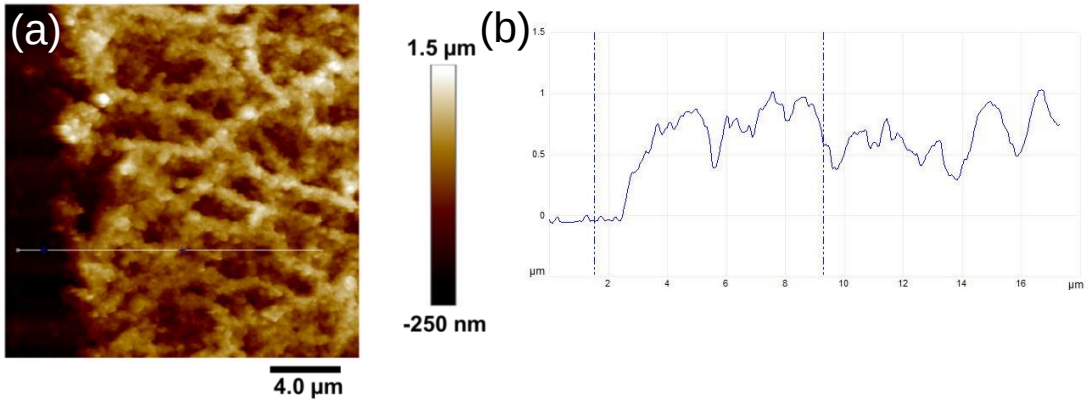

Figure 5.3. (a) AFM image and (b) the thickness of the printed BP film on the glass substrate.

5.3.2 **Device Response to Humidity**

The current-voltage (*I-V*) characteristics of the BP device under ambient air, dry air and dry N_2 atmospheres are shown in Figure 5.4a, The BP devices measured under conditions of dry air and dry N_2 show *I-V* curves that almost coincide. However, when measured in ambient (i.e. more humid) air, the current value is greater by a factor of ~ 16. This implies that the adsorption of water in the BP film drives an increased current in the printed BP films. The shift of the open circuit voltage indicates the presence of charge traps on the BP nanosheets when exposed to ambient air, which may be in response to the adsorption of water molecules.[40]

To further investigate the effect of atmospheric water molecules on the BP device, we measured its impedance as a function of frequency under various levels of RH using standard salt solutions to control humidity. The experimental set up and solutions used are provided in the Figure 5.5. The complex impedance plots were measured over a frequency range from 10 Hz to 1 MHz with a bias voltage of 0.5 V and temperature of 20 °C. The impedance spectrum of the BP device is shown as a Nyquist plot (Figure 5.4b). The complex impedance spectrum changes from a semicircle shape to a semicircle with a linear component when the humidity level increased from 11% RH to 97 % RH. The impedance spectra of the BP devices can be modelled using the equivalent circuits shown in Figure 5.4c (low humidity, 11% – 43% RH) and (high humidity, 53% - 97% RH). Here R_{ct} represents charge transfer, while *CPE1* and *CPE2* represent two constant phase elements, which are used to model the film impedance and electrode/sensing film interface impedance, respectively. The impedance of a constant phase element Z_{CPE} can be defined:

$$Z_{CPE} = Q^{-1}(i\omega)^{-n} \quad 0 \le n \le 1 \tag{5.1}$$

Where Q is a real parameter, i the imaginary unit, ω the frequency, and n a real parameter whose value can vary from 0 (pure resistor) to 1 (pure capacitor). Here we found that n was close to 1 for Z_{CPE1} under all conditions, as shown in Table 1, hence Z_{CPE1} acts as an almost pure capacitor at all humidity levels. In addition, we observed that the dependence of R_{ct} on RH, shown in Figure 4d, can be approximated by an empirical exponential relationship with,

$$\log(R_{ct}) = -0.0388(RH) + 8.2742 \tag{5.2}$$

with a linear regression coefficient, R^2, of 0.9665. The dependence of R_{ct} on humidity may indicate an interaction with PO_x functional groups in the BP film that formed during the solvent exfoliation and printing process. If small quantities of liquid water condense on the BP nanosheets, they can act as an electrolyte and increase flake-flake conductivity. A chemical interaction with the BP may lead to some dissolution and the presence of ions will lead to a capacitance contribution from a double layer mechanism at the flake/electrolyte interface and diffusion controlled processes that lead to the characteristic linear feature seen at low frequencies on the Nyquist plot. This is consistent with previous reports that mechanically exfoliated BP nanosheets show a decrease in conductivity after exposure to ambient conditions.[25]

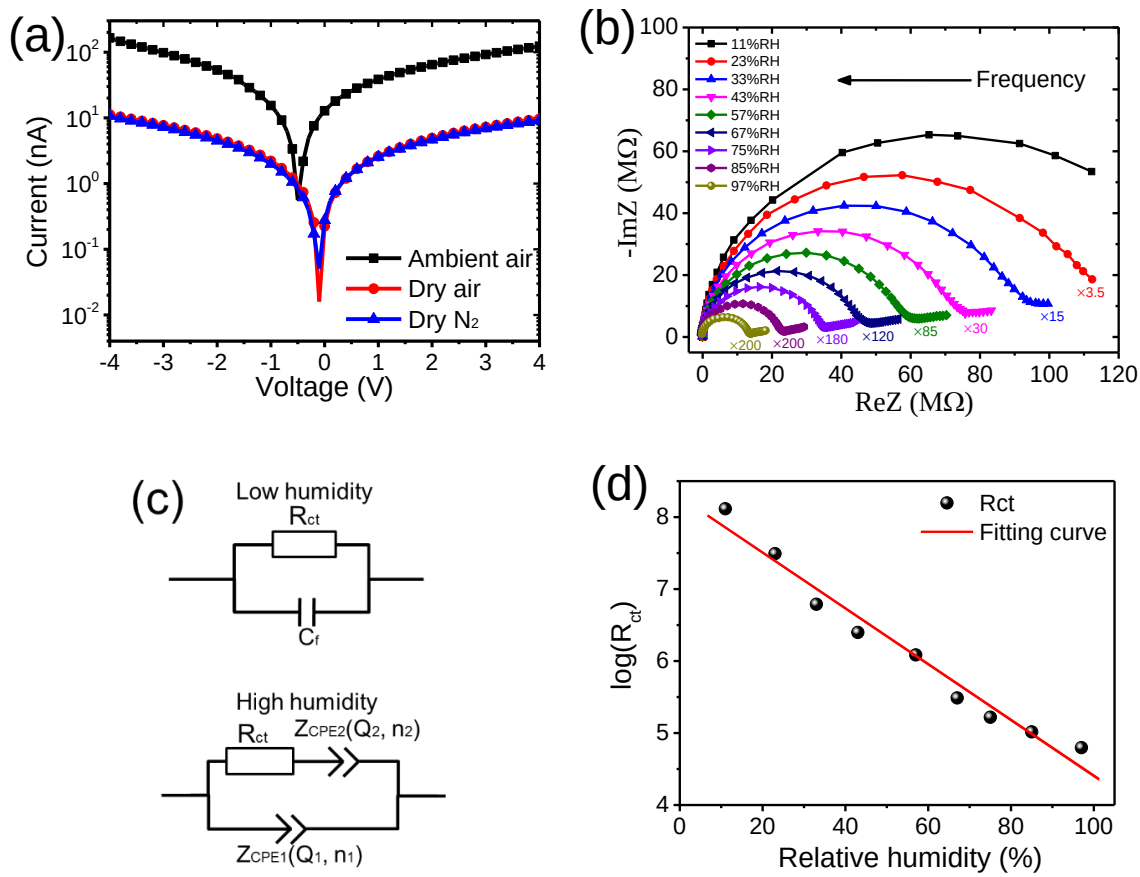

Figure 5.4. (a) *I-V* behaviours of the BP device measured under different condition. (b) Nyquist plots of the impedance of the BP device under different humidity levels within in the frequency range 10 Hz to 1 MHz. ImZ: imaginary part; ReZ: real part. (c) Equivalent circuits of the BP humidity sensor under low humidity and high humidity. (d) Exponential behaviour of the R_{ct} parameter vs humidity at 20 °C.

Table 5.1. Values of R_{ct}, n_1, and n_2 used in the equivalent circuit obtained over the range of humidity levels by analysing impedance spectra.

	Relative humidity (%)								
	11	**23**	**33**	**43**	**57**	**67**	**75**	**85**	**97**
$\boldsymbol{R_{ct}}$ **(Ω)**	1.31×10^{8}	3.11×10^{7}	6.16×10^{6}	2.50×10^{6}	1.22×10^{6}	3.07×10^{5}	1.66×10^{5}	1.04×10^{5}	6.27×10^{4}
$\boldsymbol{n_1}$	0.988	0.986	0.987	0.988	1	1	1	1	1
$\boldsymbol{n_2}$	–	–	–	–	0.042	0.179	0.215	0.261	0.278

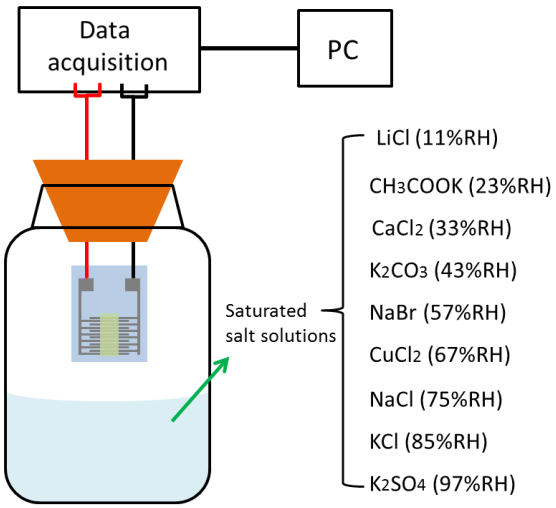

Figure 5.5. Diagram of the experimental setup used to measure the humidity sensor properties. The humidity sensor properties were tested in a sealed glass bottle held at a constant temperature of 20 °C. Various relative humidity RH levels were obtained by using the range of saturated salt solutions indicated.

The response and recovery of the device was measured by alternately transferring the BP sensor between controlled environments of 11% RH and 97% RH. Typical response and recovery curves over one cycle are presented in Figure 5.6a, with a response time of 5.4 s and a recovery time of 2.1 s. The capacitance increases by almost three orders of magnitude over the same range of RH. The increased capacitance is tentatively attributed to the adsorption of water molecules, which strengthen the polarization and increase the dielectric constant of the BP films. The device shows a highly repeatable response after several cycles (Figure 5.6b). The sensor was sequentially transferred from ambient laboratory humidity (36% RH) to atmospheres in the range 11 - 97% RH; the device shows high sensitivity and a rapid response (Figure 5.6c). These data show that the BP film interacts rapidly with the environment and the response over short timescales (exposure up to several minutes) is both reversible and repeatable. The high sensitivity of the BP nanosheets humidity sensor to moisture enables its use as a non-contact switch. Figure 5.6d shows the change in capacitance of the BP device induced by the water evaporating from a finger held proximally (ca. 1 cm) to the BP layer of the device. This ultrasensitive performance will allow the capture of fine features due to moisture modulation on the near surface of human fingertip.[41]

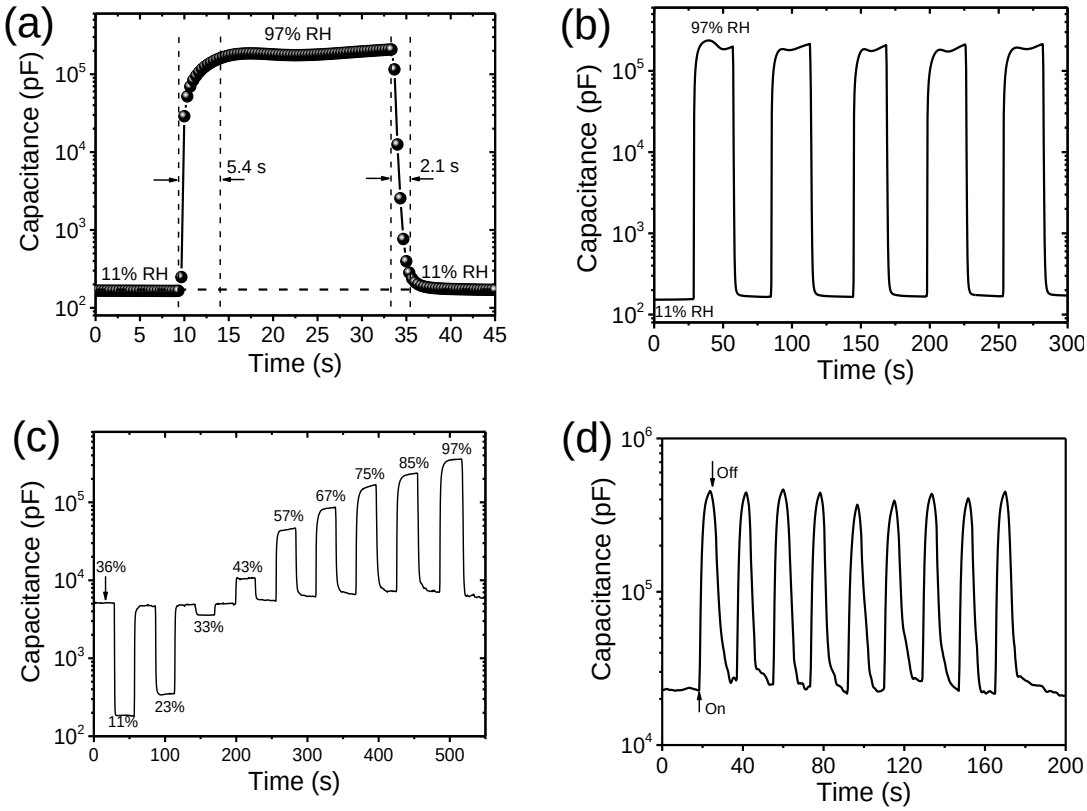

Figure 5.6. Response and recovery of the BP device to changes in humidity. (a) Time-resolved response to humidity change and recovery of the device showing a response time of 5.4 s (from 11% RH to 97% RH) and a recovery time of 2.1 s (from 97% RH to 11% RH). (b) Time-resolved response behaviour transferred from room humidity (36% RH) to different humidity levels (11% RH - 97% RH). (c) Time-resolved response behaviour transferred from room humidity (36% RH) to different humidity levels (11% RH - 97% RH). (d) Time-resolved dynamic tests of the sensing response on the near distance of a fingertip proximal under ambient air condition, defined as finger 'on' and 'off' states. All measurements were conducted at 100 Hz and with bias voltage of 0.5 V.

Data taken at different operating frequencies and with a second device of 30 printed layers show similar results and are presented in Figures 5.7 - 5.8. The response times of the sensor is similar to that reported by Yasaei for a BP humidity sensor which used similar thickness LPE material but was fabricated by vacuum filtration and had a much greater film thickness of 26 μm.[29] However, their impedance spectroscopy data found a very small change in equivalent circuit capacitance with humidity compared to our data.

The impedance spectra obtained from our BP sensors show significant similarities with those reported by Borini [42] using graphene oxide (GO) flakes and by Zhang [38] using GO flakes co-deposited with polystyrene sulfonate (PSS). Both studies show similar

changes in the Nyquist plot, with the diameter of the characteristic semicircle decreasing with increasing humidity. Similar equivalent circuits can be used to model this behaviour and the change in R_{ct} can be described by an empirical exponential relation similar to Equation 5.2. However, the BP sesnsor shows a greater change in R_{ct} with RH than GO, but the GO sensor of Boroni shows a more rapid response to changes in humidity.[42] Both Boroni and Zhang found a strong linear feature at low frequencies, as also seen at low frequencies with the BP sensor (Figure 5.4d), although this is much less pronounced with the PSS/GO sensor and only evident at the highest humidity values. These data suggest considerable similarities in the humidity interactions of GO and BP over short time scales.

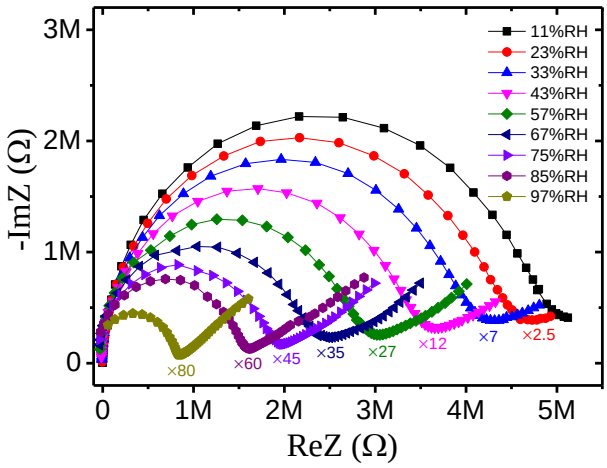

Figure 5.7. Nyquist plots of the impedance of the BP humidity sensor (30 printed layers) under conditions of relative humidity within the frequency range 10 Hz - 1 MHz. ImZ: imaginary part; ReZ: real part.

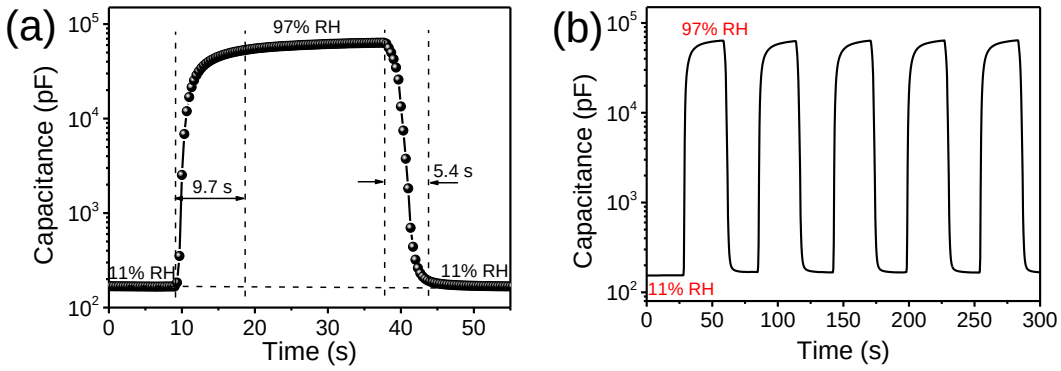

Figure 5.8. (a) Time-resolved response and recovery behaviour of the BP humidity sensor, showing the response time of 9.7 s (from 11% RH to 97% RH) and recovery time of 5.4 s (from 97% RH to 11% RH). (b) Time-resolved response behaviour of the BP humidity sensor for relative humidity under different humidity levels by changing humidity between 11% RH and 97% RH.

5.3.3 **Long Time Exposure and Degradation of BP Films**

Device performance after longer exposure times was investigated to assess the stability of 2D BP flakes in the presence of atmospheric water. Figures 5.9a - f show impedance spectra obtained from inkjet-printed BP devices after long term exposure to a controlled humidity environment. When measured above dried silica gel at ~ 4% RH there is no systematic change in the impedance spectra after 5 days exposure (Figure 5.9a) and any variation in the spectra over the test period is ascribed to noise. However, measurements made in environments with RH ≥ 11% showed systematic changes in the impedance spectra with prolonged exposure. The impedance of the BP devices drifts after several days of continuous exposure at low humidity levels (≤ 33% RH). In Figures 5.9b and c the semicircle locus of the Nyquist plot is not complete over the frequency sweep. However, with increased exposure time, the complex impedance decreases at low frequencies and at 23% RH (Figure 5.9c) a full semicircle appears after 7 days exposure. At 33% and 43% RH the Nyquist plot shows little change over several days in the high frequency region but shows small changes in the low frequency regime from day 7. In contrast, at 55% RH (Figure 5.9f) there is a continuous steady change in the impedance response with a decrease in the radius of the semicircular part of the Nyquist plot indicating a decrease in R_{ct}. The output capacitance was also measured (Figure 5.10) and this shows little change with time until RH = 43%, when it increases after about 5 days exposure. At RH = 55% this value increases rapidly from the onset of exposure to the environment. The phase angle also shows almost no change after various exposure times to low humidity conditions (Figure 5.11).

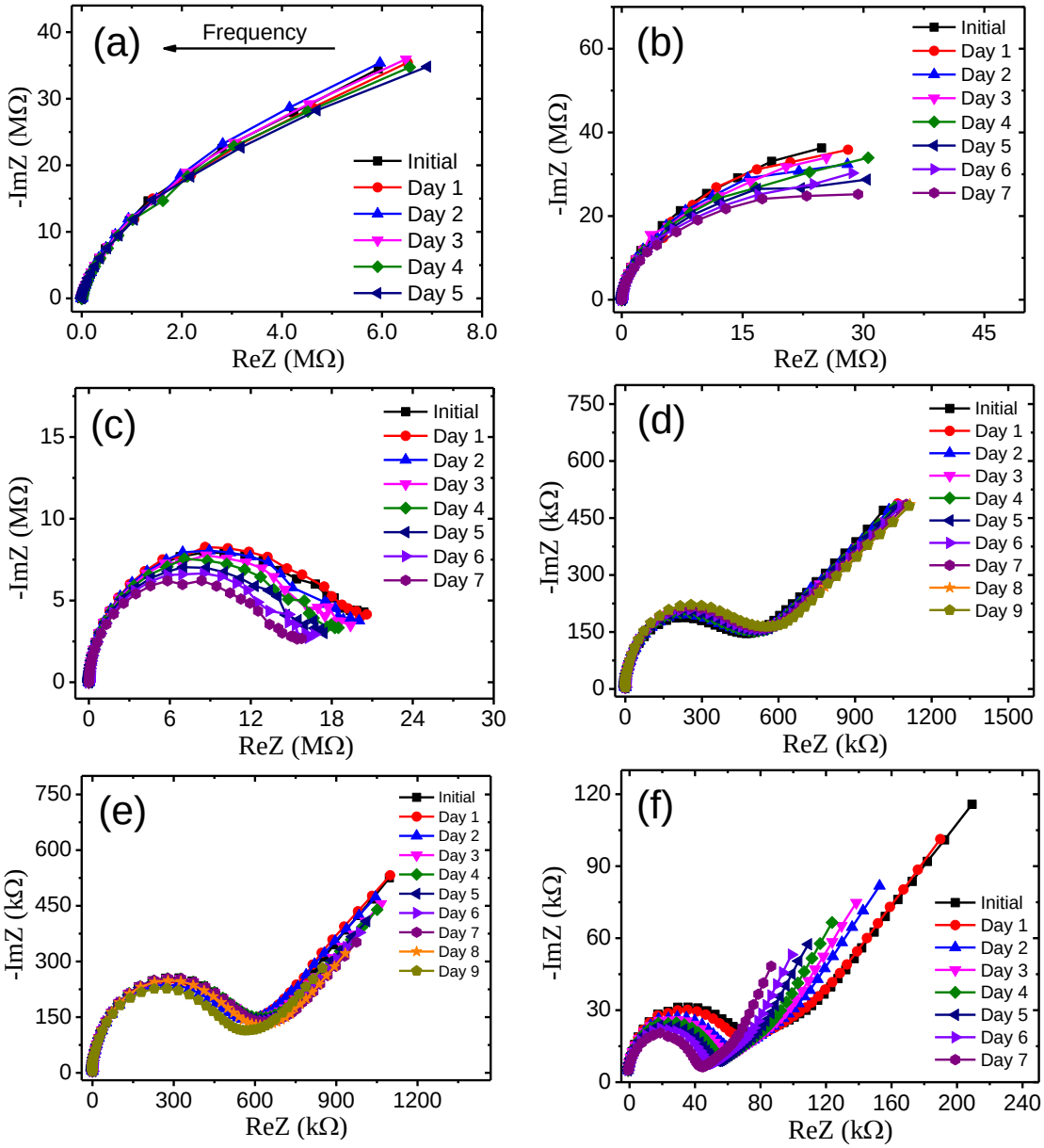

Figure 5.9. Nyquist plots of the impedance of the BP devices in the frequency range 10 Hz to 1 MHz after various exposure times under different humidity levels: (a) above dried silica gel (~ 4% RH) (b) 11% RH, (c) 23% RH, (d) 33%RH, (e) 43% RH, and (f) 55% RH.

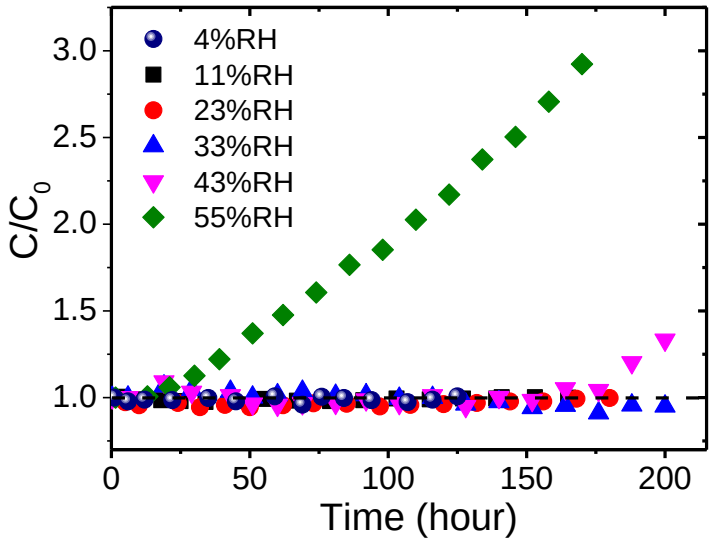

Figure 5.10. The change in output capacitance of the BP devices as a function of exposure time at 1 kHz under various humidity levels.

FTIR, XPS and Raman spectroscopy were also used to investigate the chemical changes that occur in humid environments. Figure 5.12a shows FTIR spectra obtained from BP flakes exposed to 55% RH, over time intervals up to 10 days. A broad and shallow peak at 2550 - 3650 cm^{-1} appears, which corresponds to P-O-H stretching. The peak at around 2400 cm^{-1} is the P-H stretch.[43] The two peaks close to 1650 cm^{-1} and 1450 cm^{-1} correspond to HPO_3^{2-} acids.[44, 45] Figure 5.12b shows an expanded view of the wave number range 800 - 1800 cm^{-1}. The peaks around 1220 cm^{-1} (representing either stretching P=O at 1220 cm^{-1} or P-O at 1212 cm^{-1}) and 895 cm^{-1} (P-O-P stretching) disappear over time and are replaced by two new and more intense peaks: the sharp peak at 1162 cm^{-1}, which is associated with the HPO_3^{2-} group, [43-45] and another broad peak including three peaks at around 1052 cm^{-1}, 1000 cm^{-1} and 970 cm^{-1} that are associated with the HOOPO group, P-OH bending and the symmetric $-PO_2$ stretch of $HP(O_2)O$, respectively.[46] Figure 5.12 c - f shows further results of FTIR spectra over a range of environment humidity levels. The behaviour of the peak at around 1220 cm^{-1} (P=O or P-O stretching) is a marker of the interaction with humid atmospheres. In the lowest humidity atmosphere environment (Figure 5.12f) this peak remains constant over 7 days exposure to ~ 4% RH and there is no obvious change in the FTIR spectrum in the range 800- 1800 cm^{-1}. At low humidity (11% RH and 23% RH) the spectrum remains unchanged or little changed until 3 days exposure when it decreases accompanied by an increase in the peak around 1162 cm^{-1} (HPO_3^{2-} group). However, at higher humidity levels (43% RH and 55% RH) the spectrum changes more rapidly after 1 day exposure.

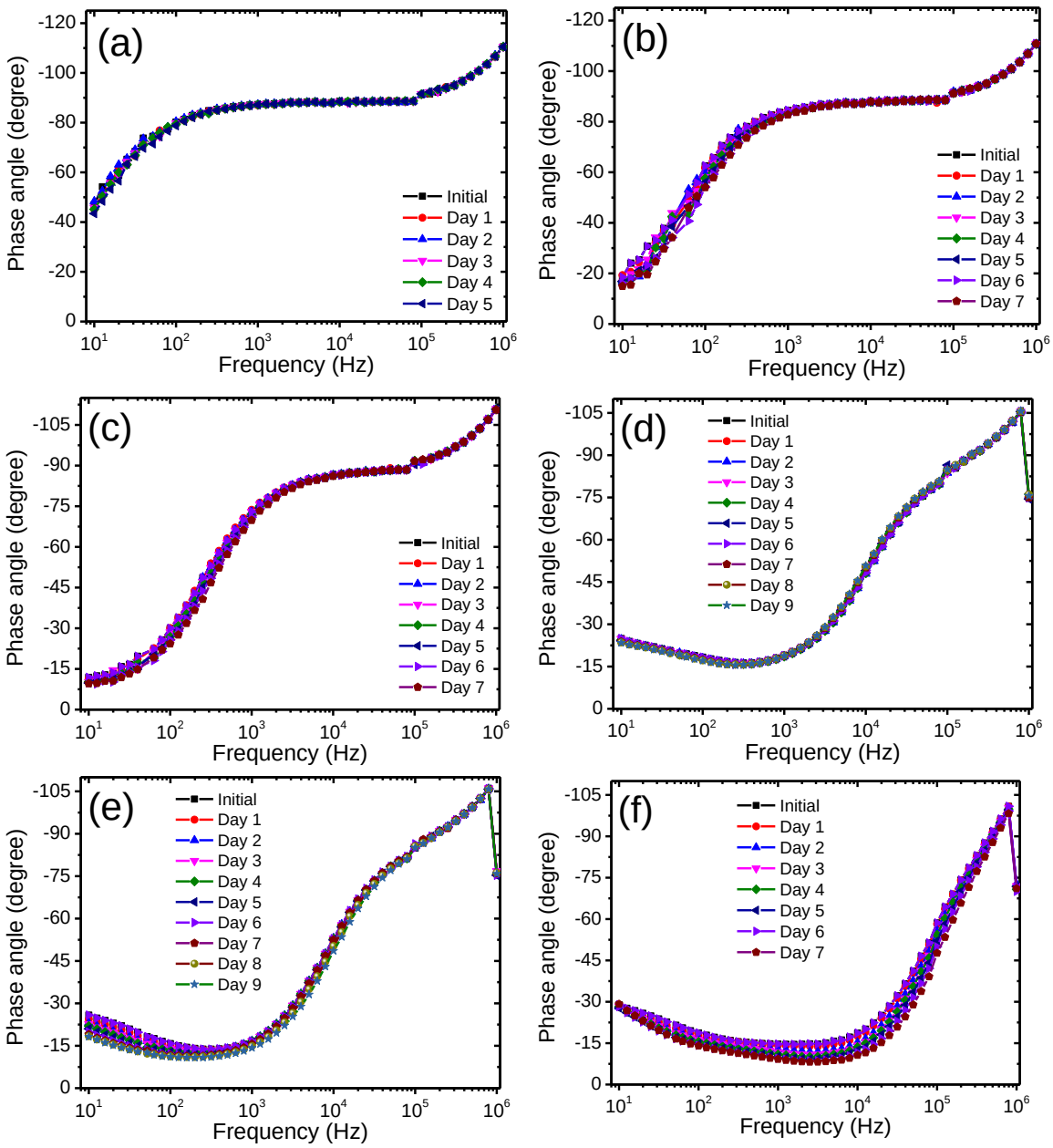

Figure 5.11. Phase angle of the BP devices in the frequency range 10 Hz to 1 MHz after various exposure times in under different humidity levels: (a) ~ 4% RH, (b) 11% RH, (c) 23% RH, (d) 33%RH, (e) 43% RH, and (f) 55% RH.

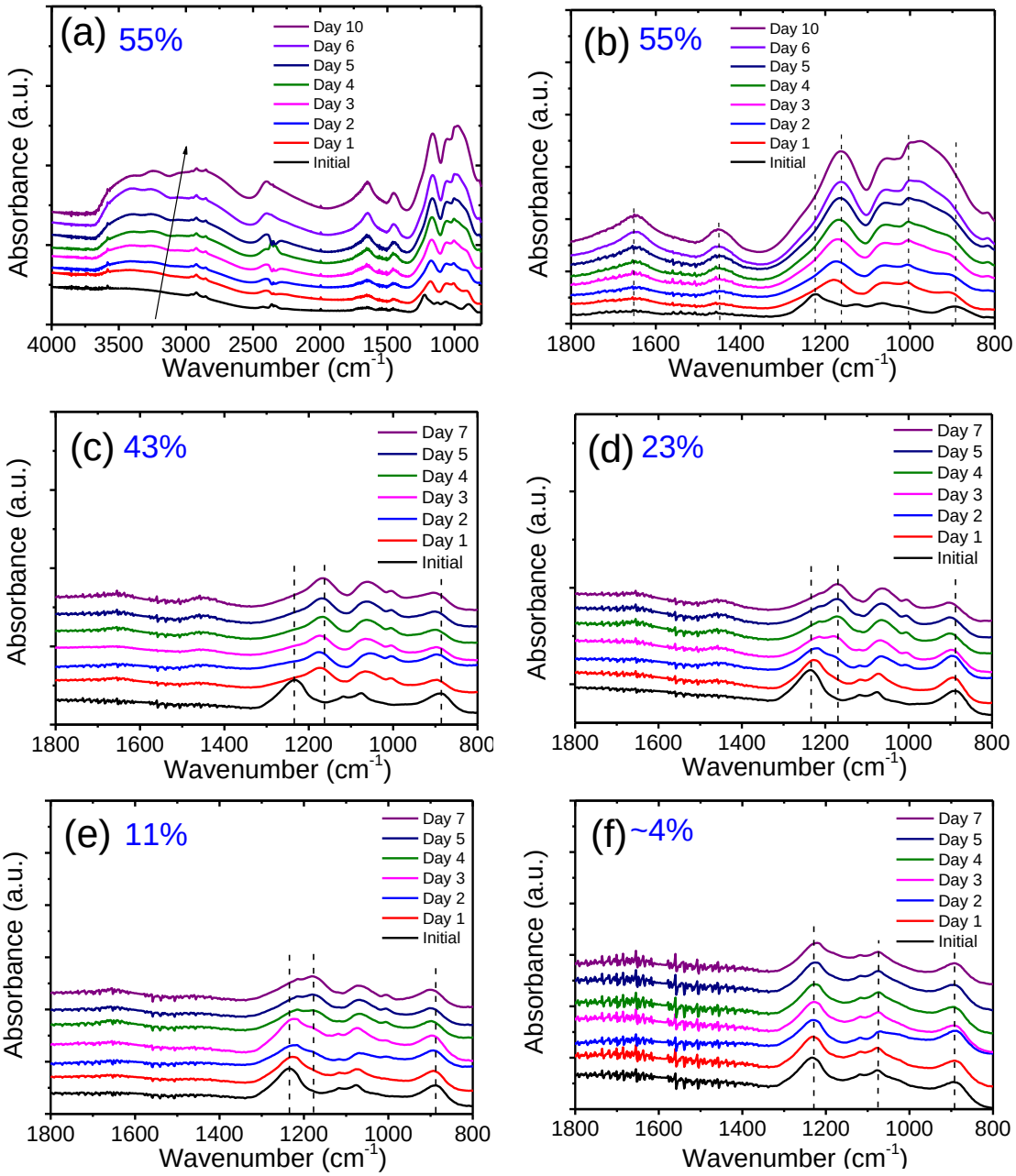

Figure 5.12. FTIR spectra obtained from BP films after exposure to environments of different of relative humidity. (a) After exposure to 55% RH; (b) FTIR spectra in the wavenumber range 800- 1800 cm^{-1}: 55% RH; (c) 43% RH; (d) 23% RH; (e) 11% RH; (f) ~ 4% RH, for up to 7 days.

Wood *et al* earlier presented an FTIR study of the degradation of mechanically exfoliated BP flakes after exposure to air at an ambient humidity of 36.8%.[25] In this study, the BP was deposited on a Si/SiO_2 substrate and the strong peaks from the substrate masked a number of the peaks found in our study. However, Wood reported the formation of P=O bonds and after longer periods of exposure the presence of a strong peak at 1180 cm^{-1}, which we associate with the peak we recorded at 1162 cm^{-1}.

Our data at 43% RH is broadly similar to that of Wood, albeit with a slightly faster onset of degradation, although this may be masked in Wood's study by the convolution of signals from the Si/SiO_2 substrate. Our work extends the range of RH investigated and shows its strong influence on the degradation rate of BP and the absence of degradation products from the FTIR data at 4% RH.

Figure 5.13a shows the P 2*p* core-level XPS spectra from an inkjet-printed BP film on an Au-on-Si wafer as printed, on exposure to a 2 mbar water vapour atmosphere, and after 1 hour exposure. All spectra are referenced on the binding energy scale to the position of the Au 4f7/2 peaks of the substrate at 84 eV. All three spectra of the BP films show the $2p^{3/2}$ and $2p^{1/2}$ doublet at 130.0 and 131.1 eV respectively, corresponding to the P-P bonds within BP.[47] The other small doublets apparent at around 133.8 eV arise from oxidation of the BP nanosheets during exfoliation and printing, as observed in previous reports.[23, 28] The peak centred at 133.8 eV is consistent with P^{5+} and is assigned to phosphonates [48] and phosphates. [49] Nevertheless, the surface of the BP film is not further oxidized by water vapour at 2 mbar over a time period of around 1 hour, illustrating the slow degradation kinetics of solvent-exfoliated BP nanosheets.[23, 28] Raman spectra from the printed BP film show a relatively broad peak of weak intensity, likely composed of several overlapping new peaks, from 800 to 900 cm^{-1} (Figure 5.13b). These small peaks have been observed in aged exfoliated BP flakes,[50] which are consistent with the P-O stretching modes in mixed phosphorus oxide compounds,[51, 52] lending support to the presence of oxides or oxyacids in the BP film.

Thus the action of atmospheric water degrades the printed BP films after exposure to humid conditions over a number of days. Impedance spectroscopy and FTIR data taken over a range of RH indicate that the degradation is associated with the presence of atmospheric water rather than the action of oxygen alone and this is supported by the XPS data. FTIR data shows the reduction in intensity and elimination of P=O and P-O-P peaks in the BP films and the consequent emergence of peaks associated with phosphorus acid groups in the films, suggesting that water hydrolyses these bonds and also disrupts the BP structure.

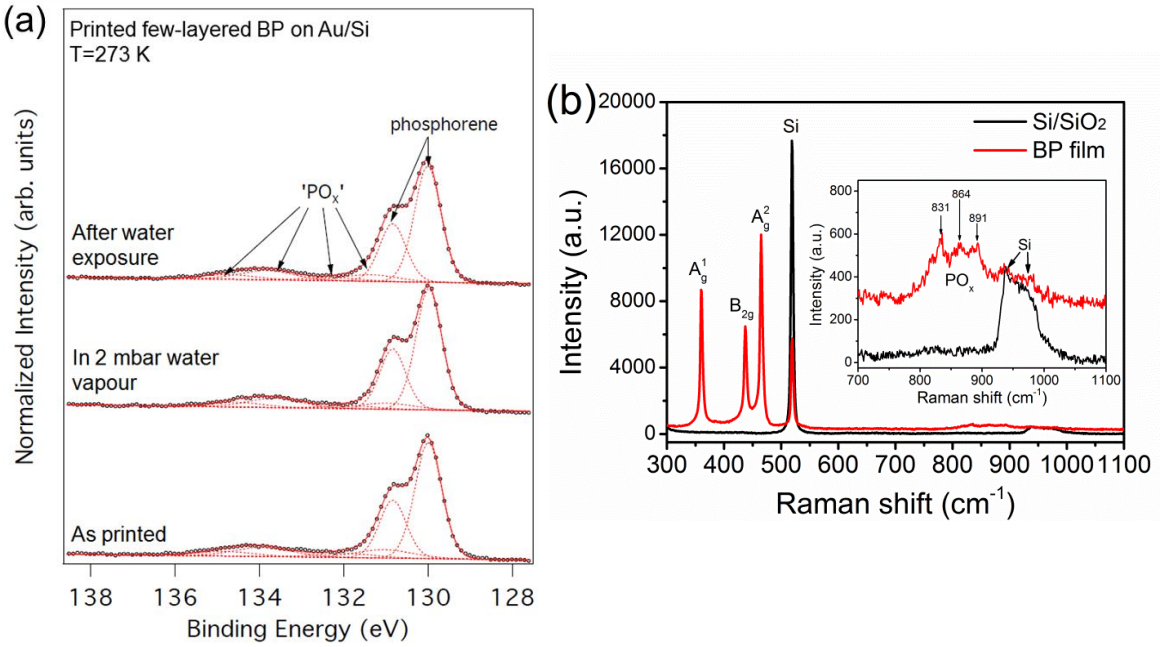

Figure 5.13. (a) P 2*p* core-level XPS spectra from inkjet-printed BP film onto an Au on Si wafer as presented (bottom), exposing in 2 mbar water vapour (middle), and after 1 hour water exposure (top). The open circles are the experimental data, red dashed lines are the fitted components and the solid red line the fit to the experimental data. (b) Raman spectrum from the BP film on a Si/SiO_2 substrate (red line) and the bare Si/SiO_2 substrate (black line). The inset shows the detailed Raman spectrum of the oxidised BP film with obvious peak from 800 to 900 cm^{-1}, while the Si/SiO_2 substrate shows no obvious peak at this region.

5.3.4 **Recovery of BP Films after Thermal Treatment**

In the absence of liquid water external to the film, it is likely that the reaction products from interactions with atmospheric water are retained within the BP film and thus it is possible that some of the hydrolytic degradation might be reversible when the film is dried. Hence the structural characteristics of printed BP films, pre-exposed to an atmosphere of 55% RH for 10 days, after a range of drying treatments in different atmospheres were explored. Figure 5.14a shows the FTIR spectra obtained from BP films exposed to 55% RH for 10 days, followed by drying for 1 hour at a range of temperatures from room temperature to 150 °C in anhydrous nitrogen, with an enlarged view of the spectra shown in Figure 5.14b. The spectrum of the BP film exposed to 55% RH does not change when dried at either room temperature or 50 °C. However, after heating to 80 °C, the broad peak at 2550 - 3650 cm^{-1} (P-OH stretching) is weakened, accompanied by attenuation of the peaks at 1650 cm^{-1}, 1450 cm^{-1} and 1160 cm^{-1} all associated with HPO_3^{2-}. Two peaks at 902 cm^{-1} (P-O-P stretching) and around 1210 -

1220 cm^{-1} (P-O or P=O stretching), that were not present in the as-received film after exposure to humid air but are seen in films prior to exposure (Figure 5.12), now reappear. On increasing the temperature to 150 °C, the broad peak at 2550 - 3650 cm^{-1} becomes very weak, as do the two peaks at 1650 cm^{-1} and 1450 cm^{-1}. The two new peaks are stable at around 1236 and 895 cm^{-1}, which are similar to the peaks of the BP film before exposure to high RH conditions. Significantly, this suggests that some of the structural changes to the BP film, which are the result of interactions with atmospheric water molecules, can be reversed under moderate temperature heating in a dry environment.

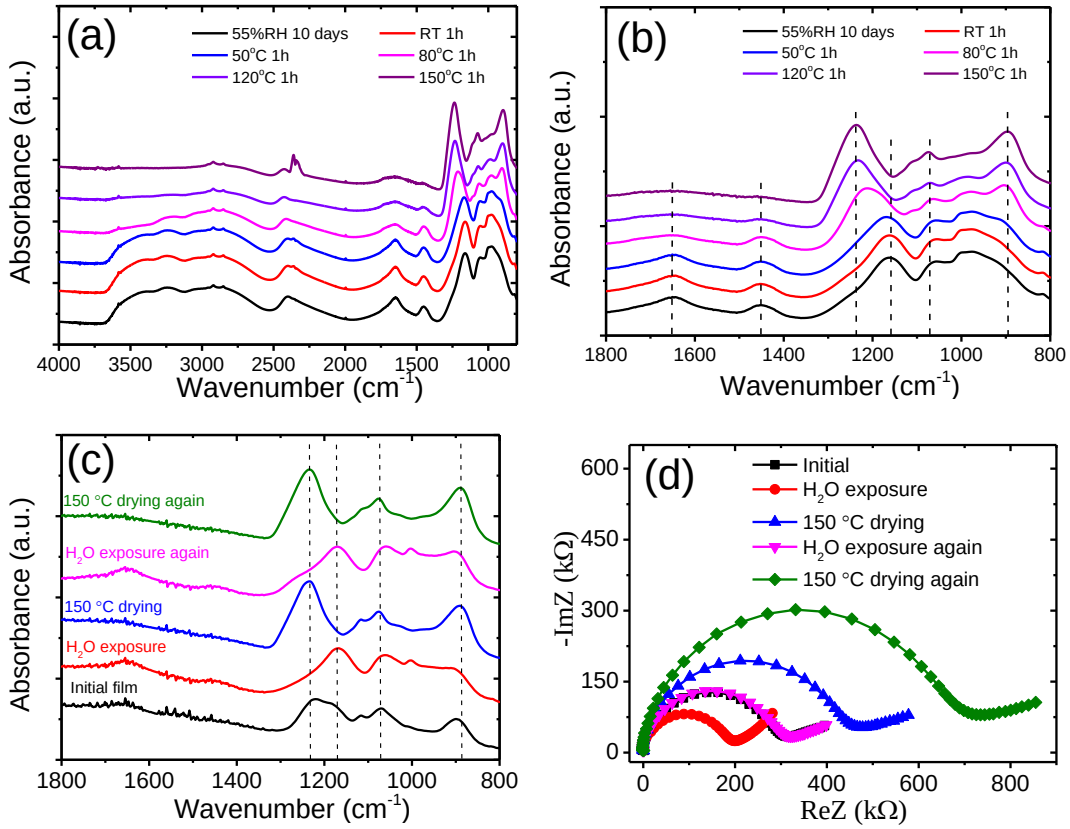

Figure 5.14. Influence of heat treatment in a dry atmosphere on the BP films. (a) FTIR spectra of the BP film after exposure to 55% RH for 10 days, followed by drying in N_2 for 1 hour held at: RT, 50 °C, 80 °C, 120 °C, and 150 °C. (b) FTIR spectra showing an expanded view of (a) in the wave number range 800 - 1800 cm^{-1}. (c) FTIR spectra of a BP film following repeated exposed to 55% RH for 2 days, followed by drying in N_2 at 150 °C for 1 hour. (d) Nyquist plots of the impedance of the printed BP device in the frequency range 10 Hz - 1 MHz following an exposure to 55% RH and a N_2 drying cycle.

To further investigate the influence of humidity and the subsequent drying process we repeatedly exposed the BP films to 55% RH air for 2 days, followed by drying in

nitrogen for 1 hour at 150 °C (Figure 5.14c). The response to cyclic exposures to moisture followed by drying shows similar behaviour to the effect of a single drying process (Figure 5.14c) with the presence of moisture eliminating the peaks at around 1220 cm^{-1} (P=O or P-O stretching) and 895 cm^{-1} (P-O-P stretching) but with their reappearance after a 1 hour heat treatment in dry nitrogen. However, the FTIR response around 1220 cm^{-1} after drying shows a much stronger response after the first and subsequent drying treatment than is seen in the initial film prior to exposure to a humid atmosphere. Impedance measurements after repeated exposure to humidity and elevated temperature drying (Figure 5.14d) also indicate a continuing change in the BP film after repeated exposure to a 55% RH atmosphere. The diameter of the characteristic semicircle on the Nyquist decreases after each exposure to moisture and increases with each drying cycle. However, after each cycle the diameter, which equates to an increase in the resistance component in the equivalent circuit shown in Figure 5.4c. We believe that this indicates a permanent disruption in the BP flake network caused by oxidation that cannot be fully recovered by heat treatment under dry nitrogen condition.

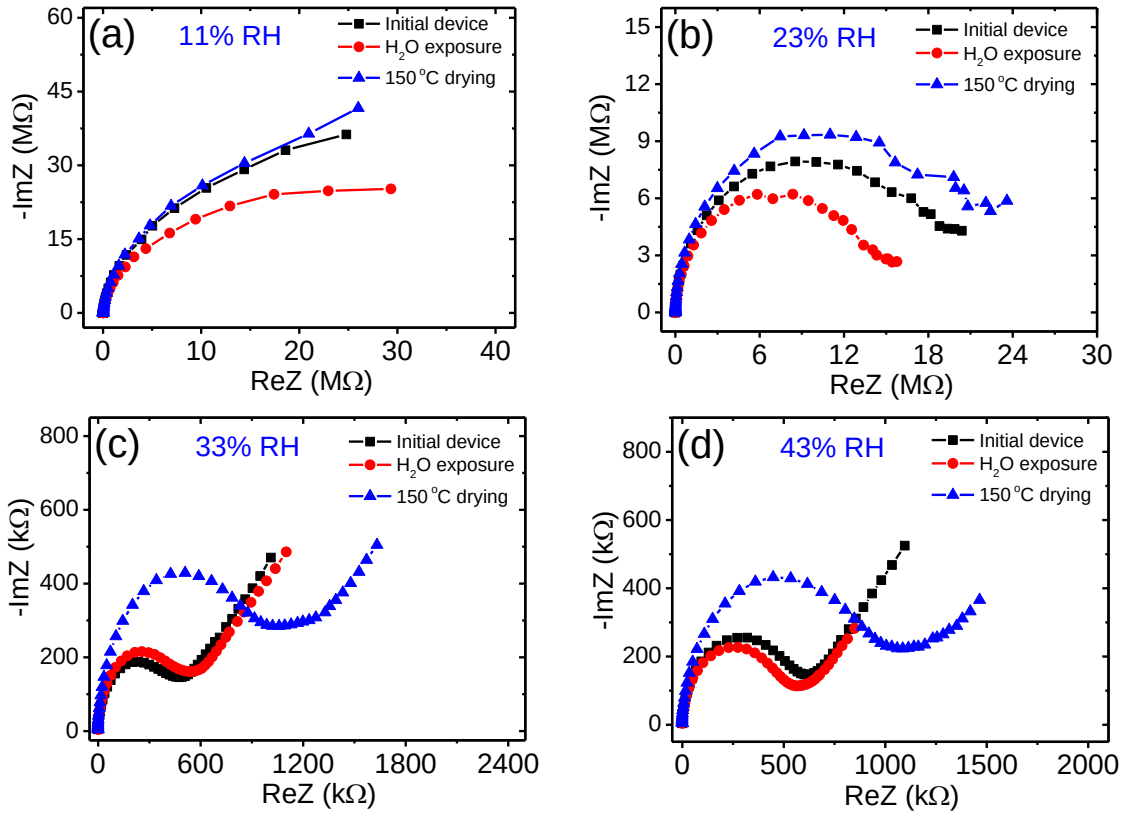

Figure 5.15. Nyquist plots of the impedance of the printed BP device in the frequency range 10 Hz to 1 MHz following an exposure to different humidity levels and a N_2 drying cycle.

Further results show that the increased impedance is related to the RH of the environment (Figure 5.15) with permanent damage not fully recovered at RH of 23%, 33% and 43% after thermal treatment in a dry environment. However, at RH = 11% (Figure 5.15a) only a very small difference in the impedance spectrum is seen on comparing the as-printed film with that after exposure and thermal treatment. Thus we conclude that exposure to moisture through an atmosphere with RH > 11% results in permanent damage to a BP film, although some recovery is possible after drying in a dry atmosphere at elevated temperature.

5.3.5 **Mechanisms for BP Flake Interaction with Humid Environments**

BP flakes interact with atmospheric water in a complex manner, which is strongly dependent on both the timescale of the interaction and the relative humidity. The printed BP device has a thickness in the range of 1 μm and thus contains many individual flakes of BP in an open structure (Figure 5.2f). In a completely inert environment the electrical properties of the structure will depend on the local nature of flake/flake contacts and can be represented by a resistor and capacitor network. In the presence of humidity, water vapour will condense in the interstices between flakes to form stable liquid bridges with capillary radius determined by the Kelvin equation. Thus both the resistance and capacitance of the inter-flake contacts will be governed by the properties of these liquid bridges.

The humidity sensing mechanism shows a characteristic and repeatable time constant of a few seconds (Figure 5.6a) and this time constant increases with printed film thickness (Figure 5.8). We hypothesize that the time scale is consistent with the growth and shrinking of the liquid bridges as they achieve local equilibrium with atmospheric moisture and does not require any extensive chemical reaction at the water/flake interface. This mechanism is responsible for the observed interaction of the BP device with the environment at low levels of humidity and over small time scales. This is consistent with the impedance spectroscopy data in the regime of RH < 43% where a simple resistor and capacitor model can be used to interpret the data. The decrease in low frequency resistance (the high impedance termination of the characteristic semicircle seen in the Nyquist plots) can also be explained if the exfoliation of BP has introduced some oxidation damage to the surface of the flakes and there are species that can ionise the water in the liquid bridges. In which case the contact resistance will be inversely proportional to the diameter of the liquid bridges and hence decrease with

increasing humidity. The presence of a linear tail at low frequencies on the Nyquist plots indicates a charge diffusion regime consistent with the presence of ions. This is identical to the mechanisms proposed by Borini for the operation of GO flake humidity sensors with a very similar design to our BP device.[42]

The absence of further changes to the printed BP film at low levels of humidity is supported by the XPS data that show that the presence of 2 mbar H_2O exposure for 1 hour leads to no significant change in the oxidation state of the printed BP film (Figure. 5.13a). However, at higher humidity levels, and over longer exposure times, the BP is believed to react with water in the liquid bridges or with oxygen dissolved in the water. There have been a number of observations reported in the literature that both bulk BP and BP flakes react with either water or oxygen in the atmosphere.[24-28] Similarly, there have been a number of chemical pathways suggested for the inferred oxidation of BP. Favron proposed a photoinduced oxidation of BP to explain their observation that no degradation was seen on exposure to air and water in the absence of light.[26] In this mechanism light quanta create excitons in the BP lattice that interact with O_2 in aqueous solution to form the superoxide (O_2^-) ion which then oxidises the BP. Ziletti carried out density functional theory (DFT) calculations and found that photo-oxidation can occur after the physisorption of O_2 in the absence of H_2O.[53] Hanlon, in contrast proposed, also using DFT calculations, that the edges of the planes of P atoms exposed on the BP flakes induce a disproportionation reaction of H_2O, [28] with:

$$P + 3H_2O \rightarrow PH_3 + H_3PO_3 \qquad (5.3)$$

Although this hypothesis appears to be counter to BP degradation observed as "bubbles" or circular bumps on the flat surface of BP flakes.[24-26] A further possible mechanism or reaction pathway for the degradation of BP follows a galvanic process with cathodic and anodic reactions on the surface of electrically connected BP surfaces. Possible anodic reactions, with their standard potentials are:[54]

$$P + 2OH^- \leftrightarrow H_2PO_2^- + e^- \qquad E° = +1.82\ V \qquad (5.4a)$$

$$P + 5OH^- \leftrightarrow HPO_3^{2-} + 3H^+ + 3e^- \qquad E° = +1.71\ V \qquad (5.4b)$$

With the complementary cathodic reactions:

$$P + 3H^+ + 3e^- \leftrightarrow PH_{3(g)} \qquad E° = -0.11\ V \qquad (5.5a)$$

$$O_{2(g)} + 2H_2O + 4e^- \leftrightarrow 4OH^- \qquad E° = +0.40\ V \qquad (5.5b)$$

Reactions 5.5a and 5.5b are expected to be more prevalent at the surface of the BP film (to allow PH_3 escape/or O_2 access), with anodic reactions more important in the film interior. These reactions increase the electrolyte concentration in the liquid bridges, reducing further the contact resistance, but also introducing physical damage to the BP network and possibly reducing its connectivity. The presence of significant populations of ions in solution will lead to double layer capacitance and diffusion controlled conductance in an oscillating electric field, all of which lead to the linear diffusive region on the Nyquist plots at low frequency seen after exposure to RH > 23% (Figures 5.9d - f).

On drying in a moisture free atmosphere the water in the liquid bridges will evaporate to a lower volume or be eliminated, leading to an increase in contact resistance, subsequently the phosphonate and similar ions may condense to oxide phases, reversing the earlier hydrolysis, and the associated IR absorbance peaks will disappear to be replaced with strong P=O and P-O-P absorbance in the FTIR spectrum. However, the resistance of the BP network will be greater than before long term interaction with water because the corrosive oxidation process forms insulating phosphorus oxides at the intergrain contacts, reducing network electrical connectivity and increasing local contact resistance (Figure 5.14d and Figure 5.15). Thus we hypothesise that the electrical behaviour of thick films (> 1 μm) of BP flakes is described by a combination of physical condensation of water from the environment over a time scale of a few seconds (Figure 5.8a) and a longer scale chemical interaction with the environment (with a time scale of several minutes to hours) leading to an aqueous mediated corrosion of the flakes. Both the physical absorption mechanism at short timescales and the longer term degradation mechanisms are expected to be dependent on factors such as total film thickness and this may in some part explain the differences between the sensitivity of BP films to ambient humidity reported here and in the earlier study of Yasaei.[29] Finally our results indicate that in conditions of low humidity with RH of 4% or less, damage to printed BP flakes is either eliminated or occurs at a rate sufficiently low that no change to the FTIR or impedance spectra is observed over a period of several days.

5.4 Conclusions

Black phosphorus crystals can be successfully exfoliated in the volatile solvent, acetonitrile. The resulting few-layer BP ink can be efficiently deposited on a glass substrate by inkjet printing. A fully printed humidity sensing device has been assembled by integrating printed BP nanosheets with printed silver nanoparticle electrodes. The device can be used as a probe for the interactions between few-layer BP nanosheets and moisture. At low humidity, the electrical response of the printed BP film can be modelled by a simple resistor and capacitor equivalent circuit. This device shows a rapid response to changes in humidity and a repeatable performance when cycled between low and high humidity environments over a time scale of some minutes. However, after longer term (several hours) exposure to atmospheres with RH > 11%, irreversible chemical change is seen with strong infrared absorption associated with the presence of phosphonate and other acidic phosphorus oxide ions. FTIR spectroscopy shows that this degradation is partially reversible by a low temperature heat treatment under dry conditions leading to the removal of the phosphonate ions. However, permanent damage has occurred during environmental exposure with stronger absorbance associated with P=O and P-O-P bonds seen after repeated exposure and drying, accompanied by an increase in the low frequency impedance of the BP. However on exposure to atmospheres of RH ~ 4% these damage mechanisms are not observed or occur at a rate too slow for the resolution of our experiments. These results indicate that the atmospheric degradation of 2D BP flakes is strongly mediated by the presence of water and that any oxidation degradation in a water free environment occurs at a much lower rate than resolvable with our experiments.

References

1. Novoselov, K.S., Geim, A.K., Morozov, S.V., Jiang, D., Zhang, Y., Dubonos, S.V., Grigorieva, I.V., and Firsov, A.A., Electric field effect in atomically thin carbon films. *Science*, 2004. **306**(5696): p. 666-669.

2. Kou, L., Chen, C., and Smith, S.C., Phosphorene: Fabrication, Properties, and Applications. *The Journal of Physical Chemistry Letters*, 2015. **6**(14): p. 2794-2805.

3. Xia, F., Wang, H., and Jia, Y., Rediscovering black phosphorus as an anisotropic layered material for optoelectronics and electronics. *Nature Communications*, 2014. **5**: p. 4458.

4. Bridgman, P.W., Two new modifications of phosphorus. *Journal of the American Chemical Society*, 1914. **36**: p. 1344-1363.

5. Mak, K.F., Lee, C., Hone, J., Shan, J., and Heinz, T.F., Atomically Thin MoS2: A New Direct-Gap Semiconductor. *Physical Review Letters*, 2010. **105**(13): p. 136805.

6. Cai, Y., Zhang, G., and Zhang, Y.W., Layer-dependent band alignment and work function of few-layer phosphorene. *Scientific Reports*, 2014. **4**: p. 6677.

7. Li, L.K., Yu, Y.J., Ye, G.J., Ge, Q.Q., Ou, X.D., Wu, H., Feng, D.L., Chen, X.H., and Zhang, Y.B., Black phosphorus field-effect transistors. *Nature Nanotechnology*, 2014. **9**(5): p. 372-377.

8. Wang, Q.H., Kalantar-Zadeh, K., Kis, A., Coleman, J.N., and Strano, M.S., Electronics and optoelectronics of two-dimensional transition metal dichalcogenides. *Nature Nanotechnology*, 2012. **7**(11): p. 699-712.

9. Liu, H., Neal, A.T., Zhu, Z., Luo, Z., Xu, X.F., Tomanek, D., and Ye, P.D.D., Phosphorene: An Unexplored 2D Semiconductor with a High Hole Mobility. *ACS Nano*, 2014. **8**(4): p. 4033-4041.

10. Appalakondaiah, S., Vaitheeswaran, G., Lebegue, S., Christensen, N.E., and Svane, A., Effect of van der Waals interactions on the structural and elastic properties of black phosphorus. *Physical Review B*, 2012. **86**(3): p. 035105.

11. Wang, H., Wang, X.M., Xia, F.N., Wang, L.H., Jiang, H., Xia, Q.F., Chin, M.L., Dubey, M., and Han, S.J., Black Phosphorus Radio-Frequency Transistors. *Nano Letters*, 2014. **14**(11): p. 6424-6429.

12. Abbas, A.N., Liu, B.L., Chen, L., Ma, Y.Q., Cong, S., Aroonyadet, N., Kopf, M., Nilges, T., and Zhou, C.W., Black Phosphorus Gas Sensors. *ACS Nano*, 2015. **9**(5): p. 5618-5624.

13. Viti, L., Hu, J., Coquillat, D., Knap, W., Tredicucci, A., Politano, A., and Vitiello, M.S., Black Phosphorus Terahertz Photodetectors. *Advanced Materials*, 2015. **27**(37): p. 5567-5572.

14. Mu, H.R., Lin, S.H., Wang, Z.C., Xiao, S., Li, P.F., Chen, Y., Zhang, H., Bao, H.F., Lau, S.P., Pan, C.X., Fan, D.Y., and Bao, Q.L., Black Phosphorus-Polymer Composites for Pulsed Lasers. *Advanced Optical Materials*, 2015. **3**(10): p. 1447-1453.

15. Hernandez, Y., Nicolosi, V., Lotya, M., Blighe, F.M., Sun, Z.Y., De, S., McGovern, I.T., Holland, B., Byrne, M., Gun'ko, Y.K., Boland, J.J., Niraj, P., Duesberg, G., Krishnamurthy, S., Goodhue, R., Hutchison, J., Scardaci, V., Ferrari, A.C., and Coleman, J.N., High-yield production of graphene by liquid-phase exfoliation of graphite. *Nature Nanotechnology*, 2008. **3**(9): p. 563-568.

16. Lin, Y., Williams, T.V., and Connell, J.W., Soluble, Exfoliated Hexagonal Boron Nitride Nanosheets. *Journal of Physical Chemistry Letters*, 2010. **1**(1): p. 277-283.

17. Coleman, J.N., Lotya, M., O'Neill, A., Bergin, S.D., King, P.J., Khan, U., Young, K., Gaucher, A., De, S., Smith, R.J., Shvets, I.V., Arora, S.K., Stanton, G., Kim, H.Y., Lee, K., Kim, G.T., Duesberg, G.S., Hallam, T., Boland, J.J., Wang, J.J., Donegan, J.F., Grunlan, J.C., Moriarty, G., Shmeliov, A., Nicholls, R.J., Perkins, J.M., Grieveson, E.M., Theuwissen, K., McComb, D.W., Nellist, P.D., and Nicolosi, V., Two-Dimensional Nanosheets Produced by Liquid Exfoliation of Layered Materials. *Science*, 2011. **331**(6017): p. 568-571.

18. Coleman, J.N., Liquid exfoliation of defect-free graphene. *Accounts of Chemical Research*, 2013. **46**(1): p. 14-22.

19. Brent, J.R., Savjani, N., Lewis, E.A., Haigh, S.J., Lewis, D.J., and O'Brien, P., Production of few-layer phosphorene by liquid exfoliation of black phosphorus. *Chemical communications*, 2014. **50**(87): p. 13338-13341.

20. Brent, J.R., Lewis, D.J., Lorenz, T., Lewis, E.A., Savjani, N., Haigh, S.J., Seifert, G., Derby, B., and O'Brien, P., Tin(II) Sulfide (SnS) Nanosheets by Liquid-Phase Exfoliation of Herzenbergite: IV-VI Main Group Two-Dimensional Atomic Crystals. *Journal of the American Chemical Society*, 2015. **137**(39): p. 12689-96.

21. Zhang, X., Xie, H., Liu, Z., Tan, C., Luo, Z., Li, H., Lin, J., Sun, L., Chen, W., Xu, Z., Xie, L., Huang, W., and Zhang, H., Black phosphorus quantum dots. *Angew Chem Int Ed Engl*, 2015. **54**(12): p. 3653-3657.

22. Yasaei, P., Kumar, B., Foroozan, T., Wang, C., Asadi, M., Tuschel, D., Indacochea, J.E., Klie, R.F., and Salehi-Khojin, A., High-quality black phosphorus atomic layers by liquid-phase exfoliation. *Advanced Materials*, 2015. **27**(11): p. 1887-1892.

23. Kang, J., Wood, J.D., Wells, S.A., Lee, J.H., Liu, X., Chen, K.S., and Hersam, M.C., Solvent exfoliation of electronic-grade, two-dimensional black phosphorus. *ACS Nano*, 2015. **9**(4): p. 3596-3604.

24. Joshua, O.I., Gary, A.S., Herre, S.J.v.d.Z., and Andres, C.-G., Environmental instability of few-layer black phosphorus. *2D Materials*, 2015. **2**(1): p. 011002.

25. Wood, J.D., Wells, S.A., Jariwala, D., Chen, K.S., Cho, E., Sangwan, V.K., Liu, X.L., Lauhon, L.J., Marks, T.J., and Hersam, M.C., Effective Passivation of Exfoliated Black Phosphorus Transistors against Ambient Degradation. *Nano Letters*, 2014. **14**(12): p. 6964-6970.

26. Favron, A., Gaufres, E., Fossard, F., Phaneuf-L'Heureux, A.L., Tang, N.Y.W., Levesque, P.L., Loiseau, A., Leonelli, R., Francoeur, S., and Martel, R., Photooxidation and quantum confinement effects in exfoliated black phosphorus. *Nature Materials*, 2015. **14**(8): p. 826-832.

27. Yau, S.L., Moffat, T.P., Bard, A.J., Zhang, Z.W., and Lerner, M.M., Stm of the (010) Surface of Orthorhombic Phosphorus. *Chemical Physics Letters*, 1992. **198**(3-4): p. 383-388.

28. Hanlon, D., Backes, C., Doherty, E., Cucinotta, C.S., Berner, N.C., Boland, C., Lee, K., Harvey, A., Lynch, P., Gholamvand, Z., Zhang, S., Wang, K., Moynihan, G., Pokle, A., Ramasse, Q.M., McEvoy, N., Blau, W.J., Wang, J., Abellan, G., Hauke, F., Hirsch, A., Sanvito, S., O'Regan, D.D., Duesberg, G.S., Nicolosi, V., and Coleman, J.N., Liquid exfoliation of solvent-stabilized few-layer black phosphorus for applications beyond electronics. *Nature Communications*, 2015. **6**: p. 8563.

29. Yasaei, P., Behranginia, A., Foroozan, T., Asadi, M., Kim, K., Khalili-Araghi, F., and Salehi-Khojin, A., Stable and Selective Humidity Sensing Using Stacked Black Phosphorus Flakes. *ACS Nano*, 2015. **9**(10): p. 9898-9905.

30. Derby, B., Inkjet Printing of Functional and Structural Materials: Fluid Property Requirements, Feature Stability, and Resolution. *Annual Review of Materials Research, Vol 40*, 2010. **40**: p. 395-414.

31. Torrisi, F., Hasan, T., Wu, W.P., Sun, Z.P., Lombardo, A., Kulmala, T.S., Hsieh, G.W., Jung, S.J., Bonaccorso, F., Paul, P.J., Chu, D.P., and Ferrari, A.C., Inkjet-Printed Graphene Electronics. *ACS Nano*, 2012. **6**(4): p. 2992-3006.

32. Li, J., Ye, F., Vaziri, S., Muhammed, M., Lemme, M.C., and Ostling, M., Efficient inkjet printing of graphene. *Advanced Materials*, 2013. **25**(29): p. 3985-3992.

33. Gao, Y.H., Shi, W., Wang, W.C., Leng, Y.P., and Zhao, Y.P., Inkjet Printing Patterns of Highly Conductive Pristine Graphene on Flexible Substrates. *Industrial & Engineering Chemistry Research*, 2014. **53**(43): p. 16777-16784.

34. Finn, D.J., Lotya, M., Cunningham, G., Smith, R.J., McCloskey, D., Donegan, J.F., and Coleman, J.N., Inkjet deposition of liquid-exfoliated graphene and MoS2 nanosheets for printed device applications. *Journal of Materials Chemistry C*, 2014. **2**(5): p. 925-932.

35. Li, J.T., Naiini, M.M., Vaziri, S., Lemme, M.C., and Ostling, M., Inkjet Printing of MoS2. *Advanced Functional Materials*, 2014. **24**(41): p. 6524-6531.

36. Zheng, J., Zhang, H., Dong, S., Liu, Y., Nai, C.T., Shin, H.S., Jeong, H.Y., Liu, B., and Loh, K.P., High yield exfoliation of two-dimensional chalcogenides using sodium naphthalenide. *Nature Communications*, 2014. **5**: p. 2995.

37. Jackman, M.J., Thomas, A.G., and Muryn, C., Photoelectron Spectroscopy Study of Stoichiometric and Reduced Anatase TiO2(101) Surfaces: The Effect of Subsurface Defects on Water Adsorption at Near-Ambient Pressures. *Journal of Physical Chemistry C*, 2015. **119**(24): p. 13682-13690.

38. Zhang, D.Z., Tong, J., Xia, B.K., and Xue, Q.Z., Ultrahigh performance humidity sensor based on layer-by-layer self-assembly of graphene oxide/polyelectrolyte nanocomposite film. *Sensors and Actuators B-Chemical*, 2014. **203**: p. 263-270.

39. Park, S., An, J.H., Jung, I.W., Piner, R.D., An, S.J., Li, X.S., Velamakanni, A., and Ruoff, R.S., Colloidal Suspensions of Highly Reduced Graphene Oxide in a Wide Variety of Organic Solvents. *Nano Letters*, 2009. **9**(4): p. 1593-1597.

40. Kim, W., Javey, A., Vermesh, O., Wang, O., Li, Y.M., and Dai, H.J., Hysteresis caused by water molecules in carbon nanotube field-effect transistors. *Nano Letters*, 2003. **3**(2): p. 193-198.

41. Feng, J., Peng, L.L., Wu, C.Z., Sun, X., Hu, S.L., Lin, C.W., Dai, J., Yang, J.L., and Xie, Y., Giant Moisture Responsiveness of VS2 Ultrathin Nanosheets for Novel Touchless Positioning Interface. *Advanced Materials*, 2012. **24**(15): p. 1969-1974.

42. Borini, S., White, R., Wei, D., Astley, M., Haque, S., Spigone, E., Harris, N., Kivioja, J., and Ryhanen, T., Ultrafast Graphene Oxide Humidity Sensors. *ACS Nano*, 2013. **7**(12): p. 11166-11173.

43. Corbrjdge, D.E.C., Infra-red analysis of phosphorus compounds. *Journal of Applied Chemistry*, 1956. **6**(10): p. 456-465.

44. Thomas, L.C. and Chittenden, R.A., Characteristic Infrared Absorption Frequencies of Organophosphorus Compounds .1. The Phosphoryl (P=O) Group. *Spectrochimica Acta*, 1964. **20**(3): p. 467-487.

45. Thomas, L.C. and Chittenden, R.A., Characteristic Infrared Absorption Frequencies of Organophosphorus Compounds .2. P-O-(X) Bonds. *Spectrochimica Acta*, 1964. **20**(3): p. 489-502.

46. Withnall, R. and Andrews, L., Ftir Spectra of the Photolysis Products of the Phosphine Ozone Complex in Solid Argon. *Journal of Physical Chemistry*, 1987. **91**(4): p. 784-797.

47. Edmonds, M.T., Tadich, A., Carvalho, A., Ziletti, A., O'Donnell, K.M., Koenig, S.P., Coker, D.F., Özyilmaz, B., Neto, A.H.C., and Fuhrer, M.S., Creating a Stable Oxide at the Surface of Black Phosphorus. *ACS Applied Materials & Interfaces*, 2015. **7**(27): p. 14557-14562.

48. Tsud, N. and Yoshitake, M., Vacuum vapour deposition of phenylphosphonic acid on amorphous alumina. *Surface Science*, 2007. **601**(14): p. 3060-3066.

49. Barbaux, Y., Dekiouk, M., Lemaguer, D., Gengembre, L., Huchette, D., and Grimblot, J., Bulk and Surface-Analysis of a Fe-P-O Oxydehydrogenation Catalyst. *Applied Catalysis a-General*, 1992. **90**(1): p. 51-60.

50. Kim, J.S., Liu, Y., Zhu, W., Kim, S., Wu, D., Tao, L., Dodabalapur, A., Lai, K., and Akinwande, D., Toward air-stable multilayer phosphorene thin-films and transistors. *Scientific Reports*, 2015. **5**: p. 8989.

51. Hanwick, T.J. and Hoffmann, P.O., Raman Spectra of Several Compounds Containing Phosphorus. *Journal of Chemical Physics*, 1951. **19**(6): p. 708-711.

52. Rudolph, W.W., Raman- and infrared-spectroscopic investigations of dilute aqueous phosphoric acid solutions. *Dalton Transactions*, 2010. **39**(40): p. 9642-9653.

53. Ziletti, A., Carvalho, A., Campbell, D.K., Coker, D.F., and Castro Neto, A.H., Oxygen defects in phosphorene. *Physical Review Letters*, 2015. **114**(4): p. 046801.

54. Vanýsek, P., Electrochemical Series. In Handbook of Chemistry and Physics: 93rd Edition. Haynes. *Haynes, W. M. Ed.; CRC Press: Boca Raton*, FL. 2012: p. 5–80.

Chapter 6 Conclusions and Future Work

6.1 Conclusions

The goal of this thesis was to explore the use of inkjet printing to deposit 2D materials for electronic applications. Graphene oxide (GO) and other black phosphorous inks have been produced in large quantities by exfoliating 2D crystals in appropriate liquid phase solvents. Such dispersions were shown to be compatible with inkjet printing and were successfully used to produce 2D materials-based conductors and devices. Conductive graphene patterns have been successfully printed for electronic application from GO inks followed by a reduction process. However, to obtain graphene patterns with high conductive and good morphology, there are still many problems to be resolved.

First, high conductivity rGO films with bulk conductivity in excess of 2×10^4 Sm^{-1} have been prepared by inkjet printing of a GO aqueous ink with a 60 μm nozzle head. The large GO sheets was synthesized using a modified Hummers' method and through careful control of processing conditions GO flakes were produced with a size ranging up to 200 μm, with mean flake size 35.9 μm. These GO flakes have been successfully ejected through a 60 μm inkjet printer nozzle without any blocking occurring, even though a significant fraction of the flakes are larger than the nozzle diameter. This observation can be explained if high shear forces in the print head during drop ejection cause alignment and reversible elastic folding or crumpling of the GO flakes. It was found that the large sized flakes show no greater incidence of permanent folding or wrinkling after printing when compared with smaller flakes in the same droplet or compared with flakes deposited by large drop casting.

GO is an insulator, thus, to form a conductive film the printed GO films were reduced to rGO by a low temperature gas phase reduction using HI at temperatures < 100 °C. The conductivity of these printed rGO films was found to increase with increasing number of printed layers to a maximum value with a printed film thickness of about 250 nm, which followed with a power law consistent with a percolation model of conductivity. GO inks covering a range of mean flake size from 0.69 μm to 35.9 μm were prepared to investigate the influence of flake size on rGO film conductivity. The conductivity of the rGO films over this size range is a weak function of the mean flake size in the GO inks

prior to printing and with there being a 60% improvement in film conductivity as the mean flake size increases from < 1 μm to 36.9 μm.

Further studies on the morphology of dried GO droplets were carried out. By printing droplets with different size of GO flakes, we observed that uniform dried drops form when using a substrate at a temperature of 30 °C when the size is larger than 10.3 μm, with inks containing smaller flakes showing an inhomogeneous coffee stain after drying. This transition GO flake size decreased to 3.68 μm with the substrate temperature increasing to 50 °C. Furthermore, decreasing the droplet size allows for the coffee ring formation down weaken or disappeared. A model based on the critical distance for flake migration during the drying process has been developed to explain this behaviour.

Besides GO, a BP ink was successfully deposited on substrates by inkjet printing, where the BP ink was produced by exfoliating BP in acetonitrile. A printed BP device showed a high sensitivity to moisture over a range of humidity from 11% to 97%. However, due to the instability of few-layer BP flakes, an irreversible change in device performance was observed when the BP film was exposed to atmospheres with RH > 11%. Further analysis of the degradation of BP film under humid conditions with infrared absorption showed the presence of phosphonate and other acidic phophorus oxide ions. It is found that the damage of BP film was not observed or occurred at slow rate when exposed to atmospheres of RH ~4%. These results indicate that the degradation of 2D BP flakes is strongly mediated by the presence of water. However, the full mechanism of BP degradation under atmospheric conditions still needs further study.

6.2 **Outlook and Future Work**

The work presented in this thesis demonstrated the use of inkjet printing to deposit 2D materials for functional applications. While this work provides a useful route for producing 2D materials-based functional electrical components, further investigation into the morphology of printed patterns of 2D nanoflakes and their properties is warranted. Thus, the following part will consider the outlook for future work based on the foundation of the results presented in this thesis.

In chapter 3, it was shown that GO flakes with size larger than the diameter of nozzle can be inkjet printed, and that this benefits the formation of uniform patterns after

drying. However, the upper limited of the printable size of GO flakes is currently unclear. Understanding the relationship between printable GO size and nozzle diameter will be also very useful for printing other 2D materials. Reduced GO films with high conductivity were obtained by reducing printed GO films with HI. It would be beneficial to replicate the action of HI using other environmentally and bio- friendly reducing agents such as Vitamin C. This work showed that the conductivity of the rGO films increased with increasing GO flake size, it would be interesting to measure the conductivity of these rGO films under different strains to find out their resistance to deformation of these rGO films at different flake size for flexible electronics applications.

The results in chapter 4 showed the coffee ring effect in printed GO droplets can be overcome by using large size GO flakes. However, the value of observed critical length is larger than that of the theoretical value. This is probably due to the non-uniform distribution of GO flakes prepared by sonication process. Thus, it is important to further find a route to prepare uniform size of GO flakes or separate the different size of GO more efficiently. Moreover, the effect of GO concentration on the final morphology of droplets is also important to further understand the controlling mechanism of CRE through flake size.

For the work in chapter 5, it would be interesting to further investigate the degradation mechanism of BP flakes in the presence of water and oxygen. It was observed that the degradation of BP flakes is very slow under dry air conditions, investigating the degradation of BP flakes occurs under moderate humidity but in an oxygen free environment is important to complete understand the degradation of BP flakes.

In recent years, 2D materials devices based on combining different 2D crystals to from vertical van der Walls heterostructures have already become very promising either for fundamental research or practical applications. The main versatile technique to assemble 2D crystal stacks now is direct mechanically assembly, which is slow and cumbersome. As 2D materials can be exfoliated in liquid phase to form inks, it is possible to assemble these van der Waals heterostructures through layer-by-layer deposition using inkjet printing. As we presented in chapter 3, small numbers of GO flakes can be deposited from a single droplet by using big flakes. Therefore, by adjusting the flake size and concentration, it is possible to eject a single flake per drop.

Using this principle and multiple ink compositions, printing procedures can be developed to print a second 2D flake material on top of previous drop pattern to form a stack structure. The ability to print combinations of 2D materials will open up a new route for low-cost fabrication of van der Waals heterostructures based devices.